

Aus dem Institut für Signalverarbeitung und Prozeßrechentechnik der  
Universität zu Lübeck

Direktor: Professor Dr.-Ing. Til Aach

**Technologien und Methoden für  
die akute, neuronale Vielfach-Ableitung**

Mikrostrukturtechnik, Datenaufnahme und Signal-Analyse in Echtzeit auf dem  
Weg zur direkten Gehirn-Maschine-Kopplung

Habilitationsschrift

verfaßt und der Technisch-Naturwissenschaftlichen-Fakultät  
der  
Universität zu Lübeck  
zur Erlangung der Venia legendi für das Fach Informatik  
vorgelegt von

Dr. rer.nat. Ulrich G. Hofmann  
aus München

Lübeck 2002

<b>1.</b>	<i>Originalarbeiten</i>	3
<b>2.</b>	<i>Motivierendes Ziel: Die direkte Gehirn-Maschine Kopplung</i>	5
<b>3.</b>	<i>Überblick über diese Arbeit</i>	7
<b>4.</b>	<i>Biologische Grundlagen des Gehirns</i>	8
<b>5.</b>	<i>Grundannahmen und Pflichtenheft: Meßsystem für die elektrophysiologische Vielfach-Ableitung</i>	10
<b>5.1.</b>	Experimentelle Anforderungen: Wetware	11
<b>5.2.</b>	Technische Anforderungen: Hardware	12
<b>5.3.</b>	Informationstechnische Anforderungen: Software	13
<b>6.</b>	<i>Methoden</i>	13
<b>6.1.</b>	Mikrostrukturtechnisch erzeugte Mikrosonden	13
6.1.1.	Design-Prinzipien	14
6.1.2.	Herstellungs-Prozess	14
6.1.3.	Resultate der Mikrostrukturtechnik	16
6.1.4.	Verbindungstechnik und Qualitätskontrolle	17
6.1.5.	Fortentwicklung für 64 Ableitpunkte und alternative Sonden	19
<b>6.2.</b>	DSP-gestützte Digitalisierung	20
6.2.1.	Signalverstärkung	20
6.2.2.	Vielkanal-Digitalisierung	22
<b>6.3.</b>	Datenaufnahme-Programm	24
6.3.1.	Grundfunktionen	24
6.3.2.	Signalverarbeitung mittels Wavelets	27
<b>6.4.</b>	Simulation realistischer Netzwerke	30
<b>7.</b>	<i>Ergebnisse</i>	31
<b>7.1.</b>	Virtuelle Experimente	31
<b>7.2.</b>	Reale Experimente	33
<b>8.</b>	<i>Vergleich mit anderen Projekten</i>	36
<b>9.</b>	<i>Ausblick</i>	38
<b>10.</b>	<i>Danksagung</i>	39
<b>11.</b>	<i>Glossar</i>	40
<b>12.</b>	<i>Literatur</i>	42
<b>13.</b>	<i>Appendix A: Beigefügte Arbeiten</i>	51
<b>14.</b>	<i>Appendix B: Technische Berichte des EU-Projektes VSAMUEL</i>	

## 1. Originalarbeiten

(♦ beigefügt im Appendix A)

### Mikrostrukturtechnik

- \* Hofmann UG, De Schutter E, de Curtis M, Yoshida K, Thomas U, and Norlin P, *On the design of multi-site microelectrodes for neuronal recordings*. MICRO.tec 2000, Vol1: (2000) 283-288.
- \* Hofmann UG, Folkers A, et al., *Towards a versatile system for advanced neuronal recordings using silicon multisite microelectrodes*. Biomedizinische Technik - Biomedical Engineering, 45(E 1): (2000) 169-170.
- \* Norlin P, Kindlundh M, Mouroux A, Yoshida K, Jensen W, and Hofmann UG. *A 32-site neural recording probe fabricated by double-sided deep reactive ion etching of Silicon-on-Insulator substrates*. in *12th Micromechanics Europe Workshop (MME-2001)*. (2001). Cork, Ireland.
- \* Yoshida K, Jensen W, Norlin P, Kindlundh M, and Hofmann UG, *Characterization of silicon microelectrodes from the EU VSAMUEL project*. Biomedizinische Technik, 46 E1: (2001) 446-447.
- ♦ Norlin P, Kindlundh M, Mouroux A, Yoshida K, and Hofmann UG, *A 32-site neural recording probe fabricated by DRIE of SOI substrates*. J. Micromechanics and Microelectronics, 12(4): (2002) 414-419.
- \* Kindlundh M, Norlin P, and Hofmann UG. *Development of multisite microelectrodes for neuroscience*. in *Proceedings of the Micro Structure Workshop MSW'02*. (2002). B8.1-B8.6 Aronsborg, Bålsta, Sweden.
- \* Hofmann, U.G., W. Jensen, K. Yoshida, M. Kindlundh, and P. Norlin, (2002) *Silizium Vielfachsonden für die Neurowissenschaften*. FOCUS MUL, 19(3): p. 132-139.

### Datenaufnahme

- \* Hofmann UG, Folkers A, et al., *Towards a versatile system for advanced neuronal recordings using silicon multisite microelectrodes*. Biomedizinische Technik - Biomedical Engineering, 45(E 1): (2000) 169-170.
- ♦ Folkers, A. and U.G. Hofmann, *A multichannel data acquisition and analysis system based on off-the-shelf DSP boards*, in *Proceedings of the EURASIP Conference on Digital Signal Processing for Multimedia Communications and Services*, K. Fazekas, Editor. 2001, Scientific Association of Infocommunications - HTE: Budapest. p. 249-252.
- \* Malina T, Folkers A, Mösch F, Labusch K, Schürmann M, and Hofmann UG, *An integrated system to trigger feedback-coupled event related brain potentials (ERPs)*. Biomedizinische Technik, 46 E1: (2001) 322-323.
- \* Malina T, Folkers A, and Hofmann UG, *Real-time EEG processing based on Wavelet Transformation*. FMBE - 12th Nordic Baltic Conference on Biomedical Engineering and Medical Physics, : (2002) 166-167.
- \* Hofmann UG, Folkers A, Mösch F, Höhl D, Kindlundh M, and Norlin P, *A 64(128)-channel multisite neuronal recording system*. Biomedizinische Technik, 47(E 1): (2002) 194-197.

### Signalverarbeitung

- \* Weber B, Malina T, Menne K, Folkers A, and Hofmann UG, *Handling large files of multisite microelectrode recordings for the European VSAMUEL consortium*. Neurocomputing, 38-40(1-4): (2001) 1725-1734.
- ♦ Folkers, A., F. Mösch, T. Malina, and U.G. Hofmann, (2002) *Realtime bioelectrical data acquisition and processing from 128 channels utilizing the Wavelet-Transformation*. in press with Neurocomputing.

## Simulation

- ◆ Menne K, Malina T, Folkers A, and Hofmann UG, *Biologically realistic simulation of a part of hippocampal CA3: Generation of testdata for the evaluation of spike detection algorithms*, in *5th German Workshop on Artificial Life - Abstracting and Synthesizing the Principles of Living Systems*, J.K. D. Polani, T. Martinetz, Editor. (IOS Press Infinix: 2002. Lübeck) 17-25.
- \* Menne KML, Folkers A, Maex R, Malina T, and Hofmann UG, *Test of spike sorting algorithms on the basis of simulated data*. Neurocomputing, 44-46: (2002) 1119-1126.
- \* Schuhart H, Menne K, and Hofmann U. *GROGRA and GENESIS: in computo grown neurons used for realistic compartmental modeling*. Abstract und Poster in *CNS\*02*. (2002). Chicago
- \* Menne KML, Maex R, and Hofmann U. *Biologically realistic simulated extracellular potential data as benchmark for the evaluation of spike detection algorithms*. Abstract und Poster in *CNS\*02*. (2002). Chicago
- \* Menne, K.M.L., H. Schuhart, M. Lipphardt, and U.G. Hofmann, (2003) *Benchmarking spike detection algorithms on the basis of virtual experimental data*. in preparation for IEEE TBME.

## Experimentelle Arbeiten

- \* Van Hooser SD, Hofmann UG, Kewley DT, and Bower JM, *Relationship between field potentials and spike activity in rat S1: multi-site cortical recordings and simulations*. Neurocomputing 32-33, : (2000) 591-596.
- \* Jensen W, Malina T, Hofmann UG, and Yoshida K. *Measurement of intrafascicular insertion force of a tungsten needle into peripheral nerve*. in *IEEE EMBS*. (2001). PaperID 517 Istanbul, Turkey.
- ◆ Biella, G.R., L. Uva, U.G. Hofmann, and M. deCurtis, (2002) *Associative interactions within the superficial layers of the entorhinal cortex of the guinea pig*. J. Neurophysiol, **88**(3): p. 1159-1165.1.
- ◆ Freiwald W, Stemman H, Wannig A, Kreiter AK, Hofmann UG, Hills MD, Kovacs GTA, Kewley DT, Bower JM, Eurich CW, and Wilke SD, *Stimulus representation in rat primary visual cortex: multi-electrode recordings and estimation theory*. Neurocomputing, 44-46: (2002) 407-416.

## 2 . Motivierendes Ziel: Die direkte Gehirn-Maschine Kopplung

Eine bedeutende Antriebsfeder menschlicher Erfindungsgabe besteht darin, die Reichweite persönlicher Einflußnahme über die eigene Zungen- oder Fingerspitzen hinaus zu erweitern. Besonders deutlich wird dieser Wunsch zur Reichweitenerhöhung sowohl in der Kommunikationstechnik<sup>1</sup>, als auch in der Waffentechnik<sup>2</sup> [1]. Dabei basiert aber ganz offensichtlich jeder Reichweiten-Fortschritt grundsätzlich darauf, dass das Individuum in der Lage ist, mittels seiner primären Aktoren, den Muskeln, mit der "technischen Reichweitenvergrößerung" (heutzutage z.B. Mobiltelefon oder Computer-Terminal) wechselzuwirken, also Aktionen hervorzurufen und dafür eine Erfolgskontrolle zu erhalten (Mensch-Maschine-Kommunikation) (siehe Abbildung 1).

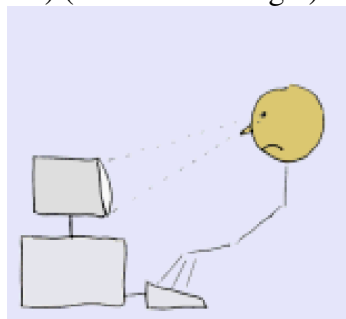


Abbildung 1: Schematische Darstellung klassischer Mensch-Maschine-Kommunikation [2]

Von den Vorteilen dieser Einflussnahme werden aber diejenigen Menschen vollkommen ausgeschlossen, die die Fähigkeit verloren haben, ihre eigenen Muskeln zu kontrollieren. Wenn dieser Verlust dann auch noch mit dem Erhalt der höheren kognitiven Fähigkeiten einhergeht, der Patient also noch vollkommen bei Bewußtsein ist, er aber in seinem autonom funktionierenden Körper "eingesperrt" scheint, so spricht man vom "locked-in Syndrom" [3-5]. Obwohl es für dieses Syndrom mehrere Ursachen geben kann (v.a. eine Hirnstamm-Ischämie), ist das "Eingesperrt-Sein" beim derzeit wohl bekanntesten Betroffenen, dem britischen Physiker Stephen Hawking, die Folge einer "Amyotrophen Lateral-Sklerose" (ALS) [4, 5]. Bei dieser neurologischen Erkrankung, im amerikanischen Sprachgebrauch "Lou Gehrigs Disease" genannt, sterben im Gehirn des Patienten sehr selektiv diejenigen Nervenzellen des Motor-Kortex ab, die die peripheren Muskeln innervieren [4]. Obwohl Professor Hawking mittlerweile nur mehr ein Muskel willentlich gehorcht, arbeitet er mit computertechnischer Unterstützung weiterhin als Kosmologe. Sein Beispiel zeigt, dass der Zustand "locked-in" kein Todesurteil sein muss. Er selbst teilt dazu halb scherhaft mit, dass er seine "Lebenserwartung schon mehrfach übertragen" habe [6]. Überaus wichtig für den Überlebenswillen des Betroffenen ist dabei aber offensichtlich neben guter Primärpflege auch der Erhalt seiner Kommunikationsfähigkeit, der Anbindung an die Außenwelt. Dafür ist aber letztlich eine neue Art der Mensch-Maschine-Kommunikation nötig, die nicht auf der Nutzung peripherer Muskeln basiert, sondern die eine direkte Ankopplung von computergestützten Effektoren an die funktionstüchtigen Areale des Gehirns beinhaltet: Ein sogenanntes "brain-computer interface" (BCI) oder "brain-machine interface" (BMI) wird benötigt.

<sup>1</sup> Verbale Überlieferung - schriftliche Botschaften - stationäres und mobiles Telefon

<sup>2</sup> Faust - Stein - Pfeil - Projektil - Interkontinentalrakete

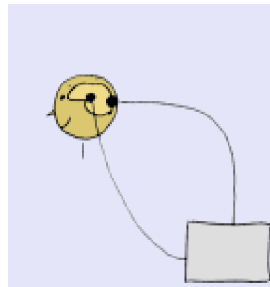


Abbildung 2: Schematische Darstellung der futuristischen, direkten Hirn-Computer-Kopplung (brain-machine interface, BMI) [2]

Bisherige Arbeiten (einen Überblick gibt [7]) haben zur Erreichung dieses Ziels zwei gangbare Wege identifiziert, den nichtinvasiven Ansatz, der im BCI realisiert wird und den invasiven Ansatz, der im BMI gipfelt.

Beim nichtinvasiven Ansatz (BCI) werden vom Kopf des Patienten abgeleitete oberflächliche, elektrische Potentiale (Elektro-Enzephalogramm) geschickt interpretiert und dienen der Steuerung einfacher Eingabesysteme, beispielsweise einer Computer-Maus [8-10]. Dabei widersetzt sich die makroskopische Struktur dieser Signale, gemäß ihrer Herkunft aus der gemittelten und verzerrten Aktivität extrem vieler Neuronen im Gehirn [11, 12], dem Versuch, präzise und schnell viele Steuerungskanäle anzusprechen. Übertragungsraten von maximal 24 bit/min sind derzeit denkbar, werden aber in der Realität zur Ansteuerung von Kommunikationsprogrammen nicht erreicht werden können [8]. Nichtsdestoweniger kann dieser Datendurchsatz aber grundsätzlich die Kommunikationsmöglichkeiten von locked-in Patienten wieder eröffnen und ihnen damit neuen Lebenswillen vermitteln [13]. Leider bleibt aber der nichtinvasive Ansatz auch in seiner optimalen Realisierung eine Einbahnstrasse, verbietet er doch grundsätzlich die spezifische und ebenso direkte Rückführung des Informationsflusses in die entscheidenden Bereiche des Gehirns.

Dem extrem herausfordernden Ziel der rückgekoppelten Hirn-Maschine-Kopplung (BMI) bleibt damit nur der invasive Weg über die Implantation technischer Hilfsmittel in das Gehirn [14-16]. Dieser Weg wird "Neuronale Prothetik" genannt, wobei die gewünschte Regelungsschleife dem technischen Ersatz spezifischer, eng umgrenzter Hirnareale und Funktionen dienen soll [17]. Entsprechend werden selbst einfache BMI-Systeme für wenige Funktionen die zeitliche (Millisekunden) und räumliche (wenige  $10 \mu\text{m}$ ) Auflösung erfordern, die die Mikroarchitektur des Gehirns vorgibt.

Jüngste Experimente zum BMI scheinen diesem Ansatz recht zu geben. Sie basieren darauf, eine Serie einzelner, ca.  $50\text{-}80\mu\text{m}$  dicker Ableitdrähte in den Cortex eines Versuchstieres zu implantieren [18-21]. Dabei wird eine hohe Traumatisierung durch Volumenverdrängung des Gewebes und eine geringe Dichte aufgezeichneter Nervenzellen in Kauf genommen. Wesentlich besser wäre es selbstverständlich, bei geringerer Traumatisierung deutlich höhere Neuronenzahlen abzuleiten und diese dann einem vielkanaligen Steuerungsmechanismus zuzuführen [22].

Konsequent zu Ende gedacht, wird in nicht allzu ferner Zukunft ein invasives Zwei-Wege-BMI die Möglichkeit eröffnen, defekte Hirnregionen von locked-in Patienten zu umgehen und durch externe Unterstützungs-Systeme (oder funktionelle Elektrostimulation [23]) wieder Bewegungen zu erzeugen. Letztendliches Ziel ist hier also eine funktionsfähige neuronale Prothese.

### 3. Überblick über diese Arbeit

Die im folgenden vorgestellten, interdisziplinären Ergebnisse stellen grundlegende Entwicklungsschritte auf dem Wege zur direkten kortikalen Gehirn-Maschine-Kopplung dar, indem sie bisher nicht erreichte Zahlen mikroskopischer, intrakortikaler Ableitpunkte bei gleichzeitiger Minimierung der Gehirnschädigung ermöglichen. Darüberhinaus führt der erfolgreiche Einsatz digitaler Signalprozessoren und moderner Verarbeitungsmethoden zu einem Quantensprung in der Automatisierung der Gewinnung extrem großer elektrophysiologischer Datenmengen und einem realistischen Schritt in Richtung Echtzeit-Auswertung und damit Echtzeit-Steuerung. Neue Kenntnisse und Informationen zur nötigen Optimierung der Verarbeitungs-Algorithmen werden dazu von der quantitativen Simulation biologisch realistischer Neuronennetze und den damit verbundenen Vorhersagemethoden geliefert.

Die durchgeföhrten Arbeiten lagen im Spannungsfeld der computergestützen Neurowissenschaften, der elektrophysiologischen Ableitungen, der Mikrostrukturtechnik (MST) und der angewandten Signalverarbeitung. Die Bandbreite erstreckt sich vom Entwurf und der Erzeugung gabelförmiger, mikroskopischer Vielkanal-Sonden, über deren experimentelle Nutzung im akuten Tierversuch, bis zur Software für die Darstellung, Aufnahme und Echtzeitanalyse der Signale.

Auf theoretischer Seite werden hochkomplexe, neurobiologisch realistische, aber künstliche Daten aus Simulationsrechnungen und virtuellen Experimenten vorgestellt und ihre Nutzung zur Verbesserung der Datenaufnahme eingeführt.

Praxis und Theorie befürworten sich dabei gegenseitig: Mikroelektrodenableitungen aus dem lebenden Gehirn liefern Daten, die durch digitale Signalverarbeitung ausgewertet werden, um dann in Übereinstimmung mit einem Computermodell neue sinnvolle Experimente zu planen und überprüfbare Vorhersagen zu treffen.

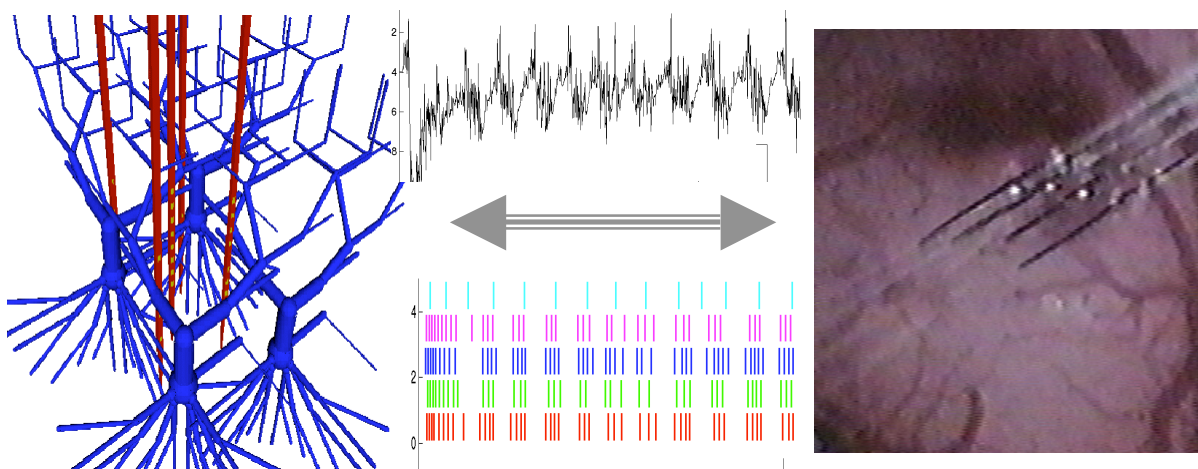


Abbildung 3: Darstellung der Bandbreite dieser Arbeit: Realistische Simulation (links) einer elektrophysiologischen Ableitung mit virtuellen Elektroden liefert ebenso Multikanal-Signale (Mitte oben) und Aktionspotentialzüge (Mitte unten) wie die realen gabelartigen Silizium-Sonden in einem akuten Ableitungsexperiment (rechts).

## 4. Biologische Grundlagen des Gehirns

Die folgende kurzgefasste Rekapitulation von neurobiologischen Grundlagen soll dem technischen Verständnis dieser Arbeit dienen. Für eine detaillierte Beschreibung des Aufbaus und der Funktionalität des Gehirns sei an dieser Stelle auf einschlägige Lehrbücher hingewiesen [11, 24-26].

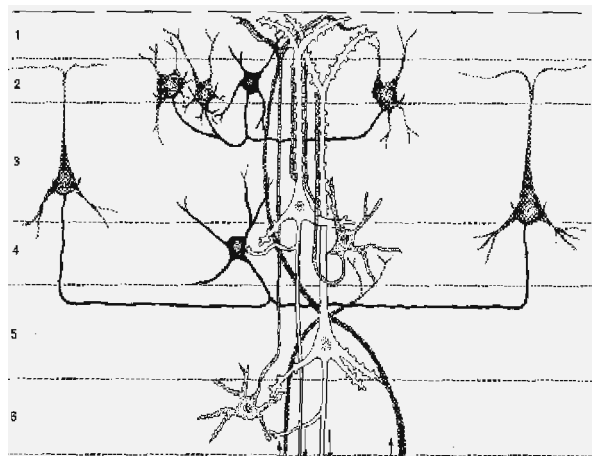


Abbildung 4: Die schematische Darstellung zeigt die idealisierte Form der elementaren kortikalen Recheneinheit, bestehend aus erregenden (dunkel) und hemmenden (hell) Zelltypen [11]. Die Ziffern am Rand bezeichnen Schichten in der vertikalen neokortikalen Anatomie, die bei entsprechender Anfärbung erkennbar werden.

Eine wichtige neurobiologische Grundlage besteht darin, dass sich die Feinstruktur nahezu aller Hirnregionen durch einen geschichteten Aufbau auszeichnet und aus einer Vielzahl von elektrisch aktiven und inaktiven Zellen besteht (siehe Abbildung 4). Dabei bestehen elementare Rechenelemente aus den funktionellen Kopplungen von elektrisch aktiven, erregenden (Abbildung 4: helle Pyramidenzellen) und hemmenden Neuronen (Abbildung 4 dunkle Interneurone). Elektrisch inaktive Zellen wie Glia-Zellen, dienen im Allgemeinen als Infrastrukturbildner und Versorgungseinheiten, nehmen aber an der schnellen interzellulären Kommunikationsverarbeitung nicht teil.

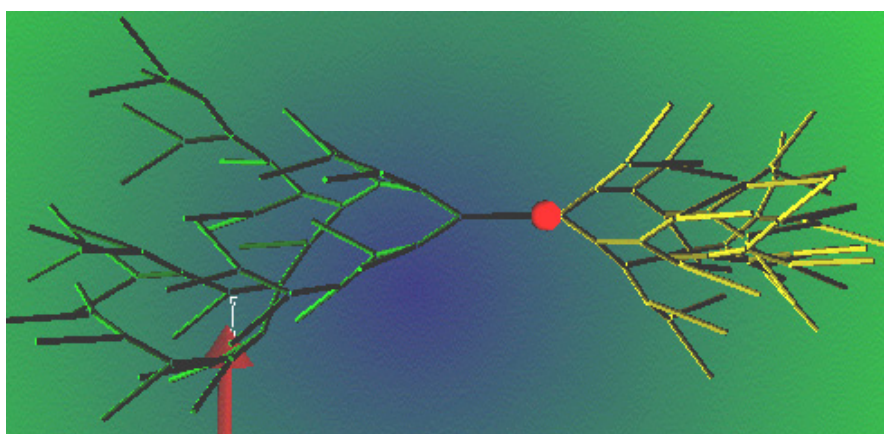


Abbildung 5: *In computo* erzeugtes Modell einer Pyramidenzelle des Hippocampus [27]: Kugelig gezeichnet ist der Zellkörper, dünne Anhängsel zeigen den apikalen, resp. den basalen Dendritenbaum. Nicht dargestellt sind das Axon und Synapsen. Der Pfeil unten liegt parallel zur Hirnoberfläche der Schichtstruktur.

Wie alle anderen Säugetierzellen sind elektrisch aktive Neuronen durch eine Lipiddoppelmembran von ihrer Umgebung abgegrenzt. Sie bestehen in der Regel aus einem Zellkörper, dem Soma, an dem als besonderes Merkmal ein langer Fortsatz, das Axon, entspringt. Ebenso entspringen am Soma einer oder mehrere Dendritenbäume (siehe Abbildung 5). Diese sind neben dem Soma der bevorzugte Zielpunkt von synaptischen Endknöpfchen anderer Neuronen und verfügen über ausgeprägte nichtlineare Eigenschaften der Informationsverarbeitung [28].

Die an der Informationsverarbeitung teilnehmenden Zellen kommunizieren zwar mittels ihrer mikroskopischen Synapsen und den dort eingesetzten hemmenden oder erregenden Neurotransmittern<sup>3</sup> auf chemischem Wege, aber die hervorgerufenen Effekte sind elektrischer Natur: Neuronen unterhalten im Intra- und Extrazellulärraum unterschiedliche Ionen-Konzentrationen<sup>4</sup>, die damit gemäß der Nernst'schen Gleichung<sup>5</sup> ein Ruhepotential von - 70mV aufbauen können. Synaptische Ereignisse können nun die Membranpotentiale im postsynaptischen Dendritenbaum und dem Soma ändern [29], welches dann quasi als Ergebnis der dendritischen Berechnungen gemäß eines "Alles-oder-Nichts-Gesetzes" beim Überschreiten eines Potentialschwellwertes ein sehr schnelles Aktionspotential abgibt - die Zelle feuert einen "Spike". Dieses Aktionspotential wird dann wiederum über das zelluläre Axon und entsprechende Synapsen an nachfolgende, verknüpfte Zellen weitergegeben. Bei allen zellulär-elektrischen Ereignissen handelt es sich letztlich um gesteuerte Umlagerungen von Ionen über die dünne Zellmembran hinweg, die physikalisch einem Strom entspricht. Ein Aktionspotential beispielsweise wird beim Überschreiten (Depolarisation) des Grenzwertes von ca. - 40mV durch den schnellen Einstrom von Natrium-Ionen und nachfolgendem langsameren Ausstrom von Kalium-Ionen erklärt [30-33]. Ein Spike zeigt eine charakteristische Dauer von 1-2 msec. Unterschwellwertige, synaptisch-dendritische Ströme laufen dagegen viel langsamer ab, eher in der Zeitskala von 10-100 msec. Da es sich aber im Allgemeinen bei allen zellulär elektrischen Ereignissen um lokale, disjunkte Transmembranströme handelt, deren Stromfluss im Zellinneren axial verbunden ist, muss der Extrazellulärraum den jeweiligen Stromkreis schließen. Man kann also auf der Zelloberfläche elektrische Quellen und Senken angeben, die jeweils im Inneren und Äußeren der Zelle durch Ionenleitung verbunden sind. Der spezifische Widerstand im Außenraum liegt dabei vor allem wegen seiner eng kanalisierten Ausbreitung in Zwischenzellräumen des Gehirns etwa in der Größenordnung von 1000-4000  $\Omega$ cm [34, 35]. Der intrazelluläre co-axiale Widerstand liegt dagegen bei etwa 100  $\Omega$ cm [26]. Da der transmembrane Widerstand diese Werte um Größenordnungen übertrifft, ist es also möglich, dass der ionische Strom große Strecken im Axon fließt, bis er an einer geeigneten Stelle durch die Ionenkanäle der Membran hindurch in den Extrazellulärraum austritt. Im Extrazellulärraum des Gehirngewebes können damit Mikroelektroden die elektrischen Ereignisse im Inneren einzelner Neuronen dokumentieren [36, 37]. Dabei zeigt sich neben der unterschiedlichen Zeitkonstante der beiden erwähnten elektrischen Ereignisse auch noch ein weiterer wichtiger Unterschied: Dendritische Potentiale sind großräumig gekoppelt, ändern sich langsam und liefern durch die großen beteiligten Membranflächen und Ionenflüsse extrazelluläre Potentiale in der Größenordnung von 1-10mV, die man dann "lokale Feldpotentiale" (LFP) nennt [38-40]. Dagegen sind die Quellen einzelner Spikes weitgehend auf den Ursprung des Axons am Soma festlegbar und in ihren Signalstärken sehr gering, etwa 50-250  $\mu$ V [35, 41]. Da die zugrundeliegenden Ströme mit steigendem Abstand zur Quelle abnehmen, kann man davon ausgehen, dass Spikes einer

<sup>3</sup> Erregend z.B.: Acetylcholin oder Dopamin; hemmend z.B.:  $\gamma$ -Aminobuttersäure (GABA) oder Glyzin

<sup>4</sup> Verhältnis der wichtigsten Ionenkonzentrationen Innen zu Außen: K<sup>+</sup>: 20:1; Na<sup>+</sup>: 1:9; Cl<sup>-</sup>: 1:14; Ca<sup>2+</sup>: 1:30000;

<sup>5</sup> Die Nernst'sche Gleichung besagt, dass über eine Membran, die zwei Bereiche unterschiedlicher Ionenkonzentration c(1) und c(2) trennt, ein elektrisches Potential V<sub>21</sub> gemessen werden kann:  $V_{21} = (RT/zF) \ln[c(2)/c(1)]$ . z bezeichnet die Ladung des Ions, R die Gaskonstante, T die Temperatur und F die Faradaykonstante

bestimmten Zelle bereits etwa  $60\mu\text{m}$  bis  $100\mu\text{m}$  von der Quelle entfernt im generellen Hintergrundrauschen untergehen<sup>6</sup>. Andererseits ermöglicht es dieser Messhorizont, mit einer einzelnen Elektrode von mehreren Neuronen im Umkreis abzuleiten [42, 43].

Im Gegensatz dazu zielt die mikroskopische Ableitung und Interpretation von lokalen Feldpotentialen auf die präzise Kartierung von mikroskopischen, synaptischen Netzwerken und damit auf die mikrofunktionelle Analyse von mehr oder weniger ausgeprägten "Schaltkreisen" [44, 45].

Ohne an dieser Stelle den Raum zu haben, auf Details einzugehen, sei erwähnt, dass Signale z.B. aus den Sinnesorganen, über mehrere Verschaltungsstationen zu höheren Gehirnregionen weitergegeben und dabei wieder und wieder bearbeitet werden. Ein Beispiel ist der hierarchische und zugleich hochparallele Aufbau des Riechsystems vom Riechepithel über die Glomeruli zum dreischichtigen Riechkoben, dem entorhinalen und schließlich dem piriformen Kortex [46, 47]. Dabei besteht die allgemeine Annahme darin, dass Informationen in Form von Aktionspotentialfolgen, sogenannten "spike trains" und ihren Feuer-Häufigkeiten codiert werden. Man kann zum Beispiel Neuronen des visuellen Kortex finden, die eine maximale Feuerrate von etwa 100 Spikes/sec aufweisen, wenn im zugehörigen rezeptiven Feld der Netzhaut ein Balken im Winkel  $\alpha$  präsentiert wird. Jede Abweichung vom optimalen Winkel  $\alpha$  wird durch eine Veränderung der Feuerrate quittiert. Insgesamt werden auf diese Art und Weise sogenannte Empfindlichkeitskurven ("tuning curves") definiert [48-50]. Einer grundlegenden Eigenschaft des Gehirnaufbaus entspricht es dabei, identische Informationen auf eine Vielzahl von Zellen und verarbeitenden Netzwerken zu verteilen - im Ganzen also hochredundant und parallel Information zu prozessieren.

Informationen werden also im Gegensatz zur Digitalelektronik parallel und in assoziativer Form gespeichert und weiterverarbeitet [51, 52]. Dadurch kann eine relevante Information in einer Vielzahl von Neuronen präsent sein und ist somit prinzipiell auch durch Ableitung verschiedener Zellen zugänglich. Wie oben erwähnt, kann somit durch die vielfache Ableitung von neuronalen Signalen sehr präzise die Informationsverarbeitung im Gehirn nachverfolgt werden, sofern man Zugriff auf mehrere Verschaltungsebenen und eine Vielzahl von Zellen hat [53, 54].

Dabei ist es durch die hohe Redundanz glücklicherweise nicht notwendig jede einzelne Zelle zu überwachen, um Rückschlüsse auf den zugrundeliegenden Reiz, d.h. die zugrundeliegende Information, zu ziehen. Ein Unterfangen, das bei etwa  $10^5$  Zellen pro Kubikmillimeter Hirnvolumen schon bei der Maus hoffnungslos wäre [55]. Ausschließlich diese biologischen Gegebenheiten der assoziativen Speicherung und der Informationsverarbeitung in parallelen Netzen erlauben die realistische Hoffnung auf eine funktionsfähige kortikale Schnittstelle mit weniger Kontaktstellen als Zellen im Gehirn. Dagegen können bereits heute wichtige Fragen der angewandten und grundlegenden Hirnforschung mit Hilfe der vielkanaligen extrazellulären Ableitung bearbeitet werden.

## **5. Grundannahmen und Pflichtenheft: Meßsystem für die elektrophysiologische Vielfach-Ableitung**

Die konkrete Aufgabe dieser Arbeit besteht entsprechend darin, ein komplettes, global nutzbares Experimentalsystem zu entwerfen und aufzubauen, das auf möglichst unkomplizierte Weise die Ableitung von möglichst vielen Zellen aus der Zielregion des Gehirns eines anästhesierten Versuchstieres ermöglicht. Abbildung 6 zeigt den gewünschten prinzipiellen Aufbau eines vollständigen Ableitsystems mit Vielfach-Mikroelektroden nahe an den Zellkörpern einiger kortikaler Pyramidenzellen.

<sup>6</sup> Diese Entfernung entspricht etwa 3-5 mal dem durchschnittlichen Soma-Durchmesser.

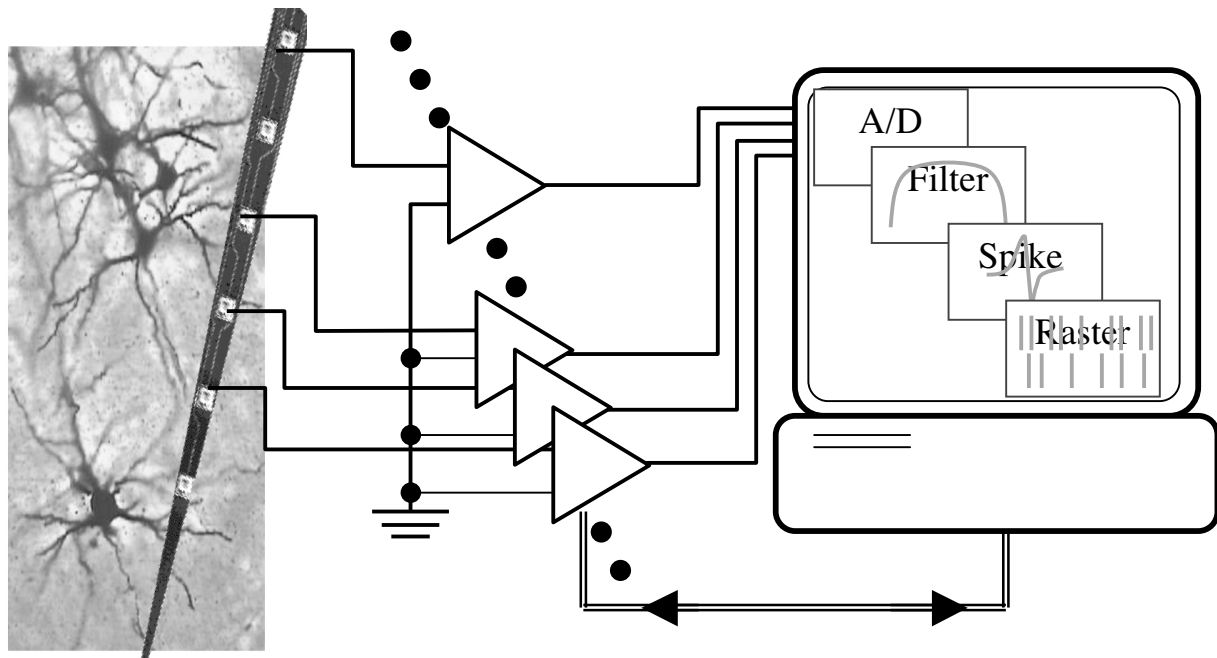


Abbildung 6: Überblick über ein neuronales Vielkanal-Messsystem: Mikroelektroden (gelb) auf einem Siliziumträger (blau) messen die extrazellulären Signale kortikaler Pyramidenzellen (Golgi-gefärbt, Hintergrund links) (Ausschnitt aus [56]). Die Ableitungen dieser Mikroelektroden werden über Verstärker (Mitte) in einen PC weitergeleitet, wo sie digitalisiert, gefiltert, gespeichert, dargestellt und prozessiert werden. Der PC dient gleichzeitig dazu, die Verstärker zu steuern.

### 5.1. Experimentelle Anforderungen: Wetware

Aus einer Unzahl von verschiedenen Tiermodellen und Zielregionen haben wir zur technischen Spezifikation die Vorgaben von akute Präparationen im Gehirn von Ratten und Meerschweinchen ausgewählt: Primärer somatosensorischer Kortex [57, 58] und Crus IIa Region des Kleinhirns von anästhesierten Laborratten [59-62], sowie der entorhinale und piriforme Kortex einer Ganzhirn-Präparation am Meerschweinchen [44, 45, 63, 64]. In diese bewußt unterschiedlichen anatomischen Zielregionen sollten jeweils bis zu 128 Mikroelektroden mit möglichst geringer Gewebeverletzung und optimiert auf die Zellverteilung in einem einzigen Präparationsschritt implantiert werden.

Tabelle 1:

Tier	Region, Größe	Zielzellen	$\varnothing$ Soma	Dendriten Ausdehnung	Vertikale Position	Anordnung	Gewünschte Signale
Ratte	Kortex, SI 5x5 mm	Pyramidenzelle (Pyr)	$\approx 20 - 30 \mu\text{m}$	$\approx 1000 \mu\text{m}$ , baumförmig	$\approx 300 - 1200 \mu\text{m}$	Siehe Abbildung 4	Spikes, evtl. repetitiv
Ratte	Kleinhirn, 4x4 mm	Purkinje Zelle (PC)	$\approx 20 - 30 \mu\text{m}$	$\approx 350 \mu\text{m}$ , sehr flach	$\approx 40 - 400 \mu\text{m}$	Senkrecht zu Parallelfaser	Spikes
		Golgi Zelle (GC)	$\approx 30 \mu\text{m}$	$\approx 200 \mu\text{m}$ , zylindrisch	$\approx 400 - 1000 \mu\text{m}$	$\approx 300 \mu\text{m}$ von GC zu GC	
Meerschwein	Pirif. Kortex 4x4 mm	Pyramiden und Interneurone	$\approx 15 - 30 \mu\text{m}$	$\approx 1200 \mu\text{m}$	$\approx 0 - 1400 \mu\text{m}$	"Unterseite" des Gehirns	LFP
	Entorhinaler Kortex	"Funktionelles Modul"	$\varnothing 600 \mu\text{m}$		$\approx 0 - 1500 \mu\text{m}$		

Tabelle 1 nennt einige der unterschiedlichen Anforderungen, die sich aus der Mikroanatomie der Zielregionen ergeben [11, 65-68].

Insgesamt sollen die gewünschten Elektrodenpositionen einerseits den horizontalen, oberflächlich erkennbaren Strukturen folgen, aber zugleich müssen sie der vertikalen Verteilungen der Zielzellen und ihrer Dendriten gerecht werden. Entsprechend ist eine

Anordnung der Elektroden in Form eines Gitters senkrecht zur Hirnoberfläche (z.B. parallel oder coaxial zu den Parallelfasern des Kleinhirn-Foliums) erforderlich, zum Zwecke der Trauma-Minimierung am besten in mehreren Reihen. Abbildung 7 zeigt beispielhaft jeweils eine maßstabsgerechte, kortikale und eine zerebellare Design-Anordnung auf angefärbten Querschnitten der jeweiligen Hirnregionen [66, 69].

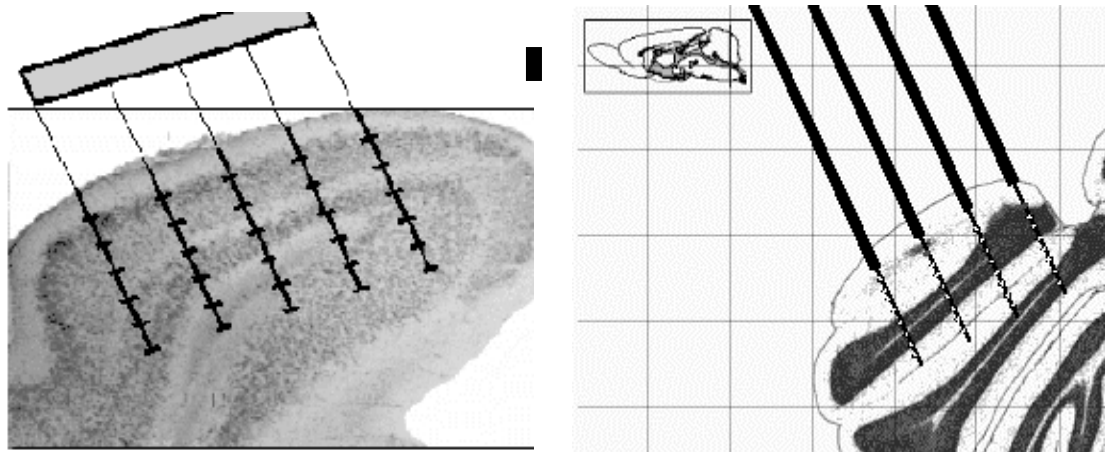


Abbildung 7: Gewünschte maßstäbliche Anordnung von Mikroelektroden auf gefärbten Querschnitten des Rattenhirns. Die kortikale Elektrodenmatrix (links) beinhaltet 5 Schäfte im Abstand von  $500\text{ }\mu\text{m}$  mit jeweils 6 Elektroden im Abstand von  $200\text{ }\mu\text{m}$ . Die zerebellare Matrix enthält 4 Schäfte im Abstand von  $400\text{ }\mu\text{m}$  mit jeweils 8 Elektroden im Abstand von jeweils  $100\text{ }\mu\text{m}$ .

Die Mikroelektroden müssen einerseits im Gewebe eine optimale elektrische Ankopplung bei minimaler Toxizität gewährleisten und andererseits in einem mikrostrukturtechnischen (MST) Massenverfahren günstig herstellbar sein. Als Träger wird also Silizium in Betracht gezogen, da es kompatibel mit üblichen Halbleiterprozessen ist und nach dem Herstellungsprozess durch eine native Oxid-Schicht passiviert wird [70-78]. Durch die gewünschte Herstellung in einem CMOS-kompatiblen Prozess stehen als mögliche Elektrodenmaterialien nur Edelmetalle wie Platin (Pt), Rhodium (Rh), Iridium (Ir), Gold (Au), oder Kombinationen davon zur Verfügung [79-81]. Da diese Materialien aber leider sogenannte polarisierbare Grenzflächen zum umgebenden elektrolytischen Medium bilden [82-84], muss eine frequenzabhängige Übergangsimpedanz in Kauf genommen werden. Im Anbetracht der geringen Signalstärken ist es in der Elektrophysiologie gewünscht, Übergangsimpedanzen der Mikroelektroden von wenigen Megaohm ( $1\text{-}4\text{ M}\Omega$ ) bei Anregungsfrequenzen um  $1\text{ kHz}$  zu erreichen [85].

Die Kontakte der fertigen Mikroelektrodensonden sollten außerdem in einem Mikrolötprozess, dem sog. "wire bonding", über makroskopische Verbindungen und handelsübliche Steckverbinder zur Vorverstärkung geführt werden. Diese Verbindungskabel müssen den implantierten und damit immobilen Mikroelektroden und dem umgebenden experimentellen Aufbau flexibel angepasst werden und zeitweise dem aggressiven physiologischen Salzmedium widerstehen können.

## 5.2. Technische Anforderungen: Hardware

Verstärkte Daten sollen mit vollständiger, relevanter Frequenzbandbreite intrakortikaler neuronaler Signale erfasst werden (z.B. [12, 65]): Feldpotentiale im Frequenzbereich von  $0,05\text{Hz} - 300\text{Hz}$  sollen ebenso aufgenommen werden wie darauf aufgeprägte Aktionspotentiale von ca.  $400\text{Hz} - 15\text{kHz}$  Bandbreite. Um die Ausbaufähigkeit auf weitere, noch offene biophysikalische Fragestellungen zu erhalten und um eine möglichst detaillierte Aufzeichnung von Spikes zu gewährleisten, wurde eine digitale Abtastrate von  $50\text{kHz}$  pro Kanal projektiert. Das entspricht einer Nyquist-Frequenz von  $25\text{ kHz}$ , also weit oberhalb der

derzeit höchsten interessierenden Frequenz von 15 kHz. Um der oben erwähnten Dynamik der spezifizierten Signale Rechnung zu tragen (Feldpotentiale 1-10 mV, darauf aufgeprägt Aktionspotentiale 50-250  $\mu$ V) [58], müssen die Abtastwerte jeweils in 16 bit Datentiefe digitalisiert werden, was einem kontinuierlichen, unprozessierten Datenaufkommen von 100 kByte pro Sekunde und Kanal entspricht. Diese an und für sich nicht sehr beeindruckende Zahl wird nun mit den maximal gewünschten 128 Ableitkanälen multipliziert und führt dann zu einem rohen Datenaufkommen von mindestens 12,8 Mbyte pro Sekunde, das prozessiert, visualisiert und gespeichert werden muß.

Dabei erscheint es uns ebenso wichtig, das gesamte Datenaufnahmesystem möglichst preiswert zu realisieren, um eine nachfolgende verbreitete Nutzung auch in kleineren elektrophysiologischen Labors zu ermöglichen. Hierzu bietet sich als Basis ein Windows®-basierter Personal-Computer an.

### **5.3. Informationstechnische Anforderungen: Software**

In Anbetracht des erwarteten immensen Datenaufkommens einerseits und dem standesgemäßen Misstrauen von experimentellen Elektrophysiologen andererseits muss die intuitiv handhabbare Datenaufnahme-Software zumindest auch eine Funktionensammlung zur Datenreduktion und automatischen Analyse in Echtzeit beinhalten, die auf nachprüfbarer und verlässlicher Algorithmen basiert. Im Wesentlichen sind Neurobiologen meist nicht an den breitbandigen Roh-Signalen interessiert, sondern entweder an der zeitlich präzisen und zellulär-individuellen Abfolge von Spikes (den sog. "spike-trains") (z.B. [86, 87]) oder an der elektrischen Quellen-Senken-Verteilung [39, 40] entlang einer Sonden-Trajektorie, wie sie aus den Feldpotentialen abgeleitet werden kann ("current-source-density", CSD). Letzteres kann mittels eines diskreten zweidimensionalen Laplace-Operators [88, 89] errechnet werden, während ersteres ein aufwändiges Verfahren voraussetzt, das sog. "Spike-Sorting". Dabei müssen zunächst einzelne Spikes im meist verrauschten Ursprungssignal detektiert werden, um anschließend mittels einer hochdimensionalen Klassifizierung wieder einzelnen Quelleinheiten zugeordnet zu werden [65, 90]. Andererseits entspricht offensichtlich die Reduktion des gesamten Datensatzes auf die schlichten Ereigniszeiten (den "spike-trains") einer maximalen Datenkomprimierung [65].

Bei allen automatischen Analysemethoden ist jedenfalls die mathematische Vertrauenswürdigkeit der eingesetzten Algorithmen ein Aspekt, der der besonderen Beachtung bedarf, basieren doch alle bisherigen, vergleichenden Ansätze im Grunde nur auf subjektiv bewerteten Daten [42, 90-93]. Ein echtes, vergleichendes Benchmarking basierend auf vollkommen kontrollier- und nachprüfbar Simulations-Daten muss deshalb die Basis für alle eingesetzten Analyse-Methoden bilden.

Dem Nutzer soll insgesamt die größtmögliche Freiheit zugestanden werden, seine Daten mit immensem Speicherbedarf unbearbeitet zu speichern oder synchron zur Aufzeichnung zu bearbeiten und zu analysieren; aber auch eine nachfolgende, off-line-Weiterverarbeitung muss ihm unbenommen bleiben.

## **6. Methoden**

### **6.1. Mikrostrukturtechnisch erzeugte Mikrosonden**

Die im Folgenden zusammengefassten Ergebnisse der MST-Arbeiten [69, 94, 95] wurden in den Reinräumen der Königlich Schwedischen Hochschule, Stockholm, in Zusammenarbeit mit Peter Norlin und Maria Kindlundh der Forschungseinrichtung Acreo AB erzielt.

### 6.1.1. Design-Prinzipien

Die erwähnten Zielregionen unterscheiden sich deutlich in ihren anatomischen und signaltechnischen Anforderungen (siehe Tabelle 1), was dazu führt, einen recht großen Teil des experimentell überhaupt wünschenswerten Parameterraumes abdecken zu müssen:

Tabelle 2 listet 8 verschiedene Entwürfe für 32-kanalige Sonden nach Anzahl ihrer Schäfte, dem Mittelpunktsabstand der Elektroden und Schäfte, der Gesamtlänge der Schäfte und der Länge des besonders dünnen, elektrodenträgenden Teils, hier als "aktive" Länge bezeichnet.

Tabelle 2:

Id.Nr.	Schäfte x Elektroden	Elektrodendist. / $\mu\text{m}$	Schaftdistanz / $\mu\text{m}$	Gesamtlänge / $\mu\text{m}$	"Aktive" Länge / $\mu\text{m}$	Zielregion, Signale
M1	1 x 32	50	-	7000	1860	Kortex; LFP
M2	5 x 6	200	500	10000	1700	Kortex; LFP, Spikes
E1	4 x 8	100	400	5000	1200	Kleinhirn; LFP, Spikes
E2	8 x 4	≈200	200	4000	1200	Kleinhirn; Spikes
E3	4 x 8	200	200	5000	2000	Tiefe Kleinhirn-Kerne; Spikes
K1	4 x 8	100	500	15000	1200	Peripherie Nerven; Spikes
U1	4 x 8	100	250	10000	4000	Pontine Kerne; Spikes
U2	4 x 8	50	60	5000	1000	Triangulation [96-98]

Zusätzlich sind die jeweiligen projektierten Zielregionen genannt. Die einzelnen Designs werden in einer Graphik zusammengefasst (Abbildung 8 links), wobei alle Sonden zur Vereinfachung dasselbe Kontaktschema erhalten. Diese graphische Einheit ("stepper-unit") wird durch ein schrittweises, photolithographisches Verfahren vielfach auf eine photolackbeschichtete Silizium-Scheibe ("Wafer") projiziert (Abbildung 8 rechts).

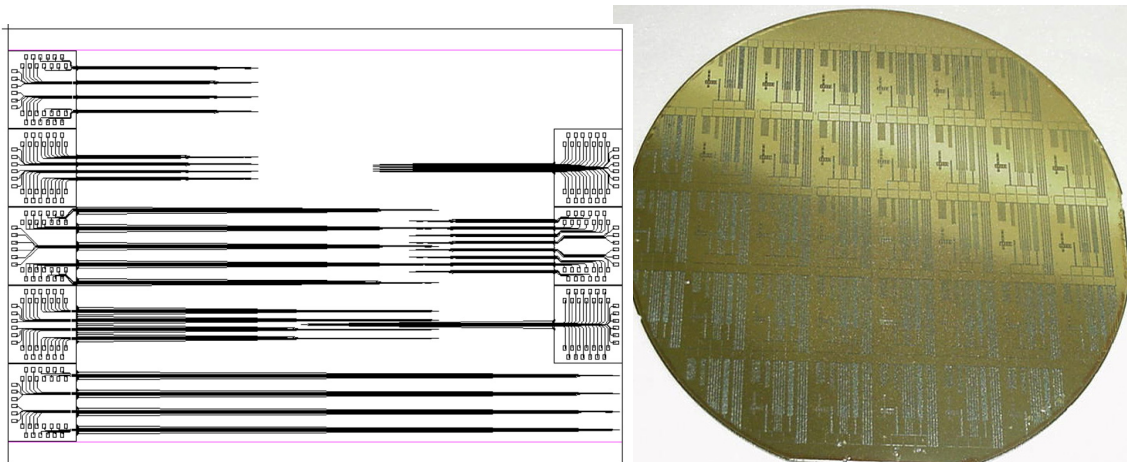


Abbildung 8: "Stepper-Unit" (links) und kompletter Wafer mit Goldbedampfung (rechts). Sonden auf der Stepper-Unit v.l.o.: E1, E3, M2, U1, K1, M1, E2, U2. Deutlich ist auf dem Wafer die 36fache Wiederholung der Stepper-Unit in Gold zu erkennen.

### 6.1.2. Herstellungs-Prozess

Das Besondere unserer Wafer liegt in ihrem Inneren: Eine  $2 \mu\text{m}$  dicke Silizium-Oxid-Schicht liegt  $25 \mu\text{m}$  tief unter der hochpolierten Si-Oberfläche "begraben" (Abbildung 9a). Die Oberfläche dieses "silicon-on-insulator" (SOI) Wafers wird, wie im CMOS-Verfahren üblich, durch die sog. "lift-off" Technik mittels 4 Masken (Abbildung 9 b - e), Photolack (siehe

Abbildung 9) und verspannungsarmer Dünnschichtaufdampfung strukturiert. Die Anforderungen an die Strukturgrößen sind mit  $1\text{-}3 \mu\text{m}$  aber im Gegensatz zu heutigen Mikrochips (routinemäßig  $0,18 \mu\text{m}$  [99]) recht moderat. Die Verbindungslien werden durch das Aufdampfen einer dünnen Schicht Titan als Haftvermittler gefolgt von Gold als Leiterbahn erzeugt (Abbildung 9 b). Als nächste Schicht und Isolation folgt eine Lage besonders stress-armen Siliziumnitrits ( $\text{Si}_3\text{N}_4$ ) (Abbildung 9 c), erzeugt in einem Doppel-frequenz Plasmaverfahren (PECVD, "plasma enhanced chemical vapor deposition") [100]. Nach einem Ätzschritt, der die Verbindungswege zur Durchkontaktierung im nächsten Depositionsschritt öffnet, werden mittels Titan/Iridium oder Platin die Mikroelektroden erzeugt (Abbildung 9 d) und wieder mit  $\text{Si}_3\text{N}_4$  isoliert (Abbildung 9 e).

Die Besonderheit unserer eingesetzten Mikrostrukturtechnik besteht im Trockenätzprozess und kommt mit den Masken 5 (Rückseite, Abbildung 9 f) und 6 (Vorderseite, Abbildung 9 g) zum vollen Einsatz. Das tief, reaktive Ionen-Ätzen ("deep reactive ion etching", DRIE, auch Bosch-Prozess genannt) bringt zwar ein grundsätzlich isotrop ätzendes Ionen-Plasma zum Einsatz, jedoch schlagen sich beigelegte, organische Bestandteile auf den freigelegten Seitenflächen des Siliziums nieder und schützen es vor weiterem Abtrag. Daraus resultiert ein quasi anisotroper Ätzprozess, der besonders hohe Ansichtsverhältnisse bei geringem Unterschnitt erlaubt. Nacheinander auf die Rück- und Frontseite des Wafers angewandt und jeweils am vergrabenen Silizium-Oxid in  $25 \mu\text{m}$  Tiefe stoppend, ermöglicht der letzte Ätzschritt dieses Oxids (Abbildung 9 g) die Freilegung der extrem langen,  $25 \mu\text{m}$  dicken Sonden. Durch geeignete Masken für die Rückseite des Wafers können wir die volle Wafer-Dicke an der  $2,2 \times 1,9 \text{ mm}^2$  Basis erhalten. Letzteres ermöglicht es im Prinzip, die fertigen Sonden auch vor Ort mit einer gewöhnlichen Pinzette zu ergreifen.

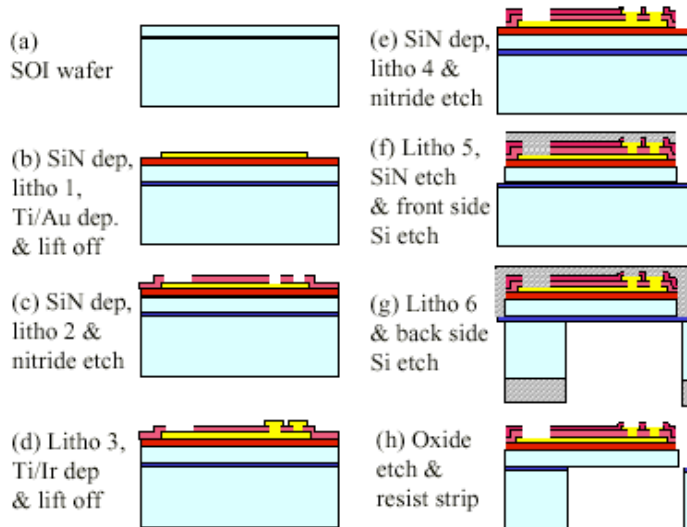


Abbildung 9: Schema des eingesetzten Halbleiterprozesses. Erklärung siehe Text.

Sehr klar wird durch den linken Teil der Abbildung 10 die Bedeutung des letzten Prozessschrittes, in dem sowohl die letzte Photolack-Schicht entfernt, als auch die ehemals verdeckte, jetzt freigelegte Oxid-Schicht endgültig entfernt werden muss. Dort sieht man an den sondenartigen Teststrukturen sägezahnartige Silizium-Oxid-Grade (Pfeile in Abbildung 10), die entfernt werden müssen.

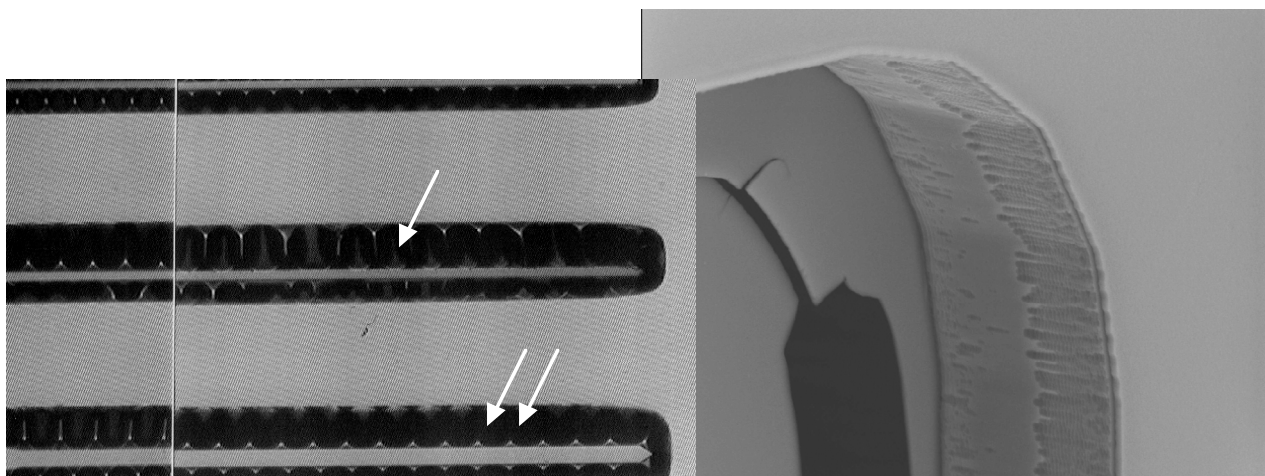


Abbildung 10: REM Aufnahmen eines fast fertig prozessierten Test-Wafer. Bildgröße ca.  $3 \times 5 \text{ mm}^2$  (links) und  $70 \times 75 \mu\text{m}^2$  (rechts). Die dünnen, gezähnten oder gebrochenen Strukturen am Rande des Siliziums (siehe Pfeile) stammen aus dem ehemals vergrabenen, durch DRIE-Ätzen freigelegten Ätzstop aus Silizium-Oxid.

### 6.1.3. Resultate der Mikrostrukturtechnik

Endgültige Resultate dieses MST-Prozesses sind in Abbildung 11 und 12 anhand von rasterelektronenmikroskopischen (REM) Aufnahmen der Sonden E2 und M1 zu sehen. Der durchschnittliche Querschnitt von  $25 \times 25 \mu\text{m}^2$  eines Schafes, der Spitzenöffnungswinkel von  $4^\circ$ , sowie ein leichter Unterschnitt der Spitzenregion helfen bei der besonders schwierigen Implantation in Bereiche des Kleinhirns [62], aber auch bei der Suche nach lokalen Feldpotentialen im entorhinalen Kortex [44, 45].

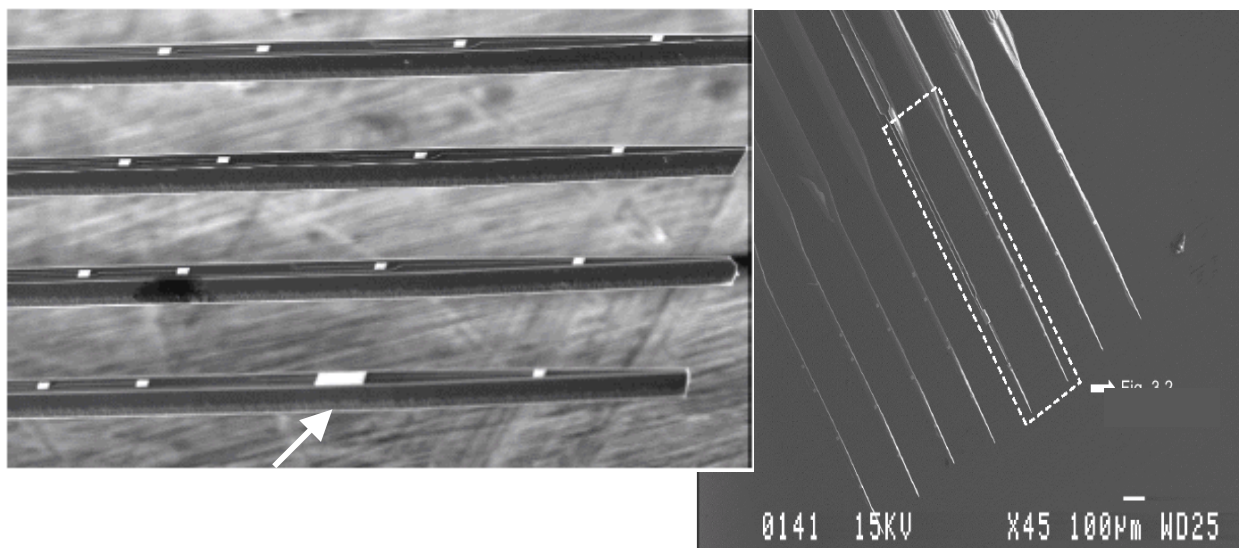


Abbildung 11: REM Ergebnisse des 32-Kanal MST-Prozesses am Beispiel der Sonde E2. Deutlich erkennbar sind die einzelnen Schäfte und die Ableitelektroden ( $10 \times 10 \mu\text{m}^2$ ), sowie eine Läsionselektrode (siehe Abschnitt 7.2; Pfeil, ca. $1000 \mu\text{m}^2$ ) [95].

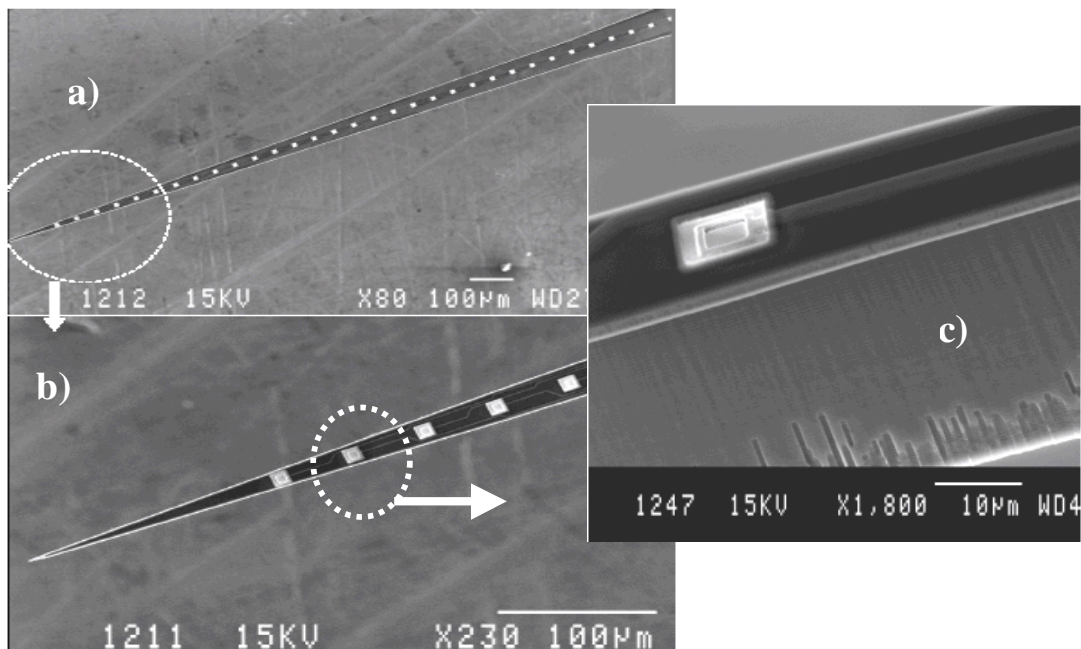


Abbildung 12: REM Ergebnisse des 32-Kanal MST-Prozesses am Beispiel der Sonde M1. Hier weitet sich der Schaft zwar durch die wachsende Zahl der Leiterbahnen (a), aber der geringe Spitzenöffnungswinkel (b) und die Größe der Ableitelektroden (c) bleiben konstant [94].

#### 6.1.4. Verbindungstechnik und Qualitätskontrolle

Gemäß den experimentellen Anforderungen soll die Verbindung der maximal  $2,2 \times 15 \text{ mm}^2$  großen Silizium-Gabeln (davon nur 1,9 mm für die Kontaktbasis) durch eine möglichst flexible Anschlußmöglichkeit erfolgen. Im Gegensatz zu unseren nächsten Mitbewerbern, den Sonden der University of Michigan, werden unsere Sonden folglich nicht auf einer rigiden Leiterplatte montiert, sondern per "wire-bonding" wie ein Computerchip mit einer flexiblen, insgesamt 125 µm dicken, 12 cm langen Polyimid-Folie verbunden. Die Leiterbahnen darauf bestehen aus 5 µm dickem Kupfer und werden ebenso photolithographisch prozessiert wie übliche kupferkaschierte Elektronikplatten [101, 102]. Die 25 µm breiten Leitungen sind hierbei durch 50 µm breite Lücken voneinander getrennt. Das breitere Ende ist entsprechend den Designanforderungen eines handelsüblichen, 32-kanaligen, "zero-insertion-force" (ZIF) Flachbandsteckers der Firma Molex, Japan, entworfen (52559 ZIF FPC). Flexible Polyimid-Kabel (FlexBoard) dieser Art sind in handelsüblicher Miniaturelektronik wie Mobiltelefonen oder Laptops zu finden. Der Sonden-Kontaktbereich wird zum Schutz der dünnen Kontaktdrähte mittels einer Kunststoffverstärkung verstärkt und durch eine Epoxidharz-Perle elektrisch isoliert (Abbildung 13, Pfeil oben rechts). Abbildung 13 zeigt diese Verbindung komplett mit einer Sonde (weisser Pfeil) mit einer schwedischen Krone als Maßstab.



Abbildung 13: Das Kapton®-Verbindungskabel zwischen einer Sonde U1 (Pfeil) und einem ZIF-Adapter der Firma Molex (weisser Pfeil). Die schwedische Krone dient als Veranschaulichung des Maßstabs.

Derart kontaktierte Sonden konnten damit auf ihre wunschgemäßen elektrischen Eigenschaften hin überprüft werden. Dazu wurde zunächst in 2-Punkt-, später in 3-Punkt-Messungen die Übergangsimpedanz der Elektroden in Kochsalzlösung gemessen [81, 85, 95, 103, 104]. Abbildung 14 zeigt graphisch Impedanz-Spektren (links) und rechts die zusammengefassten Ergebnisse dieser Messungen. Es wird deutlich, dass unsere  $10 \times 10 \mu\text{m}^2$  großen Mikroelektroden mit Iridium als Kontaktmaterial durchaus Impedanzen um die  $1,4 \text{ M}\Omega$  bei einer Anregungsfrequenz von 1 kHz erreichen. Die nicht ganz zufriedenstellende Streuung der Messungen, eine mechanische Instabilität (Abplatzen) und weitere produktionstechnische Gründe haben uns aber veranlasst, letztlich als Elektrodenmaterial Platin zu verwenden. Dieses Material hat zwar doppelt so hohe Übergangsimpedanzen (um 3-5  $\text{M}\Omega$ ), erweist sich in der experimentellen Praxis aber als durchaus ebenbürtig.

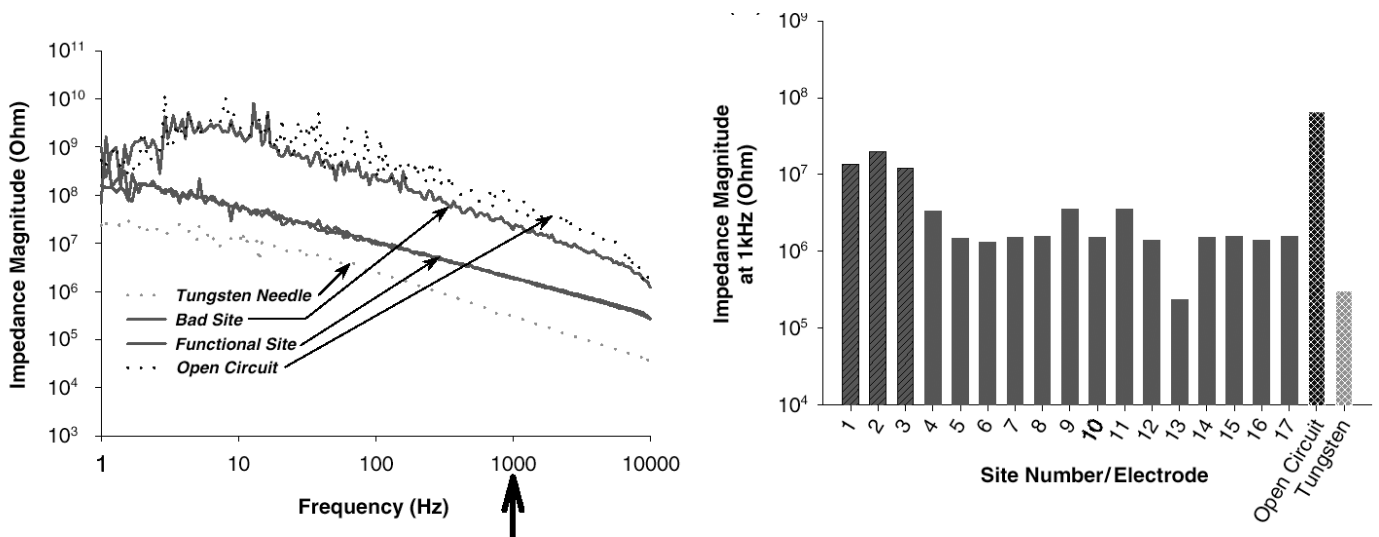


Abbildung 14: (links) Typische Impedanzspektren zweier Ir-Elektroden ("Functional Site") im Vergleich mit einem Kontaktierungsfehler ("Bad Site"), einer kommerziellen Wolfram-Mikroelektrode und dem oberen Mess-Limit. (rechts) Impedanz-Werte bei 1 kHz Anregungsfrequenz. Elektroden Nr 1-3 zeigen den Kontaktierungsfehler, Nr 4-17 zeigen einen Wert um die  $1,5 \text{ M}\Omega$ , wobei der Ausreißer-Wert von Elektrode 13 durch ihre um den Faktor 10 größere Fläche zustandekommt (Läsionselektrode! )

### 6.1.5. Fortentwicklung für 64 Ableitpunkte und alternative Sonden

Bisher nur teilweise veröffentlicht [95]<sup>7</sup> sind die folgenden Resultate zur Herstellung von 64-kanaligen Sonden. Der Herstellungsprozess unterscheidet sich nicht von den 32-kanaligen Sonden, jedoch wurde die Prozess-Auflösung um den Faktor 2 verbessert. Die Strukturgrößen liegen damit um 1-1.5  $\mu\text{m}$ . Der Hauptunterschied beider Designs liegt schlicht darin, dass im neuen Design jede einzelne Elektrode durch zwei ersetzt wurde, die nur 30  $\mu\text{m}$  Mittenabstand aufweisen. Wir machen uns damit bei nahezu gleichbleibender Gewebetraumatisierung die elektrophysiologischen Vorteile des sog. Stereotrodeneffektes zunutze [42, 106]. Zwei Elektroden in kleinem, aber bekannten Abstand voneinander (Stereotroden) zeichnen das Aktionspotential ein und derselben Zelle zeitgleich mit unterschiedlichen Amplituden auf. Damit erhält man zusätzliche Informationen, die das spätere Klassifikationsproblem erleichtern [90, 96, 107]. Die logische Verbesserung zu Tetroden (4 Elektroden nahe beieinander) wird in unserem Fall durch die harte Voraussetzung der minimalen Schaftgröße verhindert, ist aber prinzipiell möglich [108, 109].

Die technischen Resultate unserer Entwicklung von 64-kanaligen Sonden werden im folgenden Bild 15 vorgestellt.

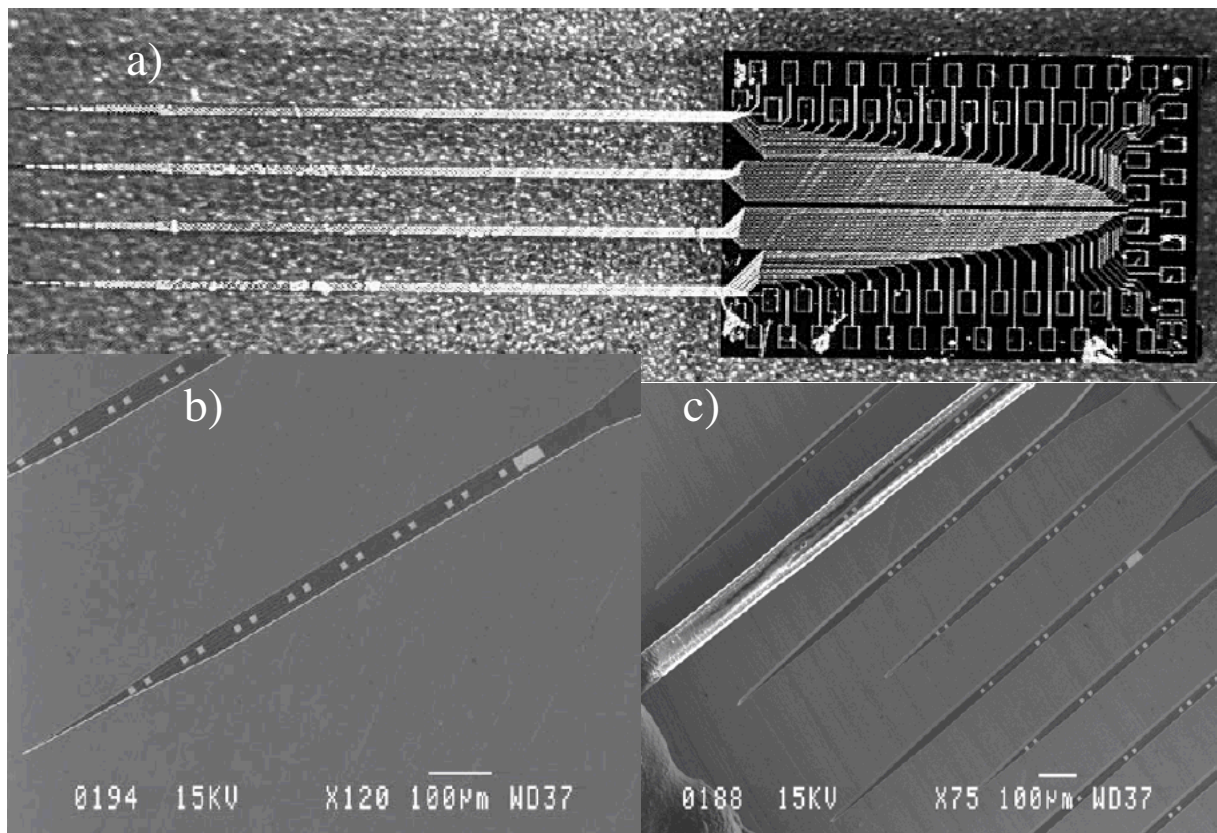


Abbildung 15: a) Mikrosonde mit 64 Ableitpunkten ; b) REM-Aufnahme der sensitiven Region mit deutlich erkennbaren Stereotroden und der überdimensionierten Läsionselektrode; c) alternative Schaftanordnung. Man bemerke in c) die 25  $\mu\text{m}$  Breite der Schäfte im Vergleich zu einem menschlichen Haar.

An dieser Stelle sei nur kurz darauf hingewiesen, dass ebenfalls 32-kanalige Sonden im Rahmen eines Gemeinschaftsprojektes mit der Stanford Universität, Palo Alto, CA, etwa zeitgleich von mir mitentwickelt wurden [108, 109]. Diese Sonden werden dort mit einem vergleichbaren Prozess, jedoch ohne SOI-Ätzstop erzeugt und haben eine größere Schaftbreite. Wir zielen in unserem Projekt auf die vereinheitlichte Herstellung von mikroelektronischen Schaltungen und mikrostrukturtechnischen Sonden in einem einzelnen

<sup>7</sup> Begutachtet und akzeptiert durch **KIIS**. EU Kindlundh, M. and P. Norlin, *Custom designed 64 microelectrode probes*. 2002, Acreo AB: Kista, Sweden.

CMOS-kompatiblen Prozess. Dieses Ziel wurde zwar noch nicht erreicht, jedoch konnten wir passive, 32-kanalige Sonden mit Elektroden in einer Tetrodenanordnung erfolgreich zur Ableitung am visuellen Kortex der Ratte einsetzen [57, 108-111].

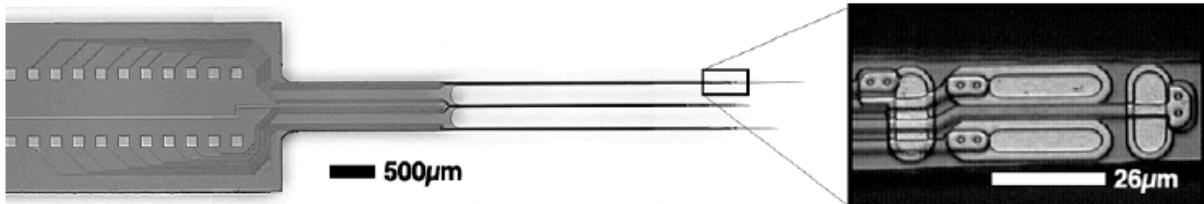


Abbildung 16: Eine Vielfach-Sonde (T1), die ohne SOI-Wafer in einem Trockenätzprozess am Center for Integrated Circuits der Stanford University, Palo Alto, CA, nach meinen Designs hergestellt wurde. Die breiten Schäfte haben unterschiedliche Öffnungswinkel und tragen Elektroden in Tetrodenanordnung, die die Spike-Detektion deutlich verbessern können [42].

Silizium-Sonden wurden mittlerweile erfolgreich in kortikalen Experimenten, sowohl am visuellen [109], als auch am entorhinalen Kortex [44, 45], als auch in zerebellaren Experimenten eingesetzt [62].

Insgesamt kann festgestellt werden, dass der eingeführte Trockenätzprozess die mikrostrukturtechnischen Voraussetzungen für eine erfolgversprechende Vielfachsonden-Ableitung am anästhesierten Tier bereitgestellt hat.

## 6.2. DSP-gestützte Digitalisierung

Wie im anfänglichen Überblick dargestellt, sind Vielfach-Sonden für sich alleine bei weitem noch nicht ausreichend, um Informationen von lebenden Neuronen zu erhalten. Ihre charakteristischen Amplituden verlangen zwingenderweise eine Verstärkung der Signale.

### 6.2.1. Signalverstärkung

Dazu muß das Kontaktende der flexiblen Leiterplatte unserer kontaktierten Sonden mittels eines handelsüblichen Flachbandsteckers mit einem analogen Verstärkungssystem verbunden werden. Für unser Messsystem hat dazu die Firma Uwe Thomas Recording GmbH, Gießen, eine Verstärkerkette entwickelt, die unseren Anforderungen sowohl bezüglich Bandbreite, als auch Verstärkungsfaktoren, Flexibilität und Handhabbarkeit genügt.

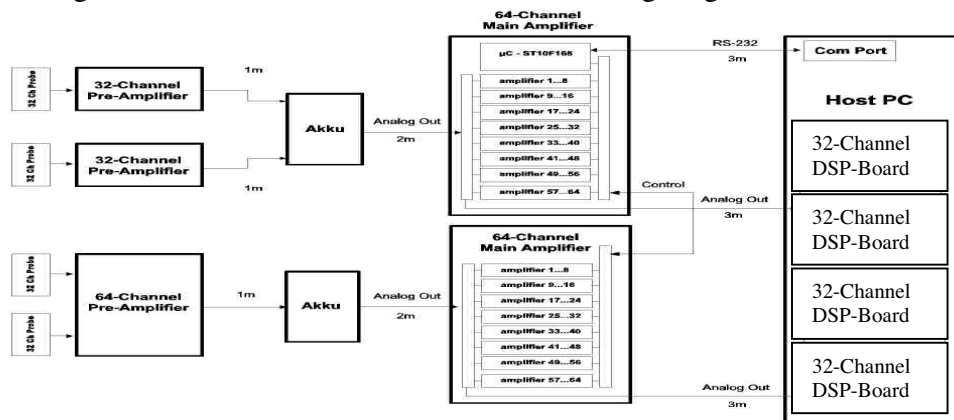


Abbildung 17: Schematischer Aufbau der gesamten Hardware für 128 Ableitkanäle (v.l.): Mehrere 32- oder 64-kanalige Vielfach-Sonden werden mit akkumulatorbetriebenen Vorverstärkern verbunden. Diese verstärken das Signal um den Faktor 40 und leiten es über maximal 1m lange Kabel an den skalierbaren Hauptverstärker weiter.

Die Verstärkung kann dort für jeden Kanal über einen Mikrocontroller und die serielle Schnittstelle vom Datenaufnahmesystem (Host PC) kontrolliert werden. Das Datenaufnahmesystem selbst besteht aus bis zu vier digitalen Signalprozessorkarten, die jeweils 32 Kanäle bearbeiten können.

Diese Verstärkerkette, bestehend aus Vorverstärker und zugehörigen Hauptverstärkern (Abbildung 17, Mitte), soll hier nur der Vollständigkeit halber vorgestellt werden, da unsere Datenaufnahmesoftware alle ihre relevanten Parameter steuern kann.

Die Vorverstärker wurden in miniaturisierter Bauweise aufgebaut und verstärken das eingehende Signal um den Faktor  $40 \pm 0,2$  bei einem Eingangswiderstand von  $1\text{G}\Omega$ . Sie sind sowohl für 64, als auch für 32 Kanäle verfügbar und beanspruchen in erster Bauform weniger als die doppelte Größe einer Zigarettenzschachtel ( $95 \times 63 \times 35 \text{ mm}^3$ , Abbildung 18, links). Sie sind zur Rauschreduktion Akkumulator betrieben und bilden über ein handelsübliches 68-kanaliges SCSI-Kabel die Verbindung zum Hauptverstärker (Abbildung 18, rechts). Ersteres erwies sich als eine wichtige Voraussetzung für möglichst rauscharme Ableitungen, wobei letzteres wiederum der maximalen Flexibilität dient.

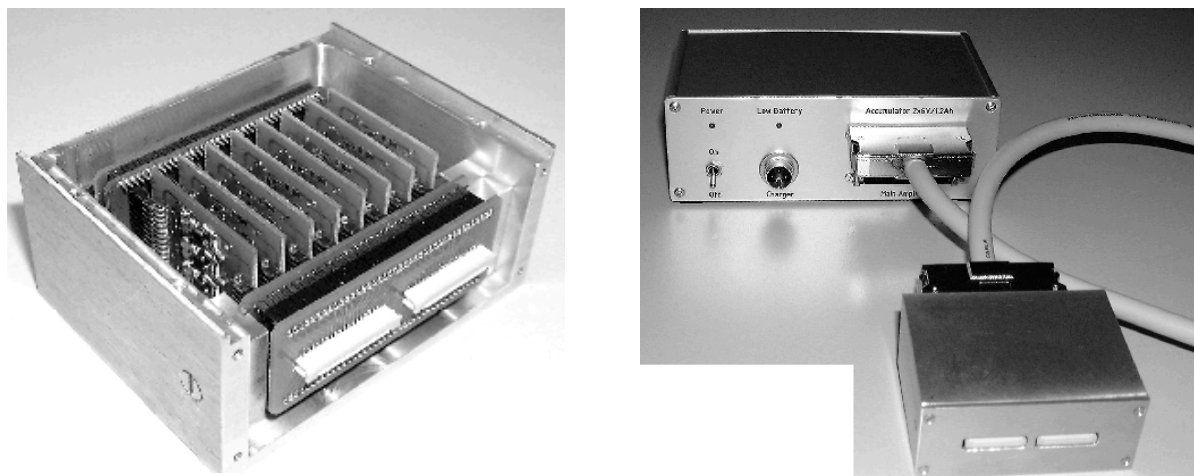


Abbildung 18: (links) 64-Kanal Vorverstärkereinheit mit offener Abdeckung. Deutlich zu erkennen sind die auswechselbare Frontplatte mit zwei Molex ZIF Verbindern und dahinter die acht Mini-Platinen zur Vorverstärkung von jeweils acht Signalkanälen. (rechts) Die Vorverstärkereinheit ist akkumulatorbetrieben (Hintergrund) und mit handelsüblichen SCSI-Kabeln mit dem Hauptverstärker verbunden. Bilder © Uwe ThomasRecording GmbH, 2001

Der skalierbare Hauptverstärker für 64 differentielle Eingangskanäle nimmt 6 Höheneinheiten eines 19 Zoll Einschubsystems ein (Abbildung 19 links). Er besteht aus einem Mikrocontroller und maximal 8 Verstärker-Platinen zu je 8 Signalkanälen. Ersterer, ein ST10F168 von STMicroelectronics, Genf, Schweiz, dient sowohl der Kontrolle der Verstärkungsfaktoren einzelner Kanäle, als auch der Kommunikation und Kontrolle durch die serielle Schnittstelle, sowie der möglichen manuellen Kontrolle und Darstellung der eingestellten Parameter an der Frontplatte.

Im Gegensatz zu den meisten konkurrierenden Verstärkersystemen wird in unserem Fall lediglich eine festeingestellte analoge Bandpassfilterung in den Frequenzbereichen von 0,034 Hz bis 16 kHz vorgenommen. Eine weitergehende Filterung erfolgt dann erst nach der Digitalisierung der Signale durch Nutzung der Wavelet-Transformation (s.u.).

Die jeweils gültigen Verstärkungsfaktoren können zwar an zwei Drehschaltern der Frontplatte ein- und dargestellt werden, jedoch existiert auch ein Kontrollmodul im Rahmen unserer Datenaufnahmesoftware, die eine komfortablere Steuerung ermöglicht (Abbildung 19 rechts). Gleichzeitig hat diese Programm-Steuerung Vorrang vor der Schaltersteuerung, die sogar komplett gesperrt werden kann. Als mögliche Gesamtverstärkung (Vorverstärkung x Hauptverstärkung) kann der Nutzer die Werte 80x, 160x, 400x, 800x, 1600x, 4000x, 8000x, 16000x, 40000x oder 80000x wählen.

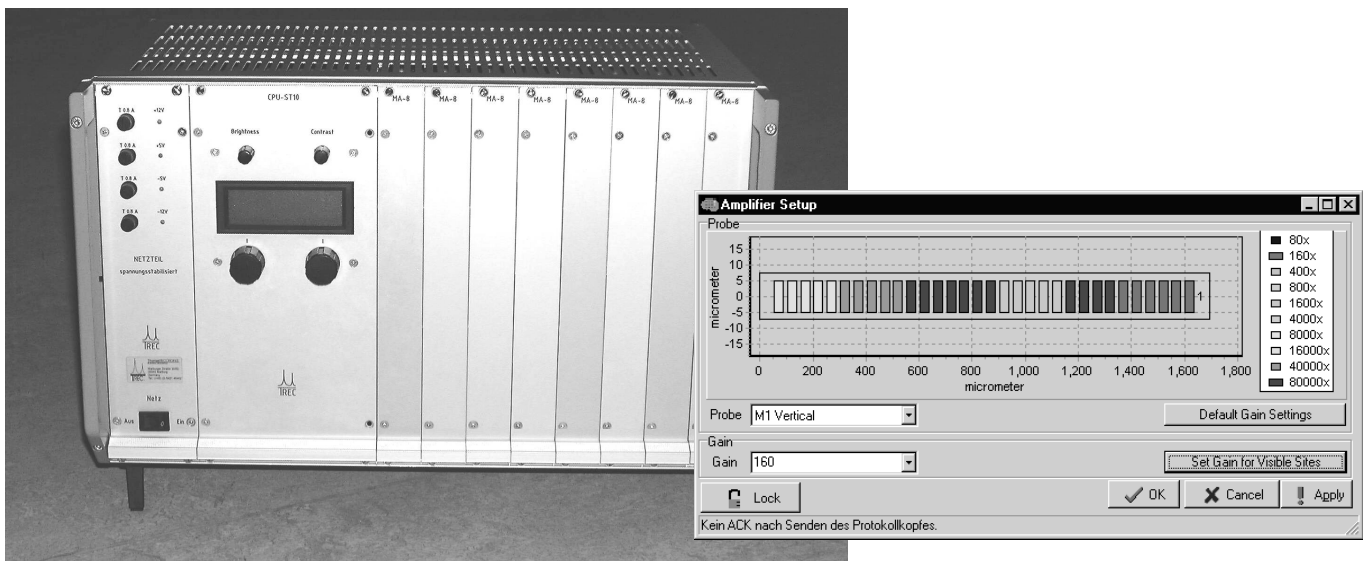


Abbildung 19: (links) Frontansicht des 64-Kanal-Verstärkers PGMA-64 von Uwe Thomas Recording GmbH. (rechts) Das Kontrollfenster unseres Software-Moduls zur Steuerung der Verstärkungsfaktoren. Man kann farbkodiert die eingestellten Verstärkungsfaktoren für jede einzelne Elektrode einer stilisierten M1 Sonde erkennen. Eine Änderung erfolgt für alle Elektroden, Gruppen oder nur einzelne Elektroden über die graphische Menüführung.

Ziel dieser Verstärkung ist es, einen Ausgangspegel von etwa  $\pm 10V$  auf allen Signalkanälen zu erreichen, der dann dem Datenaufnahmesystem wieder über 68-polige SCSI-Kabel zur Verfügung gestellt wird.

### 6.2.2. Vielkanal-Digitalisierung

Die in [112, 113, Folkers, 2001 #690, 114, 115] vom Institut für Signalverarbeitung und Prozeßrechentechnik der Universität zu Lübeck publizierten Ergebnisse zur Datenaufnahme werden im folgenden zusammengefasst.

Das zu erwartende Datenaufkommen und die anderen Spezifikationen, wie 16 bit Auflösung bei 50 kHz Abtastrate pro Kanal und Skalierbarkeit auf 128 Kanäle, ließen nur eine bescheidene Zahl an existierenden technischen Lösungen für die Vielkanal-Digitalisierung zur Auswahl.

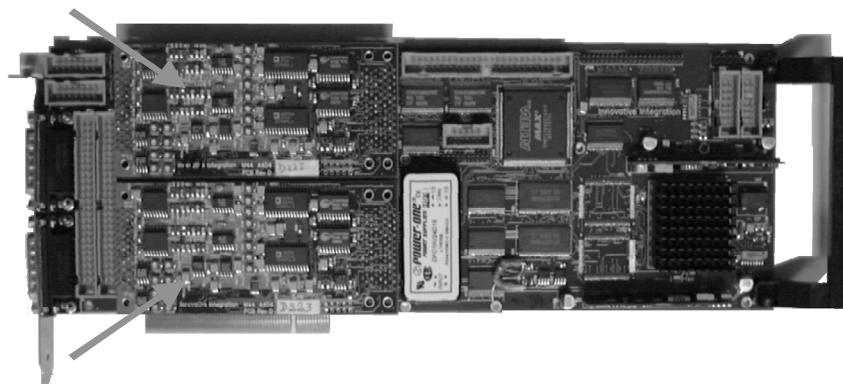


Abbildung 20: Eine digitale Signalprozessor-Karte (DSP) M67 (Innovative Integration, Thousand Oaks, CA) ausgestattet mit 2 AD16 (Pfeile) OMNIBUS-Modulen. Dadurch erhält man ein nicht-multiplexendes Digitalisierungssystem für 32 Signalkanäle mit nominell bis zu 195 kHz Abtastrate pro Kanal.

Wir entschieden uns für das skalierbare, PCI-Bus kompatible M67-System der Firma Innovative Integration, Thousand Oaks, CA. M67-Karten können wegen ihres PCI-Formates in gewöhnliche Personal Computer des Industriestandards eingebaut werden ("Host") und sind damit dem günstigen Massenmarkt zugänglich. Das Betriebssystem der Wahl ist dabei Microsoft ®Windows NT oder 2000.

Jede M67-Karte trägt einen hochperformanten Gleitkomma-Signalprozessor TMS320C6701 (Texas Instruments, Dallas, TX) der, mit 160 MHz Taktrate und 128 kB integrierten Speicher (RAM) betrieben, bis zu 1 GFLOPS Rechenleistung liefern kann. Ebenso wichtig wie die reine Rechenleistung des digitalen Signalprozessors (DSP) ist aber der in sich selbst modulare Aufbau der Karte. Sie verfügt über zwei Steckplätze für OMNIBUS-Erweiterungsmodule. In unserem Fall nutzen wir zwei sogenannte AD16-Module, die jeweils 16 einzelne Analog-Digital-Wandler (A/D-Konverter) des hochpräzisen, gleichstromgekoppelten Sigma-Delta-Typs AD7722 (Analog Devices, Norwood MA) beherbergen. Dadurch kann jeder einzelne Signalkanal mit nominell bis zu 195 kHz bei 16 bit Auflösung pro Datenpunkt abgetastet werden.

Sämtliche mit dem alternativ sonst üblichen *Multiplexing* verbundene Signalverarbeitungsprobleme werden dadurch vermieden [116]. Jeder einzelne Signalkanal vom Hauptverstärker wird also über eine selbstgebaute Adapterplatine ("SCSI to latch board") mit jeweils einem differentiellen Eingang eines A/D-Konverters verbunden. Konvertierungsergebnisse werden durch eine DSP-getriebene Taktrate in einen AD16-eigenen Speicherbereich (FIFO, "first-in-first-out") geschrieben, der maximal 512 Datenpunkte aufnehmen kann. Sobald jedoch dieser FIFO halbvoll geschrieben ist, löst die AD16-Karte einen Transfer der Daten mittels DMA ("direct memory access") in den internen Speicher des DSPs aus. Diese Daten verarbeitet dann der DSP weiter und stellt sie über den PCI-Bus dem Host-PC zur Verfügung. Abbildung 21 zeigt schematisch diesen Aufbau.

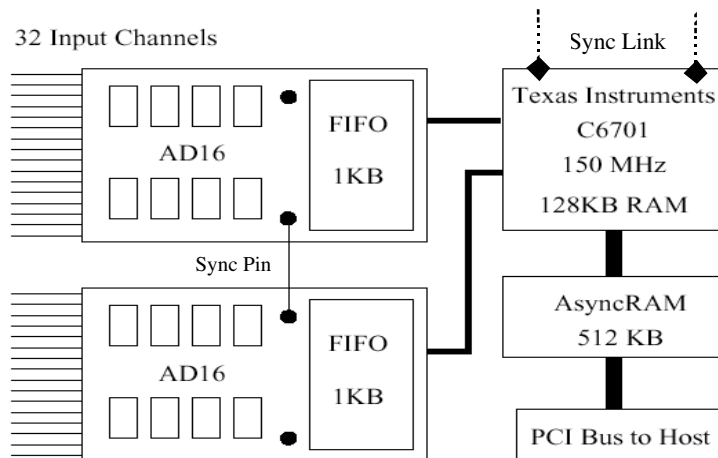


Abbildung 21: v.l. 32 Signalkanäle werden über jeweils einen A/D-Wandler der zwei AD16-Module zu digitalen Daten konvertiert und im AD16-FIFO zwischengespeichert. Von dort werden die Daten dem DSP C6701 zur Verfügung gestellt und über den PCI-Bus an den HostPC weitergereicht. Details siehe Text.

Die Skalierbarkeit der M67-Familie basiert nun insbesondere darauf, dass sowohl mehrere AD16-Module, als auch mehrere DSP-Karten untereinander in eine "master-slave"-Konfiguration gebracht werden können, die einer einzelnen Taktrate folgen. Dadurch können prinzipiell mehrere 32-Kanal-Einheiten ( $1 \times \text{M67} + 2 \times \text{AD16} = \text{"Target"}$ ) auf einem PCI-Bus synchron Daten aufnehmen. Nötig ist dazu eine elektrische Verkettung jeweils aller DSP-Karten über die sog. "SyncLink"-Eingänge und die Verkettung aller AD16 über deren entsprechende Synchronisations-Zugänge ("Sync Pin") (Abbildung 21). Darüber hinaus muss selbstverständlich die Datenaufnahmesoftware in der Lage sein, die zusätzlichen Karten zu

nutzen und die vervielfachte Datenmenge über den PCI-Bus dem Host zur Verfügung zu stellen.

Host und Target, d.h. Industrie PC und M67-AD16-Einheit, können durch die PCI-Bus-Verbindung wechselseitig Daten austauschen (Abbildung 22). Dabei kommen je nach der Größe der Datenblöcke zwei unterschiedliche Methoden zum Einsatz.

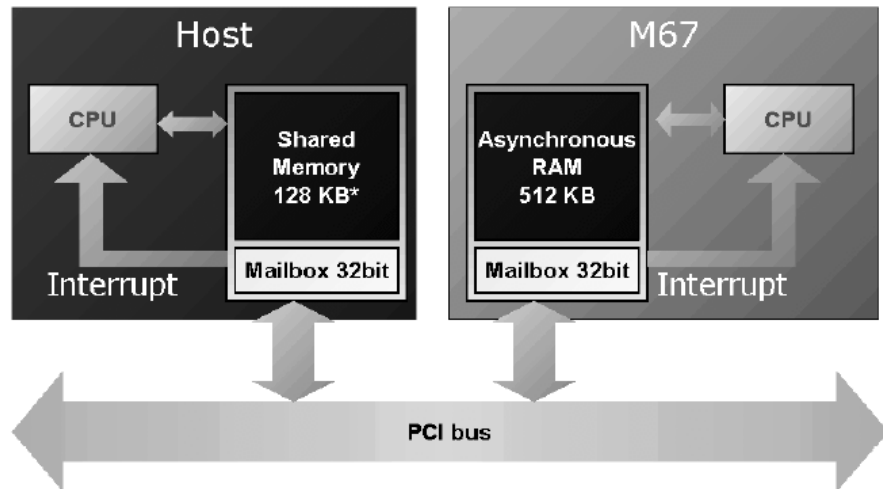


Abbildung 22: Datenaustausch zwischen PC und [M67-AD16]-Einheit (Host und Target). Beide Untereinheiten teilen den gemeinsamen PCI-Bus und können wechselseitig unter Umgehung der jeweiligen CPU (Busmaster Transfer) Daten in spezielle Speicherbereiche der empfangenden Seite schreiben [112].

Große Datenmengen werden unter Umgehung der jeweiligen CPU durch einen speziellen Chip auf der lokalen PCI-Brückekarte entweder vom asynchronen RAM des Targets (siehe Abbildung 21) in den gemeinsamen Speicherbereich ("shared memory"; 128 KB unter Windows NT, 2 MB unter Windows 2000) des Hosts geschrieben oder umgekehrt. Nach Beendigung des Transfers werden die entsprechenden Empfänger durch einen Betriebssystem-Interrupt auf die neuen Daten hingewiesen.

Kleine Datenblöcke von 32 bit Größe werden in die jeweiligen Mailbox-Bereiche auf der Empfängerseite geschrieben und lösen ebenfalls ein Interrupt-Signal aus. Auf diese Weise benachrichtigt z.B. das Target die Host-Anwendung, dass ein kompletter Datenblock vom asynchronen RAM im gemeinsamen Speicher abgelegt wurde.

Dieser Datentransfer kann sowohl bei Vorhandensein eines entsprechend großen Rohdatenblockes erfolgen, kann aber auch erst nach geeigneter Bearbeitung, wie z.B. Filterung oder Fourier-Transformation, erfolgen.

### 6.3. Datenaufnahme-Programm

#### 6.3.1. Grundfunktionen

Die Bearbeitung der Daten erfolgt weitgehend auf dem speziell für hohe Rechenlast ausgelegten digitalen Signalprozessor. Beispielsweise kann der Signalprozessor leicht eine digitale Hochpass-Filterung aller seiner zugeordneten Kanäle durchführen. Entsprechend werden dann gefilterte Daten auf den Host übertragen. Ebenso nutzen wir optimierte Routinen von Texas Instruments, Dallas, TX, zur Berechnung der Fast-Fourier-Transformation um die Koeffizienten des Leistungsdichtespektrums eines auswählbaren Kanals darzustellen. Die Darstellung und Weiterbearbeitung erfolgt dann durch die Visualisierungsroutinen des Anwendungsprogrammes auf der Host-Seite.

Dieses Anwendungsprogramm hat zusammengefasst folgende Aufgaben:

- Steuerung der Digitalisierung über das oben erwähnte Mailbox-System
- Empfang, Organisation und Speicherung digitaler Daten

- Visuelle und Audio-Datenausgabe
- Bearbeitung und Echtzeit-Analyse neuronaler Daten

Daten, welche ein Target-DSP digitalisiert oder berechnet hat, werden von der Host-Anwendung nach Aufforderung durch das Target vom gemeinsamen Speicher in eine zugeordnete Liste geschrieben ("Queue", Abbildung 23).

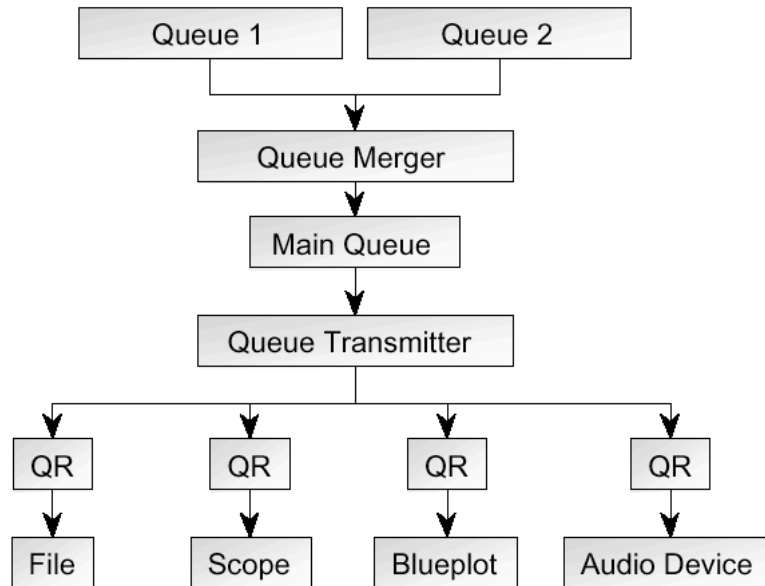


Abbildung 23: Schematischer Datenfluß im Anwendungs-Programm (Beschreibung siehe Text).

Daten eines einzelnen Targets ("Queue 1, 2,...") aus dem gemeinsamen Speicher werden zentral vereinigt ("Queue Merger") und in den Hauptdatenstrom ("Main Queue") eingefügt. Dieser kopiert ("Queue Transmitter") dann über Empfängerstrukturen ("QR", "Queue Receiver") die Daten in entsprechende, beliebige Untermodule. Dies können zum Beispiel Abspeicherung (File), Oszilloskop-Darstellung (Scope), farbkodierte Darstellung (Blueplot), Lautsprecher-Ausgabe (Audio Device) oder anderes sein.

Durch diese zentralisierte Weiterleitung kann der Datenstrom in einzelnen Datenpaketen von jeweils einem Messwert aller Kanäle erfolgen, die jeweils 64 bit große Zeitmarkierungen beinhalten. Dadurch sind selbst bei einer Datenrate von 50 kHz immense Zeiträume von mehreren Millionen Jahren eindeutig zuzuordnen.

Das Hauptmodul des Anwendungs-Programmes (Abbildung 24) steuert sowohl die Echtzeit-Aufnahme, als auch die Wiederholung abgespeicherter Datensätze über die zentrale Queue. Neue Experimente können durch detaillierte Angaben z.B. der Abtastrate oder der verwendeten Sonde (eine Auswahl von uns bekannten Sondenformen wird zur Verfügung gestellt) und durch ausführliche Kommentare beschrieben werden. Eine Neu-Konfiguration von Elektrodenanordnungen (sollten beispielsweise Schäfte abgebrochen sein) wird unterstützt. Das Hauptmodul überprüft, ob die Targets betriebsbereit sind.

Der Nutzer steuert die wichtigsten Funktionen ähnlich wie bei einem Kassetten-Rekorder, kann aber die Wiedergabegeschwindigkeit gespeicherter Daten und den ungefähren Abspielzeitpunkt über Verschieberegler einstellen. Daten werden im HDF5-Format des National Center for Supercomputing Applications, Urbana Champain, IL, abgelegt (z.B. [117]), welches zur Abspeicherung vielkanaliger Daten etnwickelt wurde und auch Datenkompression unterstützt.

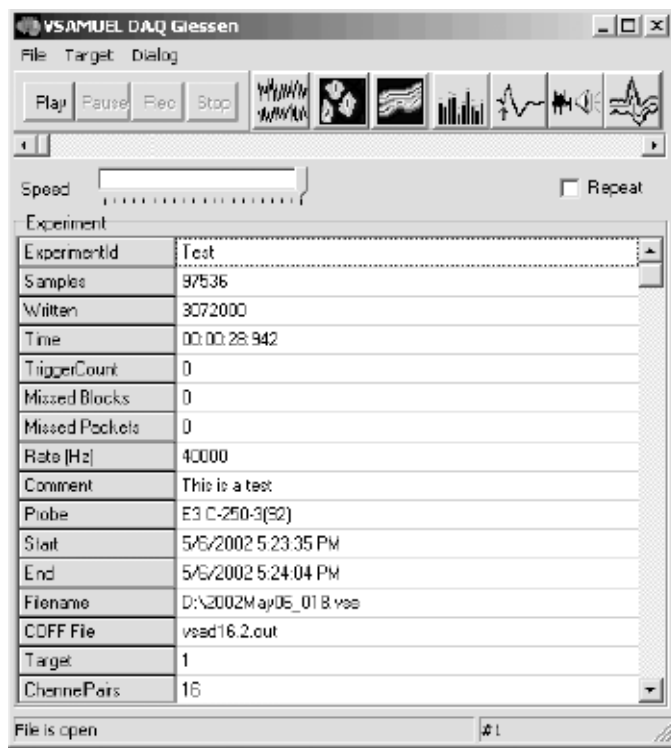


Abbildung 24: Kontrollfenster der Datenaufnahmesoftware. Neben den hauptsächlichen Funktionen Abspielen und Aufnehmen werden einzelne Unterprogramme in graphischer Form dargestellt: Oszilloskop-Darstellung, farbkodierte Signaldarstellung, Spektrogramm und Leistungsdichtespektrum, Meldung von Signalen, Audio-Ausgabe und Spike-Visualisierung. Weitere Funktionalitäten sind die Abspielgeschwindigkeit und Sprungfunktion neben einer Reihe von Kommentarmöglichkeiten.

Eine wichtige Aufgabe des Datenaufnahmesystems ist natürlich die visuelle Darstellung digitalisierter Daten. Dazu stehen dem Nutzer zwei unterschiedliche Modi zur Verfügung: Die Darstellung selektierbarer Kanäle in Form eines virtuellen Vielkanal-Oszilloskops oder die Farbkodierung der Daten und ihre Darstellung im sog. "Blueplot". Dabei werden die Mess- in Farbwerte umgewandelt, wobei Mess-Werte im Rauschpegel einen neutralen Blauton erhalten, alle anderen aber deutlich stärkere, einstellbare Farbwerte. Die y-Koordinate entspricht dann der Position der Ableiteelektrode, und die x-Achse dem kontinuierlich aktualisierten Zeitpunkt. Diese Darstellung erleichtert gerade bei sehr vielen Datenkanälen (>8) die Erkennung von Zusammenhängen, wie sie z.B. bei Feldpotentialen oder Tetrodendaten auftreten. Abbildung 25 zeigt oben den Schnappschuss von 5 Kanälen einer Vielkanalableitung und die entsprechende farbkodierte Darstellung.

Die hörbare Ausgabe von Signalen wird dadurch erreicht, dass ein beliebiger Signalkanal über die interne Sound-Karte des Host-PC ausgegeben wird.

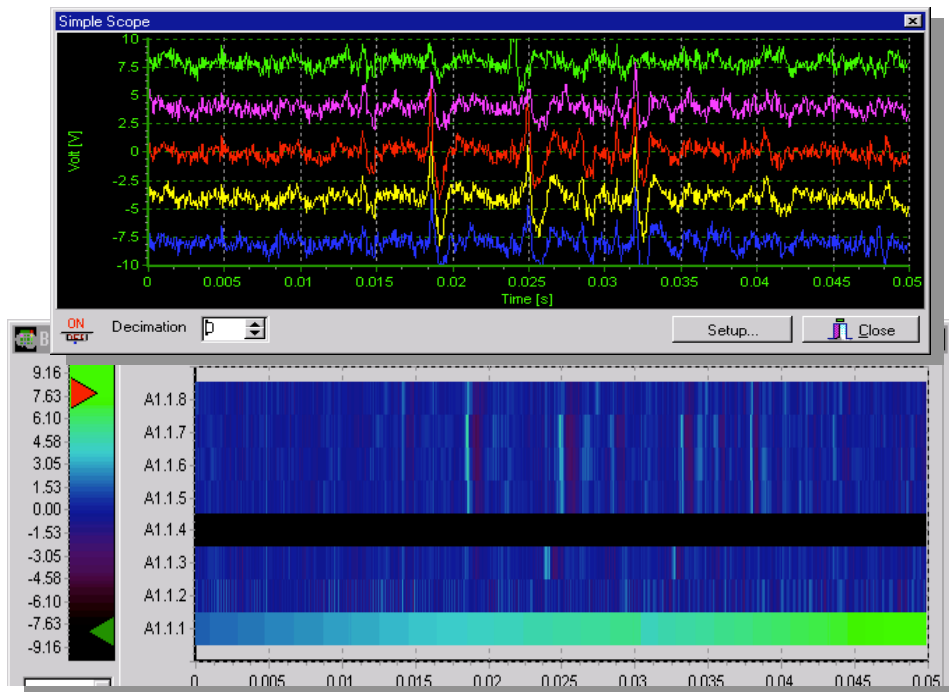


Abbildung 25: Oszilloskopartige Darstellung von fünf realen Aufzeichnungskanälen. Unten sind zusätzlich die übrigen Signalkanäle (inkl. einem funktionslosen) in der farbkodierten Blueplot-Darstellung zu sehen.

### 6.3.2. Signalverarbeitung mittels Wavelets

Details der folgenden Signalverarbeitung wurden in [112, 113] veröffentlicht und sind ebenfalls in [115, 118, 119] dargelegt.

Über die oben genannten Grundfunktionen hinaus hat die Datenaufnahmesoftware aber auch noch die wichtige Funktion, die Filterung und Analyse der Daten vorzunehmen. Um dabei trotz der prinzipiell hohen Rechenleistung des DSP eine Minimierung der nötigen Rechenschritte zu erreichen, haben wir einen Verarbeitungsrahmen entwickelt, der vollständig auf der Diskreten Wavelet-Transformation (DWT) basiert.

Die Wavelet-Transformation ist eine recht junge Methode der Signalanalyse und repräsentiert in ihrer diskreten Form Signale im Gegensatz zur Fourier-Transformation mit kompakt unterstützten Basisfunktionen (Wavelets und Skalierungsfunktionen) die sowohl frequenz- wie auch zeitbegrenzt sein können [120]. Geeignete Basisfunktion, sog. Mutter-Wavelets, können mit ihren zugehörigen, orthogonalen Skalierungsfunktionen in Koeffizienten entwickelt werden, die wiederum als Filterkoeffizienten auf das Signal angewendet werden [121]. Durch Anwendung der diskreten Wavelet-Transformation ergibt sich zwar eine schlechtere Frequenzlokalisierung, dafür aber eine wesentlich bessere Zeitlokalisation als durch die Fourier-Transformation. Für Interessierte seien die einschlägigen Lehrbücher von Mallat [122] und Chui [123] empfohlen.

Die übliche pyramidenförmige Zerlegung des Signals erfolgt durch die Nutzung der Entwicklungskoeffizienten von Mutter-Wavelets und Skalierungsfunktionen als diskreten Hoch- resp. Tiefpassfiltern mit anschließender Unterabtastung um den Faktor 2 (Abbildung 28 links). Der hochpassgefilterte Anteil wird als sogenanntes "Detail" gespeichert, wogegen der tiefpassgefilterte Anteil als "Approximation" weiterbearbeitet wird. Die Weiterbearbeitung erfolgt durch die Zerlegung in die beiden Anteile mittels der durch die Unterabtastung implizit gedehnten Mutter-Wavelets. Ganz offensichtlich wird dadurch die Bandbreite von hohen Frequenzen kommend schrittweise halbiert, so dass die Details der ersten Zerlegung vor allem sehr hohe Frequenzen bis zur halben maximalen Bandbreite enthalten. Die nächsten Detail-Koeffizienten enthalten dann die Frequenzen von der halben

bis zu einem Viertel der Bandbreite und so fort. Die beschriebene Zerlegung wird standardmäßig durch sog. Spiegel-Filter-Bänke ("Quadrature Mirror Filter", QMF) ausgeführt und findet ein natürliches Ende, wenn die Approximation nicht mehr unterabtastbar ist. Es kann aber auch früher durch Speicherung der Approximation erreicht werden. Kehrt man dann die Zerlegung um, sind die ursprünglichen Daten perfekt zu rekonstruieren. Aus der oben beschriebenen Zerlegung in sukzessiv schrumpfende Frequenzbereiche wird aber auch deutlich, dass z.B. das schlichte Streichen von Detail-Koeffizienten vor der Rekonstruktion einer gewünschten Bandpass-Filterung gleicht. Abbildung 26 zeigt ein Beispielsignal (unten) das durch Beseitigung der Koeffizienten für 0 - 312 Hz hochpassgefiltert wurde (oben).

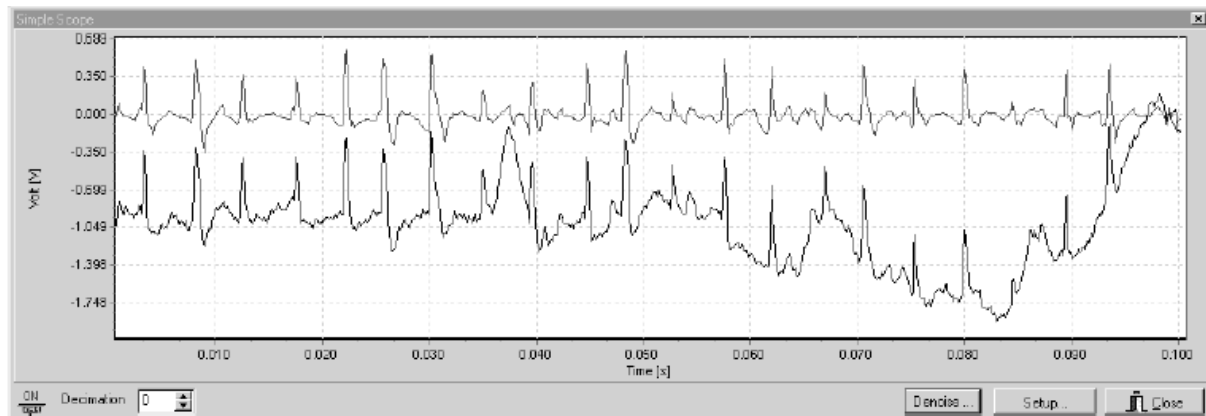


Abbildung 26: Hochpassgefiltertes (oben) und ungefiltertes (unten) Beispielsignal. Man beachte die Erhaltung der Form der Spike-Signale oben und unten.

Unser Rahmensystem der Wavelet-Zerlegung geht deutlich über die in der Elektrophysiologie übliche Filterung mit analogen oder digitalen FIR- oder IIR-Filters hinaus. Z.B. ist es damit möglich, die Größe des unerwünschten Rauschanteiles in einzelnen Detail-Niveaus zu schätzen und dann die entsprechenden Koeffizienten zu Null zu setzen. Übrig bleiben in diesen Niveaus dann Koeffizienten, die in der Rekonstruktion zum Nutzsignal, z.B. zu Spikes, beitragen. Dieses Verfahren, genannt Ent-Rauschen ("De-Noising"), kann in unserem Programm mit unterschiedlichen Zerlegungstiefen, Schätzstrategien, Schwellwertbehandlung<sup>8</sup>, und Mutter-Wavelets aufgerufen werden.

Abbildung 27 zeigt links das Ergebnis eines kontinuierlichen Denoising-Prozesses eines neuronalen Beispielsignals. Der Erfolg des "Entrauschen" ist im unteren Graphen deutlich zu erkennen. Die Grenzwerte werden hier im kontinuierlichen Modus für jedes Bearbeitungsfenster ("Window Length") neu berechnet und angewandt. Im alternativen Einzel-Modus wird dagegen zu Beginn des Signals der Grenzwert geschätzt und dann bis zum Ende des Signals angewandt. Im rechten Teil von Abbildung 26 ist das Auswahlfenster zum De-Noising eines Kanals dargestellt, hier mit der Funktion Daubechies 2 als Mutter-Wavelet.

In jedem Fall muss sich der Nutzer aber darüber im Klaren sein, dass seine Signale durch das Ent-Rauschen nicht mehr in ihrer originalen Form vorliegen, er also ein verlustbehaftetes Verfahren anwendet.

---

<sup>8</sup> Harte Schwellwertbehandlung: Alle Koeffizienten dazwischen werden zu Null gesetzt; Weiche Schwellwertbehandlung: Koeffizienten im Schwellwert werden zu Null und allen anderen um den Schwellwert verkleinert.

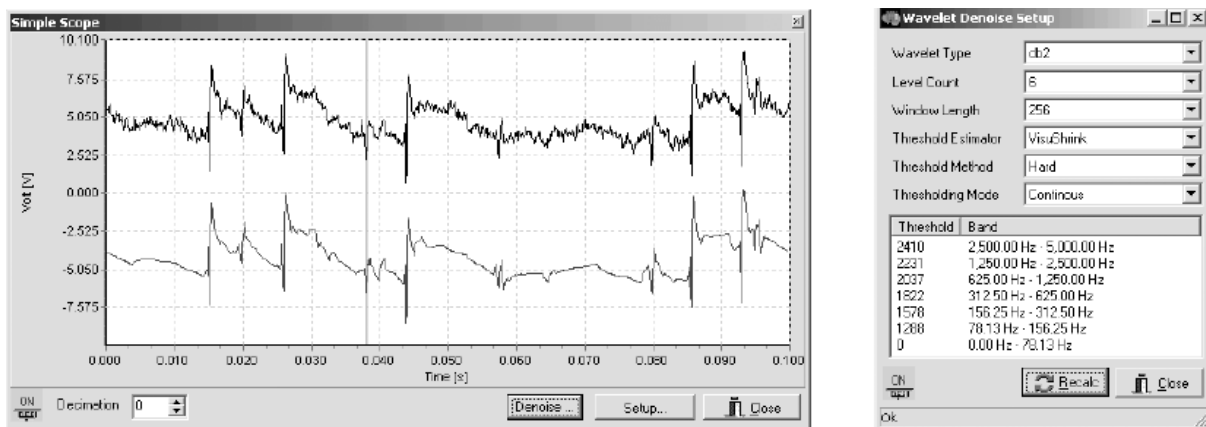


Abbildung 27: links; der obere Graph zeigt ein verrauschtes neuronales Beispieldesignal, wogegen der untere das in Echtzeit entrauschte Signal darstellt. Die dabei angewandten Parameter sind im rechten Teil zu erkennen: Mutter-Wavelet war das Daubechies 2 Wavelet, die Zerlegung erfolgte bis zum 6. Niveau, wobei das De-Noising kontinuierlich an 256 Datenpunkten mittels der Strategie VisuShrink und der harten Schwellwertbehandlung vorgenommen wurde.

Ein entrauschtes Signal kann nun als weiterer Vorteil des Wavelet-Einsatzes sowohl zur verbesserten Detektion von Spike-Vorkommnissen dienen (s.u.), als auch zur Kompression des Datensatzes [124, 125]. Gewöhnliche Komprimierungsalgorithmen erreichen durch die hohe Entropie des Ursprungs-Signals von ca. 15 bit eine maximale Kompression um den Faktor 2 [118]. Durch den Einsatz des De-Noising-Verfahrens werden aber sehr viele Koeffizienten zu Null gesetzt, was dann sowohl die Entropie reduziert, als auch durch Lauflängen-Codierung zur Kompression genutzt wird [115, 126, 127].

Oben beschriebene dyadisch-hierarchische Wavelet-Zerlegung kann nun noch um mehr als den Faktor 2 im Rechenaufwand reduziert werden, indem man das sogenannte "Mehrphasen-Schema" einsetzt [128-131]. Dabei ersetzt man zunächst das vergleichbar aufwändige Prozessieren mit FIR-Filters (Abbildung 28, links; Hoch- und Tiefpaß,  $g$  und  $h$ ) und nachfolgendem Unterabtasten durch Aufspalten der Signalwerte in Folgen von geraden und ungeraden Laufindizes. Ausschließlich die ungeraden Werte dienen nun der geschickten Schätzung der geraden Werte, so dass als Detailkoeffizient nur mehr der Fehler zwischen Schätzung und tatsächlichen Werten gespeichert werden braucht ("dual lifting"). Im Gegenzug dienen die neuen Detailkoeffizienten nun dazu die ungeraden Werte anzupassen ("primal lifting", Abbildung 28 rechts). Es kann gezeigt werden, dass das wiederholte, wechselseitige Lifting äquivalent ist zur Faktorisierung der Polyphasen-Matrix, die über die ursprünglichen Filterkoeffizienten des Mutter-Wavelets definiert ist., Der Lifting-Algorihmus ist eine besonders effiziente Implementierung der Wavelet-Transformation.

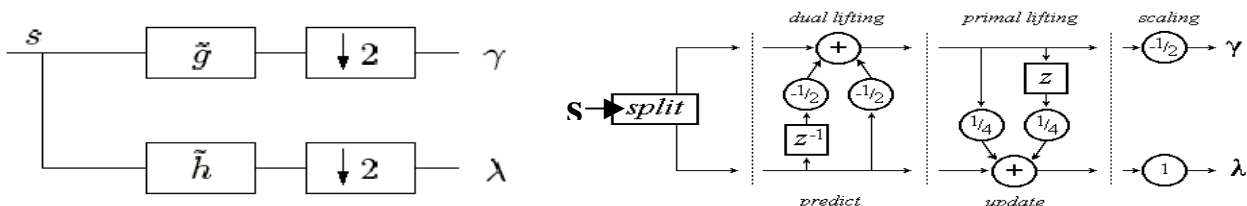


Abbildung 28: (links) Erzeugung der Zerlegungsdetails  $\gamma$  und der Approximation  $\lambda$  in einem einzelnen Niveau einer dyadiischen Wavelet-Zerlegung durch Hochpaßfilterung mit  $g$  und Tiefpaßfilterung mit  $h$ , jeweils gefolgt von einer Unterabtastung. (rechts) Korrespondierender, beispielhafter Zerlegungsschritt mittels "lifting"-Implementierung eines einfachen Wavelets. Der "split"-Operator teilt das Signal  $s$  in gerade ("even") und ungerade ("odd") Laufvariablen. Diese dienen jeweils zur Detailbildung durch Schätzung ("predict", "dual lifting"), resp. dann zur Aufdatierung der Approximation ("update", "primal lifting") [130].

Diese Implementierung der Wavelet-Transformation hat zwei weitere Vorteile: Zum einen werden die Berechnungen ohne zusätzlichen Speicherbedarf durchgeführt ("in place"), und zum anderen ermöglicht es, die Wavelet-Koeffizienten in ganzzahliger Notation zu erhalten. Die Nützlichkeit dieser besonderen Implementierung zeigt sich daran, dass die Wavelet-Zerlegung aller 32 Kanäle in voller Aufnahmegergeschwindigkeit auf dem DSP bearbeitet werden kann.

#### 6.4. Simulation realistischer Netzwerke

Ergebnisse dieses Abschnittes finden sich in den Veröffentlichungen [27, 132-136] wieder. Eine wichtige Aufgabe unserer Software besteht darin, die Aufnahme und automatische Auswertung extrem großer Datenmengen von Vielkanalsonden zu unterstützen. Zu diesem Zweck müssen aber die Daten mit überprüfbaren und vertrauenswürdigen Methoden analysiert und bearbeitet werden.

Leider haben alle bisherigen Ansätze, eine Quantifizierung von Analysemethoden durchzuführen, am selben Fehler gekrankt. Zugrundeliegende Test-Daten waren zwar meist signaltechnisch nicht zu beanstanden, weil vollsynthetisch aus Rauschanteilen und Spike-Mustern erzeugt, haben aber leider jede physiologische Relevanz vermissen lassen [93, 137]. Dagegen hat die Beurteilung und der Vergleich biologisch gemessener Test-Daten nur eine geringe, vom Betrachter abhängige Reproduzierbarkeit aufgewiesen [90, 91]. Unter diesen Umständen war es unser Ziel, Test-Daten zu generieren, die einerseits biologisch realistische Daten liefern, aber andererseits vollständig unter unserer Kontrolle stehen. Gleichzeitig besteht selbstverständlich der starke Wunsch, die experimentell aufgezeichneten neuronalen Vielkanal-Signale durch Modellbildung zu verstehen. Die Frage lautet also: Warum sehen die Signale so aus, wie sie aussehen?

Zu diesem Zweck haben wir uns der Differentialgleichungs-Beschreibung eines kleinen Stückes der Nervenzellmembran bedient, wie sie im Blockschaltbild in Abbildung 29 links gezeigt ist [32, 33].

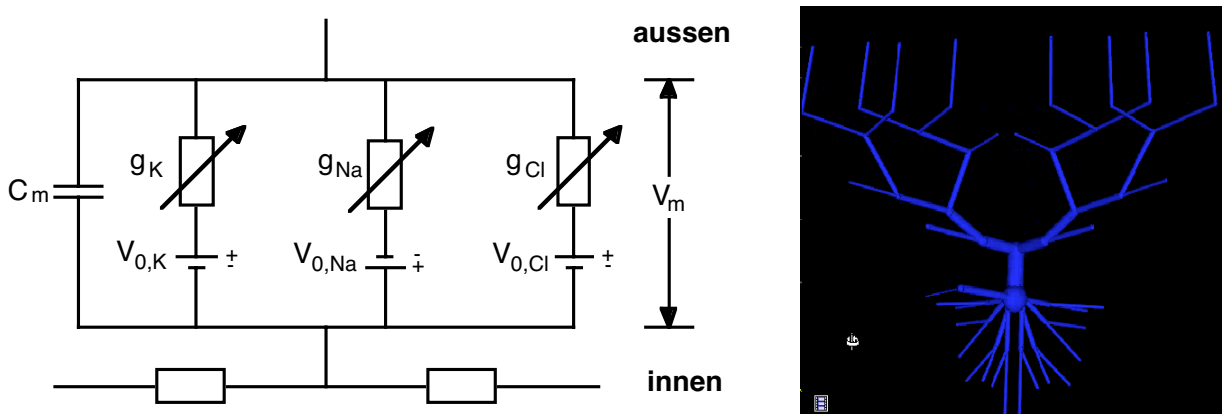


Abbildung 29: (links) Blockschaltbild eines Stückchens Nervenzellmembran. Die Membrankapazität  $C_m$  liegt parallel zu Ionenstromquellen  $V_{0,Na}$ , die durch variable Leitfähigkeiten  $g_k$  modelliert werden. (rechts) Darstellung des Modells einer Pyramidenzelle. Jedes Segment wird durch eine eigene, mit den Nachbarn gekoppelte Differentialgleichung beschrieben.

Diese Beschreibung kann dann als Vorlage für 66 Segmente einer vereinfachten Pyramidenzelle dienen [138, 139]. Diese Zelle zeigt dann im Rahmen einer numerischen Simulation ein sehr realistisches physiologisches Verhalten, sofern man zusätzlich zu den oben erwähnten Natrium-Kanälen noch Calcium-Kanäle und vier weitere Kalium-Kanäle hinzufügt. Dafür benutzen wir eines der frei verfügbaren Simulationsprogramme (GENESIS, California Institute of Technology, Pasadena, CA), die das Kanalverhalten bereits tabelliert

beinhalten und auf schnelle Lösung des Differentialgleichungssystems spezialisiert sind [140-146].

Die erwähnte vereinfachte Pyramidenzelle kann im Rahmen der GENESIS-Beschreibung mit anderen Zellen synaptisch gekoppelt werden, d.h. es werden zusätzlich Ionenkanäle in bestimmte Segmente eingefügt, die die Charakteristik von Rezeptor-gesteuerten Ionenkanälen des Hippocampus zeigen. Dadurch werden sowohl erregende, als auch hemmende Synapsen simuliert [132, 135, 136]. Die lokalen Verknüpfungen sind in Abbildung 30 links zu sehen. Dort erkennt man, dass eine Pyramidenzelle (PYR) afferent erregt wird und dabei sowohl gleichzeitig sowohl ihresgleichen erregen, als auch über vorwärts- (FF) und rückgekoppelte (FB) Interneurone gehemmt werden kann. Insgesamt ergibt das also eine Verknüpfung, wie sie in etwa in Abbildung 4, Kapitel 4, wiederzufinden ist.

Diese lokalen Verknüpfungen werden dann insgesamt zu einem flachen Netzwerk (z-Verteilung der Somata:  $\pm 50 \mu\text{m}$ ) aus 72 Pyramidenzellen und 18 Interneuronen (9 FF, 9 FB) zusammengefügt, welche Abbildung 30 rechts zeigt. Die Simulation errechnet für jedes einzelne Segment zu jedem Zeitschritt das Membranpotential, speichert Ionenflüsse und entscheidende Ereignisse wie insbesondere die Initiation eines Aktionspotentials. In diesem Netzwerk kann man damit durch geeignete Stimulation einiger weniger Pyramidenzellen ein Verhalten, wie es für biologische Netzwerke erwartet wird, beobachten und modulieren. Damit ist nicht gesagt, dass es funktionell vollständig der biologischen Wahrheit entspricht, aber gerade auch der experimentell erwiesene Zusammenhang [147] zwischen intra- und extrazellulären Signalen kann simuliert werden. Die extrazellulären Ströme an bestimmten, räumlich definierten Messpunkten ergeben sich aus der Summe der umgebenden Transmembranströme, normiert vor allem durch den Abstand der zugrundeliegenden Segmente [37, 146]. Damit können wir das ganze Netzwerk mit seinem intrazellulären Verhalten simulieren und kontrollieren und gleichzeitig resultierende extrazelluläre Ströme als Messwerte und Testdaten für die Algorithmen-Validierung heranziehen.

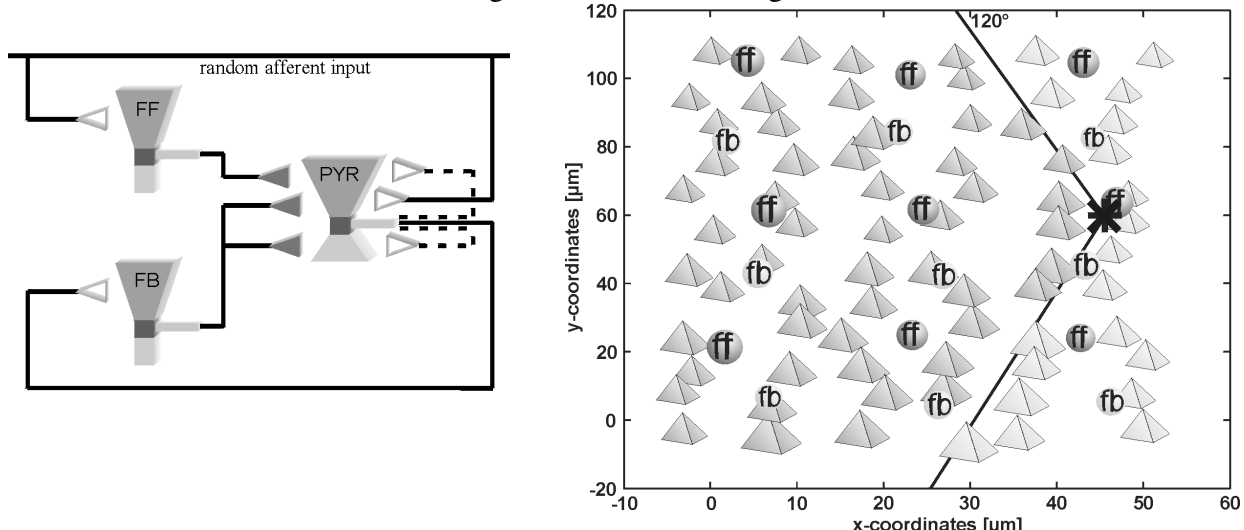


Abbildung 30: (links) Lokale Verknüpfung der simulierten Zellen, die in einem fast planaren Netzwerk zusammenfließen. (rechts) Die Draufsicht dieses Netzwerkes zeigt die Pyramidenzellen und dazwischen liegende Interneurone (ff und fb). Die vom Meßplatz (\*) ausgehenden Linien symbolisieren die richtungsabhängige Auswertung der simulierten Potentiale.

## 7. Ergebnisse

### 7.1. Virtuelle Experimente

Die Fertigstellung und erfolgreiche Simulation unseres realistischen Hippocampus-Netzwerkes, ermöglichte es uns, virtuelle Experimente durchzuführen [135, 136]. Dazu

simulierten wir Messpunkte, die nahe an einer bestimmten Zelle liegen und mit einem Öffnungswinkel von  $120^\circ$  die extrazellulären Potentiale in Betracht ziehen.

Wir erreichen damit eine ähnliche Richtungsabhängigkeit, wie sie von den einseitig leitenden Siliziumsonden erwartet wird. Als Beispiel zeigt Abbildung 31 links die Aufzeichnung von 12 dicht zusammen liegenden, linear angeordneten Elektroden. Der Einschub verdeutlicht die Positionierung der Messpunkte nahe dem Soma und entlang des Dendritenbaumes der Zelle. Die Simulation ergibt aber nicht nur synthetische extrazelluläre Signale, sondern gerade die Spike-Aktivitäten jeder einzelnen im Netzwerk beteiligten Zelle. Damit konnten wir also erstmals dem üblichen Problem der Spike-Detektion durch Vergleich beider Datensätze quantitativ zu Leibe rücken. Abbildung 31 rechts verdeutlicht dieses durch Darstellung des extrazellulären Potentials und der intrazellulären Spikereignisse von Pyramidenzelle 34 und 40.

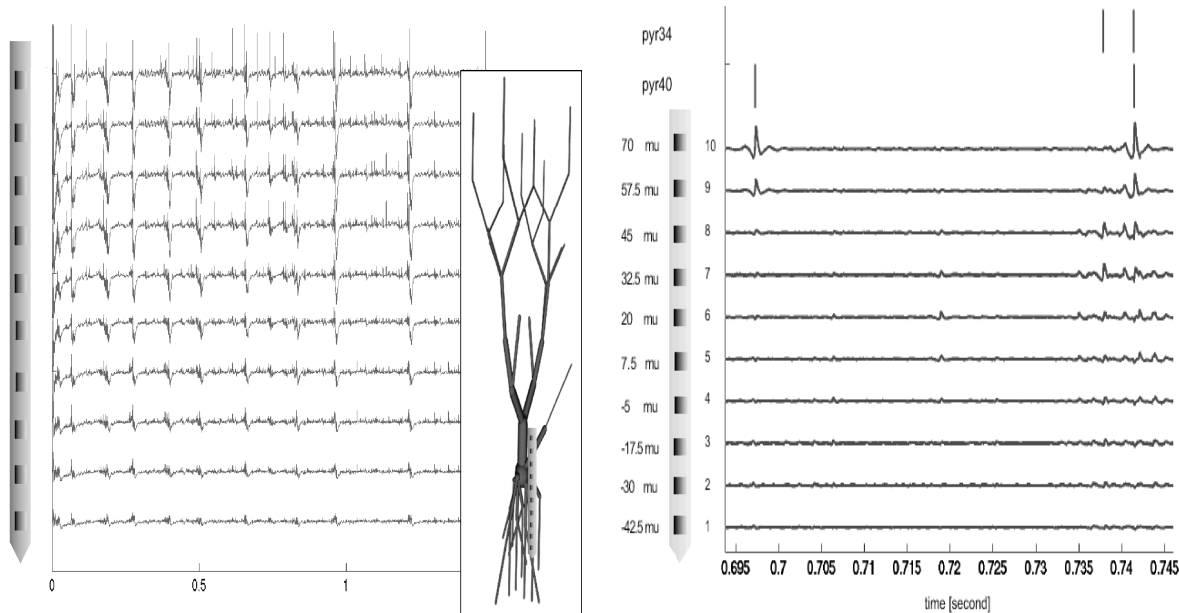


Abbildung 31: (links) Zwölf Meßpunkte nahe an einer Pyramidenzelle (Einschub) zeigen simulierte, extrazelluläre Potentiale in Abhängigkeit von ihrer Position. (rechts) Simulierte extrazelluläre Potentiale (untere Kurven) korrespondieren zu intrazellulären Spikereignissen (Striche oben) von Pyramidenzelle 34 und 40.

Dazu versuchten wir mittels folgender anerkannter, auch in Echtzeit nutzbarer Methoden, in den extrazellulären Ereignissen Spikes zu identifizieren, um sie dann mit den intrazellulären Ereignis-Zeiten zu überprüfen. Spikes sollen sich also in den Daten kenntlich machen durch:

- Überschreiten eines positiven Schwellwertes, der durch das Rausch-Niveau gegeben ist (Abbildung 32:  $pt$ ) [90]
- Schwellwertüberschreitung zusammen mit der Amplitude zwischen Minimum und Maximum (Abbildung 32:  $pt+ppa$ ) [65]
- Schwellwertüberschreitung zusammen mit der Extremadifferenz und der Ereignisbreite (Abbildung 32:  $pt+ppa-pp-time$ ) [148]
- Extremwertdifferenz in einem Fenster vorgegebener Breite (Abbildung 32:  $ppa-window$ ) [137]
- Schwellwertüberschreitung der zweiten Ableitung (Abbildung 32:  $sec\ dev+pt$ ) [149, 150]
- Schwellwertüberschreitung eines Wavelet-entrauschten Signals (Abbildung 32:  $dwt-denosing+pt$ ) [120, 151]

Nicht weiterverfolgt wurde der bisher unbefriedigende Einsatz von Kohonen-Karten [152, 153] und eines Nichtlinearen Energie-Operators [154] (Abbildung 32: TEAGER) zur Spike-Erkennung. Abbildung 32 fasst die Ergebnisse aus mehreren Simulationssätzen zusammen, in

denen jeweils bis zu 1000 Spikes zu finden waren. Künstlich addiertes Rauschen mit Gauß-Charakteristik führte jeweils zu einem Signal-zu-Rausch-Verhältnis (SNR) von etwa 20 dB.

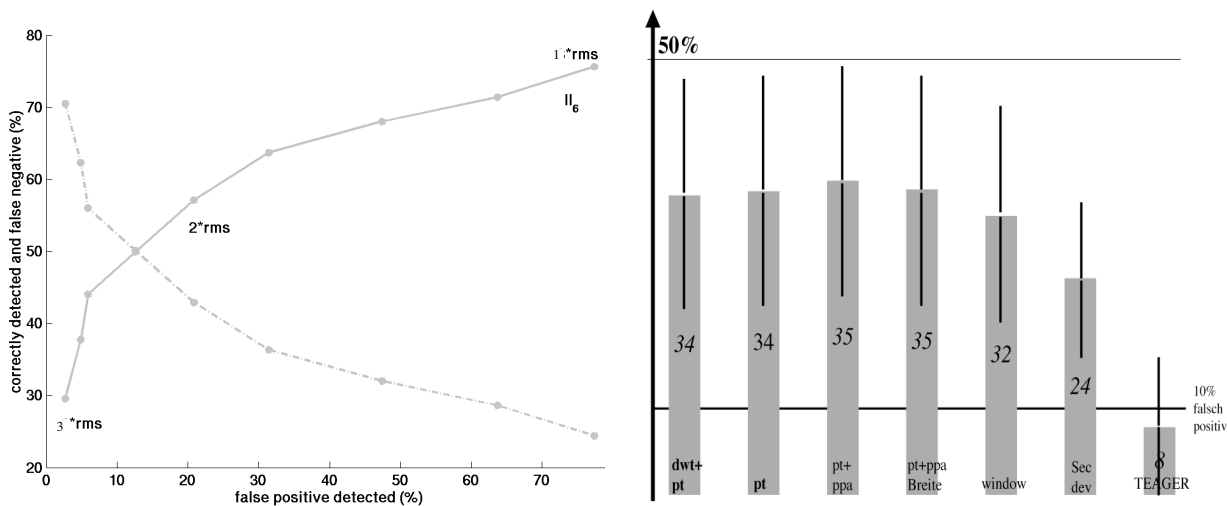


Abbildung 32: (links): Beispielhafte Operationscharakteristik eines Schwellwert-basierten Spike-Detektionsalgorithmus an einem Datensatz mit 1000 Spikes. Durchgezogen: Korrekt erkannte gegen fälschlich gefundene Spikes (falsch positiv). Gepunktet: Nicht gefundene (falsch negativ) gegen fälschlich gefundene Spikes. (rechts) Detektionsraten (mit Streuung) verschiedener Methoden, wenn jeweils 10% fälschlich erkannte Spikes akzeptiert werden.

Im einfachsten Fall wurde der Schwellwert im Verhältnis zur Standardabweichung der Amplitude des Signals definiert und Signalspitzen oberhalb dieses Schwellwertes als mögliche Spike-Ereignisse markiert. An der beispielhaften Operationscharakteristik in Abbildung 32 (links) ist deutlich zu erkennen, daß auch recht hohe Schwellwerte (das Dreifache der Standardabweichung, links im Bild) noch falsch positive Ergebnisse liefern, also Spitzen des künstlichen Rauschanteiles als Spikes detektieren. Gleichzeitig verwirft dann aber die Schwellwertbetrachtung des Signales über 70% der tatsächlich aufgetretenen Spikes und bevorzugt besonders die großen, weit über dem Schwellwert liegenden Spikes. Vergleicht man nun verschiedene Methoden der Spikedetektion, wobei eine geringe Quote an fälschlich detektierten Ereignissen akzeptiert wird, ist festzustellen, dass alle eingesetzten Spikeerkennungsmethoden mit ca. 35% korrekt erkannten Spikes ähnlich schlecht abschneiden (Abbildung 32 rechts). D.h. während eines realen, experimentellen Einsatzes solcher schwellwertgebundener Methoden (mit Schwellen bis zum fünffachen der Standardabweichung!), muss man in Kauf nehmen, daß nur wenige Prozent aller Spikes tatsächlich Verwendung für die weitere Auswertung finden.

Mit diesen quantitativen Ergebnissen stehen wir zwar erst am Anfang einer ganzen Gruppe von weiterführenden Studien, konnten aber immerhin schon eine wichtige Entscheidungshilfe für die Echtzeit-Implementierung der Wavelet-Zerlegung auf unseren DSPs gewinnen. Da gleichzeitig die Erkennungsleistung des Nicht-linearen Energie Operator von der publizierten Leistung extrem deutlich abweicht [154], vermuten wir, daß die allseits anerkannte Nutzung von Gauß-verteiltem Rauschen zu Simulation realen Hintergrundrauschens zumindest fraglich ist [155].

## 7.2. Reale Experimente

Durch unsere enge Kooperation mit elektrophysiologisch arbeitenden Laboratorien waren wir in der Lage, unser Vielkanalableitungssystem bei realen, tierphysiologischen Experimenten

einzusetzen und zu validieren. Dabei gestalteten sich die technischen Tests als überaus erfolgreich, so dass Ergebnisse nicht nur der fortlaufenden technischen Überprüfung dienten, sondern unmittelbar in entsprechende biologische Fragestellungen eingebunden wurden. Experimente wurden gemäß den lokal geltenden Richtlinien und Genehmigungen zum Tierschutz durchgeführt. Besonders befriedigend gestalteten sich die realen Experimente bei der Messung von Feldpotentialen am isolierten Meerschweinchen-Hirn, bei der im Rahmen einer existierenden in-vitro-Präparation unsere Sonden und Datenaufnahme einfach die vor Ort vorhandene Ausrüstung ersetzen konnten.

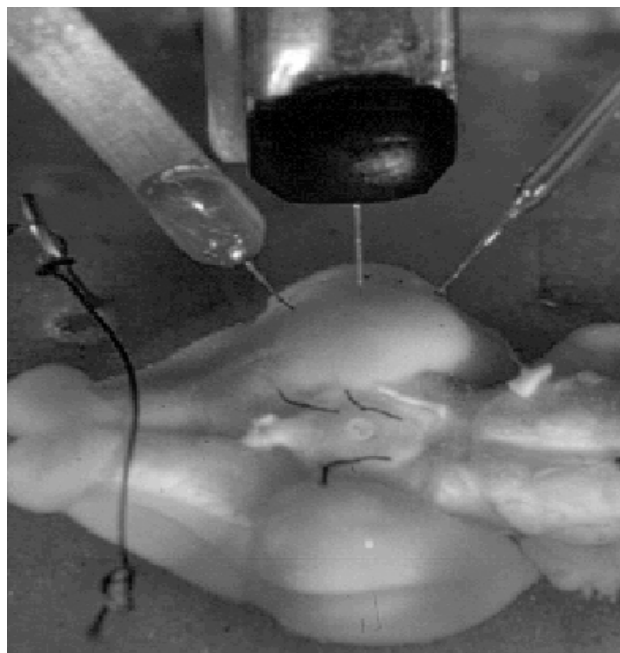


Abbildung 33: Vergleichende Illustration dreier Sonden im entorhinalen Kortex (ERC): links eine 16-Kanal Michigan-Sonde, mittig eine 32 Kanal-Sonde aus unserer Herstellung und rechts eine Glaselektrode.

Die Präparation mit Vielkanal-Elektroden wurde am Istituto Nazionale Neurologico "Carlo Besta" in Mailand entwickelt und durchgeführt. Das Ziel dieser Studie ist es, die Physiologie limbischer Kortex-Regionen zu untersuchen, die sowohl an Lern- als auch an pathologischen Prozessen beteiligt sind, wie z.B. Seitenlappen-Epilepsie und Demenz. Die Kombination der isolierten Hirnpräparation mit Silizium-Vielfachsonden hat das einzigartige Potential, lokale Hirnaktivitäten zu verstehen, da die intrinsischen synaptischen Verschaltungen innerhalb einer kortikalen Region damit detailliert und parallel zum Dendritenbaum kartiert werden können. In dieser Studie brachten wir M1 Sonden zum Einsatz, die 32 Ableitpunkte im Abstand von  $50\text{ }\mu\text{m}$  auf einem einzelnen Schaft der Länge 1,6 mm tragen. Dadurch war es möglich, die gesamte Tiefe des entorhinalen Kortex (ERC) mit einer Dicke von etwa 1,2 - 1,4 mm beim Meerschweinchen zu untersuchen. Die Sonden werden senkrecht zur kortikalen Schichtung eingesetzt, wobei damit die Möglichkeit besteht, die Aktivität zu analysieren, die aus tieferen Hirnschichten nach oben kommt. Besonders hervorzuheben ist dabei die Minimierung des Gewebetraumas bei vervielfachter Ableitdichte im Vergleich zur Einzelsonde oder auch zur Vorgängersonde der University of Michigan. Ebenso war es mit unseren Sonden erstmals in einem einzigen Schritt möglich, die komplette Schichtung vom ERC bis hinab zum Gyrus Dentati des Hippocampus zu vermessen.

Darüberhinaus ermöglichte die geringere Traumatisierung nacheinander von bis zu 12 einzelnen Stellen des ERC abzuleiten, die bis zu 6 mm weit auseinander lagen. Insgesamt konnte durch die deutlich gesteigerte Datenmenge die Anzahl an Versuchstieren in dieser Studie gering gehalten werden. Die Studie basiert darauf, die mikroskopischen Quellen und Senken im Extrazellulärraum zu bestimmen, die die Feldpotentiale bilden.

Dazu wurde die Strom-Quellen-Dichte ("current-source-density", CSD) innerhalb der Schichtungen analysiert, die sich an einer spezifischen Stelle des ERC bilden, wenn benachbarte Regionen gereizt werden. Die assoziativen Verbindungen im ERC selbst sind damit kartier- und nachvollziehbar.

Unsere Messungen zeigen, dass die Reizweiterleitung im entorhinalen Kortex weitgehend durch Fasern der obersten Schichten durchgeführt wird, mit nur geringen Beiträgen der tiefen Schichten. Dadurch konnten wir anatomische Studien bestätigen, die mittels einer Markierungstechnik ebendieses Resultat erhalten haben [67].

Um Sicherheit über die Position der Sonde im Gewebe zu erhalten, wurde als Abschluß eines jeden Experimentes 20-50 mA Strom durch die untersten beiden Elektroden ins Gewebe injiziert. Dies erzeugt lokal eine elektrolytische Zerstörung (Läsion), die wiederum bei einer histologischen Anfärbung zu erkennen ist.

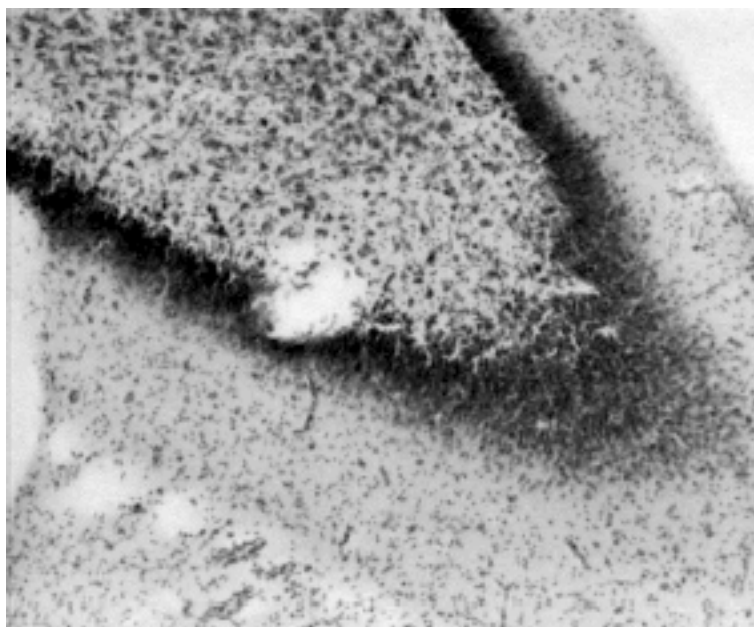


Abbildung 34: Histologischer Querschnitt mit deutlich erkennbarer elektrolytischer Läsionskavität im Zentrum.

In einer weiteren Serie von Experimenten, diesmal in Kooperation mit der Universität Bremen, wurde die Nützlichkeit von Vielfachmikrosonden in dichter Tetrodenanordnung (siehe Abbildung 16) am visuellen Kortex der anästhesierten Ratte gezeigt [109]. Wiederum bestand unser Beitrag in der Silizium-Vielfachelektroden-Ableitung als Ersatz für viele Wiederholungen einzelner Einkanalableitungen. Abbildung 25 zeigt oben die übliche und unten die Blue-Plot Darstellung von 60 ms dieser Ableitungsdaten. Mit einem Signal-zu-Rausch Verhältnis von 20 dB bei einer Übergangsimpedanz von etwa  $4 \text{ M}\Omega$  bei 1kHz Anregungsfrequenz verhalten sich auch diese Sonden ganz im Rahmen der Forderungen. Sie konnten deshalb erfolgreich zur simultanen Ableitung richtungs- und orientierungsabhängiger neuronaler Antworten (den Tuning-Kurven) sowohl von einzelnen als auch von Zell-Populationen eingesetzt werden. Die Resultate der gesamten Population konnten dadurch zur Schätzung und Rekonstruktion der Stimuli eingesetzt werden [109]. Dieser Ansatz basiert auf der Frage, warum Informationen im Gehirn soviel schneller und präziser zu einer Antwort führen, als es die maximale Feuerrate einer einzelnen Zelle erwarten lässt. Man kann nämlich feststellen, dass im Gehirn eine Reizantwort nicht wartet, bis eine einzelne, zentrale Zelle genügend Eingangssignale für eine Entscheidung empfangen hat, sondern bis an mehreren Neuronen gleichzeitig auftretende Reize für eine "Schlußfolgerung" ausreichen. Diese Art Informationen in Netzen zu repräsentieren, nennt man Populationskodierung. Mathematisch versucht man diesen Vorgang dadurch zu imitieren und zu erklären, dass Ableitungen von

vielen, eng beieinander liegenden Neuronen zur Rekonstruktion des ursprünglichen Reizes herangezogen werden [156]. In diesem Sinne konnten wir bestätigen, dass bei gleichbleibender Verarbeitungszeit der Fehler in der Schätzung des ursprünglichen Reizes durch eine steigende Anzahl abgeleiteter Neuronen minimiert werden kann [21, 157]. Durch den Einsatz unserer dichten Silizium-Mikroelektroden kann entsprechend untersucht werden, inwieweit neuronale Populationskodierung die Ungenauigkeiten kompensiert, die die Forderung nach kürzeren Verarbeitungszeiten im visuellen System und seinen Netzwerkstrukturen mit sich bringt [158].

Auch in anderen Zielregionen des Rattenhirns wurden sowohl unsere Sonden, als auch unsere Datenaufnahme erfolgreich zum Einsatz gebracht:

Am Kleinhirn der Ratte konnten wir erstmals erfolgreich Ableitungen mit Silizium-Sonden nachweisen [62], wogegen ihr primärer somatosensorischer Kortex schon früher mit Silizium-Sonden vermessen und grob simuliert wurde [58]. Aus diesem Grund dient uns die Region SI derzeit eher als Testregion zur Quantifizierung des Implantationsvorganges denn als elektrophysiologische Zielregion [159, 160].

Unsere neuen Vielfachmikroelektroden wurden in der experimentellen Elektrophysiologie überaus positiv aufgenommen. Sie erwiesen sich im täglichen Gebrauch als überraschend stabil (für eine starre Struktur dünner als ein Haar) und wiederverwendbar. Sie ermöglichen es zur Zeit, 64 Ableitpunkte in einem einzelnen Präparationsschritt in das Gehirn von Versuchstieren zu implantieren und lassen erwarten, bioelektrische Signale von 2 bis 5 Neuronen pro Messpunkt zu detektieren. Die kleinen Abmessungen, besonders der flexiblen Zuleitungen, ermöglichen es im Prinzip mehrere Sonden gleichzeitig zu implantieren und damit die von uns anvisierten Hunderte von Neuronen abzuleiten.

Unsere einfach handzuhabende Datenaufnahmesoft- und Hardware stößt darüberhinaus auf zunehmendes Interesse auch außerhalb der zellulären Elektrophysiologie und dient uns derzeit als Vorbild für weitere Anwendungen der schnellen DSPs wie sie z.B. in der physiologischen EEG-Aufzeichnung, der Elektromyographie, in der Video-Polysomnographie oder der vereinheitlichten Datendigitalisierung zu finden sind.

## 8. Vergleich mit anderen Projekten

Die Ergebnisse des gesamten EU-geförderten Projektes VSAMUEL erreichen oder übertreffen derzeit alle kommerziell erhältlichen Vielkanaldataaufzeichnungssysteme für die Elektrophysiologie. Insbesondere handelt es sich um das **erste komplett integrierte** und angepasste Multikanal Ableitsystem für neurophysiologische Applikationen überhaupt. In einzelnen Teilespekten müssen wir uns zwar unseren Mitbewerbern unterlegen geben, jedoch gibt es unserer Kenntnis nach kein weiteres *in vivo* nutzbares Vielfachelektroden-System, das in allen Teilbereichen synchron optimiert und entwickelt wurde und damit derart erfolgreich ist:

- Siliziumsonden

Unsere derzeit verfügbaren 64 Ableitpunkte unterliegen zwar dem Marktführer Bionic Technologies LLC, Salt Lake City, UT, mit 96 Ableitpunkten (Nagelbrett-Design) [15, 161-164], können dafür aber gewebefreundlicher implantiert werden [165], sind *in toto* repositionierbar und damit für akute Ableitungsexperimente besser geeignet.

Da unsere Sonden noch dazu senkrecht zur kortikalen Schicht aufzeichnen, sind diese nur mit den Siliziumsonden des Center for Neural Communication and Technology der University of Michigan, MI, zu vergleichen [73, 74, 78, 166, 167]. Diese zeigen jedoch eine

minimale Strukturgröße von  $5 \mu\text{m}$  bei maximal 16 Ableitpunkten und sind damit bei größerer Gewebeschädigung durch eine gröbere Formgebung unsern deutlich unterlegen. Auch sind sie durch eine starre Verbindungstechnik wesentlich unflexibler in der Handhabung. Weitere Sonden sind zwar in der Literatur beschrieben worden [79, 168-177], haben es aber im Gegensatz zu den VSAMUEL-Sonden bisher nicht in die breite biologische Anwendung gebracht, was unter anderem auf deren mangelnde Reproduzierbarkeit durch nicht-industrielle Fertigung zurückzuführen ist.

- Datenaufnahme und Auswertung

In diesem Bereich ist wieder ein Produkt von Bionic Technologies LLC zu nennen, das seit neuestem ein 128-Kanal-Datenaufnahmesystem im Angebot hat. Die Digitalisierung erfolgt beim CEREBUS®-System mit maximal 30 kHz, wogegen unser VSAMUEL-DAQ mit 50 kHz Abtastrate laufen kann. Filterung und Spike-Detektion können dort nur mit gewöhnlichen, festeingestellten, digitalen Filtern und dem klassischen "Template-Matching"-Verfahren durchgeführt werden. Das kann eine Verfremdung der Nutzsignale durch die Phasenverschiebung der Filter zur Folge haben, wogegen die perfekte Rekonstruktionseigenschaft der Wavelet-Zerlegung zusammen mit dem Entrausch-Verfahren die Spike-Formen optimal erhält [115]. Da zudem unsere Software im Prinzip offen zugänglich ist, darf der interessierte Nutzer weitere Prozessschritte nach Wahl hinzufügen. Dabei kann er auf einen recht großen Fundus von veröffentlichten, off-line verwendbaren Routinen zurückgreifen [42, 90, 93, 120, 148, 178-186]. Er kann somit in den Genuss von erwiesenen Routinen in einer Echtzeitanwendung kommen, wie sie sonst nur im Nachhinein ausführbar sind.

Weiterhin erreicht keines der anderen existierenden Datenaufnahmesysteme unsere 16 bit Auflösung bei kontinuierlicher Datenaufzeichnung von 128 Kanälen mit 50 kHz Abtastrate: Tucker-Davis', Gainesville, FL, neues, programmierbares MEDUSA®-System digitalisiert zwar mit 16 bit und bis zu 48 kHz Abtastrate, aber nur von bis zu 16 Kanälen [187]. Wie eine Verkettung von 8 Untereinheiten über einen einzelnen USB-Bus erfolgen soll, ist noch unklar, aber scheinbar angedacht.

Das MAP®-System von Plexon Inc, Dallas, TX, zeichnet zwar von maximal 128 Kanälen mit bis zu 40 kHz Abtastrate auf, braucht aber für die niederfrequenten Feldpotentiale eine getrennte Datenaufnahme und löst die hochfrequenten Spike-Potentiale nur mit 12 bit auf [188].

Auch Multichannel\*Systems', Reutlingen, MEA 60®-System speichert Daten nur in 12 bit Auflösung [189], ebenso wie das Cheetah® System von Neuralynx Inc, Tucson, AR [190]

Auch aus biologischer Sicht stehen die VSAMUEL-Sonden den etablierten Systemen in Nichts nach, sondern sind in Standardprozeduren leicht zu integrieren und finden sogar Anklang beim bisherigen Hauptnutzer der Sonden der University of Michigan , Prof. G. Buzsaki, Rutgers University, Newark, NJ [191].

Insgesamt ergibt obige Gegenüberstellung derzeit verfügbarer Komponenten, dass die Hard- und Software des Projektes VSAMUEL zur Unterstützung von akuten, vielkanaligen Neuronenableitungen als bahnbrechend in vielerlei Hinsicht gelten kann. So eröffnet der modulare Aufbau, die Nutzung eines hochperformanten kommerziellen Signalprozessors und eine offene, konsequent objektorientierte Programmierung die Aussicht auf Aufwärtskompatibilität und verbreitete Nutzung in weit mehr als nur den grundsätzlichen Neurowissenschaften.

## 9. Ausblick

Im Sinne des Sprichwortes "Jeder noch so lange Weg beginnt mit dem ersten Schritt" ist es uns gelungen, die ersten Schritte auf dem Weg zur direkten kortikalen Kopplung zu machen. Wir haben signifikante Fortschritte und Neuerungen bei der Vielfachelektroden-Ableitung erreicht, bei der Hochleistungsdatenaufnahme, -Analyse und realistischen Simulation. Im Sinne des Weges, den Nicolelis [18, 20, 21] und Chapin [19] bereits früher begonnen haben, sind unsere nächsten Schritte die folgenden:

- Entwicklung von Methoden zu chronischen Implantation von Siliziumsonden im Tiermodell mit automatischer Langzeitauswertung.
- Entwicklung und klinischer Einsatz von Vielfach-Sonden für die akute medizinische und Langzeit-Nutzung.
- Implementierung von lernfähigen Kontroll- und Steuerungsalgorithmen auf leistungsfähigen DSPs, die die Populationskodierung auswerten.
- Entwurf geeigneter, kortikal ansteuerbarer Ausgabegeräte, im einfachsten Fall eine "Drei-Tasten-Maus", im besten Fall eine Neuroprothese für alle am Gehen beteiligten Muskelgruppen.

Gerade die medizinische Anwendung von Vielfach-Sonden stellt eine besondere Herausforderung im Sinne der Patientensicherheit dar. Deshalb entwerfen wir gerade Sonden auf biokompatibler Metallbasis [192], die unzerbrechlich sind und damit eine lange Liegezeit versprechen. In der Zwischenzeit wird die Methode der Vielkanal-Ableitungen aber unterstützend für tiefe, stereotaktische Hirnoperationen weiterentwickelt (BMBF-Projekt "navEgate").

Ob sich eine direkte und stabile Zwei-Wege-Verbindung zwischen einem technischen System und dem Gehirn eines Menschen in absehbarer Zukunft verwirklichen lässt, ist durchaus eine offene Frage. Wir sind jedenfalls fest davon überzeugt, dass es in den kommenden 20 Jahren dazu kommen wird - evtl. unter Einbeziehung neuer Methoden der Bio- und Nanoelektronik [193].

## 10. Danksagung

Diese vorliegende Arbeit ist das erfolgreiche Ergebnis der kooperativen Anstrengung vieler Menschen, die ich das Vergnügen hatte zusammenzubringen, zu integrieren und zu motivieren, kurz, sie zu leiten und denen ich mich dankbar verbunden fühle:

Den Mitgliedern meiner Signalverarbeitungs-Gruppe:

- Andre Folkers, der in kürzester Zeit und mit grenzenloser Virtuosität einen schier unendlichen Datenozean mit kleinen Wellen zähmte.
- Kerstin Menne, die mit hohem persönlichen Einsatz (sogar im Anatomie-Saal) alles daransetzte die Simulation zu perfektionieren.
- Thomas Malina, der das Neuland eines selbstgebauten EEG-Systems unerschrocken, nur bewaffnet mit einem Surf-Kite erforschte.
- Florian Mösch, der unsere DSPs zu erfreulichem Sozialverhalten anhielt.
- Henrike Schuhart, Sabine Schwalbach, Behboud Kalantary, Birgitta Weber, Kai Labusch, Martin Lipphardt, Maren Pakura, Michael Dörr, Eva Lange, Manuel Wille und Steffi Jannasch, die mit Spaß und viel Energie Bausteine für das Große Ganze zusammentrugen.

Den räumlich entfernteren Mitstreitern meiner Mikrostrukturtechnik-Gruppe:

- Peter Norlin und Maria Kindlundh, die noch aus jedem Traum ein wunderbares Stück Silizium formen konnten.

Allen anderen Mitgliedern unseres Konsortiums VSAMUEL:

- Marco de Curtis und Gerardo Biella, die auch flüchtige Signale zu schätzen wussten
- Ken Yoshida und Winnie Jensen, die ausdauernd zähe Nerven angingen
- Erik De Schutter, Patrik Fagerstedt, Antonia Volny-Luraghi und Reinoud Maex, die der weichen Natur des Kleinhirns Spikes abtrotzten
- Uwe Thomas und Dirk Höhl, die den Nutzer zum König machen
- Alejandro Sachez-Grueso der die Förderung durch die EU wohlwollend begleitete

Der freundschaftlichen Zusammenarbeit mit Winrich Freiwald, Ulrich Knopp und Erhardt Barth.

Der wohlwollenden und großzügigen Aufnahme durch den Institutsleiter des ISIP, Til Aach, und seiner ganzen Mannschaft, die meine ungewöhnlichen Arbeitsgebiete und süddeutsche Art klaglos ertrugen.

Mein besonderer Dank geht an David Kewley, Judy Macias und Jim Bower, die mir durch günstige Weichenstellung den Wechsel auf ein spannendes Forschungsgleis ermöglichten.

Zu guter Letzt möchte ich mich noch bei Sabine, Vanessa und Mika bedanken, die mir gleichzeitig genug Bodenhaftung und Auftrieb zu verleihen wussten.

## 11. Glossar

16 bit Datentiefe		Genauigkeit der A/D Wandlung. Bei 16 bit stehen 65536 diskrete Werte zur Verfügung, bei 12 bit nur 4096.
A/D	Analog to Digital	Analoge Signale werden mit einer bestimmten Abtastrate und Genauigkeit in Zahlen-Werte umgesetzt
Aktionspotential		Ausgabesignal eines Neurons: Ionenflüsse über die Zellmembran hinweg führen zu einem messbaren Spannungssignal.
ALS	Amyotrophe Lateral-Sklerose, Lou-Gehrigs-Disease	Degenerationskrankheit der ersten und zweiten Motoneurone mit zunehmender Bewegungseinschränkung.
BCI	Brain-Computer Interface	Traditionell nicht-invasiver Ansatz eine direkte Verbindung zwischen Mensch und Maschine zu schaffen.
Benchmarking		Vergleichende Qualitätsmessung mit vereinheitlichten Methoden.
Blueplot		Farbkodierte Darstellung eines zeitdiskreten Signales auf einem neutralen (blauen) Untergrund, der dem Hintergrundrauschen entspricht.
BMI	Brain-Machine Interface	Invasiver Ansatz eine direkte Verbindung zwischen Mensch und Maschine zu schaffen.
CMOS	Complementary Metal Oxide Semiconductor	Standardmethode der Mikroelektronik zur Herstellung von Halbleiterbauelementen (Chips).
CPU	Central Processing Unit	Zentralprozessor, hier ein Intel Pentium-Chip.
CSD	Current Source Density	Darstellung der interpolierten und abgeleiteten Stromdichten in der Umgebung von Ableitpunkten.
De-Noising		Verfahren zum Entfernen von Rauschanteilen aus einem Nutzsignal.
DRIE	Deep Reactive Ion Etching	Anisotrope Ätzmethode, die ein Plasma zum Abtrag von Substratmaterial verwendet (Trockenätzen).
DSP	Digital Signal Processor	Integrierter Schaltkreis (Chip), der speziell entworfen wurde, um schnell extrem viele, aber einfache Rechenoperationen auszuführen.
ERC	Entorhinal Cortex	Bereich der Großhirnrinde, der für die Verarbeitung von Gerüchen verantwortlich gemacht wird..
FES	Funktionelle Elektrostimulation	Methoden zur künstlichen, intrakorporalen elektrischen Reizung von anderweitig nicht innervierten Muskelgruppen.
FIFO	First In First Out	Speicherart.
FIR	Finite Impulse Response	Lineares System mit endlicher Impulsantwort, meist zur Charakterisierung von Filtern genutzt.
FLOPS	Floating Point Operations	Masseinheit, um die numerische Rechenleistung eines DSP anzugeben. Gemessen werden die durchgeföhrten Gleitkomma-Operationen pro Sekunde.
GENESIS	GEneral Neural Simulation System	Programmumgebung, die die Beschreibung und Simulation morphologisch korrekter Neuronennetze ermöglicht.
HDF5	Hierarchical Data Format, Rev. 5	Methoden des National Center for Supercomputing Applications, um große Datenmengen strukturiert zu archivieren.
Host		Hier: Personal Computer, der das Umfeld zur Nutzung eines "Targets" bereitstellt.
Impedanz		Frequenzabhängiger Widerstand eines elektronischen Bauelements aus Kapazitäten und Ohm'schen Widerständen.
In place		Schnelle Berechnungsvorschrift, die ohne Zwischenspeicherung eines Zwischenergebnisses auskommt.
In vitro		Experimente, die an Zellkulturen oder separaten Organpräparationen ausgeführt werden.
In vivo		Experimente, die an einem lebenden Organismus durchgeführt werden.
Interneuron		Neuronentyp, der meist mittels hemmender Wechselwirkung ein realistisches Neuronennetzwerk stabilisiert.
Interrupt		Asynchron auftretendes Steuersignal für die CPU, das zeitweise die Kontrolle an einen anderen Teil des Rechnersystems überträgt.
LFP	Local Field Potential	Extrazellulär messbare Summe von synaptischen Strömen mit Frequenzen zwischen 0,5 Hz und 500 Hz.
MEMS	Micro-Electro-Mechanical Systems	Systeme der Mikroelektronik, die sowohl aus mikroskopischen mechanischen, als auch elektronischen Komponenten bestehen.
MSNR	Multi Site Neuronal Recording	Elektrophysiologische Ableitungen von mehreren aktiven Neuronen mit einer Vielzahl von Mikrolektroden.
MST	Micro-structuring Technology	Mikrostrukturtechnik: Methoden, um MEMS-Bauteile auf Mikrometer-Skala zu erzeugen.
Multiplexing		Sequentielle Abtastung mehrerer Eingangskanäle mittels eines einzelnen Abtastkanals.

PC Karte	Printed Circuit board	Makroskopische Dickfilmtechnik, um elektron. Bauteile auf einem Kunststoffträger zu verbinden.
PCI-Bus	Peripheral Component Interconnect	32 bit breiter Standard-Bus zur unmittelbaren Anbindung von Rechner-Komponenten an eine CPU.
PECVD	Plasma Enhanced Chemical Vapour Deposition	Methode zum Aufbau von dünnen Schichten aus der Gasphase. Dabei wird der Abscheidevorgang durch eine Mikrowellen-Plasma gesteuert.
Pyramidenzelle		Erregender Neuronentyp, der die Ausgaben mikroskopischer Verschaltungseinheiten im Großhirn erzeugt.
RAM	Random Access Memory	Schreib- und Lese-Speicherzelle.
SCSI	Small Computer Systems Interface	Standard zur Anbindung von peripheren Komponenten an ein Rechnersystem.
SNR	Signal to Noise Ratio	Signal zu Rausch-Verhältnis; Qualitätsmaß für Signale.
SOI	Silicon On Insulator	Silizium-Scheibe mit vergrabener Isolatorschicht im Inneren.
Spike Trains		Zeitliche Abfolge von Aktionspotentialen eines einzelnen Neurons.
Stepper Unit		Anordnung aller, in einem Schritt auf Photolack abgebildeter Strukturen.
Target		Hier: DSP-Karte, die über den PCI-Bus mit dem Host-PC kommuniziert.
Tetrode / Stereotrode		Anordnung von vier / zwei Mikrodrähten, die miteinander verdrillt vier / zwei Messpunkte nahe beieinander auf einer einzigen Sonde im Gewebe bereitstellt.
Vielfachsonde	Silicon probe	Synonym für gabelartige, mikroskopische MEMS-Bauteile die eine Vielzahl von Mikroelektroden tragen.
Wire-bonding		Halbautomatisches Mikrolöt-Verfahren, das Chips mit dünnen Gold-Drähten meist mittels Ultraschall mit einem Träger verbindet.
ZIF	Zero Insertion Force	Steckmechanismus, der ein kraftloses Verbinden eines flexiblen Kabels mit einem fixierten Stecker erlaubt.

## 12. Literatur

1. von Ransom, G., *Werfen, schleudern, schießen*, in *Frankfurter Allgemeine Sonntagszeitung*. 2002: Frankfurt. p. 67.
2. Fromherz, P., (2001) *gezeichnet für das 20. Winterseminar „Molecules, Memory and Information“ Klosters 1985.*, Physikalische Blätter, **57**(2): p. 43-48.
3. Patterson, J.R. and M. Grabois, (1986) *Locked-in syndrome: A review of 139 cases*. Stroke, **17**(4): p. 758-764.
4. Schirmer, M., *Neurochirurgie*. 9. ed. 1998, München: Urban&Schwarzenberg. 432.
5. Scheid, W. and E. Gibbels, *Lehrbuch der Neurologie*. 5. ed. 1983, Stuttgart: Thieme. 1199.
6. Hawking, S., *Personal Communication*. 1998.
7. Craelius, W., (2002) *The Bionic Man: Restoring Mobility*. Science, **295**(5557): p. 1018-1021.
8. Wolpaw, J., N. Birbaumer, W. Heetderks, D. McFarland, P. Peckham, G. Schalk, E. Donchin, L. Quatrano, C. Robinson, and T. Vaughan, (2000) *Brain-computer interface technology: a review of the first international meeting*. IEEE Trans. Rehab. Eng., **8**(2): p. 164-173.
9. Pfurtscheller, G. and C. Neuper, (2001) *Motor imagery and direct brain-computer communication*. Proceedings of the IEEE, **89**(7): p. 1123-1134.
10. Bayliss, J.D. and D.H. Ballard, (2001) *A virtual reality testbed for brain-computer interface research*. IEEE Trans Rehab. Eng., **in press**.
11. Kandel, E.R., J.H. Schwartz, and T.M. Jessel, *Principles of neural science*. 3rd ed. 1991, London: Prentice-Hall.
12. Windhorst, U. and H. Johansson, *Modern Techniques in Neuroscience Research*. 1 ed. 1999, Berlin: Springer.
13. Birbaumer, N. and A. Kübler, (2000) *The thought translation device (TTD) for completely paralyzed patients*. IEEE Trans. Rehab. Eng., **8**: p. 190-193.
14. Kennedy, P.R., S.S. Mirra, and R.A.E. Bakay, (1992) *The cone electrode - ultrastructural studies following long-term recording in rat and monkey cortex*. Neuroscience Letters, **142**(1): p. 89-94.
15. Maynard, E., C. Nordhausen, and R. Normann, (1997) *The Utah Intracortical Electrode Array: A recording structure for potential brain-computer interfaces*. Electroencephalography and Clinical Neurophysiology, **102**(3): p. 228-239.
16. Kennedy, P.R., R.A.E. Bakay, M.M. Moore, K. Adams, and J. Goldwaith, (2000) *Direct control of a computer from the human central nervous system*. IEEE Trans. Rehab. Eng., **8**(2): p. 198-202.
17. Berger, T., M. Baudry, R. Diaz Brinton, J.-S. Liaw, V. Marmarelis, A. Park, B. Sheu, and A. Tangy, (2001) *Brain-implantable biomimetic electronics as the next era in neural prosthetics*. Proceedings of the IEEE, **89**(7): p. 993-1012.
18. Nicolelis, M.A.L., A.A. Ghazanfar, C.R. Stambaugh, L.M.O. Oliveira, M. Laubach, J.K. Chapin, R.J. Nelson, and J.H. Kaas, (1998) *Simultaneous encoding of tactile information by three primate cortical areas*. Nature neuroscience, **1**(7): p. 621-630.
19. Chapin, J., K. Moxon, R. Markowitz, and M. Nicolelis, (1999) *Real-time control of a robot arm using simultaneously recorded neurons in the motor cortex*. nature neuroscience, **2**: p. 664-670.
20. Wessberg, J., C.R. Stambaugh, J.D. Kralik, P.D. Beck, M. Laubach, J.K. Chapin, J. Kim, S.J. Biggs, M.A. Srinivasan, and M.A.L. Nicolelis, (2000) *Real-time prediction of hand trajectory by ensembles of cortical neurons in primates*. Nature, **408**: p. 361 - 365.
21. Laubach, M., J. Wessberg, and M.A.L. Nicolelis, (2000) *Cortical ensemble activity increasingly predicts behaviour outcomes during learning of a motor task*. Nature, **405**: p. 567 - 571.
22. Serruya, M., N. Hatsopoulos, L. Paninski, M. Fellows, and J. Donoghue, (2002) *Instant neural control of a movement signal*. Nature, **416**: p. 141-142.
23. Stieglitz, T. and J.U. Meyer, (1998) *Microtechnical interfaces to neurons*. Microsystems Technology in Chemistry and Life Science, **194**: p. 131-162.

24. Toga, A.W. and J.C. Mazziotta, *Introduction to the cartography of the brain*, in *Brain Mapping - the methods*, A.W. Toga and J.C. Mazziotta, Editors. 1996, Academic Press: San Diego. p. 3-25.
25. Damasio, H., *Human brain anatomy in computerized images*. 1 ed. 1995, New York: Oxford University Press. 303.
26. Nicholls, J.G., A.R. Martin, and B.G. Wallace, *From Neuron to Brain*. 3rd ed. 1992, Sunderland, MA: Sinauer Assoc., Inc. 807.
27. Schuhart, H., K.M.L. Menne, and U.G. Hofmann. *GROGRA and GENESIS: in computo grown neurons used for realistic compartmental modeling*. in *CNS\*02 accepted with Neurocomputing*. 2002. Chicago: Elsevier.
28. Segev, I. and M. London, (2000) *Untangling dendrites with quantitative models*. Science, **290**: p. 744-750.
29. Langmoen, I.A. and P. Anderson, (1983) *Summation of excitatory post synaptic potentials in hippocampal pyramidal cells*. J. Neurophysiol., **50**: p. 1320-1329.
30. Hodgkin, A.L. and H.J. Huxley, (1939) *Action potentials recorded from inside a nerve fibre*. Nature, **144**: p. 710-711.
31. Hodgkin, A.L. and A.F. Huxley, (1945) *Resting and action potential in single nerve fibres*. Journal of Physiology, **104**: p. 176.
32. Hodgkin, A.L. and A.F. Huxley, (1952) *A quantitative description of membrane current and its application to conduction and excitation in nerve*. Journal of Physiology, **117**: p. 500 - 544.
33. Hodgkin, A.L. and A.F. Huxley, (1952) *The dual effect of membrane potential on sodium conductance in the giant axon of loligo*. Journal of Physiology, **116**: p. 497 - 506.
34. Geddes, L.A. and L.E. Baker, (1967) *The specific resistance of biological material - a compendium of data for the biomedical engineer and physiologist*. Med. & Biol. Engng., **5**: p. 271-293.
35. Claverol-Tinture, E. and J. Pine, (2002) *Extracellular potentials in low-density dissociated neuronal cultures*. J. Neurosci. Meth., **117**: p. 13-21.
36. Plonsey, R., (1974) *The formulation of bioelectric source-field relationship in terms of surface discontinuities*. J. Franklin Inst., **297**: p. 317-324.
37. Nunez, P.L., *Electric Fields of the Brain: The Neurophysics of EEG*. 1st ed. 1981, Oxford: Oxford University Press. 484.
38. Buzsáki, G., Z. Horváth, R. Urioste, J. Hetke, and K.D. Wise, (1992) *High-frequency network oscillations in the Hippocampus*. Science, **256**: p. 1025-1027.
39. Buzsaki, G., R.G. Bickford, L.J. Ryan, S. Young, O. Pohaska, R.J. Mandel, and F.H. Gage, (1989) *Multisite recording of brain field potentials and unit-activity in freely moving rats*. J. Neurosci. Meth., **28**(3): p. 209-217.
40. Rappelsberger, P., H. Pockeberger, and H. Petsche, (1993) *Sources of electrical brain activity-intracortical current dipoles*. Physiol. Meas., **14**(4A): p. A17-A20.
41. Holt, G.R., *A critical reexamination of some assumptions and implications of cable theory in neurobiology*, in *Biology*. 1998, California Institute of Technology: Pasadena, CA. p. 155.
42. Gray, C., P. Maldonado, M. Wilson, and B. McNaughton, (1995) *Tetrodes markedly improve the reliability and yield of multiple single-unit isolation from multi-unit recordings in cat striate cortex*. J. Neurosci. Meth., **63**(1-2): p. 43-54.
43. Lind, R., P. Conolly, C.D.W. Wilkinson, and R.D. Thomson, (1991) *Finite-element analysis applied to extracellular microelectrode design*. Sensors and Actuators B, **3**(1): p. 23-30.
44. Biella, G.R., L. Uva, U.G. Hofmann, and M. deCurtis, (2002) *Associative interactions within the superficial layers of the entorhinal cortex of the guinea pig*. J. Neurophysiol, **88**(3): p. 1159-1165.
45. Biella, G.R., L. Uva, U.G. Hofmann, and M. deCurtis. *Intrinsic and associative synaptic circuit in the temporal neocortex, perirhinal and entorhinal cortex: an intra- and extracellular electrophysiological study*. in *Forum of European Neurosciences - Abstracts*. 2002. Paris.
46. Laurent, G., (1999) *A systems perspective on early olfactory coding*. Science, **286**: p. 723-728.
47. Buck, L. and R. Axel, (1991) *A novel multigene family may encode odorant receptors: A molecular basis for odor recognition*. Cell, **65**: p. 175-187.
48. Lettvin, J., H. Maturana, and e. al., (1959) *What the frog's eye tells the frog's brain*. Proceedings IRE, **47**: p. 1940-1951.

49. Eggermont, J., W. Epping, and A. Aertsen, (1983) *Stimulus dependent neural correlations in the auditory midbrain of the grassfrog*. Biol. Cybern., **47**: p. 103-117.
50. Dayan, P. and L.F. Abbot, *Theoretical Neurosciences - Computational and Mathematical Modelling of Neural Systems*. 2001, Boston: MIT Press. 476.
51. Freiwald, W.A., A.A. Kreiter, and W. Singer, (1995) *Stimulus dependent intercolumnar synchronization of single unit responses in cat area 17*. NeuroReport, **6**: p. 2348-2352.
52. Singer, W., C. Gray, A. Engel, P. König, A. Artola, and S. Bröcher, (1990) *Formation of cortical cell assemblies*. Symp.Quant.Biol., **LV**: p. 939-952.
53. Stanley, G.B., F.F. Li, and Y. Dan, (1999) *Reconstruction of natural scenes from ensemble responses in the lateral geniculate nucleus*. J. Neuroscience, **19**(18): p. 8036-8042.
54. Dan, Y., J.-M. Alonso, W.M. Usrey, and R.C. Reid, (1998) *Coding of visual information by precisely correlated spikes in the lateral geniculate nucleus*. Nature Neuroscience( 1): p. 501-507.
55. Schütz, A., *Wie die Großhirnrinde mit sich selbst verschaltet ist*. 2001.
56. Robbins, J. and G.D. Fischbach, (1992) *Golgi stained neurons in "Mind and Brain"*. Scientific American, **267**(3): p. 26.
57. Hofmann, U.G., D.T. Kewley, M. Hills, S.D. VanHooser, G.T.A. Kovacs, and J.M. Bower, (1998) *Depth profiling of neuronal activity by multisite microelectrode arrays*. Europ. J. Neurosci., **10**(Supp. 10): p. 431.
58. Van Hooser, S.D., U.G. Hofmann, D.T. Kewley, and J.M. Bower, (2000) *Relationship between field potentials and spike activity in rat S1: multi-site cortical recordings and simulations*. Neurocomputing 32-33: p. 591-596.
59. Sasaki, K., J.M. Bower, and R. Llinás, (1989) *Multiple Purkinje cell recording in rodent cerebellar cortex*. Eur. J. Neuroscience, **1**: p. 572-586.
60. Bower, J.M. and D.C. Woolston, (1983) *Congruence of spatial organization of tactile projections to Granule Cell and Purkinje Cell layers of cerebellar hemispheres of the albino rat: Vertical organization of cerebellar cortex*. J. Neurophys., **49**(3): p. 745-765.
61. De Schutter, E., (1995) *Cerebellar long-term depression might normalize excitation of Purkinje cells: a hypothesis*. Trends Neurosci., **18**: p. 281-295.
62. Fagerstedt, P., A. Volny-Luraghi, M. Kindlundh, P. Norlin, U. Hofmann, and E. DeSchutter. *A new type of silicon probes with multi-site microelectrodes for single unit and local field potential (LFP) recordings from cerebellar cortex of anesthetized rats*. in *Forum of European Neurosciences - Abstracts*. 2002. Paris.
63. de Curtis, M., G. Biella, M. Forti, and F. Panzica, (1994) *Multifocal spontaneous epileptic activity in the piriform cortex of the isolated guinea pig brain*. J. Neurophysiol., **71**: p. 2463-2476.
64. Biella, G., F. Panzica, and M. de Curtis, (1996) *Interactions between associative potentials in the piriform cortex of the in vitro isolated guinea pig brain*. Eur. J. Neurosci., **8**: p. 1350-1357.
65. Nicolelis, M.A.L., ed. *Methods for Neural Ensemble Recordings*. 1st ed. CRC Methods in Neuroscience, ed. S. Simon and M. Nicolelis. 1999, CRC Press: Boca Raton, FL. 257.
66. Swanson, L.W., *Brain Maps: Structure of the Rat Brain*. 1 ed. 1992, Amsterdam: Elsevier. 240.
67. Dickson, C.T., G. Biella, and M. de Curtis, (2000) *Evidence for spatial modules mediated by temporal synchronization of carbachol-induced gamma rythm in medial entorhinal cortex*. J. Neurosci., **20**(20): p. 7846-7854.
68. Biella, G., L. Uva, and M. de Curtis, (2001) *Network activity evoked by neocortical stimulation in area 36 of the perirhinalcortex*. J Neurophysiol., **86**(164-172.).
69. Hofmann, U.G., E. De Schutter, M. de Curtis, K. Yoshida, U. Thomas, and P. Norlin, (2000) *On the design of multi-site microelectrodes for neuronal recordings*. MICRO.tec 2000, **Voll**: p. 283-288.
70. Bousse, L., D. Hafeman, and N. Tran, (1990) *Time-dependence of the chemical response of Silicon Nitride Surfaces*. Sensors and Actuators, **B1**: p. 361-367.
71. Bousse, L., (1982) *Single electrode potentials related to flat-band voltage measurements on EOS and MOS structures*. J.Chem.Phys., **76**(10): p. 5128-5133.
72. Kovacs, G.T.A., *Micromachined Transducers Sourcebook*. McGraw-Hill Series in Electrical and Computer Engineering, ed. S.W. Director. 1998, Boston: WCB/MacGraw-Hill. 911.

73. Anderson, D.J., K. Najafi, S.J. Tanghe, D.A. Evans, K.L. Levy, J.F. Hetke, X. Xue, J.J. Zappia, and K.D. Wise, (1989) *Batch-fabricated thin-film electrodes for stimulation of the central auditory system*. IEEE Transactions on Biomedical Engineering, **36**(7): p. 693 - 704.
74. Wise, K.D. and K. Najafi, (1991) *Microfabrication techniques for integrated sensors and microsystems*. Science, **254**: p. 1335 - 1342.
75. Najafi, K. and K.D. Wise, (1986) *An implantable multielectrode array with on-chip signal processing*. IEEE J. Solid-State Circ., **21**: p. 1035-1044.
76. Drake, K.L., K.D. Wise, J. Farraye, and D.J. Anderson, (1988) *Performance of planar multisite micropoles in recording single unit introcortical activity*. IEEE Trans. Bomed. Eng., **BME-35**: p. 719-732.
77. BeMent, S.L., K.D. Wise, D.J. Anderson, K. Najafi, and K.L. Drake, (1986) *Solid state electrodes for multichannel multiplexed intracortical neuronal recording*. IEEE Trans. on Biomed. Eng., **33**(2): p. 230-241.
78. Najafi, K., K.D. Wise, and T. Mochizuki, (1985) *A high-yield IC-compatible multichannel recording array*. IEEE Trans Electron Devices, **32**(7): p. 1206-1211.
79. Blum, N., B. Carkhuff, H. Charles, R. Edwards, and R. Meyer, (1991) *Multisite micropoles for neural recordings*. IEEE Trans. Biomed. Eng., **38**(1): p. 68-74.
80. Connolly, P., G. Moores, W. Monaghan, J. Shen, S. Britland, and P. Clark, (1992) *Microelectronic and nanoelectronic interfacing techniques for biological systems*. Sensors and Actuators B - Chemical, **6**(1-3): p. 113-121.
81. Yoshida, K., A. Inmann, and M.K. Haugland. *Measurement of complex impedance spectra of implanted electrodes*. in *4th Ann. Conf. of the Int. Functional Eletrical Stimulation Society*. 1999. Sendai, Japan.
82. Brett, C.M.A. and A.M.O. Brett, *Electrochemistry*. 1. ed. Oxford Science Publications. 1993, Oxford: Oxford University Press. 419.
83. Bockris, J.O. and S.U.M. Khan, *Surface Electrochemistry: A Molecular Level Approach*. 1st ed. 1993, New York: Plenum Press. 1014.
84. Bronzino, J.D., *Biomedical Engineering Handbook*. 2. ed. Electrical Engineering Handbook Series, ed. R.C. Dorf. Vol. 1. 2000, Boca Raton, FL: CRC Press LLC.
85. Yoshida, K., W. Jensen, P. Norlin, M. Kindlundh, and U.G. Hofmann, (2001) *Characterization of silicon microelectrodes from the EU VSAMUEL project*. Biomedizinische Technik, **46 E1**: p. 446-447.
86. Rieke, F., D. Warland, R. de Ruyter van Steveninck, and W. Bialek, eds. *Spikes - Exploring the Neural Code*. Computational Neuroscience, ed. T.J. Sejnowski and T.A. Poggio. 1998, MIT Press: Cambridge, MA. 395.
87. Martignon, L., H. Von Hasseln, S. Grün, A. Aertsen, and P. G, (1995) *Detecting higher-order interactions among the spiking events in a group of neurons*. Biol.Cybern., **73**: p. 69-81.
88. Bringmann, A. and F. Klingberg, (1991) *Depth distribution of frontal cortical field potential to acoustic stimulation in unrestrained non-anaesthetized rats*. Neuroscience Letters, **133**: p. 179-182.
89. Ulbert, I., E. Halgren, G. Heit, and G. Karmos, (2001) *Multiple microelectrode-recording system for human intracortical applications*. J. Neurosci. Meth., **106**: p. 69-79.
90. Lewicki, M., (1998) *A review of methods for spike sorting: the detection and classification of neuronal potentials*. Comp. Neural. Syst., **9**: p. R53-R78.
91. Wheeler, B. and W. Heetderks, (1982) *A comparison of techniques for classification of multiple neural signals*. IEEE Trans Biomed Eng, **29**: p. 752-9.
92. Lewicki, M., (1994) *Bayesian modeling and classification of neural signals*. Neural Comp, **6**(1005-1030.).
93. Oweiss, K.G. and D.J. Anderson. *A new approach to array denoising*. in *ICASPP*. 2000.
94. Norlin, P., M. Kindlundh, A. Mouroux, K. Yoshida, and U.G. Hofmann, (2002) *A 32-site neural recording probe fabricated by DRIE of SOI substrates*. J. Micromechanics and Microelectronics, **12**(4): p. 414-419.
95. Kindlundh, M., P. Norlin, and U.G. Hofmann. *Development of multisite microelectrodes for neuroscience*. in *Proceedings of the Micro Structure Workshop MSW'02*. 2002. Aronsborg, Bålsta, Sweden.

96. Jog, M., C. Connolly, Y. Kubota, D. Iyengar, L. Garrido, R. Harlan, and A. Graybiel, (2002) *Tetrode technology: advances in implantable hardware, neuroimaging, and data analysis techniques*. J. Neurosci. Methods, **117**: p. 141-152.
97. Hetherington, P., T. Blanche, and N. Swindale. *Prediction of neuron 3D cortical location by triangulation of spike signals from silicon electrode recording arrays*. in *Soc. Neurosci. Abstr.* 1999. Miami beach: Society for Neuroscience.
98. Blanche, T.J., P.A. Hetherington, L. Kojic, and N.V. Swindale. *Validation of the prediction of neuron 3D cortical location: Application to the study of spatiotemporal dynamics of local circuitry*. in *Soc. Neurosci. Abstr.* 1999. Miami Beach: Society for Neuroscience.
99. Windeck, C., *AMDs Thorougbred galoppiert vor*, in *c't.* 2001. p. news.
100. Sze, S., *Semiconductor Devices: Physics and Technology*. 2nd ed. 2001, New York: John Wiley & Sons. 572.
101. All-Flex-Inc, *Flex Design Guide*. 2000, All Flex Inc: <http://www.allflexinc.com/guid.shtml>.
102. Stearns, T., *Flexible Printed Circuitry*. Electronic Packaging and Interconnect Series, ed. C.M. Harper. 1995, New York: MacGraw Hill. 290.
103. Yoshida, K., K. Jovanovic, and R.B. Stein, (2000) *Application of intrafascicular electrodes to the mudpuppy preparation*. J. Neurosci. Meth., **96**: p. 47-55.
104. Norlin, P., M. Kindlundh, A. Mouroux, K. Yoshida, W. Jensen, and U.G. Hofmann. *A 32-site neural recording probe fabricated by double-sided deep reactive ion etching of Silicon-on-Insulator substrates*. in *12th Micromechanics Europe Workshop (MME-2001)*. 2001. Cork, Ireland.
105. Kindlundh, M. and P. Norlin, *Custom designed 64 microelectrode probes*. 2002, Acreo AB: Kista, Sweden.
106. McNaughton, B., J. O'Keefe, and C. Barnes, (1983) *The stereotrode: A new techniques for simultaneous isolation of several single units in the central nervous system from multiple unit recording*. J. Neurosci. Methods, **8**: p. 391-97.
107. Harris, K., D. Henze, J. Csicsvari, H. Hirase, and G. Buzsaki, (2000) *Accuracy of tetrode spike separation as determined by simultaneous intracellular and extracellular measurements*. J. Neurophysiol., **84**: p. 401-14.
108. Hofmann, U.G., D.T. Kewley, and J.M. Bower. *Factors affecting brain dimpling during microelectrode insertion*. in *Soc. Neurosci. Abstr.* 1998. Los Angeles: Society for Neuroscience.
109. Freiwald, W., H. Stemman, A. Wannig, A.K. Kreiter, U.G. Hofmann, M.D. Hills, G.T.A. Kovacs, D.T. Kewley, J.M. Bower, C.W. Eurich, and S.D. Wilke, (2002) *Stimulus representation in rat primary visual cortex: multi-electrode recordings and estimation theory*. Neurocomputing, **44-46**: p. 407-416.
110. Kewley, D.T., U.G. Hofmann, M. Hills, S.D. VanHooser, G.T.A. Kovacs, and J.M. Bower. *Progress on an integrated multichannel recording system*. in *28th NIH-Workshop on Neural Prostheses*. 1997. Bethesda, MA.
111. Bower, J.M., U.G. Hofmann, D.T. Kewley, and S.D. VanHooser. *Caltech/Stanford multiunit recording system*. in *Satellite Symposium on new developments of multichannel recording systems*. 1997. New Orleans: Society for Neuroscience.
112. Folkers, A. and U.G. Hofmann, *Data acquisition system for 64 channels including compression schemes*. 2002, ISIP, University of Lübeck: Lübeck. p. 30.
113. Folkers, A. and U.G. Hofmann, *Data acquisition system for 32 channels*. 2002, ISIP, University of Lübeck: Lübeck. p. 30.
114. Hofmann, U.G., A. Folkers, F. Mösch, D. Höhl, M. Kindlundh, and P. Norlin, (2002) *A 64(128)-channel multisite neuronal recording system*. Biomedizinische Technik, **47**(E 1): p. 194-197.
115. Folkers, A., F. Mösch, T. Malina, and U.G. Hofmann, (2002) *Realtime bioelectrical data acquisition and processing from 128 channels utilizing the Wavelet-Transformation*. in press with Neurocomputing.
116. Lüke, H., *Signalübertragung*. 6. ed. 1995, Berlin: Springer. 381.
117. Folk, M., *Introduction to HDF5*. 1998, The National Center for Supercomputing Applications.

118. Weber, B., T. Malina, K. Menne, A. Folkers, and U.G. Hofmann, (2001) *Handling large files of multisite microelectrode recordings for the European VSAMUEL consortium*. Neurocomputing, **38-40**(1-4): p. 1725-1734.
119. Malina, T., A. Folkers, and U.G. Hofmann, (2002) *Real-time EEG processing based on Wavelet Transformation*. FMBE - 12th Nordic Baltic Conference on Biomedical Engineering and Medical Physics: p. 166-167.
120. Letelier, J.C. and P.P. Weber, (2000) *Spike sorting based on discrete wavelet transform coefficients*. Journal of Neuroscience Methods, **101**: p. 93-106.
121. Fliege, N., *Multiraten-Signalverarbeitung*. Informationstechnik, ed. N. Fliege. 1993, Stuttgart: Teucner. 405.
122. Mallat, S., *A wavelet tour of signal processing*. 2 ed. 1998, San Diego: Academic Press. 637.
123. Chui, C.K., *An Introduction to Wavelets*. 1 ed. Wavelet analysis and its applications. Vol. 1. 1992, San Diego: Academic Press.
124. Nelson, M. and J.-L. Gailly, *The Data Compression Book*. 2nd ed. 1996, New York, NY: M&T Books. 557.
125. Salomon, D., *Data compression : the complete reference*. 1998, New York: Springer. xx, 427.
126. Franzen, A., (1998) *Compression of process data with a wavelet method*. Steel Research, **69**(1): p. 28-30.
127. Lu, Z., D.Y. Kim, and W.A. Pearlman, (2000) *Wavelet compression of ECG signals by the set partitioning in hierarchical trees algorithm*. IEEE Trans Biomed. Eng., **47**(7): p. 849-856.
128. Sweldens, W. *The lifting scheme: A new philosophy in biorthogonal wavelet constructions*. in *Wavelet Applications in Signal and Image Processing III*. 1995: SPIE.
129. Daubechies, I. and W. Sweldens, (1998) *Factoring wavelet transforms into lifting steps*. J. Fourier Anal. Appl., **4**(3): p. 27.
130. Valens, C., *The fast lifting wavelet transform*. 1999.
131. Averbuch, A. and V. Zheludev, (2002) *Lifting scheme for bioorthogonal multiwavelets originated from Hermite spline*. IEEE Trans. Signal Proc., **50**(3): p. 487-500.
132. Menne, K., R. Maex, and U.G. Hofmann. *Extracellular potential data generated in a network simulation*. in *The Neurosciences at the Turn of the Century, Proceedings of the 4th Meeting of the German Neuroscience Society*. 2001. Göttingen: Georg Thieme Verlag, Stuttgart.
133. Menne, K.M.L., R. Maex, and U.G. Hofmann. *Biologically realistic simulated extracellular potential data as benchmark for the evaluation of spike detection algorithms*. in *CNS\*02*. 2002. Chicago: Elsevier.
134. Menne, K.M.L., R. Maex, and U.G. Hofmann. *A realistical simulation of a small CA3 network to benchmark spike sorting algorithms and feature detection*. in *Forum of European Neurosciences Abstracts*. 2002. Paris.
135. Menne, K.M.L., T. Malina, A. Folkers, and U.G. Hofmann, *Biologically realistic simulation of a part of hippocampal CA3: Generation of testdata for the evaluation of spike detection algorithms*, in *5th German Workshop on Artificial Life - Abstracting and Synthesizing the Principles of Living Systems*, J.K. D. Polani, T. Martinetz, Editor. 2002, IOS Press Infinix: Lübeck. p. 17-25.
136. Menne, K.M.L., A. Folkers, R. Maex, T. Malina, and U.G. Hofmann, (2002) *Test of spike sorting algorithms on the basis of simulated data*. Neurocomputing, **44-46**: p. 1119-1126.
137. Atiya, A., (1992) *Recognition of multiunit neural signals*. IEEE Trans. on Biomed. Eng., **39**(7): p. 723-729.
138. Traub, R.D., R.K.S. Wong, R. Miles, and H. Michelson, (1991) *A model of a CA3 hippocampal pyramidal neuron incorporating voltage-clamp data on intrinsic conductances*. J. neurophysiol., **66**: p. 635-650.
139. Traub, R.D. and J.R. Jefferys, (1994) *A branching dendritic model of a rodent CA3 pyramidal neurone*. Journal of Physiology, **481**(1): p. 79-95.
140. Wilson, M.A. and J.M. Bower, *The simulation of large scale neural networks*, in *Methods in Neuronal Modeling*, C. Koch and I.Segev, Editors. 1989, MIT Press: Cambridge, MA. p. 291-333.
141. Hines, M., (1984) *Efficient computation of branched nerve equations*. Int. J. Bio-Med. Comput., **15**: p. 69-79.

142. Hines, M., (1989) *A program for the simulation of nerve equations with branching geometries*. Int. J. Bio.-Med. Comput., **24**: p. 55-68.
143. Hines, M. and N.T. Carnevale, (1997) *The NEURON simulation environment*. Neural Computation, **9**: p. 1179-1209.
144. Bhalla, U.S. and J.M. Bower, (1990) *Genesis: a neuronal simulation system*.
145. Wilson, M.A., U.S. Bhalla, J.D. Uhley, and J.M. Bower, *GENESIS: A system for simulating neural networks*, in *Advances in Neural Network Information Processing Systems*, D. Touretzky, Editor. 1990, Morgan Kaufman Publ.: San Mateo.
146. Bower, J.M. and D. Beeman, *The Book of GENESIS*. 2nd ed. 1998, New York: Springer. 458 + CDRom.
147. Henze, D., Z. Borhegyi, J. Csicsvari, A. Mamiya, K. Harris, and G. Buzsaki, (2000) *Intracellular features predicted by extracellular recordings in the hippocampus in vivo*. J. Neurophysiol., **84**: p. 390-400.
148. Abeles, M. and M. Goldstein, (1977) *Multi spike train analysis*. IEEE Trans Biomed. Eng BME, **65**: p. 762-773.
149. Usui, S. and I. Amidror, (1982) *Digital low-pass differentiation for biological signal processing*. IEEE Transactions on Biomedical Engineering,, **29**: p. 686-693.
150. McGill, K., K. Cummins, and L. Dorfman, (1985) *Automatic decomposition of the clinical electromyogram*. IEEE Transactions on Biomedical Engineering, **32**: p. 470-477.
151. Fang, J., G.C. Agarwal, and B.T. Shahani, (1999) *Decomposition of multiunit electromyographic signals*. IEEE Transactions on Biomedical Engineering, **46**: p. 685-697.
152. Chandra, R. and L. Optican, (1997) *Detection, classification, and superposition resolution of action potentials in multiunit single-channel recordings by an on-line real-time neural network*. IEEE Transactions on Biomedical Engineering, **44**(5): p. 403-412.
153. Parks, R.W., D.S. Levine, and D.L. Long, *Fundamentals od Neural Network Modeling*. Computational Neuroscience, ed. T.J. Sejnowski and T.A. Poggio. 1998, Cambridge, MA: MIT Press. 416.
154. Kim, K.H. and S.J. Kim, (2000) *Neural spike sorting under nearly 0-dB signal-to-noise-ratio unsing nonlinear energy operator and artificial neural-network classifier*. IEEE Trans. Biomed. Eng., **47**: p. 1406-1411.
155. Menne, K.M.L., H. Schuhart, M. Lipphardt, and U.G. Hofmann, (2003) *Benchmarking spike detection algorithms on the basis of virtual experimental data*. in preparation for IEEE TB;E.
156. Zhang, K., I. Ginzburg, B. McNaughton, and T. Sejnowski, (1998) *Interpreting neuronal population activity by reconstruction:uni ed framework with application to hippocampal place cells*. J.Neurophysiol., **79**: p. 1017-1044.
157. Nicolelis, M.A.L. and J.K. Chapin, (1994) *Spatiotemporal structure of somatosensory responses of many-neuron ensembles in the rat ventral posterior medial nucleus of the thalamus*. J.Neurosci., **14**: p. 3511-3532.
158. Paradiso, M.A., (1988) *A theory for the use of visual orientation information which exploits the columnar structure of striate cortex*. Biol. Cybernet., **58**: p. 35-49.
159. Jensen, W., U. Hofmann, and K. Yoshida, (2002) *Microscopical effects of microprobe insertion into nervous tissue*. in preparation.
160. Jensen, W., T. Malina, U. Hofmann, and K. Yoshida. *Measurement of intrafascicular insertion force of a tungsten needle into peripheral nerve*. in IEEE EMBS. 2001. Istanbul, Turkey.
161. Norman, R.A., B.W. Hatt, and S. Hatt, *Webpage der Bionic Technologies LLC*. 2002, Bionic Technologies LLC.
162. Campbell, P.K., K.E. Jones, R.J. Huber, K.W. Horch, and R.A. Normann, (1991) *A Silicon Based Three Dimensional Neural Interface: Manufacturing Processes for an Intracortical Electrode Array*. IEEE Trans. Biomed. Eng., **38**: p. 758-768.
163. Branner, A. and R.A. Normann, (2000) *A multielectrode array for intrafascicular recording and stimulation in sciatic nerve of cats*. Brain Res. Bull., **51**(4): p. 293-306.
164. Nordhausen, C., E. Maynard, and R. Normann, (1996) *Single unit recording capabilities of a 100 microelectrode array*. BRAIN RESEARCH, **726**(1-2): p. 129-140.

165. Rousche, P.J. and R.A. Normann, (1992) *A method for pneumatically inserting an array of penetrating electrodes into cortical tissue.* Ann. Biomed. Eng., **20**: p. 413-422.
166. Hetke, J.F., K.D. Wise, and D.J. Anderson, *Center for Neural Communication Technology - [www.engin.unich.edu/facility/cnct](http://www.engin.unich.edu/facility/cnct).* 2002, University of Michigan.
167. Ji, J., K. Najafi, and K.D. Wise, (1990) *A scaled electronically-configurable multichannel recording array.* Sensors and Actuators A - Physical, **22**(1-3): p. 589-591.
168. Burmeister, J.J., K. Moxon, and G.A. Gerhardt, (2000) *Ceramic-based multisite microelectrodes for electrochemical recordings.* Analytical Chemistry, **72**(1): p. 187-192.
169. Edell, D., J. Churchill, and I. Gourley, (1982) *Biocompatibility of a silicon based peripheral-nerve electrode.* Biomaterials, Medical Devices, and Artificial Organs, **10**(2): p. 103-122.
170. Ensell, G., D. Banks, D. Ewins, W. Balachandran, and P. Richards, (1996) *Silicon-based microelectrodes for neurophysiology fabricated using a gold metallization nitride passivation system.* JOURNAL OF MICROELECTROMECHANICAL SYSTEMS, **5**(2): p. 117-121.
171. Yoon, T.H., E.J. Hwang, D.Y. Shin, S.I. Park, S.J. Oh, S.C. Jung, H.C. Shin, and S.J. Kim, (2000) *A micromachined silicon depth probe for multichannel neural recording.* IEEE Trans. Biomed. Eng., **47**(8): p. 1082-1087.
172. Weiland, J.D. and D.J. Anderson, (2000) *Chronic neural stimulation with thin-film, Iridium oxide electrodes.* IEEE Trans. Biomed. Eng., **47**(7): p. 911-918.
173. Bai, Q., K.D. Wise, and D.J. Anderson, (2000) *A high-yield microassembly structure for three-dimensional microelectrode arrays.* IEEE Trans Biomed Eng, **47**(3): p. 281-289.
174. Cheung, K., G. Lee, K. Djupsund, Y. Dan, and L.P. Lee. *A new neural probe using SOI wafers with topological interlocking mechanisms.* in *1st Annual International IEEE-EMBS Special Topic Conference on Microtechnologies in Medicine & Biology.* 2000. Lyon, France.
175. Eichenbaum, H. and M. Kuperstein, (1986) *Extracellular neural recording with multichannel microelectrodes.* J. Electrophysiol. Tech., **13**(3): p. 189-209.
176. Kuperstein, M., *Microelectrode and assembly for parallel recording of neuron groups,* in *US Patent No. 4,461,304.* 1984, MIT: USA.
177. Kewley, D.T., M.D. Hills, D.A. Borkholder, I.E. Opris, N.I. Maluf, C.W. Storment, J.M. Bower, and G.T.A. Kovacs, (1997) *Plasma-etched neural probes.* Sensors and Actuators A, **58**: p. 27-35.
178. Garcia, P., C.P. Suàrez, J. Rodriguez, and M. Rodriguez, (1998) *Unsupervised classification of neural spikes with a hybrid multilayer artificial network.* J. Neuroscience, **82**: p. 59-71.
179. Rebrik, S.P., B.D. Wright, A.A. Emondi, and K.D. Miller, (1999) *Cross-channel correlations in tetrode recordings: implications for spike-sorting.* Neurocomputing, **26-7**: p. 1033-1038.
180. Bierer, S. and D. Anderson, (1999) *Multi-channel spike detection and sorting using an array processing technique.* Neurocomputing, **26-7**: p. 947-956.
181. Chapa, J.O. and R.M. Rao, (2000) *Algorithms for designing wavelets to match a specified signal.* IEEE Trans Signal Processing, **48**(12): p. 3395.
182. Rebrik, S., B.D. Wright, S. Tzonev, A. Emondi, and K. Miller, *Spiker - a free GUI program for tetrode spike clustering.* 2001, UCSF.
183. Egert, U., T. Knott, C. Schwarz, M. Nawrot, A. Brandt, S. Rotter, and M. Diesmann, (2002) *MEA-Tools: an open source toolbox for the analysis of multi-electrode data with MATLAB.* J. Neurosci. Meth., **117**: p. 33-42.
184. Hulata, E., R. Segev, and E. Ben-Jacob, (2002) *A method for spike sorting and detection based on wavelet packets and Shannon's mutual information.* J. Neurosci. Meth., **117**: p. 1-12.
185. Calvin, W., (1973) *Some simple spike separation techniques for simultaneously recorded spikes.* Electroenceph. Clin.Neurophysiol., **34**: p. 94-96.
186. d'Hollander, E. and G. Orban, (1979) *Spike recognition and on-line classification by unsupervised learning system.* IEEE Trans Biomed. Eng. BME, **26**: p. 279-284.
187. Tucker, T., *Webpage der Tucker-Davis Technologies Inc -[www.tdt.com](http://www.tdt.com).* 2002, Tucker-Davis Technologies Inc.
188. Wiggins, H., *Webpage der Plexon Inc.* 2002, Plexon Inc.
189. Fejtl, M., *Webpage der MCS GmbH.* 2002, Multichannel\*Systems GmbH.
190. Stengel, K.C., *Webpage der Neuralynx Inc.* 2002, Neuralynx Inc.

191. Buzsáki, G., "... we are happy with the handling, impedance and number of recording sites of your probes.... 2002, personal email.
192. Hofmann, U.G., F. Hertlein, U. Knopp, and E. Langer, (2000) *On the design of intracranial multi-site microelectrodes for electro impedance tomography*. Biomedizinische Technik, **45 E1**: p. 167-168.
193. Maher, M.P., J. Pine, J. Wright, and Y.-C. Tai, (1999) *The neurochip: a new multielectrode device for stimulating and recording from cultured neurons*. J. Neurosci. Meth., **87**: p. 45-56.

## 13. Appendix A: Beigefügte Arbeiten

### Mikrostrukturtechnik

- ◆ Norlin P, Kindlund M, Mouroux A, Yoshida K, and Hofmann UG, *A 32-site neural recording probe fabricated by DRIE of SOI substrates.* J. Micromechanics and Microelectronics, 12(4): (2002) 414-419.

### Datenaufnahme

- ◆ Folkers, A. and U.G. Hofmann, *A multichannel data acquisition and analysis system based on off-the-shelf DSP boards,* in *Proceedings of the EURASIP Conference on Digital Signal Processing for Multimedia Communications and Services*, K. Fazekas, Editor. 2001, Scientific Association of Infocommunications - HTE: Budapest. p. 249-252.

### Signalverarbeitung

- ◆ Folkers, A., F. Mösch, T. Malina, and U.G. Hofmann, (2002) *Realtime bioelectrical data acquisition and processing from 128 channels utilizing the Wavelet-Transformation.* in press with Neurocomputing.

### Simulation

- ◆ Menne K, Malina T, Folkers A, and Hofmann UG, *Biologically realistic simulation of a part of hippocampal CA3: Generation of testdata for the evaluation of spike detection algorithms,* in *5th German Workshop on Artificial Life - Abstracting and Synthesizing the Principles of Living Systems*, J.K. D. Polani, T. Martinetz, Editor. (IOS Press Infinix: 2002. Lübeck) 17-25.

### Experimentelle Arbeiten

- ◆ Biella, G.R., L. Uva, U.G. Hofmann, and M. deCurtis, (2002) *Associative interactions within the superficial layers of the entorhinal cortex of the guinea pig.* J. Neurophysiol, **88**(3): p. 1159-1165.1.
- ◆ Freiwald W, Stemman H, Wannig A, Kreiter AK, Hofmann UG, Hills MD, Kovacs GTA, Kewley DT, Bower JM, Eurich CW, and Wilke SD, *Stimulus representation in rat primary visual cortex: multi-electrode recordings and estimation theory.* Neurocomputing, 44-46: (2002) 407-416.

## **14. Appendix B: Relevante technische Berichte des EU-Projektes VSAMUEL**

### **14.1. Workpackage 1: Management**

Deliverable 1.1 Nutzerbedürfnisse und Spezifikationen

### **14.2. Workpackage 2: Siliziumsonden und Verbindungstechnik**

Deliverable 2.1: 32 Kanalsonden

Deliverable 2.3: 64 Kanalsonde

Deliverable 2.2: 32 Kanalverbindung

Deliverable 2.4: 64 Kanalverbindung

### **14.3. (Workpackage 3: Verstärkertechnik)**

### **14.4. Workpackage 4: Datenaufnahmesystem**

Deliverable 4.1: 32 Kanalsystem

Deliverable 4.2: 64 Kanalsystem mit Auswerteroutinen

# A 32-site neural recording probe fabricated by DRIE of SOI substrates

**Peter Norlin<sup>1</sup>, Maria Kindlundh<sup>1</sup>, Aliette Mouroux<sup>1,4</sup>,  
Ken Yoshida<sup>2</sup> and Ulrich G Hofmann<sup>3</sup>**

<sup>1</sup> Acreo AB, Electrum 236, SE-164 40 Kista, Sweden

<sup>2</sup> Center for Sensory-Motor Interaction, Aalborg University, DK-9220 Aalborg Øst, Denmark

<sup>3</sup> Institute for Signal Processing, Medizinische Universität zu Lübeck, Seelandstr. 1a,  
D-23569 Lübeck, Germany

E-mail: peter.norlin@acreo.se

Received 9 January 2002, in final form 8 May 2002

Published 19 June 2002

Online at [stacks.iop.org/JMM/12/414](http://stacks.iop.org/JMM/12/414)

## Abstract

An all-dry silicon-etch based micromachining process for neural probes was demonstrated in the manufacture of a probe with a 32-site recording electrode array. The fork-like probe shafts were formed by double-sided deep reactive ion etching (DRIE) of a silicon-on-insulator (SOI) substrate, with the buried SiO<sub>2</sub> layer acting as an etch stop. The shafts typically had the dimensions 5 mm × 25 μm × 20 μm and ended in chisel-shaped tips with lateral taper angles of 4°. An array of Ir electrodes, each 100 μm<sup>2</sup>, and Au conductor traces were formed on top of the shafts by e-beam evaporation. An accompanying interconnect solution based on flexible printed circuitry was designed, enabling precise and flexible positioning of the probes in neural tissue. SEM studies showed sharply defined probes and probe tips. The electrical yield and function were verified in bench-top measurements in saline. The magnitude of the electrode impedance was in the 1 MΩ range at 1 kHz, which is consistent with neurophysiological recordings.

(Some figures in this article are in colour only in the electronic version)

## 1. Introduction

It is believed that a key to the understanding of the nervous system is to make simultaneous observations of the activity of a large number of cells [1]. Probes that can penetrate neural tissue and insert a large number of recording sites, while tissue damage is kept to a minimum, are thus needed. Micro system technology (MST) is well suited to this end, and several MST based neural probe concepts have been presented.

A wet silicon-etch based process was demonstrated early [2], and later a combination of wet silicon etching and a p<sup>++</sup> diffused etch stop was used to define fork-like probe shapes [3]. Neural probes combined with on-chip integrated circuitry were also demonstrated [4, 5]. In a later approach, a combination of patterned deep reactive ion etching (DRIE) of the wafer front side, and blank wet silicon etching of the back side was

used to form the probe shapes [6]. Two-dimensional arrays of recording electrodes, distributed on fork-like silicon probe structures are the most common approach, but the distribution of the recording sites on the tips of a ‘bed-of-nails’ structure has also been shown [7]. Alternatives to silicon have also been presented, e.g. flexible polyimide-based devices [8, 9].

Nevertheless, there is still room for improvements on previous processes and designs, in order to optimize the trade-off between different requirements. Requirements to be considered are, e.g., the possibility of independently tailoring the shape of the probe tips for reduced tissue dimpling, the inclusion of a thicker support structure to facilitate handling of the thin probes after processing, increased electrode density through reduced linewidths, process uniformity, yield, complexity, manufacturability, and in the end cost.

An all-dry silicon-etch based process where the buried oxide layer of a silicon-on-insulator (SOI) substrate acts as an etch stop, was introduced by us in [10], and independently by Cheung *et al* in [11]. The process avoids the visual

<sup>4</sup> Present address: Centro Nacional de Microelectrónica, Campus UAB, 08193 Bellaterra, Barcelona, Spain.

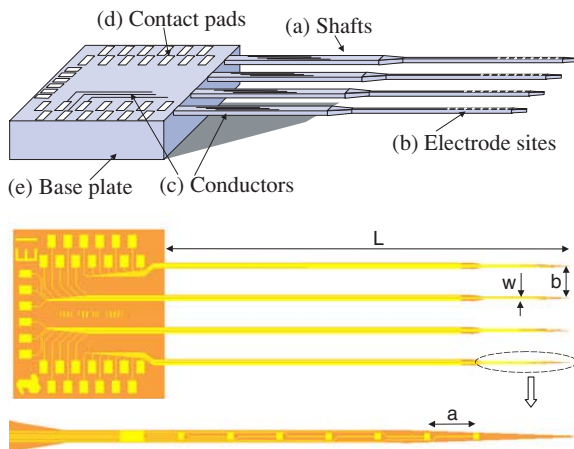


**Figure 1.** Schematic drawing of the probe structure described in the text (not to scale) and a typical CAD layout.

end conditions, which should improve upon uniformity and manufacturability. Double-sided lithography and etching allow a thicker base plate to be part of the design. In this work, we demonstrate the process in the fabrication of neural recording probes with 32-site recording arrays. A double metal layer process allows a larger number of electrodes and conductors to be fitted on narrower shafts.

In the MST field, the design of an appropriate and cost-effective interconnect and packaging solution is often of nearly equal importance as the device design itself. Here, the silicon device is accompanied by a tailor-made connector solution based on flexible printed circuitry, enabling precise and flexible positioning of the probes with micromanipulators during recordings in neural tissue.

## 2. Design

### 2.1. Silicon probes

Referring to figure 1, the main design elements of the probe structure are: (a) fine and pointed Si shafts for penetration and insertion into neural tissue, (b) microelectrode sites of Ir distributed over the outermost section of the shafts, (c) fine and narrowly spaced Au conductor traces, ending in (d) Au contact pads for external electrical interconnection using wire bonding, and (e) a thicker Si base plate as a support for the contact pads, to allow easy handling of the probes.

In a typical design, there are four shafts with eight electrode sites each, eight shafts with four sites each, alternatively one shaft with 32 sites. The shaft width ( $w$ ) is 25  $\mu\text{m}$  at the outermost section, widening to usually 75  $\mu\text{m}$  at the base plate. The shaft thickness is targeted to  $\sim 20 \mu\text{m}$ , but can be varied with the SOI wafer specification. The shaft length ( $L$ ) is typically between 4 mm and 7 mm and the

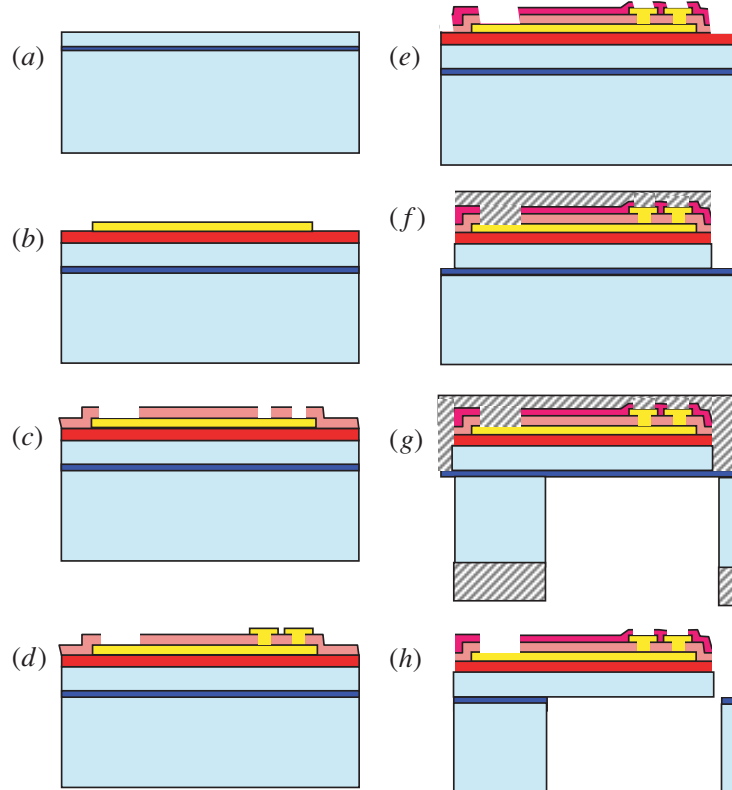


**Figure 2.** Schematic illustration of the fabrication process described in the text (not to scale). (a) SOI wafer, (b) SiN deposited, litho 1, Ti/Au deposited and lift off, (c) SiN deposited, litho 2 and nitride etch, (d) litho 3, Ti/Ir deposited and lift off, (e) SiN deposited, litho 4 and nitride etch, (f) litho 5, SiN etch and front side Si etch, (g) litho 6 and back side Si etch and (h) oxide etch and resist strip.

shaft c/c distance (*b*) is 200–400  $\mu\text{m}$ , for different designs. The recording electrode sites are 10  $\mu\text{m} \times 10 \mu\text{m}$  and are distributed with a 50–200  $\mu\text{m}$  pitch (*a*).

The lateral tip taper angle is designed to 4°. The optimization of neural probe tips with respect to tissue penetration properties and dimpling is not self-evident, see [12] for a discussion. Factors to be considered are, e.g. tip angle, tip radius, tip geometry (conical, chisel-like, pyramid-like, . . .), sharp cutting edges, shaft width and thickness, shaft roughness, surface chemistry, and insertion velocity. The present manufacturing process will result in chisel-shaped tips. The effect of very small tip taper angles (in spite of the tip not being sharpened in the third dimension) will be the subject of future investigations, but is motivated by a set of as yet unpublished experiments.

## 2.2. Interconnect and packaging

In order to interface the small probe chips with the comparatively larger amplifier system, a flexible printed circuit (FPC) solution was designed. The front end of the FPC was designed to fit the silicon probe chip and its bond pad positions. The back end was tailored to mate with the preamplifier connector (Molex 52559, 0.5 mm pitch, SMT, Zero Insertion Force type). The FPC was made of a polyimide foil with conductor traces of copper and Ni/Au metal at the contact pads. The dimensions of the FPC are 125 mm × 9 mm × ~65  $\mu\text{m}$ . A stiffening of glass fibre epoxy (FR4) was employed at the front end of the FPC to create a rigid support under the probe chip, and to function as an interface to standard micromanipulators. A thinner stiffening of polyester gives to the back end the thickness required by the connector. A commercial manufacturer [13] produced the flexible circuits, according to our designs.

## 3. Fabrication process

The silicon probe fabrication process is outlined in figure 2 and in the following text (italic letters refer to figure 2): (*a*) The probes were manufactured on silicon-on-insulator (SOI) substrates (Shin Etsu, 100 mm  $\phi$ , 525  $\mu\text{m}$  Si/1.5  $\mu\text{m}$  SiO<sub>2</sub>/20  $\mu\text{m}$  Si). (*b*) A PECVD silicon nitride film (1  $\mu\text{m}$ ) was deposited as an isolation layer. Ti/Au (~500 Å/2500 Å) was e-beam evaporated and patterned with a photo-resist lift-off process, to form conductor traces. Five times reduction step-and-repeat projection lithography was used with down to 1  $\mu\text{m}$  linewidths and spacing. (*c*) A second silicon nitride layer (0.5  $\mu\text{m}$ ) was deposited as an intermediate dielectric. Via holes were opened to the Au-layer using reactive ion etching (RIE) through a resist mask. (*d*) Ti/Ir (~300 Å/3500 Å) was e-beam evaporated and patterned with lift-off, to form the electrode sites. (*e*) A final silicon nitride layer (0.5  $\mu\text{m}$ ) was deposited as a protective layer. Windows were opened to the Au bond pads and the Ir electrode sites using RIE. The nitride covers the edges of the metal patterns for increased reliability in wet working environments. (*f*) With a resist mask the remaining nitride layer was first RIE etched, after which the top silicon layer was etched 20  $\mu\text{m}$  down to the buried oxide in an inductively coupled plasma deep reactive ion

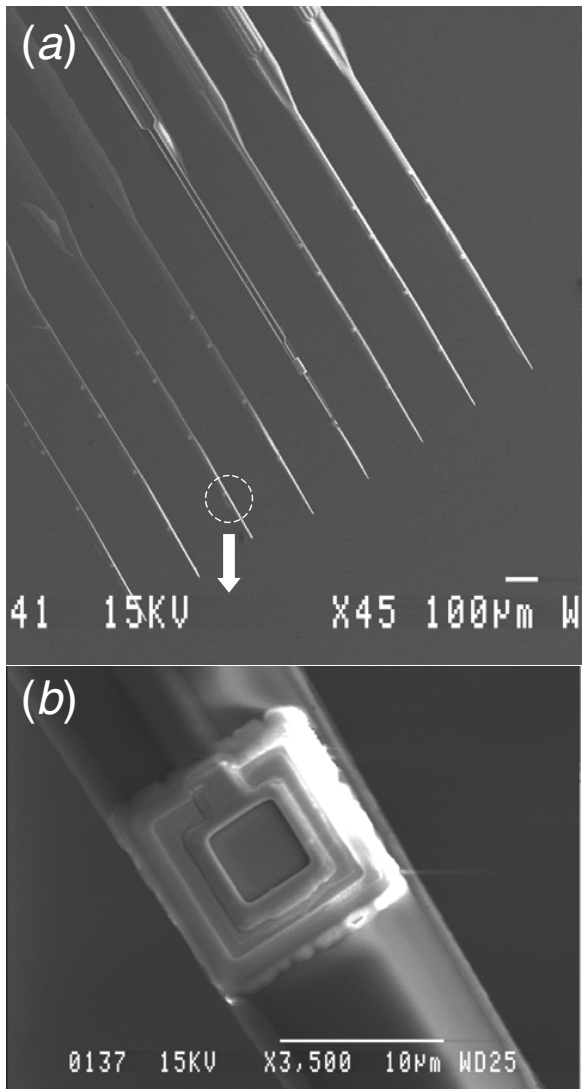


**Figure 3.** Scanning electron micrograph of (*a*) a silicon probe with 8 shafts × 4 electrodes and (*b*) close-up of a 10  $\mu\text{m} \times 10 \mu\text{m}$  Ir electrode site.

etching equipment (ICP DRIE, Surface Technology Systems). (*g*) A thick resist was spun on the wafer front side for protection. A double-sided mask alignment (Karl Suss MA6) was used to pattern a thick resist on the wafer backside, which was etched the full 525  $\mu\text{m}$  down to the buried oxide in the ICP DRIE. (*h*) The shafts were released by first etching the buried oxide in buffered HF, followed by a final resist strip.

In variations of the basic process outlined above, we have also worked with thermal silicon oxide as the first dielectric layer to achieve a stress-compensated thin film stack, and platinum as an alternative to iridium for the electrode metal.

After processing, the probe chips were mounted on FPCs with glue (cyanoacrylate). An ultrasonic wire bonder (West Bond 7400) was used to connect the bond pads on the chip with the pads on the FPC with gold wires (25  $\mu\text{m}$   $\phi$ ). An epoxy

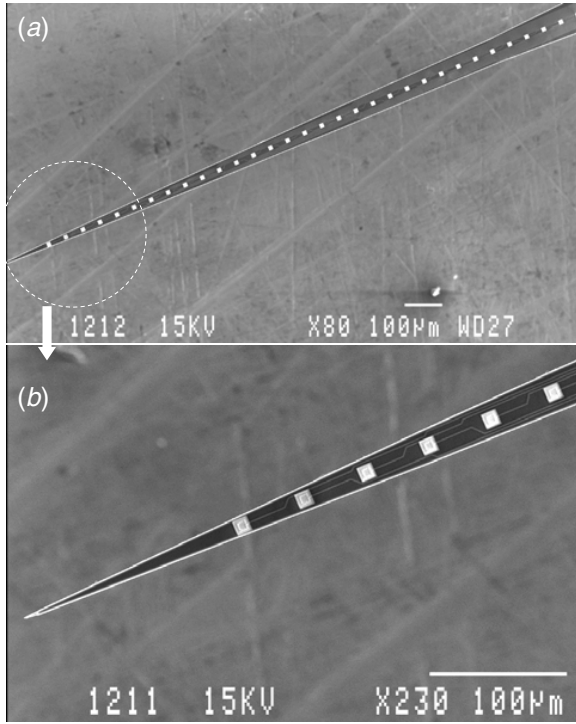


**Figure 4.** Scanning electron micrograph of (a) a silicon probe with 1 shaft × 32 electrodes and (b) close-up of a probe tip designed with 4° taper angle. The interconnect lines shown are 1 μm wide.



**Figure 5.** A neural probe chip mounted on a flexible printed circuit, wire-bonded and glob-top protected (right). A FPC without the glob-top cover is also shown (middle). The back end of the FPC was designed to mate with a 32-pin ZIF connector (shown left).

glob top (Emerson & Cuming, Amicon 50300/400 series) was applied to protect the bond wires from mechanical damage and wet working environments.

#### 4. Experimental results

Figures 3 and 4 show scanning electron micrographs of the results of the micromachining process. The DRIE process in combination with stepper lithography enabled tight control of

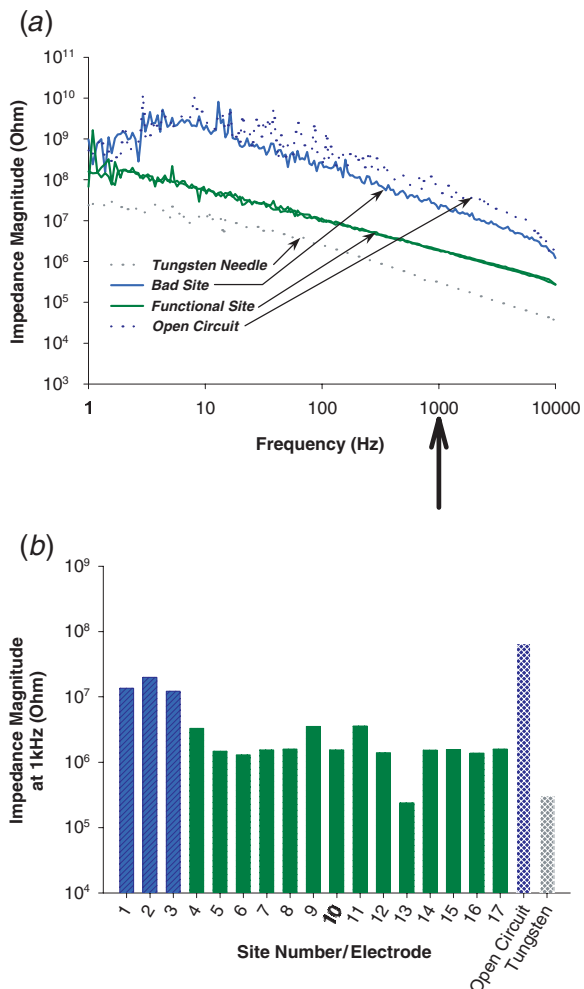


**Figure 6.** (a) Typical impedance magnitude spectra of two Ir sites on a silicon probe ('Functional Site'). For comparison a site with wire bond failure ('Bad Site'), a commercial tungsten needle electrode (AM-systems, type 5753) and the upper limit of measurement are also shown. (b) Impedance magnitudes at 1 kHz of a larger sample of sites on the same probe. Sites 1–3 show wire bond failures, number 13 is a non-standard electrode designed with a factor 10 larger area. The other sites show nominal 1.5 MΩ impedance. (To enable quick evaluation, the probe under test was not glob-top protected, which accounts for the wire bonds accidentally broken during handling.)

the structural dimensions. Electrodes and conductors could be packed close to the probe shaft edges and the probe tip taper design was well reproduced. Figure 5 shows the main parts of the developed interconnect solution.

Bench-top measurement set-ups were used to verify the electrical functionality of the probes after processing. Qualitatively we have been able to verify a satisfactory process yield, where a majority of the tested electrode sites transmits electrical signals. Quantitatively, the electrode impedance is a parameter of prime interest, since it influences the thermal (Johnson) noise and the ability to record small neural signals. For evaluation a rapid 3-point electrode impedance measurement technique was used, which is a modified

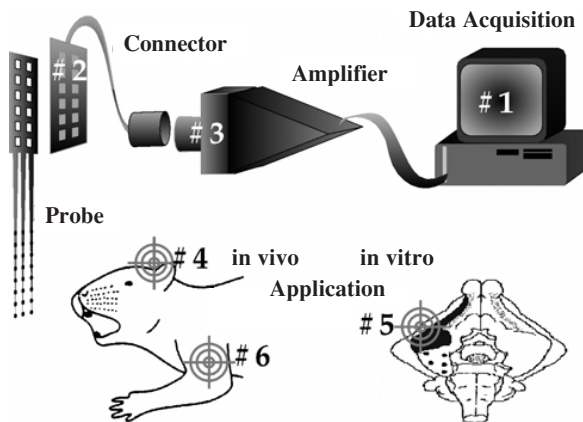


**Figure 7.** Overview of a complete recording system (1–3) and areas of application experiments (4–6) in the EU project VSAMUEL:  
1. Data acquisition system, hardware and software; 2. custom designed connectors and batch fabricated multisite microelectrode probes; 3. discrete and modular multi-channel amplifier;  
4. cerebellum; 5. cortex; 6. peripheral nerves.

version of the rapid 2-point electrode impedance measurement technique described in [14]. Use of a 3-point measurement scheme eliminates the effect of the counter-electrode impedance on the overall impedance measurement. The technique yields the electrode impedance spectrum between  $\sim 1$  Hz and 10 kHz with short 1–10 s measurements. Shortly, a bandwidth limited noise current is passed through the test electrode and a large Ag/AgCl counter electrode is immersed in 0.9% saline. The current through the test electrode and the voltage drop across the test electrode and a separate Ag/AgCl reference electrode is measured. Fast Fourier transforms are taken of the appropriately sampled and windowed voltage and current waveforms and the empirical transfer function is estimated. This estimate directly yields the impedance spectrum of the test electrode.

A typical set of impedance spectra is shown in figure 6. We found that the Ir recording sites were of the order of  $1.5\text{ M}\Omega$  at 1 kHz. This impedance is comparable to those of needle electrodes suitable for single unit recording, and the results are in good agreement with previously published data from thin film Ir microelectrodes [15]. If required, the Ir electrode impedance levels can be further reduced by oxidation by potential cycling ('activation') [15, 16].

## 5. Conclusions

A manufacturing process for micromachined neural probes, based on double-sided deep reactive ion etching of silicon-on-insulator substrates was demonstrated in the design and manufacture of probes with 32 recording electrodes, distributed on one to eight fine and pointed Si shafts. The process resulted in sharply defined probes and probe tips. The electrical yield was verified and the magnitude of the electrode impedance was shown to be consistent with neural recordings. The process appears to be attractive with respect to process complexity, uniformity and manufacturability. The

interconnect and packaging solution, based on flexible printed circuitry provides a user-friendly interface, well adapted to the requirements of neuroscientists.

Work is under way to scale up the probe design to an increased number of electrodes. Furthermore, this work is part of a larger consortial effort to develop a complete system for neural recordings, and to demonstrate the system in different application experiments [10] (cf figure 7). The systems approach as well as the collaboration between several hardware developer groups and neuroscience user groups are expected to bring added value to the neural probe concept.

## Acknowledgments

We would like to thank Sara Ahlberg (Acreo) for her help with the device fabrication and Bo Åkerlind (Acreo) for help with the FPC design. Discussions with Winnie Jensen (Aalborg University) are gratefully acknowledged. The work was supported by the European Commission under contract no IST-1999-10073.

## References

- [1] Chicurel M 2001 News feature: windows on the brain *Nature* **412** 266–8
- [2] Wise K D, Angell J B and Starr A 1970 An integrated-circuit approach to extracellular microelectrodes *IEEE Trans. Biomed. Eng.* **17** 238–47
- [3] Najafi K, Wise K D and Mochizuki T 1985 A high-yield IC-compatible multichannel recording array *IEEE Trans. Electron Devices* **32** 1206–11
- [4] Takahashi K and Matsuo T 1984 Integration of multi-microelectrode and interface circuits by silicon planar and three-dimensional fabrication technology *Sensors Actuators* **5** 89–99
- [5] Najafi K and Wise K D 1986 An implantable multielectrode array with on-chip signal processing *IEEE J. Solid-State Circuits* **21** 1035–44
- [6] Kewley D T, Hills M D, Borkholder D A, Opris I E, Maluf N I, Stormont C W, Bower J M and Kovacs G T A 1997 Plasma-etched neural probes *Sensors Actuators A* **58** 27–35
- [7] Campbell P K, Jones K E, Huber R J, Horch K W and Normann R A 1991 A silicon-based, three-dimensional neural interface: manufacturing processes for an intracortical electrode array *IEEE Trans. Biomed. Eng.* **38** 758–68
- [8] Shamma-Donoghue S A, May G A, Cotter N E, White R L and Simmons F B 1982 Thin-film multielectrode arrays for a cochlear prosthesis *IEEE Trans. Electron Devices* **29** 136–44
- [9] Stieglitz T and Gross M 2001 Flexible BIOMEMS with electrode arrangements on front and back side as key component in neural prostheses and biohybrid systems *Proc. 11th Int. Conf. on Solid-State Sensors and Actuators (TRANSDUCERS'01, Munich, Germany)* pp 358–61
- [10] Hofmann U G, De Schutter E, Yoshida K, de Curtis M and Norlin P 2000 On the design of multi-site microelectrodes for neuronal recordings *Proc. VDE World Microtechnologies Congress (MICRO.tec 2000, Hannover, Germany)* (VDE Verlag) pp 283–8
- [11] Cheung K, Lee G, Djupsund K, Dan Y and Lee L P 2000 A new neural probe using SOI wafers with topological interlocking mechanisms *Proc. 1st Ann. Int. IEEE-EMBS*

- Special Topic Conf. *Microtechnologies in Medicine & Biology* (Lyon, France) pp 507–11
- [12] Edell D J, Toi V V, McNeil V M and Clark L D 1992 Factors influencing the biocompatibility of insertable silicon microshafts in cerebral cortex *IEEE Trans. Biomed. Eng.* **39** 635–43
- [13] HP Etch AB, Järfälla, Sweden webpage <http://www.hpetch.se>
- [14] Yoshida K, Inmann A and Haugland M K 1999 Measurement of complex impedance spectra of implanted electrodes *4th Annu. Conf. Int. Functional Electrical Stimulation Society (Sendai, Japan)* pp 267–69
- [15] Akin T, Najafi K, Smoke R H and Bradley R M 1994 A micromachined silicon sieve electrode for nerve regeneration applications *IEEE Trans. Biomed. Eng.* **41** 305–13
- [16] Robblee L S, Lefko J L and Brummer S B 1983 Activated Ir: an electrode suitable for reversible charge injection in saline solution *J. Electrochem. Soc.* **130** 731–3

# A Multichannel Data Acquisition and Analysis System based on off-the-shelf DSP Boards

Andre Folkers, Ulrich G. Hofmann

Institute for Signalprocessing

Medical University of Lübeck

Seelandstr. 1a, Geb. 5, 23569 Lübeck, Germany

Phone: +49 (451) 3909 556, Fax: +49 (451) 3909 555, Email: {folkers, hofmann}@isip.mu-luebeck.de

**Abstract**— The EU-funded project VSAMUEL aims to develop a versatile system for advanced neuronal recordings with multisite microelectrodes. Within this project we are developing a data acquisition system for high channel counts. The system will be able to acquire and process data on 128 channels at a sampling rate of at least 32 kHz. We are utilizing multiple DSP boards to perform that task. Other project parts include development of multisite microelectrodes and respective pre- and main amplifier stages. Besides data acquisition the DSP boards are used to perform online analysis of the data, e.g. spike detection and spectrogram computation. Other project parts include development of multisite microelectrodes and respective pre- and main amplifier stages.

**Keywords**— Digital Signal Processors, Multichannel Data Acquisition

## I. INTRODUCTION

The principal goal of the project VSAMUEL sponsored by the European Commission is to provide a versatile data acquisition system to the neuroscience community which is able to acquire simultaneous recordings from hundreds of cells in the nervous system. The project includes the development of silicon based microelectrodes, amplifier stages, and data acquisition software and hardware, where the latter part is where we turn our attention in this paper. The data acquisition hardware is based on off-the-shelf DSP-boards in combination with a personal computer running under Windows NT. The software provides basic functionality like acquiring data on 32 channels, and streaming this raw data to disk. Furthermore, online visualization of a high channel count, and spectrogram of single channels is implemented.

## II. MICROELECTRODES AND AMPLIFIER

The next two sections give a short description of the microelectrodes and the amplifier stages.

### A. Microelectrodes

A key issue in understanding the nervous system is to make simultaneous observations of the activity of a large number of cells. Therefore, it is desired to have a large number of recording sites inserted in the neural tissue, while the insertion causes as smallest possible tissue damage. The design and construction of the microelectrodes is done by ACREO AB (Sweden) with respect to these constraints.

The microelectrodes are of fork shaped silicon with shafts of width 25  $\mu\text{m}$  having a pointed end. The recording sites (Ir, 10  $\mu\text{m} \times 10 \mu\text{m}$ ) are arranged in a two dimensional

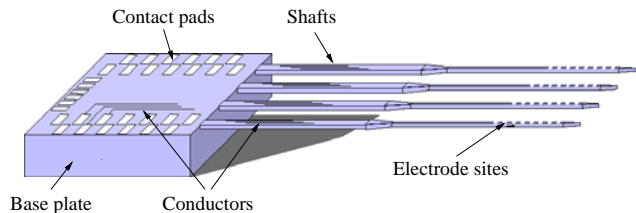


Fig. 1. Sketch of Microelectrode

array (Fig. 1) at the front end of the shafts. They are connected with the contact pads (Au) by fine and narrowly spaced metal (Au) conductor traces. There are several designs, which differ in shaft length (4 mm to 15 mm) and shaft count (1 to 4), and also in recording site spacing (see also [1, 2]).

### B. Amplifiers

The amplifier rack consists of a precision low-noise pre-amplifier with gain factor of up to 20 and main amplifier providing gain factors of up to 2000. Both pre- and main-amplifier are newly designed by Thomas RECORDING (Germany) for 64 channels. The amplifier rack gain settings are controlled by a micro controller, and can be setup either manually or by software via a PC-serial port. All channels can have an individual gain settings. The electrical connection of microelectrodes and pre-amplifier is realized with a "zero insertion force" connector on the pre-amplifier side and a several centimeters long flexible PC-board at the probe site (Fig. 2).

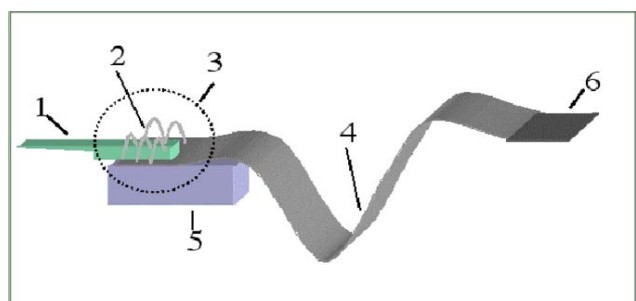


Fig. 2. Schematic drawing of a microelectrode (1), wire bonded (2) to a flexible PC-board (4) on a carrier (5). The bonded probe is epoxy sealed (3) and may be connected via the stiffened flex-board (6) to a zero insertion force connector on the pre-amplifier

### 32 Input Channels

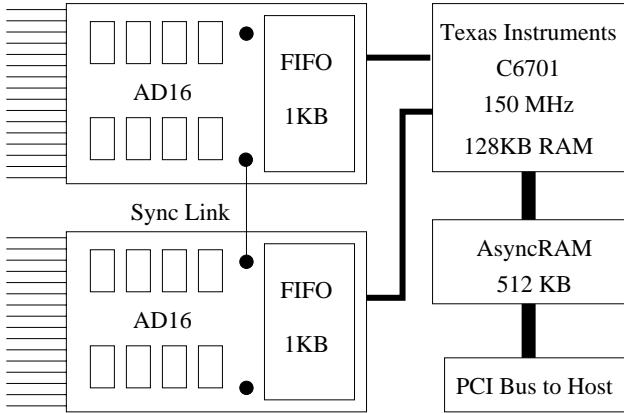


Fig. 3. Hardware arrangement and data flow of one DSP board

### III. DATA ACQUISITION HARDWARE

Our hardware consists of four DSP boards (M67, Innovative Integration, Thousand Oaks, CA, USA) which are combined with analog digital converter (ADC) modules (AD16 Omnibus modules, II). The M67 board has a single digital signal processor, i.e. a TMS3206701 processor (Texas Instruments, Dallas, TX, USA) clocked at 150 MHz with 128KB onchip memory. The CPU is provided with three different types of external memory: asynchronous SRAM (ASRAM, 512KB), synchronous DRAM (SDRAM, 16 MB), and synchronous burst SRAM (SBSRAM, 1MB). Each DSP board is equipped with two AD16 modules. Fig. 3 shows the arrangement of the hardware components and the data flow for one DSP board.

The AD16 module provides the M67 board with 16 channels of high speed 195 kHz, 16-bit resolution analog input to digital output conversion (A/D) per module site. There are 16 A/D converters for simultaneous conversion on all channels. Each of the 16 input channel consists of a high precision, DC accurate sigma-delta A/D converter (AD7722, Analog Devices, Norwood, MA, USA) with front end conditioning circuitry, which removes the need for multiplexers. The A/D converters are clocked either using a DDS timer of the M67 board or an external clock. Due to the 64 times oversampling performed by the A/D converters the clock rate is 64 times higher than the actual sampling rate. Conversion results are transferred into a FIFO which can store up to 512 16-bit samples. The AD16 triggers an interrupt when the FIFO contains a certain amount of samples. Usually this threshold is set to half of the samples which can be stored in total. This interrupt is serviced by a routine running on the DSP which fetches the data from the FIFO and stores it into the onchip memory using a DMA transfer.

#### A. Synchronization

Multiple AD16 modules may be synchronized by linking the synchronization signals between modules by a cable. Sync input and output signals allow software sync com-

mands from one AD16 module to be shared with other AD16 modules on the same M67 board and also across multiple M67 boards. This allows a single sync command to synchronize multiple AD16 modules and causes simultaneous sampling across the converters present on those modules. The A/D converters of modules residing on the same board are exactly synchronized. If the AD16 modules reside on different M67 boards and do not use the same A/D clock, then the synchronization is not quite perfect. They are only synchronized within one A/D clock cycle. The length of such a cycle is quite small with e.g. 521 ns at a sampling rate of 30 kHz. This effect may be eliminated by providing the same clock to all AD16 module, e.g. by using a synchronization link between the M67 boards or an external clock source.

### IV. DATA ACQUISITION SOFTWARE

The software can be divided into three parts, i.e. the program which runs on the DSP, the DSP application, a data acquisition server (DAQ server), and a data acquisition client (DAQ client). The DSP application performs the raw data acquisition, the transfer to the data acquisition server, and executes different online or off-line analysis modules, like for example compression, filtering, and spike sorting. The DAQ server provides a general interface to the DSP program for the DAQ clients. A user interacts with the system through the DAQ client. It configures experiments and executes them using the DAQ server. Results are sent back to the DAQ client which in turn visualizes them appropriately.

We are developing the software using Texas Instrument's "Code Composer Studio 1.20" and Borland's "C++ Builder 5.0".

#### A. DSP Application

The DSP application is organized in four parts, i.e. A/D conversion module, processing module, transfer module, and a control task. Fig. 4 illustrates how the different parts interact. The control task can send and receive messages to and from the DAQ server. A message consists of a receiver field, a command field, and a data field. The control task routes the messages with regard to the receiver field toward one of the other modules, or it handles the com-

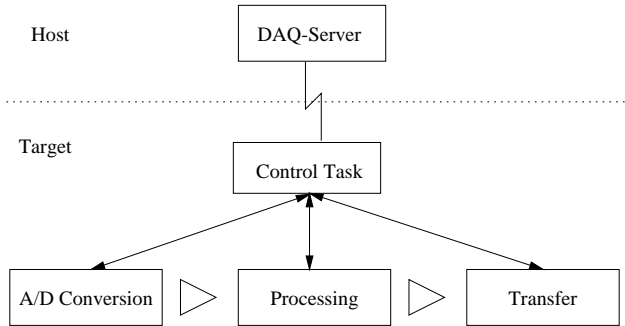


Fig. 4. Structure of the DSP application

mand directly if it is the receiver. The messages are used to configure the modules, e.g. setting the sampling rate in the A/D conversion module. A message can also request a certain parameter from a module. In this case the module sends a message back via the control task containing the requested parameter.

The data acquisition, processing and transfer is driven by interrupt events. The first interrupts in the cascade are triggered by the AD16 modules if their FIFO fill level reaches a certain threshold. Each AD16 module triggers on its own interrupt line. The FIFOs are independently read with DMA transfers into a frame in the onchip memory. Hereby the data is interleaved, such that the samples from all channels taken at the same time build a single block. The number and size of frames used is variable, but there must be at least two frames where each can hold the samples from the two FIFOs. This in turn depends on the FIFO fill level threshold of the FIFOs. The maximum number and size of frames is constrained by the size of the onchip memory.

After a frame has been filled it is put into the processing queue and a message is sent to the processing task which initiates the desired processing for this frame. During processing the raw data can either be replaced by the results or certain channels can be extracted into a separate buffer. For example given the case that only a certain frequency band is of interest raw data would be replaced by the result of the respective filtering. On the other hand if a spectrogram of a certain channel is requested a copy of this channel is created from the raw data and if enough sample points are collected the FFT is performed. After the processing is completed the frame is transferred into ASRAM and another interrupt is triggered to initiate the transfer via the PCI bus to the DAQ server.

The transfer from the DSP application to the DAQ server over the PCI bus is organized in packets. Each packet consists of a header and a data part. The header indicates which kind of data the packet contains in the data part. In order to keep the communication simple and fast the packets have a fixed length. One packet contains only one type of data, e.g. either raw data or Fourier coefficients not both. The packets are written into shared memory (shared between M67 board and Host PC), which is divided into two blocks. Each block can hold half of the packets which fit into the shared memory in total. The DAQ server is notified each time a block is filled with packets. This keeps the event rate for the DAQ server as low as possible.

### B. Data Acquisition Server

The DAQ server provides services of the DSP application, like data acquisition or analysis, and other services like data retrieval to the DAQ client. For example the DAQ client creates an experiment object initialized with the experimental parameters and sends it to the DAQ server, which in turn uses it to configure the data acquisition hardware. The DAQ server has an entry queue for each type of data that can be sent from the DSP application. These queues are connected to queue transmitters. A queue trans-

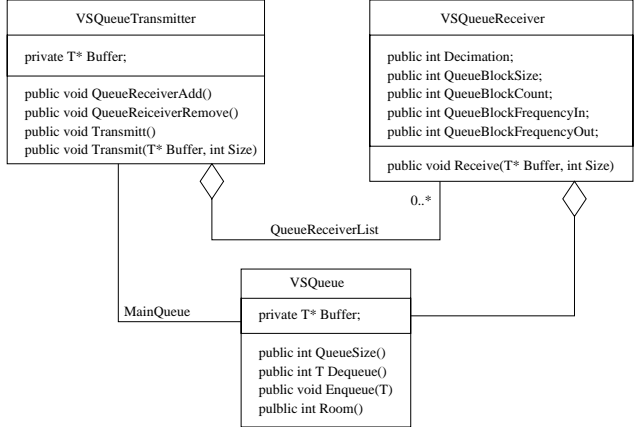


Fig. 5. Class diagram of queue receiver and queue transmitter

mitter has a list of references to queue receivers. Fig. 5 illustrates the relation of the respective classes. The association MainQueue refers to the entry queue of a certain type of data. The content of this queue is distributed to the queue receivers within the method Transmit() which copies a chunk from the queue into a buffer and calls the method Receive() of every queue receiver passing this buffer. The transmit method is periodically called by the DAQ server. A queue receiver can decimate the data which is passed to the received method according to the setting of block input frequency and block output frequency. This is e.g. used to keep the data volume for a visualization module below a specific rate. A visualization module would set the block output frequency to the number of sample points which can be displayed in one second. This feature of a queue receiver can also be turned off, e.g. streaming to disk is done without any decimation.

The data which needs to be stored is streamed to disk by the DAQ server. Only the data needed for visualization is sent to the DAQ client.

### C. Data Acquisition Client

The DAQ client consists of dialogs to setup and control an experiment and several visualization components. Data acquisition and replay is controlled by a panel having buttons like a DAT player and recorder. Currently under development is an experiment planer which schedule is processed automatically. The following section shortly introduce the visualization components which include a virtual scope, a blueplot, and a spectrogram.

#### C.1 Virtual Scope

The virtual scope (Fig. 6) can be used to inspect the details of certain channels. Currently it supports up to eight traces. Each trace can have a different scaling, offset, color, and line width. The assignment of a recording site to a trace can be done either by name, or by selecting the recording site in a schematic drawing of the probe. The scope supports arbitrary zooming.

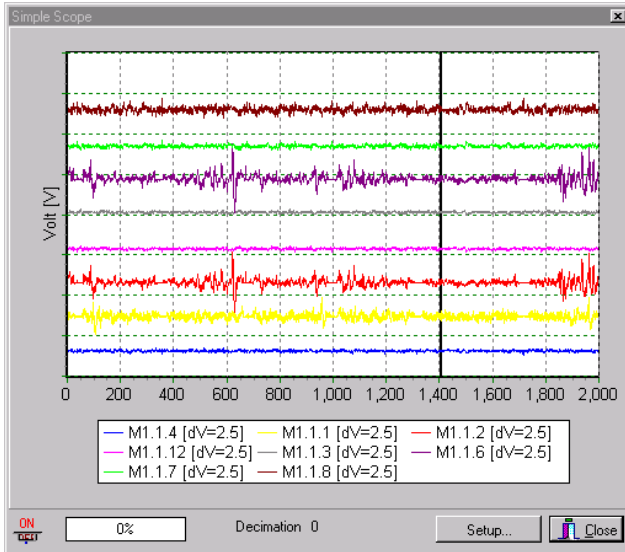


Fig. 6. Virtual scope

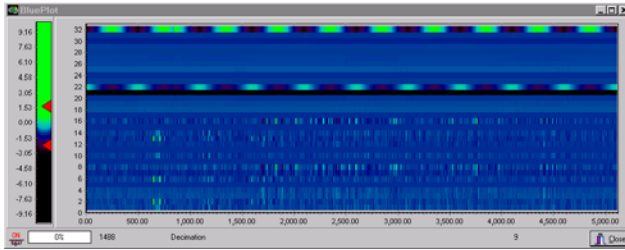


Fig. 7. Blueplot

### C.2 Blueplot

The simultaneous visualization of a high count of channels in a scope does not give an appropriate overview of the acquired data. A better mode of visualization is provided by a so called blue plot (Fig. 7). For each channel a colored bar is shown, whereby the amplitude of the channel is coded into a color value. Small amplitudes in the order of the root mean square of the signal are mapped onto blue color values with mean intensity. High positive and negative amplitudes are mapped onto green with high intensity or onto red with low intensity, respectively. Due to the variation of intensity the blueplot can also be shown using gray colors whereby the information about the amplitudes (high negative or positive, mean) is preserved. The mapping of amplitudes can be either manually or automatically adjusted in the color bar. The user can also define a threshold

### C.3 Spectrogram

One example for online processing of raw data and visualization is the spectrogram. The computation of the windowed FFT of a certain channel is done on the DSP. The log magnitudes of the Fourier coefficients are computed by the DAQ client and the result is mapped onto a color. The

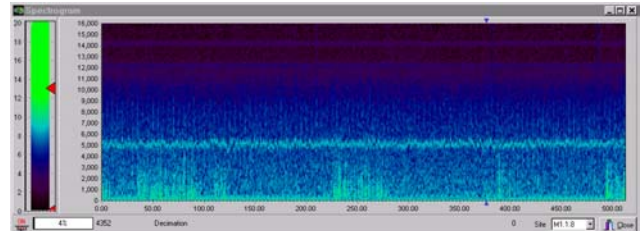


Fig. 8. Spectrogram

color mapping can be manually adjusted, such that only a range of interest is displayed (Fig. 8).

### V. CONCLUDING REMARKS AND FUTURE WORK

The described data acquisition system provides basic data acquisition functionality on a flexible hardware basis build from off-the-shelf components. The software provides a modular framework for future extensions. Already implemented is a windowed Fourier transform, which result is used to display the spectrogram. Future work will include development and implementation of methods for online and offline data processing like filtering with high-pass and lowpass FIR filters, compression based on wavelet decomposition [3], spike detection and spike sorting [4–7].

### ACKNOWLEDGMENT

We grateful acknowledge the help of our project partners at ACREO AB (Kista, Sweden), Thomas RECORDING (Giessen, Germany), Center for Sensory-Motor Interaction at Aalborg University (Denmark), Instituto Nationale Neurologico "Carlo Besta" (Mailand, Italy), Theoretical Neurobiology at University of Antwerp – UIA (Belgium).

### REFERENCES

- [1] Ulrich G. Hofmann, Erik De Schutter, Ken Yoshida, Marco De Curtis, Uwe Thomas, and Peter Norlin, "On the design of multisite microelectrodes for neural recordings," in *Proceedings of the MICRO.tec 2000*, P. M. Knoll, Ed., Berlin, 2000, vol. 1, pp. 283 – 288, VDE Verlag.
- [2] Ken Yoshida, W. Jensen, Peter Norlin, M. Kindlundh, and Ulrich G. Hofmann, "Characterization of silicon microelectrodes from the EU VSAMUEL project," in *Biomedizinische Technik*, J. Werner, Ed., Bochum, 2001, Schiele & Schön GmbH, to appear.
- [3] B. Weber, T. Malina, K. Menne, A. Folkers, V. Metzler, and U. G. Hofmann, "Handling large files of multisite microelectrode recordings for the European VSAMUEL consortium," *Neurocomputing*, Jun 2001.
- [4] M. S. Lewicki, "A review of methods for spike sorting: the detection and classification of neural action potentials," *Network*, vol. 9, no. 4, pp. 53–78, Nov 1998.
- [5] J. C. Letelier and P. P. Weber, "Spike sorting based on discrete wavelet transform coefficients," *Journal of Neuroscience Methods*, vol. 101, no. 2, pp. 93–106, Sep 2000.
- [6] M. S. Fee, P. P. Mitra, and D. Kleinfeld, "Automatic sorting of multiple unit neuronal signals in the presence of anisotropic and non-gaussian variability," *Journal of Neuroscience Methods*, vol. 69, no. 2, pp. 175–188, Nov 1996.
- [7] Maneesh Sahani, *Latent Variable Models for Neural Data Analysis*, Ph.D. thesis, California Institute of Technology, Pasadena, California, 1999.

## ARTICLE IN PRESS



Available at  
[www.ComputerScienceWeb.com](http://www.ComputerScienceWeb.com)

POWERED BY SCIENCE @ DIRECT®

NEUROCOMPUTING

Neurocomputing III (III) III-III

[www.elsevier.com/locate/neucom](http://www.elsevier.com/locate/neucom)

1

# Realtime bioelectrical data acquisition and 3 processing from 128 channels utilizing the wavelet-transformation<sup>☆</sup>

5 Andre Folkers\*, Florian Mösch, Thomas Malina,  
Ulrich G. Hofmann

7 *Institute for Signal Processing, University of Lübeck, Germany*

---

### Abstract

9 We propose a versatile signal processing and analysis framework for bioelectrical data, and in  
11 particular for neural recordings and EEG. Within this framework the signal is decomposed into  
13 subbands using fast wavelet transform algorithms, executed in real-time on a current digital sig-  
15 nal processors hardware platform. The decomposition is used to perform various processing and  
17 analysis tasks. Besides fast implementation of high, band, low pass filters, the decomposition is  
used for denoising and lossy, as well as lossless compression. Furthermore specific electophys-  
iologic analysis tasks like spike detection and sorting are performed within this decomposition  
scheme.

17 © 2002 Published by Elsevier Science B.V.

*Keywords:* Digital signal processor; Data acquisition; Spike detection; Wavelet transformation

---

### 19 1. Overview

Recording neural activity from a high number of neurons is a key issue in understand-  
21 ing how the brain works. Within the project VSAMUEL we developed successfully  
23 a versatile data acquisition system based on DSP boards [3]. The system is used for  
continuous neural data acquisition in vivo or in vitro with a high channel count (up  
to 128 channels) at sampling rate  $F = 50$  kHz with a precision of 16 bits per sample.

☆ This work has been supported by EU grant IST-1999-10073.

\* Corresponding author. Medical University of Luebeck, Seelandstr 1a Geb. 5, Luebeck 23569, Germany.  
Fax: +49-451-3909-555.

E-mail address: [folkers@isip.mu-luebeck.de](mailto:folkers@isip.mu-luebeck.de) (A. Folkers).

- 1 Important online data processing tasks include filtering and spike detection and classification,  
 2 but also compression, transmission and storage. We propose a signal processing  
 3 framework within which these tasks can be performed in an elegant way.

## 2. Wavelet transform and lifting scheme

- 5 The signal is decomposed into  $N + 1$  subbands by a  $N$ -level wavelet transform  
 7 (WT). The subbands  $d_j, j = 1, \dots, N$  represent the frequency band  $[F/2^{j+1}, F/2^{j+2}]$  and  
 9 the subband  $a_N$  represents  $[0, F/2^{N+1}]$ . Fig. 1 shows the filter bank for  $N = 3$ . In each  
 11 step the signal is decomposed by applying complementary filters to  $a_j$ , i.e. a high  
 13 pass  $\tilde{g}$  and a low pass  $\tilde{h}$ , which are determined by the selected wavelet. The results of  
 15 both filter operations are subsampled by a factor of two, leading to subbands  $d_{j+1}$  and  
 17  $a_{j+1}$ . Note, that the number of coefficients in  $d_{j+1}$  and  $a_{j+1}$  is equal to the number  
 19 of coefficients in  $a_j$ . The wavelet transform is implemented using the lifting scheme  
 21 which is faster than the standard implementation (Fig. 1). It is done in-place, and with  
 a small modification it implements a WT that maps integers onto integers [1] while  
 preserving the possibility of perfect reconstruction. Therefore, this implementation of  
 the WT is well suited for realtime processing using digital signal processors (DSP).
- 17 The lifting scheme provides another point of view to the wavelet transform. Basically  
 it consists of three stages, which are a split, a *predict*, and an *update* stage as illustrated  
 19 in Fig. 2 [6]. First the signal is split such that we obtain two sequences  $d_j$  and  $a_j$  which  
 21 in our case consist of sample points with odd and with even indices, respectively. Now,

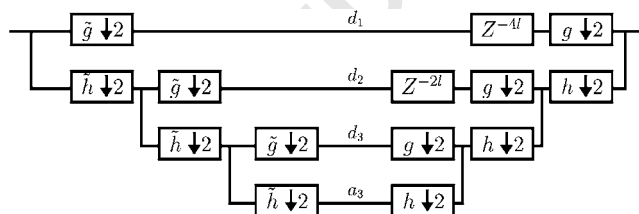


Fig. 1. Filter bank with three levels.

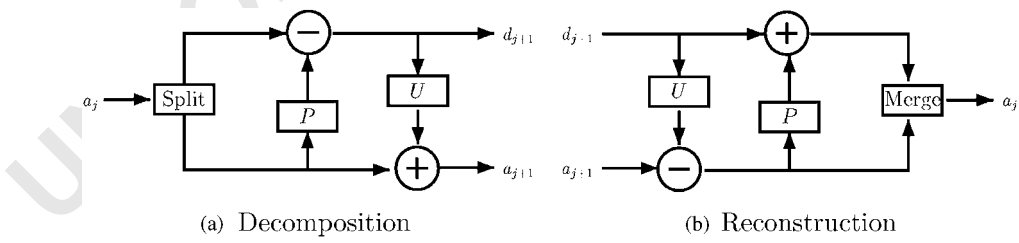


Fig. 2. Basic structure of the lifting scheme: (a) decomposition, and (b) reconstruction.

1 we predict the values in  $d_j$  based on  $a_j$  as  $P(a_j)$ . Under the assumption that the  
2 signal is continuous we have a good chance that our prediction is rather close to the  
3 actual values. We compute the difference between prediction and actual values, and  
4 keep these values which are likely to be small:  $d_{j+1} = d_{j+1} - P(a_{j+1})$ . In order to  
5 preserve certain properties of the original signal in the coefficients  $a_j$ , e.g. the mean  
6 value, we need the third stage, which is the update stage. Hereby, the values in  $a_j$   
7 are modified by using an appropriate update operator on values in  $d_j$  and  $U(d_j)$ :  
 $a_{j+1} = a_{j+1} + U(d_{j+1})$ .

8 The perfect reconstruction property of the lifting scheme is obvious, because we can  
9 obtain  $a_j$  from  $a_{j+1}$  and  $d_{j+1}$  by inverting the data flow and the signs as shown in Fig.  
10 2(b). Note, that this holds for arbitrary predict and update operators. Therefore, if these  
11 operators include a rounding to the next integer we obtain a wavelet transform that  
12 maps integer onto integers. It is possible to implement arbitrary wavelet transformations  
13 as shown in [1] by using multiple prediction and update operators successively. The  
14 respective operators are computed according to the given mother wavelet.

15 Using the lifting scheme and a routine optimized for our DSP, we can apply a six  
16 level Daubechies 2 decomposition filter bank on 32 channels sampled at 50 kHz in  
17 real time.

### 19 3. Filter

20 The decomposition allows a simple implementation of filters with different high pass,  
21 band pass, or low pass characteristics. Consider, e.g. a neural recording sampled at  
22  $F = 50$  kHz which contains both field potentials and action potentials. If it is decom-  
23 posed by a 6-level WT into 7 subbands, then the field potentials are found in subband  
24  $a_6$ . Setting the coefficients of  $a_6$  to zero, eliminates the field potentials and corresponds  
25 to a high pass filter (Fig. 3). The respective low pass filter which eliminates the action  
26 potentials is obtained by setting the coefficients  $d_j$  for  $j=1,\dots,6$  to zero. A comparison  
27 of the results of both methods can be found in Fig. 3. Fig. 4 shows a comparison of  
28 the respective frequency responses. The decomposition also allows the implementation  
29 of band pass filters. Possible cut-off frequencies for band pass filter based on the WT  
30 are determined by the sampling rate and the number of levels. Arbitrary filters can be  
31 implemented if a Wavelet Packet Transform (WPT, see [8]) is utilized. However, the  
32 computation of the WPT transform involves more operations than the WT. Because  
33 the number of operations has to be as low as possible to allow real-time computation  
on our DSP, we currently restrict ourselves to the WT.

### 35 4. Compression and denoising

36 One important property of the WT is that it decorrelates the signal, i.e. the main  
37 information about the signal is collected in a few large coefficients, while the details  
38 are collected in many small coefficients. The average information content, also called

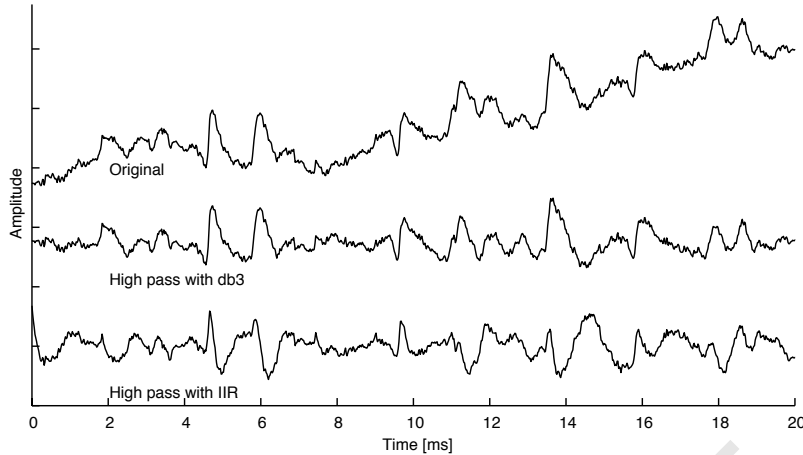


Fig. 3. High pass filtering using IIR versus elimination of wavelet approximation coefficients. The original neural recording has been decomposed with a 6 level WT using the Daubechies 4 wavelet. The coefficients of  $a_6$  have been set to zero, corresponding to a high pass filtering with cut-off at 390.62 Hz. In a second approach the signal has been filtered by a 4-pole IIR high pass filter with cut-off at frequency 400 Hz, which was designed using the Butterworth method. Spike shapes in the IIR filtered result show significant distortions, while the spike shapes are apparently not distorted by the wavelet based high pass. Field potentials are eliminated well by both filters.

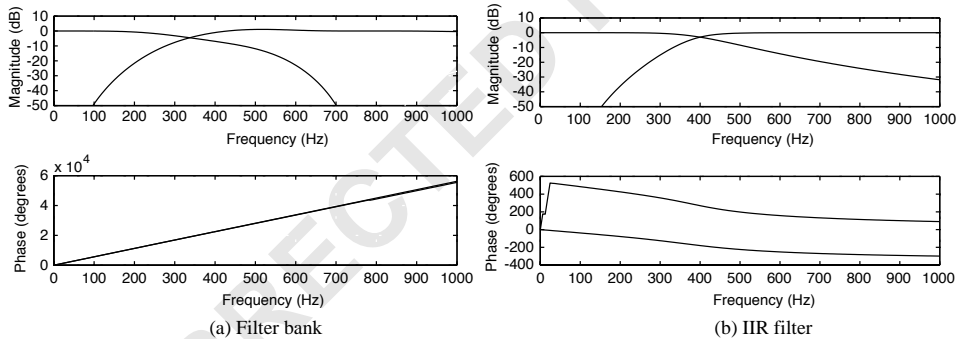


Fig. 4. Comparison of filter bank based (a) and IIR (b) high and low pass filter. For the filter bank Daubechies wavelet with four vanishing moments has been used. The IIR filter have order 4 and cut off frequency at 400 Hz. The magnitudes of the frequency responses are comparable, but the phase of the filter bank is linear while the phase of the IIR filter is nonlinear, which is the reason for the distortions found in Fig. 3.

1 *entropy*, can be computed as

$$E(s) = - \sum_{v \in \text{Values of } s} p(v) \log_2(p(v)), \quad (1)$$

where  $p(v)$  is the probability of occurrence of value  $v$  within signal  $s$ . The entropy  
3 is measured in bits per sample and since our signals are sampled in 16 bit resolution,

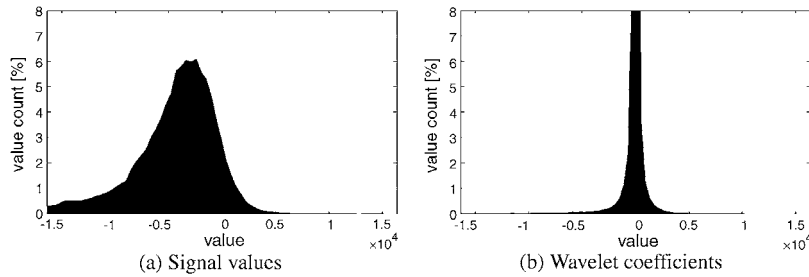


Fig. 5. Entropy reduction by wavelet transformation is illustrated by a comparison of the signal value and the wavelet coefficient histograms: (a) signal values, and (b) wavelet coefficients.

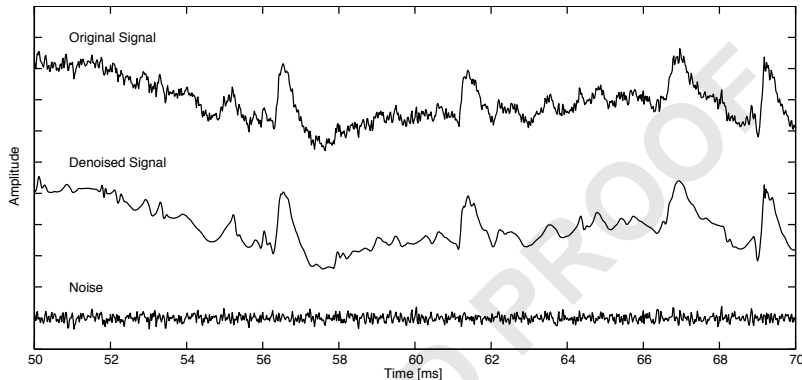


Fig. 6. Compression and denoising. The comparison of the original neural signal at the top and the denoised signal in the middle reveals no apparent distortion of the signal. This is confirmed by the difference of signal and denoised signal, i.e. the removed noise, which is shown at the bottom. The entropy of the decomposition drops from 8.34 bits per sample down to 1.04 bits per coefficient. In other words the compression rate can be improved by a factor of 8.

- 1 we can define the optimal achievable compression rate, e.g. with Huffman coding,  
 3 as  $E(s)/16$ . The entropy of the decomposition is smaller than the entropy of the raw  
 5 signal (Fig. 5). The entropy of a neural recording from a rat was quantified in [7] to be  
 about 13.9 bits per sample and it is about 8.5 bits per coefficient for the decomposition.  
 Therefore, the compression rate can be improved from 0.86 for the raw data down to  
 0.53 for the decomposition.
- 7 Another important task is the denoising of neural recordings. The typical background  
 9 noise of neural recordings is mainly found in the first few levels  $d_1, \dots, d_3$  of the de-  
 composition. Under the reasonable assumption that the background noise has a Gaussian  
 11 distribution [5], a universal threshold can be found as  $\delta = \sqrt{2\sigma^2 \log(n)}$  where  $\sigma^2$  is  
 13 the variance of the Gaussian noise and  $n$  is the length of the sequence [2]. Since the  
 true variance  $\sigma^2$  is usually unknown, it is estimated from the coefficients in  $d_1$  which  
 are dominated by the noise. We use the standard deviation estimator *median absolute  
 deviation* (MAD):  $\sigma^2 = \text{median}(|d_1|)/0.6745$ . Using the median absolute value instead of

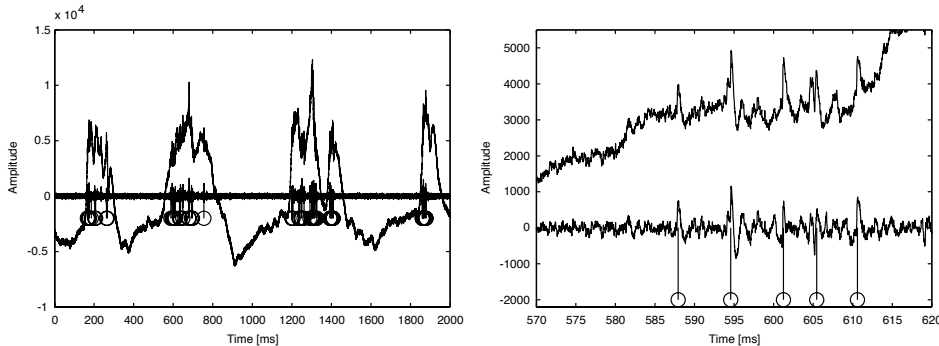


Fig. 7. Spike detection base on wavelet coefficients. Detected spikes are marked by stems. On the right an enlarged section of the signal is shown, which reveals that the signal-to-noise ratio is quite small, but still the spikes are detected well.

- 1 the mean absolute value, this estimation is robust against large coefficients representing
- 2 the signal that might occur in  $d_1$ .
- 3 Compression and denoising are closely related. The thresholded decomposition which
- 4 represents the denoised signal has a much lower entropy than the original decomposition
- 5 and thus can be compressed with a better rate. Depending on the chosen thresholds,
- 6 the compression rate can reach values below 0.1 without losing a significant part of
- 7 the signal. With the universal threshold for instance we obtain a compression rate of
- 8 about 0.06 for neural recordings from a rat (Fig. 6). Lossy compression which does
- 9 not distort the signal significantly is particularly useful for longterm recordings.

## 5. Spike detection

- 11 The decomposition is used to analyse neural recordings. Spikes, for instance, are
- 12 represented by a few large coefficients in subbands  $d_2, \dots, d_6$ . Therefore, spike detection
- 13 can be implemented by a threshold based method which uses the wavelet coefficients.
- 14 In Fig. 7 such a method has been used to detect spike in a neural recording from a rat,
- 15 which contains field potentials and action potentials. In [4] another method to detect
- spikes based on wavelet coefficients is proposed.

## 17 6. Conclusions

- 18 Altogether we can state, that our DAQ system is able to record from a high number
- 19 of channels, and furthermore it can perform sophisticated processing of the incoming
- 20 electrophysiological data in realtime, which in our case is a wavelet decomposition.
- 21 The data obtained from the wavelet decomposition represents the original data without
- 22 loss, and it provides an elegant way to compress and to denoise the signals, and also
- 23 to do further processing, like, e.g. spike detection.

1 **References**

- [1] I. Daubechies, W. Sweldens, Factoring wavelet transforms into lifting steps, *J. Fourier Anal. Appl.* 4 (3) (1998) 245–267.
- [2] D.L. Donoho, I.M. Johnstone, Ideal spatial adaptation by wavelet shrinkage, *Biometrika* 81 (3) (1994) 425–455.
- [3] A. Folkers, U.G. Hofmann, A multichannel data acquisition and analysis system based on off-the-shelf dsp boards, in: Proceedings of the EURASIP Conference on Digital Signal Processing for Multimedia Communications and Services, Budapest, September 2001.
- [4] H. Nakatani, T. Watanabe, N. Hoshimiya, Detection of nerve action potentials under low signal-to-noise ratio condition, *IEEE Trans. Biomed. Eng.* 48 (8) (2001) 845–849.
- [5] M. Sahani, Latent variable models for neural data analysis, Ph.D. Thesis, California Institute of Technology, Pasadena, California, 1999.
- [6] W. Sweldens, The lifting scheme: a new philosophy in biorthogonal wavelet constructions, in: A.F. Laine, M. Unser (Eds.), *Wavelet Applications in Signal and Image Processing III*, Proc. SPIE 2569 (1995) 68–79.
- [7] B. Weber, T. Malina, K. Menne, A. Folkers, V. Metzler, U.G. Hofmann, Handling large files of multisite microelectrode recordings for the European VSAMUEL consortium. *Neurocomputing*, June 2001.
- [8] M.V. Wickerhauser, in: *Adapted Wavelet Analysis from Theory to Software*, A K Peters, Wellesley, MA, 1994.



**Andre Folkers** has studied Computer Science with emphasis on Medical Computer Science at the Medical University of Lübeck from 1994 until 2000, where he graduated with the Dipl.-Inform. degree, having performed his diploma thesis at the University of Maryland at College Park. Since 2000 he is research assistant in the Institute for Signal Processing at the Medical University of Lübeck working in the project VSAMUEL. His main research interests are advanced biosignal processing, image processing and databases, and multichannel analysis.



**Florian Mösch** joined the project VSAMUEL in 2001 as a student of Computer Science of the Medical University of Lübeck. He graduated with the Dipl.-Inform. degree in 2002, having performed his diploma thesis on the development of a multichannel data acquisition system. Currently he is working in the Institute of Signal Processing at the Medical University of Lübeck. His research fields include multichannel data acquisition and biosignal and image processing.



**Thomas Malina** studies Computer Science at the Medical University of Lübeck since 1995. He was born 1974 in Teschen/Poland and joined the VSAMUEL project in 1999. His research interests are image and signal processing, in particular spike sorting, 3D-modelling and cluster analysis. He was an exchange student at the Aalborg Universitet in Denmark where he developed a data acquisition system. Currently he is working on his diploma thesis at the Medical University of Lübeck.

3

5

7

9

1



**Ulrich G. Hofmann** received his Diploma in Physics 1993 and his Ph.D. in Biophysics 1996 from the Technical University of Munich, Germany. He stayed at the Abo Akademi, Finland, as an EU-fellow (HCM) and as Feodor-Lynen-Fellow at the California Institute of Technology. Since 1999 he is research assistant ("Habilitanda") at the Institute for Signal Processing of the Medical University of Lübeck and project coordinator and initiator of VSAMUEL. His long term research aims to interface brains with computers.

UNCORRECTED PROOF

# **Biologically realistic simulation of a part of hippocampal CA3: Generation of testdata for the evaluation of spike detection algorithms**

Kerstin M. L. Menne, Thomas Malina, Ulrich G. Hofmann

Institut für Signalverarbeitung und Prozeßrechentechnik

Seelandstraße 1a

D-23569 Lübeck, Germany

[menne/malina/hofmann]@isip.mu-luebeck.de

## **Abstract**

Biologically realistic simulations on the neuronal network level are frequently used in computational neuroscience in order to explain and understand biological brain functions. The presented simulation mimicks a tiny part of the CA3 region of the hippocampus. But new insights about the functionality of CA3 are not the ultimate goal in this case. Rather we want to show that sound extracellular potential data can be generated within a network close to reality. The data is used for the evaluation of spike detection methods.

## **1 Introduction**

Current neurophysiology research benefits strongly from advances made in microstructural technologies [8],[16] and neurophysiological methods [6],[4],[9],[22] and thus recordings from an ever increasing number of neuronal sources become more and more ubiquitously available. However, this seems to come at the expense of thoroughness in raw data analysis, since "visual" data screening, e.g. to correctly assign spikes on incoming data, requires almost supernatural stamina in cases of data sets originating from dozens or even hundreds of recording sites over several hours of experimental time. Having noticed such problems the solution is obvious: Utilize automated analysis tools, which never get tired and always perform perfectly well. Unfortunately, to validate the performance of such tools, some kind of trustworthy test data has to be used. Real data is not quite suitable for test purposes, since it is always subjected to interpretations concerning contained spike trains. On the other hand, simulated data is controllable but at the same time usually very artificial. One frequently applied method to generate synthetic data is to extract spikes and chunks of noise from extracellular recordings, to distribute the spikes randomly in time and to add the noise sample [2], [18]. The disadvantage of this method is quite obvious. The randomly distributed spikes do not reflect any biologically realistic network behaviour, including cell interactions and synchronous spikings, and even no biologically realistic single cell behaviour. Nakatani [14] employs a peripheral nerve model in order to generate synthetic data. He adds a Gaussian noise process to the simulated signal. This method is comparable to ours, but lacks the presence of different interacting neurons within an elaborated network circuitry. The data we provide, simulated in a biologically realistic network simulation, is intended to bridge the gap between biological relevance and control, and thus is predestinated for the test of spike analysis methods like for example spike detection algorithms.

## 2 Network simulation

The network simulation is implemented in GENESIS 2.2, the GEneral NEural SImulation System [3]. The network simulation we present has nothing to do with artificial neural networks. Our network simulation is based on cell models that try to recapitulate the knowledge about anatomy and electrophysiological behaviour of hippocampal CA3 pyramidal cells and interneurons. What hides behind the simulation is mathematically speaking a system of differential equations. This is transferred into a system of difference equations and numerically solved with the implicit Crank-Nicholson method with a step size of 2.5e-5.

We applied a pyramidal cell model and an interneuron model as suggested by Traub [19], [20]. The pyramidal cell model consists of 66 compartments, representing branching dendritic trees, a soma and an axon (Figure 2(b)). Active ion channels are assigned to the compartments, namely  $\text{Na}^+$ ,  $\text{Ca}^{2+}$ ,  $\text{K}_\text{DR}$ ,  $\text{K}_\text{AHP}$ ,  $\text{K}_\text{A}$  and  $\text{K}_\text{C}$  channels. The interneuron model comprises 48 compartments and the same active ion channels as the pyramidal cell model. The network is built up from 72 pyramidal cell models, arranged in a 6 times 12 array, and 9 feedforward as well as 9 feedback interspersed interneurons (Figure 2(a)). Pyramidal cells have a distance of  $10 \mu\text{m} \pm 3 \mu\text{m}$  from each other in x- and y-direction. z-coordinates are randomized in a range from -50 to +50  $\mu\text{m}$ . The rather high cell density compared to earlier implementations [12] was made necessary by the rather small horizon of the simulated electrodes, see below. Each cell model is randomly rotated 0 to 180 degrees clockwise about its z-axis in an attempt to compensate the fact that we have identical cell morphologies ("clones"). Feedforward and feedback interneurons are derived from the same model. They differ exclusively in the way they are connected to other neurons. Synapses are simulated by AMPA, NMDA, GABA\_A and GABA\_B receptors. The interneurons have only AMPA receptors. Figure 1 reveals the network circuitry at a glance. Cell connections can be all-

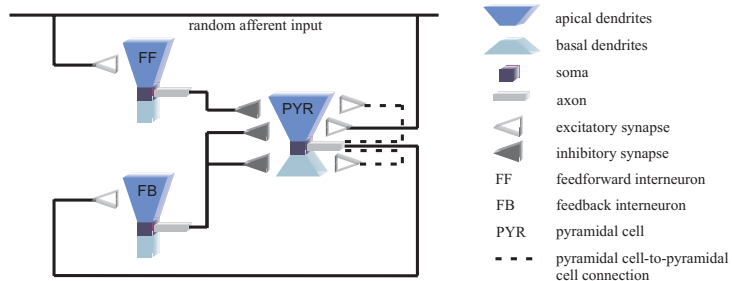


Figure 1: Network circuitry. Compared to the network circuitry published in [12], [13], pyramidal cells do not get inhibitory inputs on their basal dendrites from feedforward interneurons anymore and in turn do not excite feedback interneurons at basal dendrites.

to-all, but are established with a certain probability only. Feedforward interneurons are excited by random afferent input onto their apical dendrites. Feedback interneurons are excited in the same region, but the input originates from pyramidal cells. Pyramidal cells receive in turn feedback inhibition in the perisomatic region and feedforward inhibition at their apical dendrites. Recurrent excitation among the pyramidal cells targets onto the perisomatic region, whereas random afferent input, representing mossy fiber input, is received at the apical dendrites. CA3 projections into CA1 are not modeled. Slight changes in network circuitry compared to [12], [13] proved to be advantageous for the overall network behaviour. The distribution of activity across the pyramidal cell array is best visualized by means of a movie. A 3D representation of the array (Figure 2(b)) is generated with help of the Visualization Toolkit VTK (Kitware Inc.). Colour is assigned to each

neuron dependend on the somatic membrane potential. Colour changes mirror activity changes. The network elicits both, simultaneous bursts as well as isolated spikes.

### 3 Simulation of extracellular recordings

Single-site recording probes get simulated with the help of GENESIS "efield" objects arranged at arbitrary positions within the above described network. The "efield" object is an implementation of an equation by Nunez [17] for the calculation of extracellular field potentials:

$$F = \frac{1}{4 \cdot \pi \cdot s} \sum_{i=1}^n \frac{I_i}{r_i} \quad (1)$$

Transmembrane currents  $I_i$  of  $n$  compartments are added up with respect to their distance  $r_i$  from the "electrode".  $s$  denotes conductivity. A homogeneous resistivity and no capacitance are assumed for the extracellular space. The Nunez equation does not provide a direction characteristic: Signals are recorded throughout the whole surrounding space. In our simulation, this isotropic detection characteristic has to be changed to a more directional sensitive by exclusively taking into account the transmembrane currents of cells situated within a certain sector as seen from the probe (Figure 2(a)). An opening angle of  $90^\circ$  proved to be too small. Contrary to experimental results,

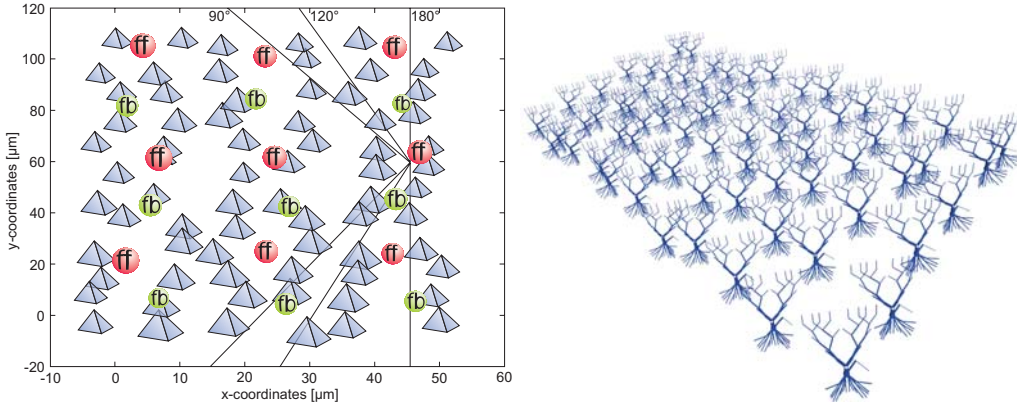


Figure 2: The graph on the left illustrates different opening angles. The discrete nature of the network restricts the possible number of gradations. The graph on the right illustrates only the pyramidal cell array making use of the compartmental model.

only spikes of the same amplitude were contained in the recorded signal. An opening angle of  $120^\circ$  allowed for different amplitude heights of spikes coming from a larger number of neurons than in the  $90^\circ$  case (Figure 3). The recordable sector for recording sites fixed on an insulating carrier most likely comes close to a  $120^\circ$  sector.

Multi-site recording probes can be simulated by the linear arrangement of "efield" objects. The "recorded" signals contain low-frequency field potentials and high-frequency spikes that mirror intracellular activity. Many overlapping spikes, originating from synchronous activity of several neurons, are contained in the data - a tough problem for all types of spike train analysis published. If individual recording sites (i.e. "efield" objects) are arranged close enough, spikes originating

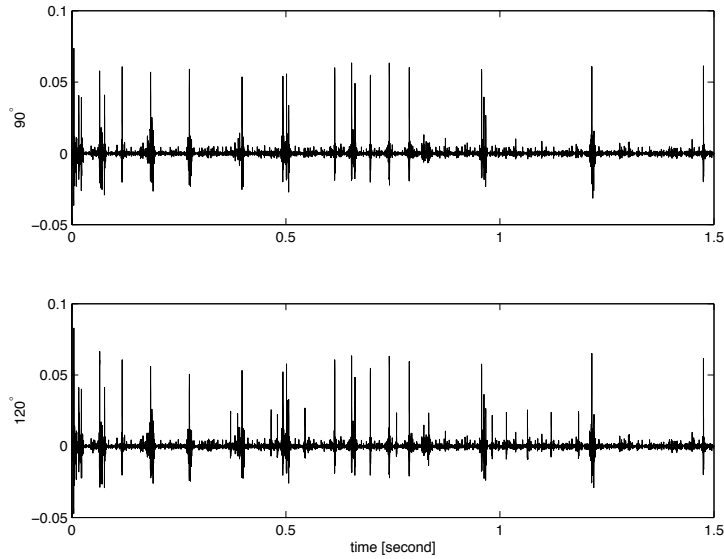
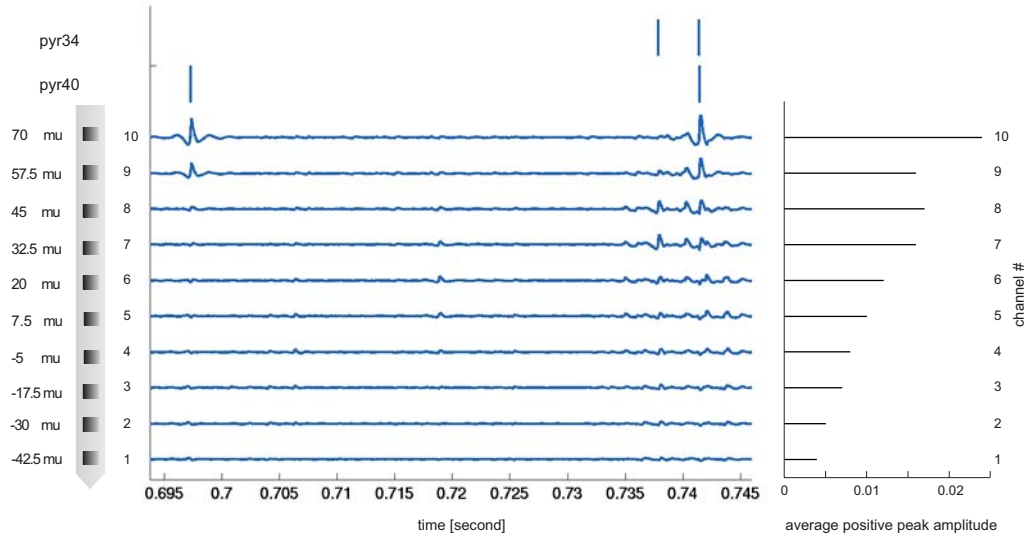
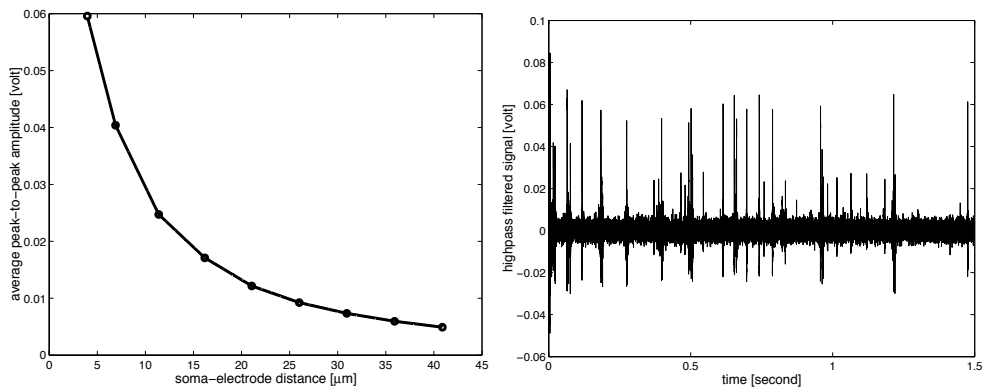


Figure 3: Comparison of extracellularly recorded signals, where the opening angles amount to  $90^\circ$  and  $120^\circ$ , respectively. Signals are given in volt.

from one cell are trackable, but exhibit a characteristic decay over distance, on several recording channels, like in real experiments. We simulated probes comprising 13 different recording sites. The individual recording sites are linearly arranged, perpendicularly to the xy-plane. The lowest z-coordinate is at -55 micrometer, the highest one at 95 micrometer. Thus individual recording sites have a distance of 12.5 micrometer. A spike amplitude decay along the site array is a feature of real multi-site recordings. Figure 4 illustrates the footprints (on 10 channels) of 4 spikes coming from pyramidal cells 34 and 40, respectively. The average positive peak amplitude distribution given on the right of Figure 4 reveals that the highest amplitudes are not always found in one and the same channel. This is due to the contribution of cells that are located at different z-coordinates. Unfortunately, individual electrodes do not have a big recording horizon, since spikes are trackable in two channels only and the simulated recording points have a distance of  $12.5 \mu\text{m}$ . Spikes originating from cells within the horizon are clearly identifiable in extracellularly recorded signals. In the experimental case, depending on the set-up, neural spikes can be tracked for many tens of microns [10], [1]. Therefore the decrease in amplitude seems to be too steep along the simulated linear array. This way too rapid decay in amplitude can be found, when the simulated multi-site recording probe is moved away from the cells, as well. This was investigated by generating a highpass filtered signal of the electrode at  $z=70 \mu\text{m}$  at different distances from the soma of the pyramidal cell 40. 17 spikes were detected with a threshold of 0.04 mV at a distance of  $4 \mu\text{m}$ . These spikes were tracked throughout the recordings at increasing distances. The average peak-to-peak amplitude of the 17 spikes was calculated at each distance. The result (Figure 5(a)) confirms the above made observation of a rapid decay. At a cell-electrode distance of  $15 \mu\text{m}$ , the amplitudes lose already more than  $2/3$  of their value. Gray [7] for example specifies for tetrode (impedance of 0.5 to  $1 \text{ M}\Omega$  at 1 kHz) recordings in the neocortex, area 17 of cats, a cell-electrode distance of  $65 \mu\text{m}$  as the distance at which a 90% reduction in voltage occurs. He outlines, that this result agrees with theoretical estimates by Rall concerning the decay of extracellular spike voltage. We therefore conclude, that the small horizon of the simulated electrodes casts doubt on the validity



**Figure 4:** Amplitude decay alongside a multi-site recording probe. Pyramidal cell 40 is  $4\mu\text{m}$  away from the probe, pyramidal cell 34  $8.1\mu\text{m}$ . The calculations of the average spike amplitudes are based on 90 to 120 threshold detected spikes in each case (after highpass filtering).



**Figure 5:** The graph on the left shows the decay of spike amplitude with increasing distance between soma and electrode. The graph on the right shows a simulated extracellularly recorded signal ( $z=70\mu\text{m}$ ) with added white noise (SNR of 21:1, calculated as ratio of average spike peak-to-peak amplitude and noise rms value (root-mean-squared)).

of the Nunez equation (1) for the calculation of fast extracellular potentials and requires further simulation and experimental work to be done in the future.

The simulated extracellular potential data per se contains background activity coming from cells farther away from the electrode. In order to make the simulated data resemble experimental data even more, white noise is added after the simulation to represent thermal noise of recording devices, and the signals get highpass filtered with a cut-off frequency of 500 Hz (Figure 5(b)). The addition of noise at this process step allows to play through different noise levels.

## 4 Results and Discussion

We were able to show the possibility to generate sound extracellular potential data in a biologically realistic network simulation. The simulated data shows a lot of features of experimental data, including spike shapes, amplitude decay over distance and contained noise. Therefore it seems justified to use our simulated data as benchmark set for spike detection algorithms. As far as we know, nobody ever applied realistically simulated data like ours for test purposes. (Our data set as well as additional information can be downloaded from [www.isip.mu-luebeck.de/~hofmann/Paper/Menne\\_CD/](http://www.isip.mu-luebeck.de/~hofmann/Paper/Menne_CD/).)

So far, we tested the following spike detection methods on the basis of our simulated data: positive voltage threshold (pt) [10, e.g.], pt plus peak-to-peak amplitude threshold (pt+ppa) [15, e.g.], pt+ppa plus peak-to-peak time (pt+ppa+pp-time) [1, e.g.], peak-to-peak amplitude only (ppa-window) [2] , thresholding of the second derivative of a signal (sec.dev+pt) [11],[21], of the energy (energy+pt) [15] or the by means of Discrete Wavelet Transform (DWT) denoised signal (dwt-denoising+pt) [5]. Figure 6 illustrates the results. The two bars on top each case result from comparisons of the detection results with the spike times of two pyramidal cells only (70 spikes in total), the two bars on bottom from comparisons with spike times of three pyramidal cells that are definitely contributing to the simulated signal (112 spikes in total).The spike amplitudes of the third pyramidal cell are hardly above the noise level and therefore difficult to detect. In the case of the pt method e.g., 24% of the 70 spikes originating from two pyramidal cells are missed, compared to 45% of 112 spikes originating from three pyramidal cells. However, even 24% of missed spikes are an alarmingly high value. The investigation of peak-to-peak amplitude and peak-to-peak time in addition to the positive peak amplitude does not improve the performance. The ppa-window, sec.dev+pt and energy+pt methods predict much more than 50% false positives an thus should not be used as stand-alone detection methods. Thresholding of the denoised signal, however, yields even better results than thresholding of the raw signal. The presented results were achieved for data shown in Figure 5(b). We tested the thresholding of raw data, a commonly applied approach in spike detection, for two lower SNRs. The results presented in Figure 7 clearly reveal, that a positive threshold method is completely unsuitable under low SNRs. The number of false positives is by far dominating and would falsify any conclusions based on the detection results. In addition, in the case of the SNR of 6:1, there are almost 50 intolerable percent false negatives.

The test of further spike detection algorithms is pending, but the best method will finally find its way into our realtime data acquisition system ([www.vsamuel.de](http://www.vsamuel.de)). Special attention will be paid to approaches that take advantage of multi-site recording data and to the performance on overlapping spikes.

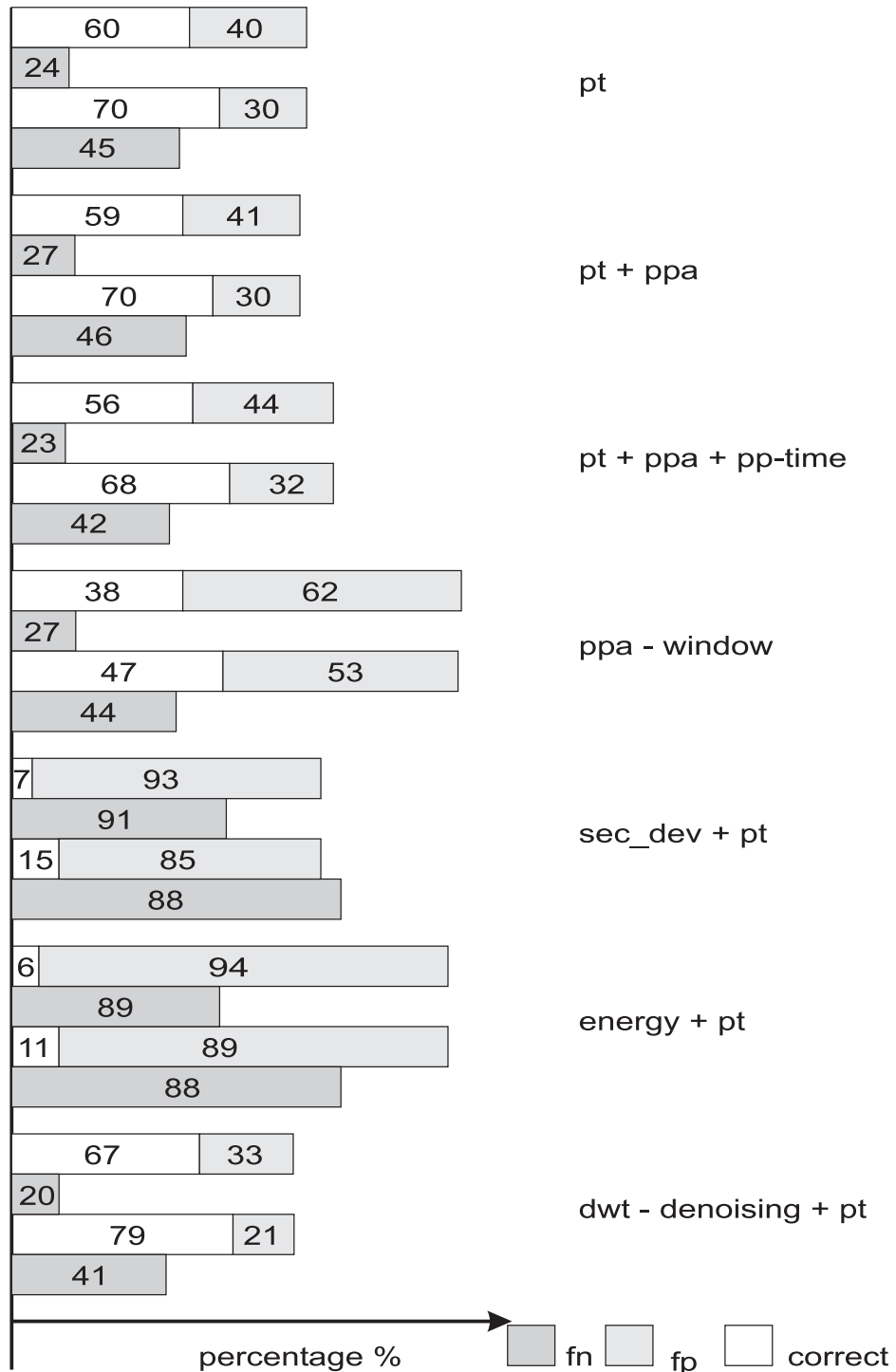


Figure 6: Percentage of correctly detected spikes (correct) and false positives (fp) are calculated on the basis of all detected spikes. False negatives (fn) are given as percentage of 70 or 112 spikes, respectively, see text for methods.

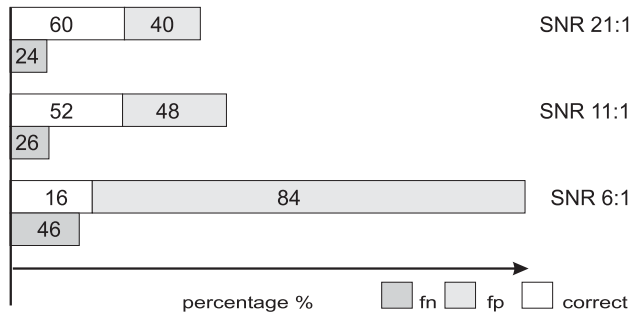


Figure 7: Results of positive threshold method for simulated data with different SNRs.

## 5 Acknowledgements

We thank Reinoud Maex, Born-Bunge Foudation, University of Antwerp, for his advice concerning the GENESIS simulation.

This work was in part supported by EU-grant IST-1999-10079 and the German research ministry BMBF grant 16SV1433.

## References

- [1] Moshe Abeles and Moise H. Goldstein. Multispike train analysis. *Proceedings of the IEEE*, 65(5):762–773, 1977.
- [2] Amir F. Atiya. Recognition of multiunit neural signals. *IEEE Transactions on Biomedical Engineering*, 39(7):723–729, 1992.
- [3] James M. Bower and David Beeman. *The Book of GENESIS*. Springer-Verlag, second edition, 1998.
- [4] J. Chapin, K. Moxon, et al. Real-time control of a robot arm using simultaneously recorded neurons in the motor cortex. *nature neuroscience*, 2:664–670, 1999.
- [5] J. Fang, G.C. Agarwal, and B.T. Shahani. Decomposition of multiunit electromyographic signals. *IEEE Transactions on Biomedical Engineering*, 46:685–697, 1999.
- [6] W. Freiwald, H. Stemman, et al. Stimulus representation in rat primary visual cortex: multi-electrode recordings and estimation theory. in press with Neurocomputing, 2001.
- [7] Charles M. Gray, Pedro E. Maldonado, et al. Tetrodes markedly improve the reliability and yield of multiple single-unit isolation from multi-unit recordings in cat striate cortex. *Journal of Neuroscience Methods*, 63:43–54, 1995.
- [8] U.G. Hofmann, E. De Schutter, et al. *On the design of multi-site microelectrodes for neuronal recordings*. in MICRO.tec 2000, VDE Verlag, Hannover, 2000.
- [9] M. Laubach, J. Wessberg, et al. Cortical ensemble activity increasingly predicts behaviour outcomes during learning of a motor task. *Nature*, 405:567–571, 2000.

- [10] Michael S. Lewicki. A review of methods for spike sorting: the detection and classification of neural action potentials. *Network: Computational Neural Systems*, 9:R53–R78, 1998.
- [11] K.C. McGill, K.L. Cummins, and L.J. Dorfman. Automatic decomposition of the clinical electromyogram. *IEEE Transactions on Biomedical Engineering*, 32:470–477, 1985.
- [12] Kerstin M. L. Menne, Ulrich G. Hofmann, et al. Test of spike sorting algorithms on the basis of simulated network data. In *Neurocomputing, Proceedings of the CNS 2001, Monterey*. To be published.
- [13] Kerstin M. L. Menne, Reinoud Maex, and Ulrich G. Hofmann. Extracellular potential data generated in a network simulation. In *The Neurosciences at the Turn of the Century, Proceedings of the 4th Meeting of the German Neuroscience Society 2001*, volume 1, page 602. Georg Thieme Verlag, 2001.
- [14] H. Nakatani, T. Watanabe, and N. Hoshimiya. Detection of nerve action potentials under low signal-to-noise ratio condition. *IEEE Transactions on Biomedical Engineering*, 48(8):845–849, 2001.
- [15] Miguel A.L. Nicolelis. *Methods for Neural Ensemble Recordings*. CRC Press LLC, 1999.
- [16] P. Norlin, M. Kindlundh, et al. A 32-site neural recording probe fabricated by double-sided deep reactive ion etching of silicon-on-insulator substrates. In *12th Micromechanics Europe Workshop (MME-2001), Cork, Ireland*, 2001.
- [17] P.L. Nunez. *Electric Fields of the Brain: The Neurophysics of EEG*. Oxford University Press, Oxford, first edition, 1981.
- [18] Karim G. Oweiss and David J. Anderson. Noise reduction in multichannel neural recordings using a new array wavelet denoising algorithm. *Neurocomputing*, 38-40:1687–1693, 2001.
- [19] Roger D. Traub, John G. R. Jefferys, et al. A branching dendritic model of a rodent CA3 pyramidal neuron. *Journal of Physiology*, 481.1:79–95, 1994.
- [20] Roger D. Traub and Richard Miles. Pyramidal cell-to-inhibitory cell spike transduction explicable by active dendritic conductances in inhibitory cell. *Journal of Computational Neuroscience*, 2:291–298, 1995.
- [21] Shiro Usui and Itzhak Amidror. Digital low-pass differentiation for biological signal processing. *IEEE Transactions on Biomedical Engineering*, 29:686–693, 1982.
- [22] J. Wessberg, C.R. Stambaugh, et al. Real-time prediction of hand trajectory by ensembles of cortical neurons in primates. *Nature*, 408:361–365, 2000.

To be published in *Fifth German Workshop on Artificial Life - Abstracting and Synthesizing the Principles of Living Systems*, D. Polani, J. Kim, T. Martinetz (Eds.), IOS Press Infix.

# Associative Interactions Within the Superficial Layers of the Entorhinal Cortex of the Guinea Pig

GERARDO BIELLA,<sup>1</sup> LAURA UVA,<sup>1</sup> ULRICH G. HOFMANN,<sup>2</sup> AND MARCO DE CURTIS<sup>1</sup>

<sup>1</sup>Department Experimental Neurophysiology, Istituto Nazionale Neurologico, 20133 Milan, Italy; and <sup>2</sup>Institute for Signal Processing, Medical University of Lübeck, 23569 Lübeck, Germany

Received 10 January 2002; accepted in final form 21 May 2002

**Biella, Gerardo, Laura Uva, Ulrich G. Hofmann, and Marco de Curtis.** Associative interactions within the superficial layers of the entorhinal cortex of the guinea pig. *J Neurophysiol* 88: 1159–1165, 2002; 10.1152/jn.00022.2002. Associative fiber systems in the entorhinal cortex (EC) have been extensively studied in different mammals with tracing techniques. The largest contingent of intra-EC cortico-cortical fibers runs in the superficial layers and is distributed predominantly within longitudinal cortical bands. We studied the patterns of intrinsic EC connectivity in the *in vitro* isolated guinea pig brain preparation by performing current-source density analysis of field potential laminar profiles recorded with multi-channel silicon probes. The response pattern evoked by stimulation of the lateral olfactory tract was utilized to identify the lateral (l-EC) and medial (m-EC) entorhinal cortex. Stimulation of the deep layers did not evoke consistent responses. Local stimulation of the superficial layers in different portions of the EC induced an early, possibly direct response restricted to layer II–III in the close proximity to the stimulating electrode, followed by a late potential in the superficial layer I, that propagated at distance with a progressively increasing latency. The monosynaptic nature of the delayed response was verified by applying a pairing test. The results demonstrated that stimulation in the rostral-medial part of the EC generated activity restricted to the rostral pole of the l-EC, stimulation of the m-EC induced an associative activation that propagated rostrocaudally within the m-EC, stimulation of the caudal pole of the m-EC induced an additional response directed laterally, and stimulation of the lateral band of the EC determined a prominent longitudinal propagation of neuronal activity, but also induced associative potentials that propagated medially. The results are in partial agreement with the general picture derived from the anatomical studies performed in different species. Even though the largest associative interactions between superficial layers are restricted within either the m-EC or the l-EC, both rostral and caudal stimuli in the EC region close to the rhinal sulcus induced activity that propagated across the border between l- and m-EC.

## INTRODUCTION

The entorhinal cortex (EC) is one of the regions of the parahippocampal area that conveys cortical inputs into and receives a feedback projection from the hippocampus (Lopes da Silva et al. 1990; Witter et al. 1989). The complex pattern of connectivity between the EC and the hippocampus has been extensively characterized in different animal species. On the basis of the projection pattern of layer II neurons to the dendrites of dentate gyrus granule cells (Brodmann 1909;

Hjorth-Simonsen and Jeune 1972; Shipley 1975; Steward 1976; Steward and Scoville 1976; Swanson and Kohler 1986) and of layer III neurons to the CA1-subiculum region (Witter 1993), the EC has been divided in two major subfields, medial (m-EC) and lateral (l-EC). The intrinsic EC connectivity in the rat is characterized by longitudinal fibers confined to the lateral band of cortex close to the rhinal sulcus that connect caudal and rostral portions of the EC and by transversal fibers at different caudal-dorsal level within the m-EC (Dolorfo and Amaral 1998). Intrinsic associative fibers within the EC are located predominantly in superficial layers and, less extensively, in the deep layers (Dolorfo and Amaral 1998; Kohler 1986, 1988). The anatomical data therefore devise a complex pattern of intrinsic interactions within and across the border between m- and l-EC.

We verified with electrophysiological techniques the pattern of intrinsic associative connections in the EC of the *in vitro* isolated brain of the guinea-pig (de Curtis et al. 1991, 1998; Llinás et al. 1981; Muhlethaler et al. 1993), a preparation that allows for a facilitated access to the entorhinal region under direct visual control. We recently demonstrated that the border between m- and l-EC in the guinea pig can be inferred by the activation pattern induced by direct olfactory input, which is largely confined to the l-EC (Biella and de Curtis 2000) and by the ability to generate fast oscillatory activity on muscarinic activation, a peculiar property of the m-EC (van der Linden et al. 1999). The identification of the borders between m- and l-EC was recently morphologically verified in the guinea pig by performing a cytoarchitectonic study of the region (Uva et al. 2001) based on the criteria utilized for the rat (Insausti et al. 1997).

## METHODS

Brains of young adult guinea-pigs (150–200 g) were dissected out according to the standard procedure (de Curtis et al. 1991, 1998) after anesthesia with Farmotal (20 mg/kg ip; Pharmacia-Upjohn, Milano, Italy). A solution containing (in mM) 126 NaCl, 3 KCl, 1.2 KH<sub>2</sub>PO<sub>4</sub>, 1.3 MgSO<sub>4</sub>, 2.4 CaCl<sub>2</sub>, 26 NaHCO<sub>3</sub>, and 15 glucose mM and 3% dextran MW 70.000, oxygenated with a 95% O<sub>2</sub>-5% CO<sub>2</sub> gas mixture (pH 7.3) was arterially perfused *in vitro* at 5.5 ml/min. Experiments were performed at 32°C. Bipolar stimulation was delivered with tungsten electrodes arrays formed by two electrode pairs at 200 μm

Address for reprint requests: G. Biella, Dept. Experimental Neurophysiology, Istituto Nazionale Neurologico “Carlo Besta,” via Celoria 11, 20133 Milan, Italy (E-mail: fiscor@istituto-bestait).

The costs of publication of this article were defrayed in part by the payment of page charges. The article must therefore be hereby marked “advertisement” in accordance with 18 U.S.C. Section 1734 solely to indicate this fact.

vertically separated by 500–1,000  $\mu\text{m}$  (FHC, Bowdoinham, ME) positioned at different depths in EC. Current stimuli of 50–150  $\mu\text{A}$  and 200–500  $\mu\text{s}$  were applied. Extracellular laminar depth profiles were performed with silicon probes (16-recording sites separated by 50  $\mu\text{m}$  on a single vertical shaft; kindly provided by Jamille Hetke of the Center of Neural Communication and Technology of the Michigan University, Ann Arbor, MI). The position of the electrodes was easily and rapidly modified during the experiment under direct visual control via a stereoscopic microscope. Signals were amplified with a 16-channel extracellular amplifier (Biomedical Engineering, Thornwood, NY), were digitized via an AT-MIO-64E3 National board (National Instruments, Milano, Italy) and were stored on a tape recorder (Biologic Instruments, Claix, France). Off-line analysis was performed by using a software (CLAMPVIEW) developed in our department by G. Biella in collaboration with the Italian branch of National Instruments. A different acquisition and analysis system (Folkers and Hofmann 2001) was also utilized to perform on-line acquisition of laminar profiles. Current-source density analysis (CSD) was implemented with 50  $\mu\text{m}$  steps on 200  $\mu\text{m}$  depth intervals according to the standard procedure previously described (Biella and de Curtis 1995, 2000; Ketchum and Haberly 1993).

Electrolytic lesions performed at the end of the experiments were utilized to mark the position of the electrodes (see METHODS in Biella and de Curtis 2000). After fixation in 4% paraformaldehyde, 75- $\mu\text{m}$  sections were cut by vibratome and were processed for thionin staining. The location of the stimulating and recording probes in the EC was identified by marking their position on a tri-dimensional reconstruction of the guinea pig EC (Uva et al. 2001). The location of the electrodes was reproduced on a photograph of the brain obtained during the electrophysiological experiment with a camera connected to the stereoscopic microscope.

## RESULTS

Recordings were performed from either one or both hemispheres of 18 guinea pig brains. Stimuli were delivered at different rostrocaudal levels in the EC (Fig. 1). The position of the recording and stimulating electrodes were reproduced in different experiments by using a large-size arterial branch of the limbic artery as surface reference point. Recordings were obtained with 16-channel silicon probes at 154 EC

sites (Fig. 1B) located either in the medial or lateral cortical bands of both the m-EC and the l-EC as defined by the response to lateral olfactory tract (LOT) stimulation (see Biella and de Curtis 2000). As previously demonstrated, l-EC responses were characterized by a large wave component at 20–25 ms that represents the direct propagation of the olfactory input (Fig. 1C, top), whereas the m-EC was characterized by a predominant delayed component at 50–60 ms (Fig. 1C, bottom) that represented a polysynaptic potential mediated through the activation of the hippocampus (Biella and de Curtis 2000).

Stimuli were delivered both in superficial and deep layers at each EC stimulation site. Superficial layer stimuli induced highly reproducible responses, whereas deep layer stimuli determined either no responses at a distance longer than 1 mm from the stimulating electrode. Depending on the intensity of deep layer stimulation, highly variable responses were observed in the EC close to the stimulating electrode. Because we could not evoke reproducible potentials in response to deep layer stimulation, we decided to restrict the study of long-range activity propagation to responses to superficial layer stimulation.

Regardless of the position of the recording and stimulating electrodes in the EC, we identified two typical, quite stereotyped patterns that were further analyzed with CSD analysis of laminar profile (Fig. 2, left). In almost all the experiments, the response pattern distinctively recorded within 1.2 mm from the stimulating electrode was characterized by a biphasic response (Fig. 2, top left). The early potential (positive at the surface and negative at depth) showed an average peak latency shorter than 10 ms and correlated to a current sink that extended between 200 and 600  $\mu\text{m}$  in layers II and III shown in the CSD contour plot. As illustrated in the example in Fig. 2, in the large majority of the experiments such an early current was divided in two separate sinks centered around 200- and 500- $\mu\text{m}$  depths. The histological control of the silicon probe track confirmed

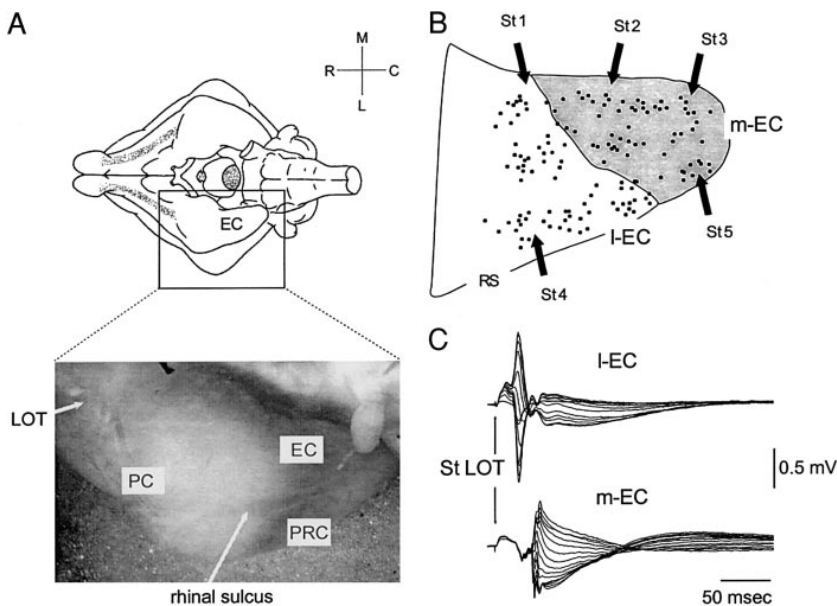
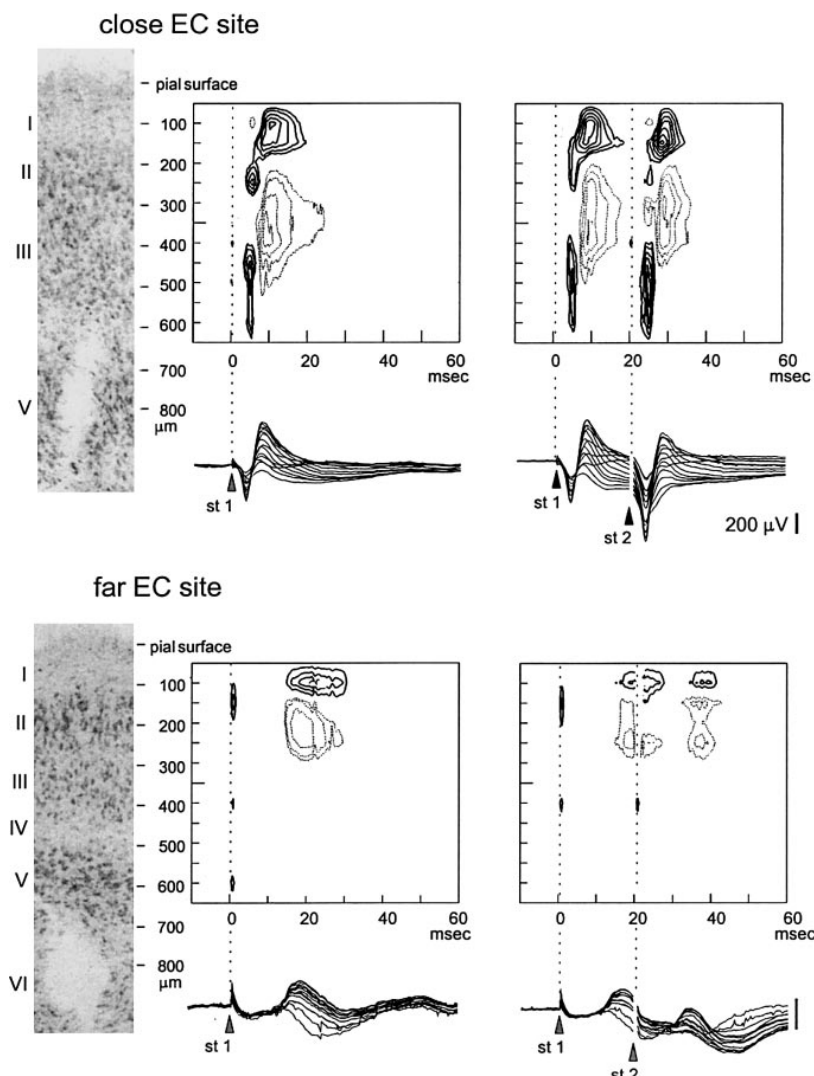


FIG. 1. A: drawing of the ventral view of a guinea pig brain and photograph of the entorhinal region taken after the electrophysiological recording. PC, piriform cortex; EC, entorhinal cortex; PRC, perirhinal cortex; LOT, lateral olfactory tract. B: scheme of the positions of the recording 16-channel silicon probes (●) and the stimulating electrodes (→) in the entorhinal area (summary of 18 experiments). The drawing of the EC was enlarged from the ventral view of the isolated guinea pig brain in A. The borders of the EC were outlined from microphotographs of the EC obtained during the experiment, such as the 1 illustrated in A. The medial EC (m-EC), as defined by the pattern to LOT response observed at each recording site, is identified by the gray shading. C: typical responses of the lateral EC (l-EC, top) and the m-EC (bottom) to stimulation of the LOT



**FIG. 2.** Response patterns evoked by local EC stimulation. The 2 recording silicon probes were positioned close to and far from the stimulating electrode positioned caudal in the l-EC band close to the rhinal sulcus (site 5 in Fig. 3). *Left:* the thionin-stained coronal section illustrate the histological control of the lesion performed at the tip of the silicon probe (see METHODS). *Top left:* a typical biphasic response recorded in the EC close to the local stimulation. current-source density (CSD) analysis of the laminar profiles is illustrated in the contour plot. Sinks and sources are identified by — and ···, respectively. The depth and time distribution of sinks and source that generate the 2 components of the response are shown. The early current is formed by 2 separate sinks that correspond to layer II and layer III (identified on the histological control sections). A typical “pure” late associative responses generate far from the stimulating electrode is shown in the *bottom left* panel. *Right:* pairing stimuli demonstrate that the late response is monosynaptic. The superficial late sink is preserved in the second response to a paired stimulation with 20-ms interval. Note that the 1st associative response is superimposed to the artifact of the 2nd paired stimulus (blanked in the CSD contour plot). Isocurrent lines at  $10 \text{ mV/mm}^2$ . The time calibration of the field traces is the same as for the CSD plots.

the location of the two sinks in layer II and in layer III, respectively (see microphotographs). The early event was followed by a delayed response at 10–20 ms that correlated with a sink in the superficial molecular layer coupled with a current source in layer II–III.

At distance from the stimulation electrode, an isolated response with a longer latency was observed (Fig. 2, *bottom left*). Such a potential was associated with a superficial sink in layer I, which was coupled with a source in layer II. Paired-pulse stimulation at 10- to 30-ms inter-stimulus interval showed that both at sites close and far from the stimulating electrode the sink associated with the late potential was not abolished in the second, conditioned response (Fig. 2, *right*). In addition to the preservation of the late layer I sink, the paired response at a site close to the stimulation electrode showed a larger early potential/sink (Fig. 2, *top right*). These results strongly suggest that the superficial late event is mediated by a associative monosynaptic potential generated by the output of layer II–III neurons directly activated in the tissue around the stimulating electrode (see DISCUSSION).

The delay of the late synaptic response increased with the distance from the EC stimulation site. Figure 3 summarizes the pattern of propagation of both the direct and the late synaptic responses obtained from recordings performed at 154 sites in which EC stimulation was delivered at different sites (1–5). With a few exceptions, the responses characterized by the biphasic activation pattern were restricted to the EC portion in close proximity (approximately 1 mm) to the stimulating electrode (marked by the white-dot-in-black-circle symbol); the increase in delay of the associative synaptic response is illustrated by different gray shadings (see legend in Fig. 3). The pattern of tangential propagation of the associative synaptic potentials differed substantially for the different stimulation sites. Stimulation of the rostral part of the medial portion of the l-EC (site 1) induced a propagation restricted to the medial and rostral portion of the l-EC. Stimulation at an intermediate longitudinal position in the medial band of the m-EC (site 2) induced a longitudinal propagation directed both rostrally and caudally within the m-EC band. Little propagation directed

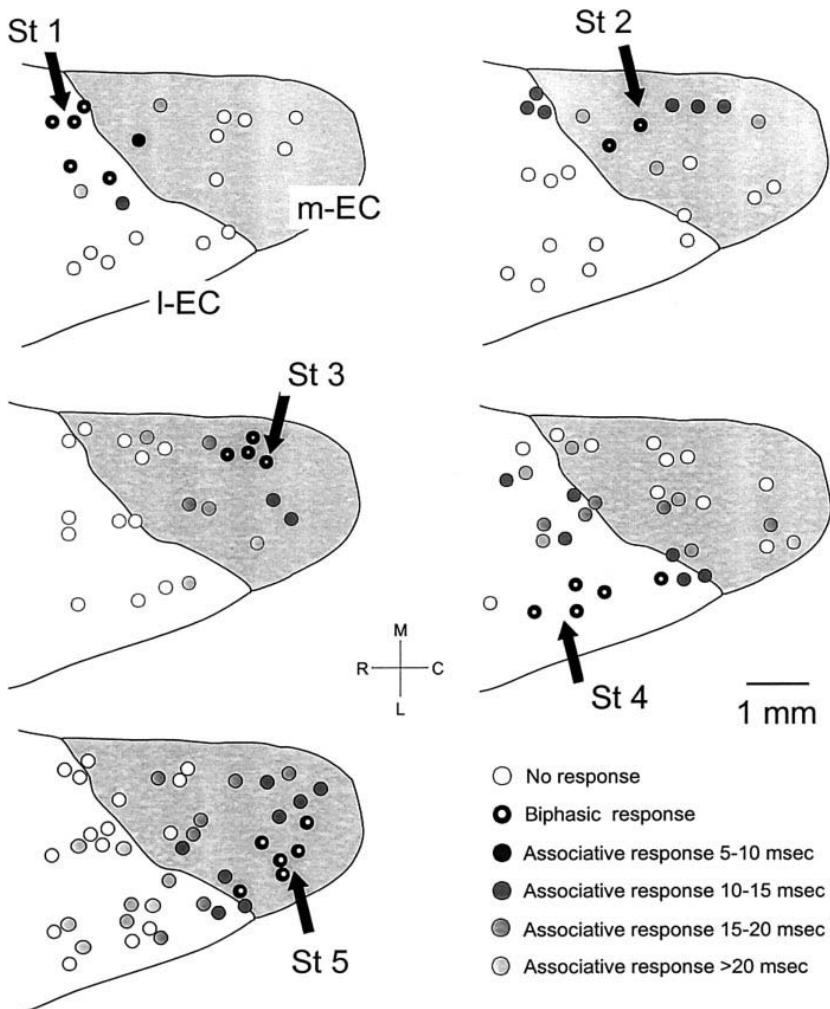


FIG. 3. Distribution of the synaptic responses to different local EC stimulation sites (1–5) in the superficial layers. The responses characterized by a biphasic potential are marked by the symbol characterized by a white dot on a black circle. The associative responses with peak amplitude values of gradually increasing delays are represented by circles of decreasing gray intensity. As for Fig. 1, the m-EC is shaded in light gray.

laterally was observed following stimuli at sites 1 and 2. Stimulation in a medial and caudal m-EC position (site 3) induced a propagation in the rostral and lateral direction limited to the caudal part of the m-EC. The associative activity induced by stimulation of the rostral part of the l-EC lateral band (site 4) propagated caudally and medially, across the border between m-EC and l-EC. Finally, caudal-lateral stimulation at site 5 determined a diffuse propagation within the m-EC, and a rostral projection at distance along the lateral band, to the l-EC.

The delay of the late responses increased with distance from the region directly activated by the local stimulation, as shown in the representative experiment illustrated in Fig. 4A. The peak latencies of the early component (●) and late component (▲) of the responses evoked by the local stimulus is illustrated in the graph in Fig. 4B. The plot includes biphasic responses (such as *a*) and pure monophasic potentials (such as *b* and *c*). The distribution of the delays was homogeneous in different directions of propagation for the different stimulation sites 1–5. The general direction pattern of associative projections derived from the experiments described in the preceding text is summarized in the scheme in Fig. 5.

## DISCUSSION

The present study describes the pattern of activity propagation along the intrinsic associative fibers that run in the superficial plexiform layer of the EC. The study has been restricted to the activity generated within the superficial layers because no activity was observed in deep layers following superficial EC stimulation, probably because of the spatial and temporal dispersion of the associative connections in deep EC layers that prevents the identification of a field potential reversal or a current sink with CSD analysis (Mitzdorf 1985). In addition, we excluded from the study the analysis of the associative potentials evoked by deep layers stimulation because a highly variable response pattern was obtained in the EC close to the stimulating electrode following stimulation of deep layers and no clear responses were observed with CSD analysis of laminar profiles at cortical sites remote from the deep stimulation site.

Local cortical stimulation induced a spatially restricted neuronal discharge in layers II and III in close proximity (less than 1.2 mm) to the stimulating electrode, represented by the early CSD sinks located at 200- to 600- $\mu$ m depth. The identification of such depth values with layers II and III was accomplished by reconstructing the silicon probe position on a detailed cytoar-

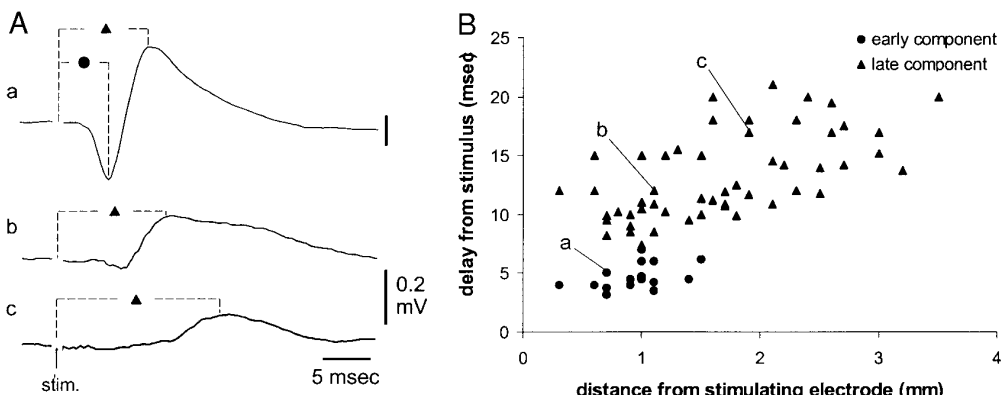


FIG. 4. Distribution of peak latencies of the early (●) and late (▲) components of the evoked response. The delay of the late component increased with the distance of the recording site from the stimulation electrode. A: recordings obtained at 3 sites 0.8 (a), 1.1 (b), and 1.9 mm (c) from the stimulating electrode positioned at site 5. The delays calculated on the peak amplitudes of the early and late components recorded in 11 experiments in which stimuli were applied at site 1 ( $n = 3$ ), site 2 ( $n = 2$ ), site 3 ( $n = 2$ ), site 4 ( $n = 4$ ), and site 5 ( $n = 6$ ) are plotted in B. The latencies from the stimulus of the early and the late peak amplitude responses are plotted against the distance from the stimulation site. The values of the field potential components illustrated in A are indicated in the graph.

chitectonic map of the guinea pig EC (Uva et al. 2001). Such a response could be mediated by the direct activation of the neurons close to the stimulating electrode and/or by the mono-synaptic activation of layer II-III cells. As expected from a response due to either the direct activation or the antidromic invasion of neuron somata in layers II-III, the early potential/sink showed a very short delay from the stimulus artifact (less than 5 ms) and was not abolished by high-frequency stimulation at and above 50 Hz, as demonstrated during the pairing tests performed with a 10- to 30-ms inter-stimulus intervals. In the lateral band of the l-EC, a possible direct activation of the olfactory input to the propagation pattern observed should be also taken in account because olfactory fibers that arise from both the olfactory bulb (Biella and de Curtis 1995, 2000; Boeijinga and Van Groen 1984; Haberly and Price 1977; Kosek et al. 1981; Krettek and Price 1977; Liu and Bilkey 1997;

Luskin and Price 1982; Schwerdtfeger et al. 1990; Van Groen et al. 1987; Wilson and Steward 1978; Wouterlood and Nederlof 1983) and the piriform cortex (Boeijinga and Van Groen 1984; Chapman and Racine 1997a,b; Krettek and Price 1977; Luskin and Price 1983; Van Groen et al. 1987) are known to run in the superficial layers of the l-EC but not the m-EC. Even though, in principle, a monosynaptic excitatory response evoked by the activation of the olfactory input fibers could contribute to both the early response close to stimulation site and the late potential at remote sites, the results of the pairing test do not support this conclusion.

The observed results suggest that the late superficial synaptic responses (late CSD sinks) are sustained by the activation of cortico-cortical associative fibers that originate from the discharge of layer II-III cells directly activated by the local stimulus. These late potentials should be mediated through monosynaptic associative responses because their delay from the direct potential are compatible with a single synapse. Moreover, a polysynaptic origin of the late associative response/sink is excluded by the demonstration that it is preserved in the conditioned response during a pairing test (Biella et al. 1996).

The anatomical connectivity within the EC has been studied in detail in the rat (Dolorfo and Amaral 1998; Kohler 1986, 1988; Kosel et al. 1982; Swanson and Köhler 1986), in the cat (Room and Groenewegen 1986; Witter et al. 1986) and in the monkey (Kosel et al. 1982; Suzuki 1996). Because no anatomical data are available in the guinea pig, the present physiological finding will be discussed with reference with the data described in the rat. Our results demonstrate that stimulation in the medial-rostral EC (site 1) generates activity that remains localized in the mediorostral pole of the EC, stimulation of the medial band of m-EC (site 2) induced an associative propagation directed longitudinally, stimulation of the caudal part of the m-EC (site 3) induces a short range propagation in the lateral and rostral directions within the m-EC, and stimulation of the lateral band (sites 4 and 5) induces a prominent longitudinal propagation of activity across the m-EC/l-EC border. Unlike suggested by the anatomical studies, the stimulation

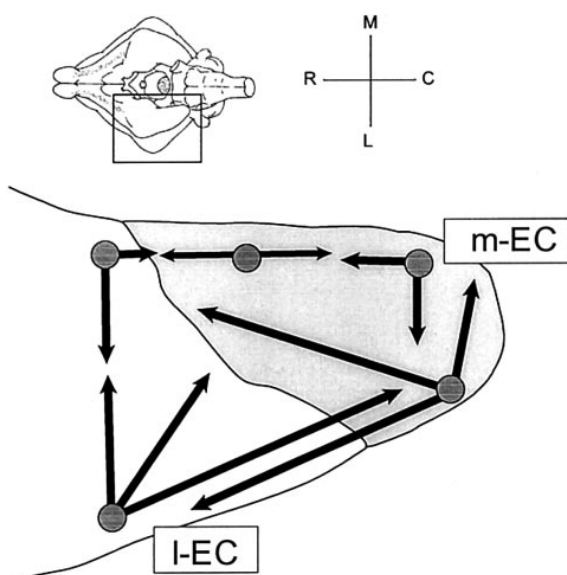


FIG. 5. Summary of the propagation direction of the associative potentials in the superficial layers of the EC.

within the m-EC band (sites 2 and 3) induces a longitudinal propagation of activity and the stimulation of the caudal pole of the m-EC in a lateral position (site 5) induces a diffuse propagation of the activity at distance in the rostral and medial directions. These discrepancies may be due to species differences. Indeed, even though preliminary cytoarchitectonic studies suggest that the general organization of the EC is similar between rat and guinea pig (Uva et al. 2001), the relative dimension of l- and m-EC and the subfields that compose these two regions, as well as the topographic organization of the projection of superficial layers to the hippocampus, may be different in the two species. A region of particular interest at this regard, for which an unequivocal attribution to either the m-EC or the l-EC has not been defined yet, is the subfield denominated F3 that represents an extended portion of the guinea pig EC (Insausti et al. 1997; Uva et al. 2001). A specific ad hoc study will be necessary to clarify this issue.

The present findings demonstrate that both rostral and caudal stimuli in the EC region close to the rhinal sulcus induced activity propagation across the border between l- and m-EC. As for the rat (Insausti et al. 1997), the guinea pig EC can be subdivided in subfields that belong to either the MEA or the LEA, i.e., the medial and lateral EC regions that project to the inner and outer portion of dentate gyrus granule cells, respectively (Steward 1976; Steward and Scoville 1976). The results obtained in a recent collaborative study (Uva et al. 2001) strongly suggest that the identification of the border between the LEA and MEA coincide with the delimitation m- and l-EC defined on the basis of the electrophysiological response to LOT stimulation (Biella and de Curtis 2000). According to this pattern, l-EC neurons do not induce a prominent projection to the m-EC. This conclusion derived from the demonstration that a large-amplitude response in the m-EC could be induced exclusively when the hippocampus was activated. Unlike previously suggested, we recently observed that small amplitude responses could be recorded in the m-EC after LOT-induced l-EC activation, mostly in an intermediate band of the EC located between m- and l-EC, that probably coincides with the above mentioned subfield identified as F3 according to the classification of Insausti (Insausti et al. 1997). Such responses were not large enough to generate reproducible sinks during CSD analysis (not shown). Therefore even though olfactory-induced m-EC activation through the hippocampus is large and easy to detect, the existence of a direct intrinsic propagation of neuronal activity within the EC cannot be excluded and, indeed, is strongly suggested by the present study and by the anatomical study by Dolorfo and Amaral (1998). Such a longitudinal propagation of excitation, directed parallel to the rhinal sulcus, is similar to the propagation pattern of neuronal activity observed in the adjacent perirhinal cortex (Biella et al. 2001; Martina et al. 2001).

The results confirm that different portions of the EC are strongly interconnected by an associative system of fibers that likely sustain the complex integrative function performed by this region before neuronal activity is propagated to the hippocampus.

Multi-channel silicon probes were kindly provided by the University of Michigan Center for Neural Communication Technology, sponsored by Division of Research Resources Grant P41-RR09754.

The study was sponsored by the European Community grant Development

of a Versatile System for Advanced Neuronal Recordings with Multisite Microelectrodes (IST-1999-10079) and by the Italian Health Ministry.

## REFERENCES

- BIELLA G AND DE CURTIS M. Associative synaptic potentials in the piriform cortex of the isolated guinea pig brain in vitro. *Eur J Neurosci* 7: 54–64, 1995.
- BIELLA G AND DE CURTIS M. Olfactory inputs activate the medial entorhinal cortex via the hippocampus. *J Neurophysiol* 83: 1924–1931, 2000.
- BIELLA G, FORTI M, AND DE CURTIS M. Propagation of epileptiform potentials in the guinea pig piriform cortex is sustained by associative fibers. *Epilepsy Res* 24: 137–146, 1996.
- BIELLA G, UVA L, AND DE CURTIS M. Network activity evoked by neocortical stimulation in area 36 of the guinea pig perirhinal cortex. *J Neurophysiol* 86: 164–172, 2001.
- BOEIJINGA PH AND VAN GROEN T. Inputs from the olfactory bulb and olfactory cortex to the entorhinal cortex in the cat. *Exp Brain Res* 57: 40–48, 1984.
- BRODMAN K. *Vergleichende Lokalisationslehre der Grosshirnrinde in ihren Prinzipien Dargestellt auf Grund der Zellenbaues*. Leipzig, Germany: Barth, 1909.
- CHAPMAN AC AND RACINE RJ. Converging inputs to the entorhinal cortex from the piriform cortex and medial septum: facilitation and current source density analysis. *J Neurophysiol* 78: 2602–2615, 1997a.
- CHAPMAN AC AND RACINE RJ. Piriform cortex efferents to the entorhinal cortex in vivo: kindling induced potentiation enhancement of LTP by low-frequency piriform cortex or medial septum stimulation. *Hippocampus* 7: 257–270, 1997b.
- DE CURTIS M, BIELLA G, BUCELLATI C, AND FOLCO G. Simultaneous investigation of the neuronal and vascular compartments in the guinea pig brain isolated in vitro. *Brain Res Brain Res Protoc* 3: 221–228, 1998.
- DE CURTIS M, PARE D, AND LLINÁS RR. The electrophysiology of the olfactory-hippocampal circuit in the isolated and perfused adult mammalian brain in vitro. *Hippocampus* 1: 341–354, 1991.
- DOLORFO CL AND AMARAL DG. Entorhinal cortex of the rat: organization of intrinsic connections. *J Comp Neurol* 398: 49–82, 1998.
- FOLKERS A AND HOFMANN UG. A multichannel data acquisition and analysis system based on off-the-shelf DSP boards. In: *Proc ECMCS 2001: Budapest*. 2001.
- HABERLY LB AND PRICE JL. The axonal projection patterns of the mitral and tufted cells of the olfactory bulb in the rat. *Brain Res* 129: 152–157, 1977.
- HJORTH-SIMONSEN A AND JEUNE B. Origin and termination of the hippocampal perforant path in the rat studied by silver impregnation. *J Comp Neurol* 144: 215–232, 1972.
- INSAUSTI R, HERRERO MT, AND WITTER MP. Entorhinal cortex of the rat: cytoarchitectonic subdivisions and the origin and distribution of cortical efferents. *Hippocampus* 7: 146–183, 1997.
- KETCHUM KL AND HABERLY LB. Membrane currents evoked by afferent fiber stimulation in rat piriform cortex. I. Current source-density analysis. *J Neurophysiol* 69: 248–260, 1993.
- KOHLER C. Intrinsic connections of the retrohippocampal region in the rat brain. II. The medial entorhinal area. *J Comp Neurol* 246: 149–169, 1986.
- KOHLER C. Intrinsic connections of the retrohippocampal region in the rat brain. III. The lateral entorhinal area. *J Comp Neurol* 271: 208–228, 1988.
- KOSEL KC, VAN HOESEN GW, AND ROSENE DL. Non-hippocampal cortical projections from the entorhinal cortex in the rat and rhesus monkey. *Brain Res* 244: 201–213, 1982.
- KOSEL KC, VAN HOESEN GW, AND WEST JR. Olfactory bulb projection to the parahippocampal area of the rat. *J Comp Neurol* 198: 467–482, 1981.
- KRETEK JE AND PRICE JL. Projections from the amygdaloid complex and adjacent olfactory structures to the entorhinal cortex and to the subiculum in the rat and cat. *J Comp Neurol* 172: 723–752, 1977.
- LIU P AND BILKEY DK. Parallel involvement of perirhinal and lateral entorhinal cortex in the polysynaptic activation of hippocampus by olfactory inputs. *Hippocampus* 7: 296–306, 1997.
- LLINÁS R, YAROM Y, AND SUGIMORI M. Isolated mammalian brain in vitro: new technique for analysis of electrical activity of neuronal circuit function. *Fed Proc* 40: 2240–2245, 1981.
- LOPES DA SILVA FH, WITTER MP, BOEIJINGA PH, AND LOHMAN AH. Anatomic organization and physiology of the limbic cortex. *Physiol Rev* 70: 453–511, 1990.
- LUSKIN MB AND PRICE JL. The distribution of axon collaterals from the olfactory bulb and the nucleus of the horizontal limb of the diagonal band to

- the olfactory cortex, demonstrated by double retrograde labeling techniques. *J Comp Neurol* 209: 249–263, 1982.
- LUSKIN MB AND PRICE JL. The laminar distribution of intracortical fibers originating in the olfactory cortex of the rat. *J Comp Neurol* 216: 292–302, 1983.
- MARTINA M, ROYER S, AND PARÉ D. Propagation of neocortical inputs in the perirhinal cortex. *J Neurosci* 21: 2878–2888, 2001.
- MITZDORF U. Current source-density method and application in cat cerebral cortex: investigation of evoked potentials and EEG phenomena. *Physiol Rev* 65: 37–100, 1985.
- MUHLETHALER M, DE CURTIS M, WALTON K, AND LLINÁS R. The isolated and perfused brain of the guinea pig in vitro. *Eur J Neurosci* 5: 915–926, 1993.
- ROOM P AND GROENEWEGEN HJ. The connections of the parahippocampal cortex in the cat. I. Cortical afferents. *J Comp Neurol* 251: 415–450, 1986.
- SCHWERDTFEGER WK, BUHL EH, AND GERMROTH P. Disynaptic olfactory input to the hippocampus mediated by stellate cells in the entorhinal cortex. *J Comp Neurol* 292: 163–177, 1990.
- SHIPLEY MT. The topographical and laminar organization of the presubiculum projection to ipsi- and contralateral entorhinal cortex in the guinea pig. *J Comp Neurol* 160: 127–146, 1975.
- STEWARD O. Topographic organization of the projections from the entorhinal area to the hippocampal formation of the rat. *J Comp Neurol* 167: 285–314, 1976.
- STEWARD O AND SCOVILLE SA. The cells of origin of entorhinal afferents to the hippocampus and fascia dentata of the rat. *J Comp Neurol* 169: 347–370, 1976.
- SUZUKI WA. Neuroanatomy of the monkey entorhinal, perirhinal and parahippocampal cortices: organization of cortical inputs and interconnections with amygdala and striatum. *J Neurosci* 8: 3–12, 1996.
- SWANSON LW AND KÖHLER C. Anatomical evidence for direct projections from the entorhinal area to the entire cortical mantle in the rat. *J Neurosci* 6: 3010–3023, 1986.
- UVA L, WITTER M, WOUTERLOOD F, AND DE CURTIS M. Cytoarchitectonic subdivisions and 3D reconstruction of the parahippocampal region of the guinea pig. (Abstract). *Italian Soc Neurosci*. Torino, Italy: D5, 2001.
- VAN DER LINDEN S, DE CURTIS M, AND PANZICA F. Carbachol induces fast oscillations in the medial but not in the later entorhinal cortex of the isolated guinea pig brain. *J Neurophysiol* 82: 2441–2450, 1999.
- VAN GROEN T, LOPEZ DA SILVA FH, AND WADMAN WJ. Synaptic organization of olfactory inputs and local circuits in the entorhinal cortex, a current-source density analysis in the cat. *Exp Brain Res* 67: 502–509, 1987.
- WILSON RC AND STEWARD O. Polysynaptic activation of the dentate gyrus of the hippocampal formation: an olfactory input via the lateral entorhinal cortex. *Exp Brain Res* 33: 523–534, 1978.
- WITTER MP. Organization of the entorhinal-hippocampal system: a review of current anatomical data. *Hippocampus* 3: 33–44, 1993.
- WITTER MP, GROENEWEGEN HJ, LOPEZ DA SILVA FH, AND LOHMAN AH. Functional organization of the extrinsic and intrinsic circuitry of the parahippocampal region. *Prog Neurobiol* 33: 161–253, 1989.
- WITTER MP, ROOM P, GROENEWEGEN HJ, AND LOHMAN AHM. Connections of the parahippocampal cortex in the cat. V. Intrinsic connections; comments on input/output connections with the hippocampus. *J Comp Neurol* 252: 78–94, 1986.
- WOUTERLOOD FG AND NEDERLOF J. Terminations of olfactory afferents on layer II and III neurons in the entorhinal area: degeneration-Golgi-electron microscopic study in the rat. *Neurosci Lett* 36: 105–110, 1983.



# Stimulus representation in rat primary visual cortex: multi-electrode recordings with micro-machined silicon probes and estimation theory

Winrich A. Freiwald<sup>a,b,\*</sup>, Heiko Stemmann<sup>a</sup>, Aurel Wannig<sup>a</sup>,  
Andreas K. Kreiter<sup>a</sup>, Ulrich G. Hofmann<sup>c</sup>, Matthew D. Hills<sup>d</sup>,  
Gregory T.A. Kovacs<sup>d</sup>, David T. Kewley<sup>e</sup>, James M. Bower<sup>f,g</sup>,  
Axel Etzold<sup>h</sup>, Stefan D. Wilke<sup>h</sup>, Christian W. Eurich<sup>h</sup>

<sup>a</sup> Institute for Brain Research, University of Bremen, FB 2, P.O. Box 330440,  
D-28334 Bremen, Germany

<sup>b</sup> MIT Brain & Cognitive Science Department, 77 Massachusetts Avenue, NE20-443,  
Cambridge, MA 02139, USA

<sup>c</sup> Institute for Signal Processing, Medical University of Lübeck, Seelandstr. 1a,  
D-23569 Lübeck, Germany

<sup>d</sup> Center for Integrated Systems, CISX 202, Stanford University, Stanford, CA 94305-4075, USA

<sup>e</sup> Computation and Neural Systems, MC 216-76, California Institute of Technology,  
Pasadena, CA 91125, USA

<sup>f</sup> Research Imaging Center, University of Texas Health Science Center, 7703 Floyd Curl Dr.,  
San Antonio, TX 78229, USA

<sup>g</sup> Cajal Neuroscience Research Center, University of Texas, 6900 N Loop 1604 West,  
San Antonio, TX 78249, USA

<sup>h</sup> Department of Theoretical Neurophysiology, University of Bremen, FB 1, P.O. Box 330440,  
D-28334 Bremen, Germany

---

## Abstract

The study of neural population codes relies on massively parallel recordings in combination with theoretically motivated analysis tools. We applied two multi-site recording techniques to

---

\* Corresponding author. Department of Brain and Cognitive Sciences, Massachusetts Institute of Technology, 77 Massachusetts Avenue, NE20-443, 02139 Cambridge, MA, USA.

E-mail addresses: freiwald@brain.uni-bremen.de (W.A. Freiwald), stemmann@brain.uni-bremen.de (H. Stemmann), awannig@brain.uni-bremen.de (A. Wannig), kreiter@brain.uni-bremen.de (A.K. Kreiter), hofmann@isip.mu-luebeck.de (U.G. Hofmann), hills@standford.edu (M.D. Hills), kovacs@cis.stanford.edu (G.T.A. Kovacs), kewley@bbb.caltech.edu (D.T. Kewley), jbower@bbb.caltech.edu (J.M. Bower), aetzold@physik.uni-bremen.de (A. Etzold), swilke@physik.uni-bremen.de (S.D. Wilke), eurich@physik.uni-bremen.de (C.W. Eurich).

record from cells throughout cortical depth in a minimally invasive way. The feasibility of such experiments in area 17 of the anesthetized rat is demonstrated. Bayesian reconstruction and the interpretative framework of Fisher information are introduced. We demonstrate applicability and usefulness of Bayesian stimulus reconstruction and show that even small numbers of neurons can yield a high degree of representational accuracy under favorable conditions. Results are discussed and future lines of research outlined. © 2002 Elsevier Science B.V. All rights reserved.

**Keywords:** Population coding; Bayesian reconstruction; Fisher information; Multi-site recording technology; Visual cortex

---

## 1. Introduction

Stimulus representation in the mammalian visual system is achieved by large groups of neurons. To study the means by which neural populations achieve high coding performance, theoretical approaches are needed to identify potentially critical parameters of population codes as well as recording techniques for the simultaneous acquisition of signals from large neural numbers. Massively parallel recordings are required because neural interactions or only very briefly generated spatio-temporal activity patterns may play a critical role for stimulus representation. A further requirement for recording techniques is the capacity for reliable isolation of single units from all cortical layers, since cells in different layers may serve different functions in information processing as indicated by their different connectivity patterns. For these reasons, we chose multi-site, silicon-based electrodes [2,8,1,12,7,10] which promise the acquisition of large neural numbers throughout cortical depth.

In this contribution we present results of an integrated approach combining electrophysiological recordings with silicon-based multi-site probes in the rat primary visual cortex, an analysis of the neural population code based on Bayesian reconstruction and the interpretative framework of Fisher information.

Neural encoding strategies can be assessed using the framework of *Fisher information* [9,6,14,3,11,15]. Fisher information employs the joint probability distribution  $P(n_1, \dots, n_N; \vec{x})$  of the spike count vector  $(n_1, \dots, n_N)$  obtained from a population of  $N$  neurons during some time interval upon the presentation of a stimulus  $\vec{x}$ . The stimulus  $\vec{x} = (x_1, \dots, x_D)$  is characterized by  $D$  features in a  $D$ -dimensional stimulus space. The Cramér–Rao inequality [6] gives a lower bound on the expected estimation error  $\epsilon_{i,\min}^2$  the  $i$ th feature for an arbitrary but unbiased estimator. In the case of a diagonal Fisher information matrix, it is given by  $\epsilon_{i,\min}^2 = 1/J_{ii}(\vec{x})$ , where the denominator is the Fisher information associated to the  $i$ th feature.

The joint probability distribution  $P(n_1, \dots, n_N; \vec{x})$  can, in principle, be determined empirically. However, additional assumptions, e.g. statistically independent firing of neurons, considerably reduce the amount of data required. Using assumptions of this type, Fisher information can be used to derive encoding strategies that yield especially small estimation errors, and thus allow for accurate stimulus representation. Recently,

considerable progress has been achieved in this direction. For the influence of different tuning widths in multiple stimulus features and how they can be used to assess optimality in codes, see [3,11]. These results give hints as to what effects can be expected in empirically obtained distributions  $P(n_1, \dots, n_N; \vec{x})$ .

While Fisher information and the Cramér–Rao inequality yield (in the unbiased case) estimates on the highest achievable neural encoding performance, in this paper, we use a Bayesian reconstruction method to assess the actual encoding accuracy of neurons in rat primary visual cortex for motion directions of drifting gratings. A comparison of the results obtained from the use of Fisher information and the Cramér–Rao inequality on the one hand with results from Bayesian reconstruction on the other hand is not straightforward; if stimulus features are visual angles, the approach for features measured in real numbers [13] has to be modified. This is because the error estimate of the mean rate given by the Cramér–Rao inequality needs to be backtransformed to an error estimate of the angle in a more complicated manner than in the case of features measured in real numbers (Etzold et al., in preparation).

## 2. Materials and methods

### 2.1. Recording technology

Recordings were performed with two types of micro-machined multi-site recording probes in addition to standard varnish-coated tungsten electrodes. One micro-machined probe was provided by a joint project of two groups at the California Institute of Technology and at Stanford University, the other was provided by the Center for Neural Communication Technology of the University of Michigan sponsored by NIH NCRR Grant P41-RR09754. The Caltech/Stanford probes (see Fig. 1) were micro-machined at Stanford's Center for Integrated Systems.

The CalTech/Stanford probes feature 32 co-planar electrodes on a silicon substrate with silicon-nitride passivation. Electrodes are  $100 \mu\text{m}^2$  gold, with typical impedances of  $1\text{--}4 \text{ M}\Omega$  at  $1 \text{ kHz}$ . The probe shafts' outlines are defined by a plasma etch and are designed to minimize insertion resistance, resulting in dimpling comparable to tungsten electrodes upon insertion [5]. Recordings were made using electrodes in tetrode arrangements.

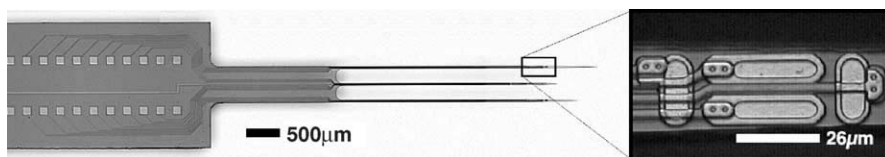


Fig. 1. Micrograph of Caltech/Stanford T1 probe. Inset on the right shows an enlarged view of four electrodes in tetrode configuration on one T1-shank. Each electrode's surface area equals  $100 \mu\text{m}^2$ .

## 2.2. Animals, preparation and maintenance

The results presented here are based on recordings in the primary visual cortex (area 17) of five rats (Brown Norway, 300–380 g). They were anesthetized with an i.m. injection of ketamin/xylacina/chlorpromacin (10 mg/0.4 mg/1 mg/100 g b.w.) during surgical preparation and maintained with a nitrous oxide/oxygen (30/70%)-isoflurane (0.5%) gas mixture during the recording session. During surgery animals were placed in a stereotaxic apparatus, body temperature was kept constant, and the heart rate was monitored continuously. The cornea was protected with a non-refractive contact lens throughout the experiment. The scalp was removed, and a small ( $2 \times 2$  mm) bone window above the left visual cortex was drilled (centered at AP = +1 and L = 3.25 mm from lambda), the dura reflected and, after electrode positioning, the cortical surface covered with 3% Agar in Ringers solution to prevent drying of the brain and decrease pulsation. All procedures used in this study were performed in accordance with the guidelines for the welfare of experimental animals issued by the Federal Government of Germany, approved by local authorities and conformed to the guidelines of the National Institutes of Health for the care and use of laboratory animals.

## 2.3. Recording and visual stimulation

Signals were amplified with conventional electrophysiological instrumentation (filter: 350–3000 Hz) and displayed on an oscilloscope. In addition, spike activity were digitized (sampled at 25 kHz) and stored on computer disk for offline analysis, which started with spike sorting.

Response properties and appropriate receptive field (RF) boundaries of cortical cells were determined qualitatively with visual stimuli generated by a hand-held pentoscope and projected on a tangent white screen. Then RFs were centered on a monitor (EIZO FlexScan F87) positioned 57 cm from the animal. Stimuli consisted of whole screen black and white gratings, moving with constant velocity (5–20°/s) and spatial frequency (0.08–0.6 cycl deg) (cf. [4]). Background illumination was kept below 1 cd/m<sup>2</sup>, and stimulus intensities ranged from 7 to 10 cd/m<sup>2</sup>. Each experiment consisted of several blocks of trials in which 18 stimuli with particular moving direction were presented in a pseudo-random order.

## 2.4. Bayesian reconstruction

Once the direction dependence of the firing rates of a group of direction-sensitive cells is known, the Bayes approach directly addresses the inverse problem: given the firing rates of one or more of these cells, what is the stimulus that triggered them? A method to derive the stimulus from the neural firing is called a *reconstruction algorithm* (e.g. [13]).

Bayesian reconstruction needs various distribution functions derived from the data. The first one is the prior probability  $P(x)$  for a single direction  $x$  to occur. This function is determined by the experimenter and was flat in our case: all stimuli appeared equally often. The second distribution needed for reconstruction is the conditional probability

$P(\mathbf{n}|x)$ , which is the probability for numbers of spikes  $\mathbf{n} = (n_1, \dots, n_N)$  to occur, given the direction of the presented stimulus. If we assume that the spikes have Poisson distribution and that different cells are statistically independent of one another, we obtain the expression

$$P(\mathbf{n}|x) = \prod_{i=1}^N P(n_i|x) = \prod_{i=1}^N \frac{(\tau f_i(x))^{n_i}}{n_i!} \exp(-\tau f_i(x)), \quad (1)$$

where  $f_i(x)$  is the average firing rate of cell  $i$  during presentation of the stimulus  $x$ , and  $\tau$  is the length of the time window for counting the spikes. The average firing rate  $f_i(x)$  is also called the *tuning function* of cell  $i$ .

Given the number of spikes fired by a population of cells within a fixed time interval, the goal is to compute the probability distribution of the direction of the stimulus. Under the assumptions mentioned above, this is achieved by applying the Bayes formula in its final form

$$P(x|\mathbf{n}) = C(\tau, \mathbf{n})P(x) \left( \prod_{i=1}^N f_i(x)^{n_i} \right) \exp \left( -\tau \sum_{i=1}^N f_i(x) \right), \quad (2)$$

where  $C(\tau, \mathbf{n})$  is a normalization factor which can be determined by the normalization condition  $\sum P(x|\mathbf{n}) = 1$ . The Bayesian reconstruction method thus computes the probability for each stimulus direction, given the number of spikes of all the cells within the analysis time window. From this probability distribution the direction of the presented stimulus can be estimated by various estimators. We applied the maximum a posteriori (MAP) estimator

$$\hat{x}_{\text{Bayes}} = \arg \max_x P(x|\mathbf{n}), \quad (3)$$

where the direction of the stimulus is reconstructed by taking the most probable direction of the stimulus.

### 3. Results

Successful multi-site recordings were obtained from rat area 17 throughout cortical depth. Example traces from seven recording sites are shown in Fig. 2. A high signal-to-noise ratio was obtained in both multi-site probe types used in our experiments. The example traces shown were obtained during high activity levels, i.e. most of the signals result from neural activity and are much larger in size than hash during low-activity, background phases. No systematic differences between probe types in recording quality or neural yield have been noticed so far.

Of all 101 neurons recorded so far, 90% were visually responsive, many of which were orientation or direction tuned. Typically, tuning properties changed substantially over time (Fig. 3). Thus, for our current purposes we can conclude that the new recording technique leaves the cortical tissue functional and allows for the investigation of population coding mechanisms.

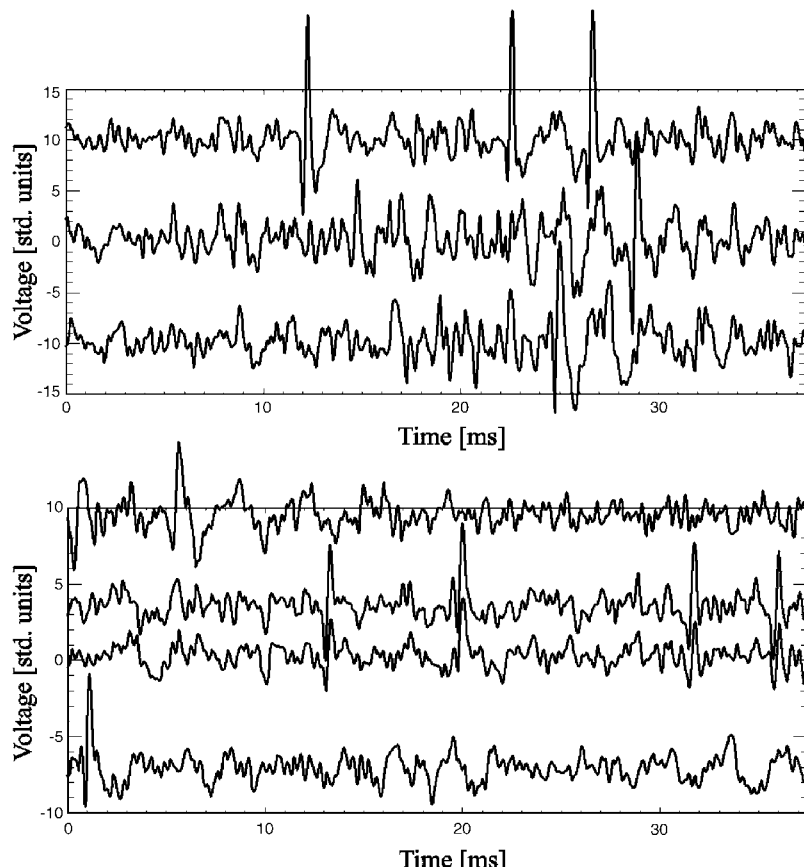
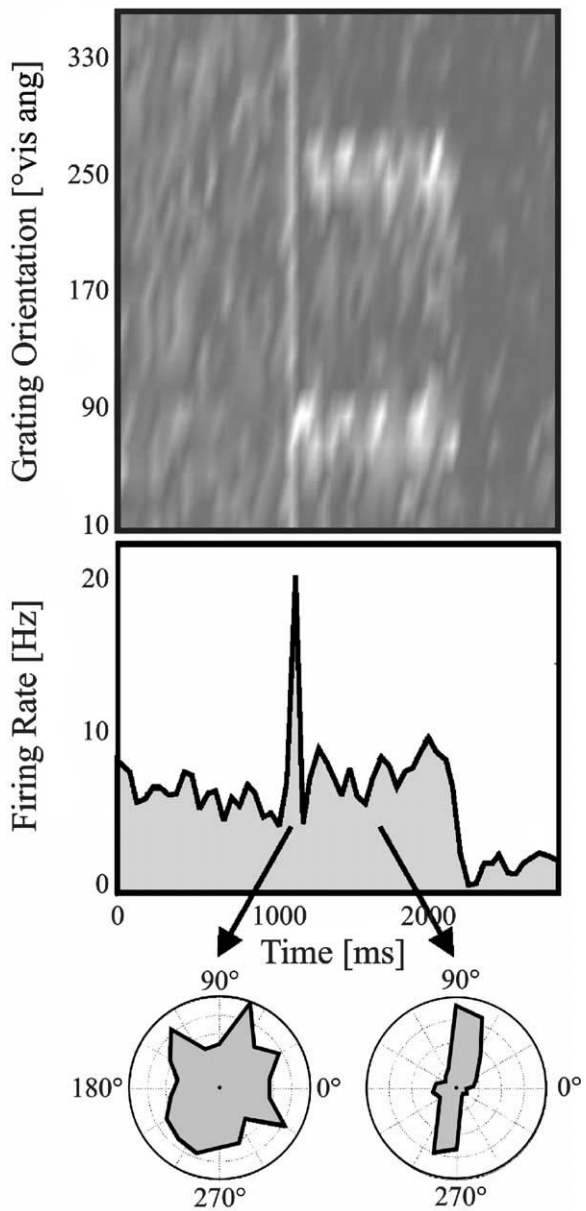


Fig. 2. Three channel simultaneous recordings with a Michigan probe (top) and four channels from a T1 probe (bottom) over 37.5 ms during cortical activation. Signals were z-transformed for comparison and shifted upwards/downwards within the two sub-plots for display purposes. Data was obtained from sites with a 200  $\mu$ m or larger spatial separation. However, the two central stretches in the bottom plot were recorded from two sites of the same tetrode arrangement. Therefore, these two signals are highly correlated. Nevertheless, not all spike activity of one channel appeared on the other one as well. Therefore, the stereo-capability of the tetrode-like geometrical arrangement of recording sites is useful for spike sorting purposes.

Fig. 3. Tuning Properties of a single neuron recorded in rat primary visual cortex. The upper graph shows firing rate as a function of time (x-axis) and stimulus orientation (y-axis) coded by color. Lighter colors indicate firing rates higher than average, darker colors, firing rates lower than average. Below, the PSTH is depicted which was computed as the average firing rate over *all* stimulus conditions (marginal distribution) of the above plot. Shown is a time interval of 2800 ms. The stimulus was turned on at 1000 ms and switched off at 2000 ms. Stimulus presentation leads to a steep increase of firing rate (to about 20 Hz on average) for about 100 ms. The tuning curve of the first 150 ms (shown as a polar plot on the lower left) shows only a weak modulation. A clear directional (orientational) tuning is only apparent after the initial burst of activity. The tuning curve of all spikes fired in the time period between 1150 and 2000 ms after stimulus onset shows two peaks around 70–90° and 250–270° of visual angle. In this phase, both response enhancement and suppression as compared to the pre-stimulus interval lead to the cell's tuning properties. Therefore, in the PSTH averaged over all stimulus conditions (middle) firing rates during stimulation are only slightly higher than that before stimulus onset. Stimulus offset leads to a strong suppression of activity in all stimulus conditions tested, lasting for about 1 s.

With Bayesian reconstruction the current stimulus configuration can be estimated based on the neurons' firing rates. As an illustration, Fig. 4 shows the probability distribution of neural responses to different stimuli,  $P(\mathbf{n}|x)$ . The cell fires most vigorously to horizontal grating stimuli (i.e. vertical motion directions). Due to the cell's high selectivity, only at high firing rates (above 20 Hz) the actual stimulus orientation



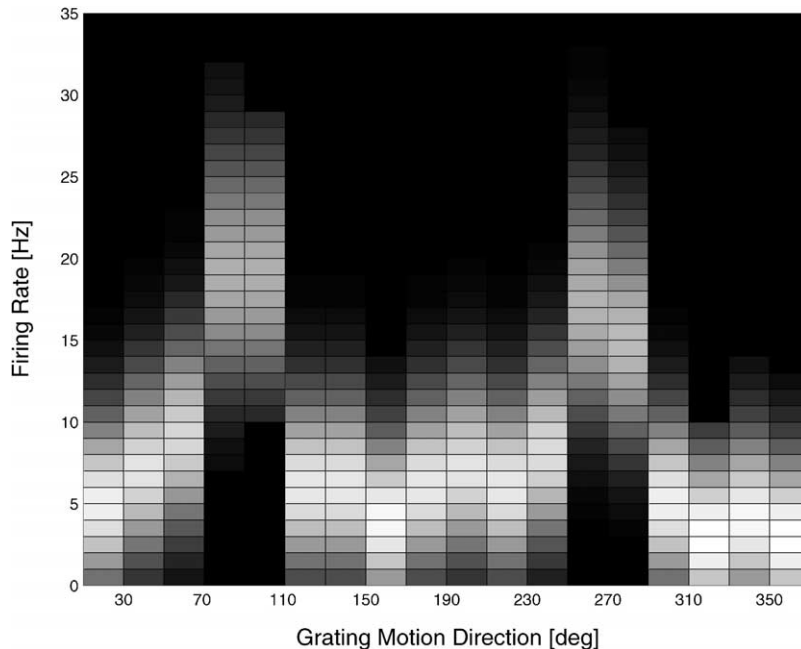


Fig. 4. Bayesian analysis of responses of neurons in rat cortical area V1 to drifting gratings. The conditional probability estimate (gray-scale coded with lighter colors indicating higher probability values) of response (depicted along the *y*-axis as mean firing rate in Hz) of a single neuron to a given stimulus direction (*x*-axis). For each of 18 directions, a Poisson distribution with the same mean as the recorded response of the cell, normalized to have an area equal to 1, was used as an estimate of the conditional probability distribution,  $P(\mathbf{n}|x)$ . Note that the actual stimulus orientation can be estimated with an acceptable error margin only at high firing rates (approx. 20 Hz and higher). This analysis is based on the same data as that of Fig. 3 for illustrative purposes.

can be estimated with an acceptable error margin. Intuitively, the quality of stimulus estimation should improve as increasing numbers of neurons are combined for this analysis. Fig. 5 illustrates this point, showing that the minimal square error of stimulus orientation decreases with population size.

Fig. 5 also shows that good estimation accuracy is already achieved with a small number of neurons. However, this result is based on an analysis of the whole response period. As Eq. (1) shows, resolution depends in a linear fashion on the amount of time the cells have at their disposal. With less time available, reliable coding can only be achieved with larger number of neurons.

#### 4. Summary and conclusions

Our experiments demonstrate the feasibility of multi-site recordings in the rat visual cortex with two kinds of micro-machined multi-site recording probes. Importantly, spike activity was successfully recorded throughout cortical depth, and visually triggered,

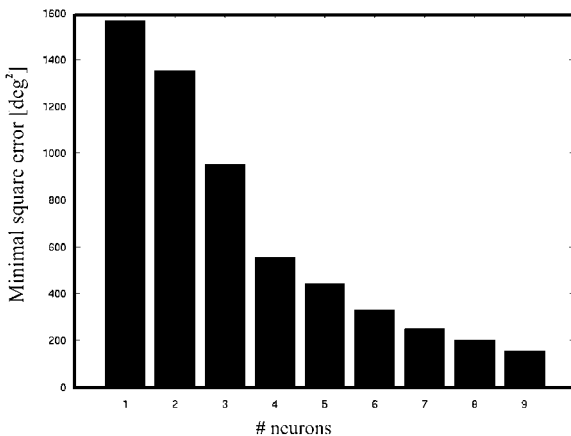


Fig. 5. Application of the Bayesian reconstruction algorithm to assess the minimum square error a population of cells makes in the reconstruction of the presented stimulus. Reconstruction error drops with an increasing number of cells in an exponential fashion. A MAP estimator was used for this analysis, because this estimator is quite robust against noisy fluctuations in the cells' activity, for it will still reconstruct the stimulus under noisy circumstances, unless noise becomes overall dominant. Thus, the reconstruction exhibits both robustness against noisy inputs and high degrees of accuracy.

orientation- or direction-tuned responses provide evidence for the integrity of the tissue after probe insertion. Thus, the activity of many cells can be simultaneously monitored with a minimal number of cortical penetrations.

We have shown that Bayesian reconstruction and the MAP estimator based on responses of small groups of neurons can yield good reconstruction results. However, data was sampled over long time intervals for this analysis. Eq. (1) implies that the resolution achieved by a population of cells depends, in a linear fashion, on the amount of time the cells have at their disposal. Thus, shorter analysis periods have to be traded for larger neural numbers, if coding accuracy is to be maintained. Furthermore, each additional stimulus feature adds a new dimension to the stimulus space, requiring a multiplication of the number of coding neurons.

How neural population size can compensate for shorter analysis intervals is one of the objectives of our future research. This will have to take deviations from Poisson assumptions into account, consider the role of neural correlations and exploit the fine temporal structuring of responses to address the question how multiple stimulus dimensions can be rapidly represented by one set of active neurons in rat visual cortex.

### Acknowledgements

Thanks are due to Sigrun Wicker and Barbara Klein for technical assistance. Multi-site recording probes were kindly provided by the University of Michigan Center for Neural Communication Technology sponsored by NIH/NCRR Grant P41 RR09754. Help and advice on the use of probes by Drs. Jamille Farraye Hetke, Chris Ellinger,

Steven M. Bierer (University of Michigan) and Tim Blanche (University of British Columbia, Vancouver) have been invaluable for our experimental work. U. Hofmann was supported by a Feodor-Lynen-Fellowship and EU Grant IST-1999-10073, J.M. Bower, G.T.A. Kovacs, M.D. Hills and D.T. Kewley by NSF Grant #PC147129-1, W.A. Freiwald and H. Stemmann by a FNK Grant of the University of Bremen. Experimental and theoretical work was supported by SFB 517 “Neurocognition”.

## References

- [1] D.J. Anderson, K. Najafi, S.J. Tanghe, D.A. Evans, K.L. Levy, J.F. Hetke, K.D. Wise, J.J. Zappia, Batch-fabricated thin-film electrodes for stimulation of the central auditory system, *IEEE Trans. Biomed. Eng.* 36 (1989) 693–704.
- [2] S.L. BeMent, K.D. Wise, D. Anderson, K. Najafi, K. Drake, Solid state electrodes for multichannel multiplexed intracortical neuronal recording, *IEEE Trans. Biomed. Eng.* 33 (1986) 230–241.
- [3] C.W. Eurich, S.D. Wilke, Multi-dimensional encoding strategy of spiking neurons, *Neural Comput.* 12 (2000) 1519–1529.
- [4] S.V. Girman, Y. Sauvé, R.D. Lund, Receptive field properties of single neurons in rat primary visual cortex, *J. Neurophysiol.* 82 (1999) 301–311.
- [5] U.G. Hofmann, D.T. Kewley, J.M. Bower, Inserting silicon-based electrodes in cerebral cortex: a study of dimpling, 2001, unpublished observations.
- [6] S.M. Kay, *Fundamentals of Statistical Signal Processing*, Prentice-Hall, Englewood Cliffs, NJ, 1993.
- [7] D.T. Kewley, M.D. Hills, D.A. Borkholder, I.E. Opris, N.I. Maluf, C.W. Storment, J.M. Bower, G.T.A. Kovacs, Plasma-etched neural probes, *Sensors Actuators A* 58 (1997) 27–35.
- [8] K. Najafi, K.D. Wise, An implantable multielectrode array with on-chip signal processing, *IEEE J. Solid-State Circ.* 21 (1986) 1035–1044.
- [9] M.A. Paradiso, A theory for the use of visual orientation information which exploits the columnar structure of striate cortex, *Biol. Cybernet.* 58 (1988) 35–49.
- [10] S.D. Van Hooser, U.G. Hofmann, D.T. Kewley, J.M. Bower, Relationship between field potentials and spike activity in rat S1: multi-site cortical recordings and simulations, *Neurocomputing* 32–33 (2000) 591–596.
- [11] S.D. Wilke, C.W. Eurich, Representational accuracy of stochastic neural populations, *Neural Comput.* 14 (2001) 155–189.
- [12] K.D. Wise, K. Najafi, Microfabrication techniques for integrated sensors and Microsystems, *Science* 254 (1991) 1335–1342.
- [13] K. Zhang, T.J. Sejnowski, Neuronal tuning: to sharpen or broaden? *Neural Comput.* 11 (1999) 75–84.
- [14] K. Zhang, I. Ginzburg, B. McNaughton, T. Sejnowski, Interpreting neuronal population activity by reconstruction: unified framework with application to hippocampal place cells, *J. Neurophysiol.* 79 (1998) 1017–1044.
- [15] A. Etzold, W. Freiwald, H. Stemmann, C.W. Eurich, Population coding of orientation tuning in the rat visual cortex: stimulus reconstruction and Fisher information, in preparation.

## **14. Appendix B: Relevante technische Berichte des EU-Projektes VSAMUEL**

### **14.1. Workpackage 1: Management**

Deliverable 1.1 Nutzerbedürfnisse und Spezifikationen

### **14.2. Workpackage 2: Siliziumsonden und Verbindungstechnik**

Deliverable 2.1: 32 Kanalsonden

Deliverable 2.3: 64 Kanalsonde

Deliverable 2.2: 32 Kanalverbindung

Deliverable 2.4: 64 Kanalverbindung

### **14.3. (Workpackage 3: Verstärkertechnik)**

### **14.4. Workpackage 4: Datenaufnahmesystem**

Deliverable 4.1: 32 Kanalsystem

Deliverable 4.2: 64 Kanalsystem

Deliverable 4.3: 128 Kanalsystem

# **PROJECT DELIVERABLE REPORT**

## **INFORMATION SOCIETIES TECHNOLOGY (IST) PROGRAMME**



Project No. IST-1999-10073

Project acronym: VSAMUEL

Work Package No. 1  
Deliverable 1.1  
Update on User Needs and Specifications  
32 Recording Sites

February 2001

Project Title:  
Development of a Versatile System for Advanced Neuronal Recordings with Multi-site Microelectrodes

Report prepared by: U.G. Hofmann, ISIP, Med. University of Lübeck

## **Cerebellar Probes**

### Aims

- 1) Record from 3-5 PCs/Gocs per applicable site along the PF beam at the same time.
- 2) Record activity in the three layers of the cerebellar cortex.

### Anatomy

**Purkinje cells:** Soma ~20-30  $\mu\text{m}$  diameter in PC layer. Dendritic tree ~350  $\mu\text{m}$  in length in molecular layer, ~40  $\mu\text{m}$  from pia matter and 350  $\mu\text{m}$  wide across PF axis.

recording distance: 40 - 400  $\mu\text{m}$  from surface. No limitation along parallel fiber axis

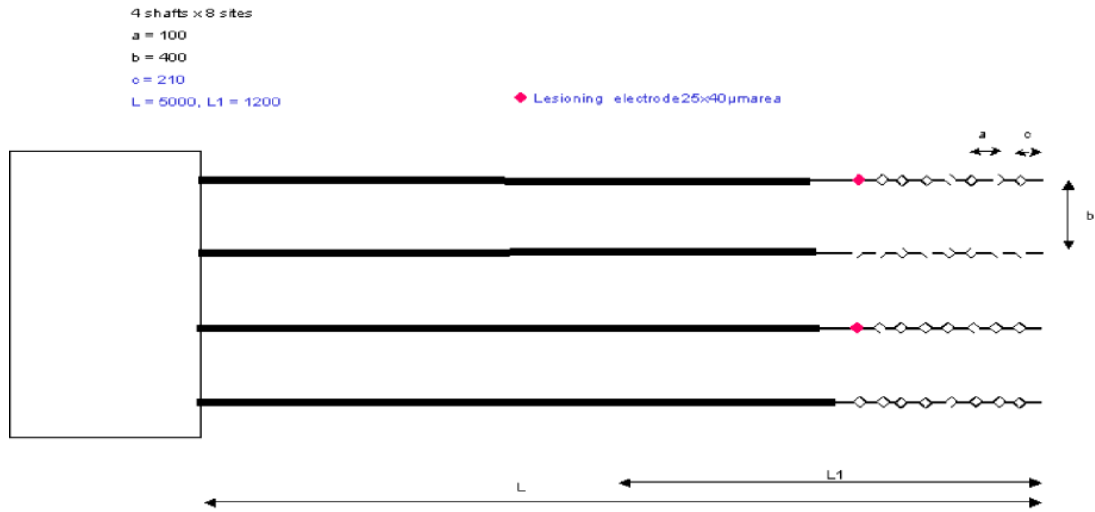
**Golgi cells:** Soma ~30  $\mu\text{m}$  diameter in grc layer. Dendritic tree ~200  $\mu\text{m}$  (forming a cylinder), mainly in molecular layer.

recording distance: 400 -1000  $\mu\text{m}$  from surface. Minimal spacing between Gocs along PF axis: 200  $\mu\text{m}$

- Purkinje Cells (PC): soma (~ 20-30  $\mu\text{m}$  diameter Dieudonne) located in PC layer. Dendritic tree in molecular layer: 350  $\mu\text{m}$  in length goes ~ 40  $\mu\text{m}$  from pial matter) and 350  $\mu\text{m}$  wide across // fibers axis. Only 9-35  $\mu\text{m}$  thickness regularly spaced: 1000 PC per  $\text{mm}^2$ .
- Parallel fibers extend for several mm: not limited in this direction, could use more than one probe in the future to cover the whole length.
- Can expect to pick up PC (ss and cs): between 40 (very small amplitude, see Nicolelis p. 84) and 400  $\mu\text{m}$  from the surface. Recording sites should cover this range.
- GC soma located at upper part of granule cell layer. Average size of dentritic tree: 200  $\mu\text{m}$  (forming a cylinder) mainly in the molecular layer. ~ 30  $\mu\text{m}$  for soma in granule cell layer. GCs with a spacing < 200  $\mu\text{m}$  can share common mossy fiber input Reinoud used 300  $\mu\text{m}$  between GC in his model (Minimum interspacing to avoid dimpling effect 100  $\mu\text{m}$ ). Tuning distance 50-150  $\mu\text{m}$  (vertical distance from smallest to max. signal amplitude for one GC). During our experiments GCs were recorded between 400-1000  $\mu\text{m}$ . A site at 600-700  $\mu\text{m}$  should permit recording of one GC. Only one cell is expected per shaft.

### Design Wishes

- 1) 4 shafts of 5 mm length, carrying 8 sites.
- 2) Site c/c distance: 100  $\mu\text{m}$ .
- 3) Shaft c/c distance: 400  $\mu\text{m}$ .



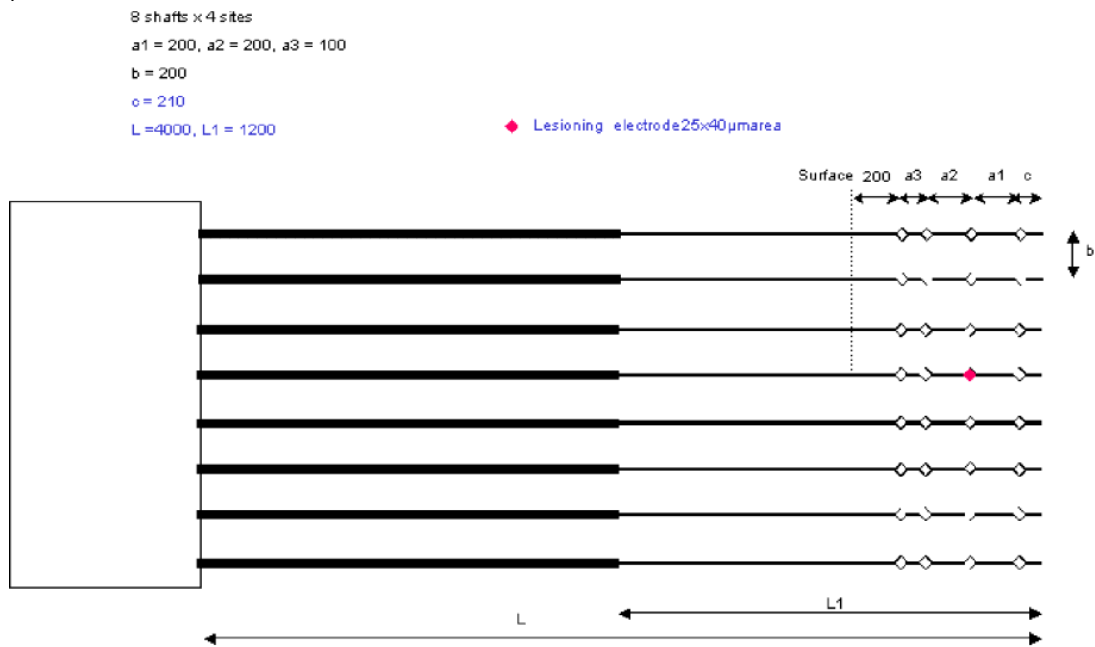
Erik 2

**8 shafts.** Each of the shafts supporting **4 recordings sites** at determined distance from each other.

Proposed distance between shafts: **200  $\mu\text{m}$**  so that the total length of the probe along the parallel fibers axis

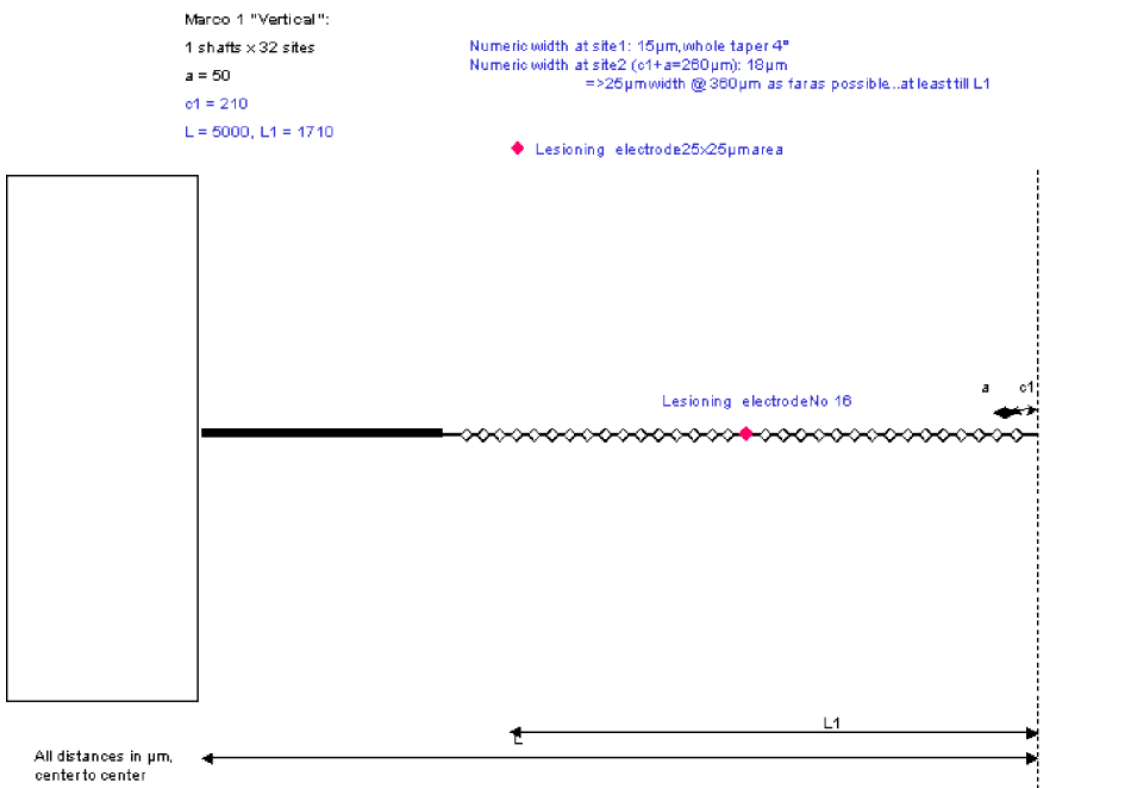
would be 1560  $\mu\text{m}$ , including the electrodes (assuming a diameter of 20  $\mu\text{m}$ ).

Position of recording sites: 4 sites per shaft. Starting 200  $\mu\text{m}$  below pial surface. Sites at 200-300-500-700  $\mu\text{m}$  should cover best the PC dendritic tree and the GCs. (spacings **100-200-200  $\mu\text{m}$** )

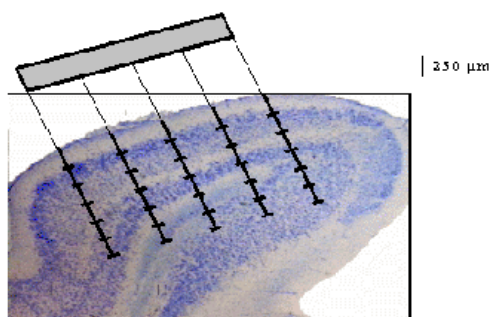


## Cortical Probes

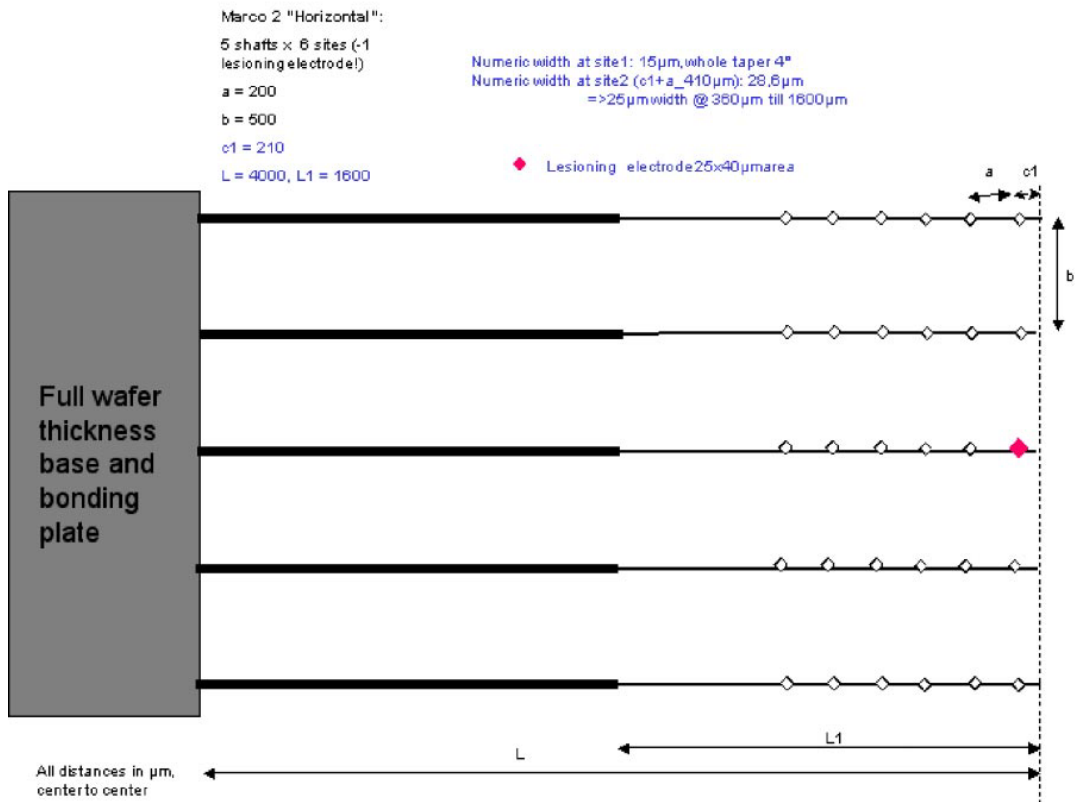
**Vertical Recordings.** Record activity simultaneously at different depths in the olfactory cortices. The probes currently in use (16 channels-50 µm spacing) allow for a partial coverage of the thickness of the entorhinal cortex (1.5 mm) and piriform cortex (1.4 mm). The vertical probes will be designed with 32 recording sites separated by 50 µm on the same shaft to record activity in all layers of the cortex. The results will be studies with the Current Source Density (CSD) analysis that allows to identify the spatial and temporal distribution of the active events (current sinks and sources) within the cortex. The inter-lead distance of 50 µm is necessary for a precise definition of the current sinks and sources (see Biella and de Curtis, J Neurophysiology 83: 1924, 2000). The probe shaft should be as long as possible, ideally 7 mm, to allow positioning in the isolated brain preparation additional stimulating or recording electrodes. The two distal leads could be utilized for passing current and mark the tissue with a lesion.



**Horizontal Recordings.** Record activity simultaneously at different sites in the entorhinal



cortex with multi-shaft probes (30 recording sites). Six recording leads positioned at different vertical depths separated by 200-250  $\mu\text{m}$  on each shaft will allow to record activity from each cortical site in different layers, covering the cortical depth (1250-1500  $\mu\text{m}$ ). A 500  $\mu\text{m}$  separation between each shaft ( $n=5$ ) will allow to record from separate positions along the medio-lateral dimension of the ERC (see figure). The experiments will be addressed at analyzing fast oscillatory activity (gamma activity) induced by carbachol and generated by functional modules, hypothetically separated by 600  $\mu\text{m}$  (see Dickson et al., J. Neuroscience 20: 7846, 2000).



## **Peripheral Nerve Probes**

SMI: Ken Yoshida

### Aims

Biophysical measurements of the electrical properties of the nerve fascicle

    Endoneurial matrix and Perineurium impedance (4-point impedance measurements)

Physical measurements of the intrafascicular electric field distribution from single active axonal units

    Effect of electrode entry/exit points

    Effect of active site depth (distance from perineurium)

Determine effect of chronic implantation of silicon structures in peripheral nerve

    Histological changes to the nerve

    Durability of silicon structures *in-vivo*

### Peripheral Nerve Anatomy

Fibre Diameters 1-20 $\mu\text{m}$

Total fascicular diameter 1-5mm

Internodal spacing 0.5~1.8mm (A-II) and 0.2~0.7mm (A-III)

Axonal spiral undulation: 40-80 $\mu\text{m}$  (Amplitude), 140-160 $\mu\text{m}$  (Wavelength)

### Electrode Design

Active (Recording/Low current Stimulation) site geometry 20x40 $\mu\text{m}$  – Pt, Ir, IrO<sub>x</sub>, or TiN

Spaced ~100 $\mu\text{m}$  along the length of the shaft, clustered in groups of at least 4

    to allow placement of at least 2 active sites between two consecutive Nodes of Ranvier of a single fibre.

Active site cluster placement: mid-shaft (if single shaft), tip, mid-shaft, hilt (if multiple shaft)

Shaft diameter ~25 $\mu\text{m}$

    on the order of the size of the largest nerve fibre

Inter-shaft distance ~500 $\mu\text{m}$

    to enable at least 2 shafts can be placed within the nerve fascicle

    >> 2-4 axonal diameters to prevent overlap of inter-shaft units

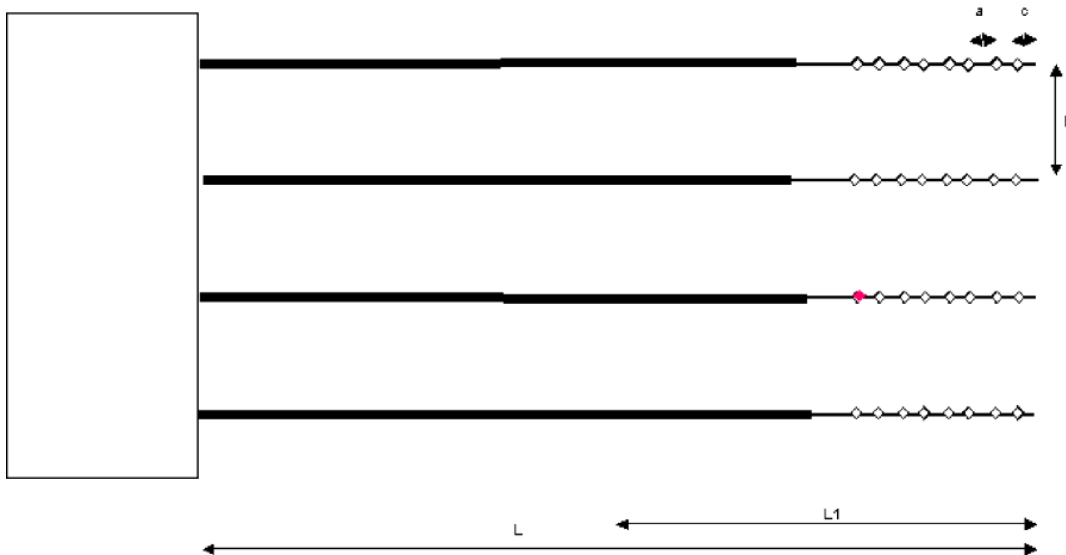
Shaft length ~10-15mm

    The typical implant length of metal LIFEs which place active sites away from fascicle entry-exit points

Able to mark sites in tissue.

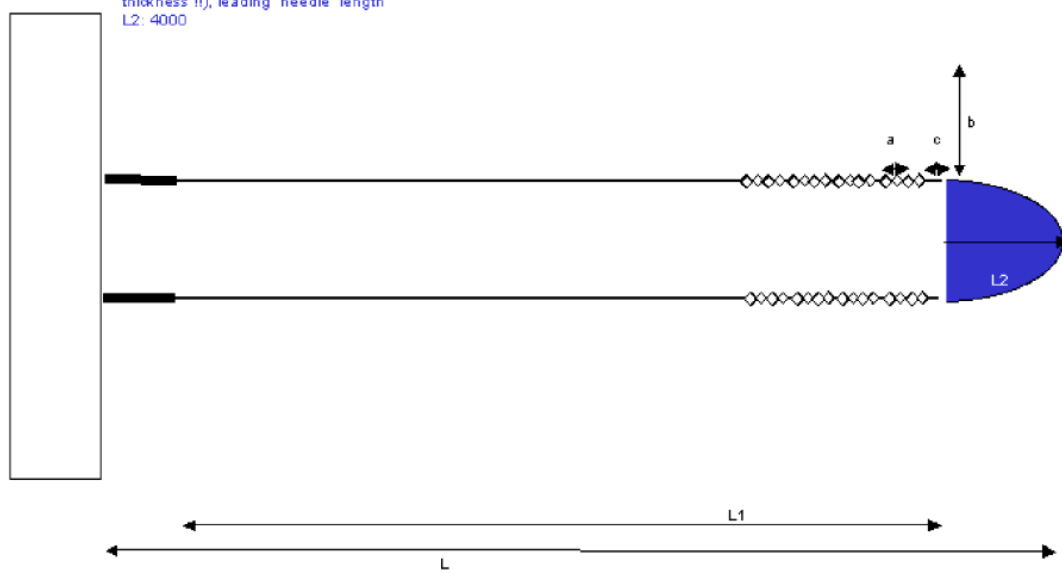
Ken 1:  
4 shafts x 8 sites  
 $a = 100$   
 $b = 500$   
 $c = 210$   
 $L = 15000, L1 = 1200$

◆ Lesioning electrode:  $25 \times 40 \mu\text{m}$  area



Not realized within this run, due to process incompatibilities!

Ken 2 "Long term peripheral":  
2 shafts x 16 sites  
 $a = 100$   
 $b = 500$   
 $c = 210$   
 $L = 15000, L1 = 10000$  (silicon cable thickness !!), leading "needle" length  $L_2: 4000$



## Anatomical and Technical Test Probes

### Aims

- 1) Record from deep cerebellar nuclei or pontine nuclei from rat
- 2) Show triangulation/position estimation of single neuron/source

### Anatomy



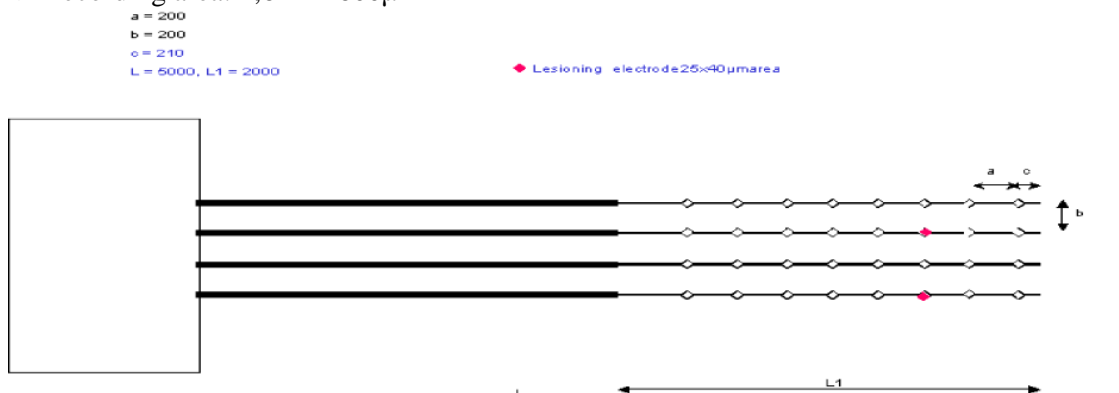
- 1) Deep cerebellar nuclei: 4-6mm below pial surface,  $0,5 \times 0,5 \times 1,5$  mm volume (->E3 DCN)  
 Pontine Nuclei: ca. 10mm below pial surface, Region of Interest approx.  $1 \times 1 \times 2$  mm volume (->Uli1)
- 2) Triangulation/source localization: Recordings with sites close to each other (ca. 50 $\mu$ m) display the spike of one neuron on up to 3 electrodes. It was shown, that with this information, at least the depth (vertical) coordinate of the source was determinable. Extending the site distance horizontally leads to data interpretable in the x,y plane as well. A tight array is needed for this type of source localization.

### Design Wishes

#### DCN:

Regular array, intersite distance: 200 $\mu$ m, intershaft distance 200  $\mu$ m, 4 shafts, 8 sites each.

-> Recording area: 1,6mm\*600 $\mu$ m



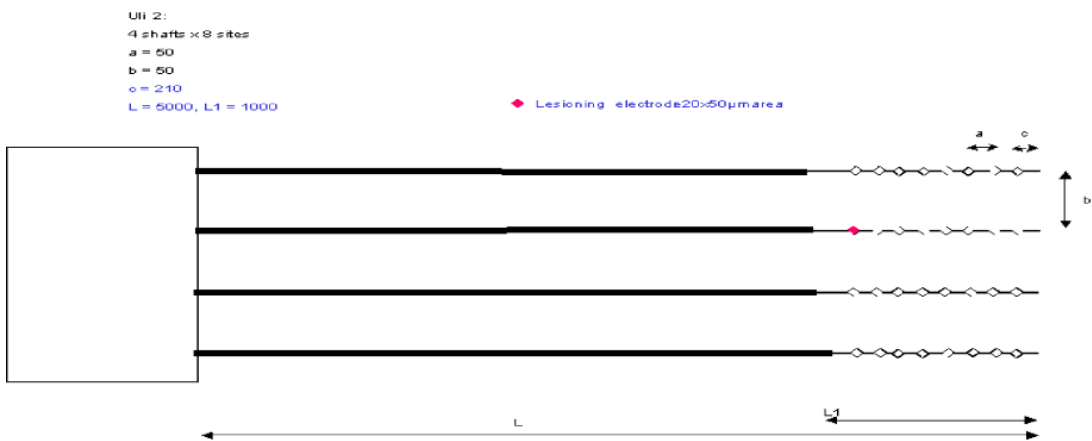
#### Pontine Nuclei:

Intersite distance: 100 $\mu$ m, intershaft distance: 250  $\mu$ m, 4 shafts, 8 sites each, 10mm overall length -> Recording area: 700 $\mu$ m\*750 $\mu$ m



Triangulation probe:

Intersite distance: 50 μm, Intershaft distance: 60-70 μm, 4 shafts, 8 sites each -> Recording area: 350 μm \* 150 μm



### Overview: Run1, 32 channels

Ident. No	Prong sites	Site spacing /μm	Prong spacing /μm	Overall length /μm	Thin length /μm
M1	1 x 32	50	-	7000	1860
M2	5 x 6	250	500	10000	1700
E1	4 x 8	100	400	5000	1200
E2	8 x 4	≈200	200	4000	1200
E3	4 x 8	200	200	5000	2000
K1	4 x 8	100	500	15000	1200
U1	4 x 8	100	250	10000	4000
U2	4 x 8	50	60	5000	1000

# **PROJECT DELIVERABLE REPORT**

## **INFORMATION SOCIETIES TECHNOLOGY (IST) PROGRAMME**



Project No. IST-1999-10073

Project acronym: VSAMUEL

Work Package No. 2  
Deliverable 2.1  
Custom designed 32 microelectrode probes

Date of Delivery May 2001

Project Title:  
Development of a Versatile System for Advanced Neuronal Recordings with Multi-site  
Microelectrodes

Report prepared by:  
Peter Norlin and Maria Kindlundh  
ACREO AB

## 1. Background

The objective of the project VSAMUEL is to develop a system for the recording of multiple signals from neural tissue, and to demonstrate the system in different application experiments [1-2]. The complete system consists of the following building blocks (figure 1.1):

- Micromachined fork-like silicon probes with multiple recording sites
- Pre-amplifier/amplifier hardware
- A connector solution, interfacing the miniaturized probes with the pre-amplifier
- Data acquisition/analysis hardware and software

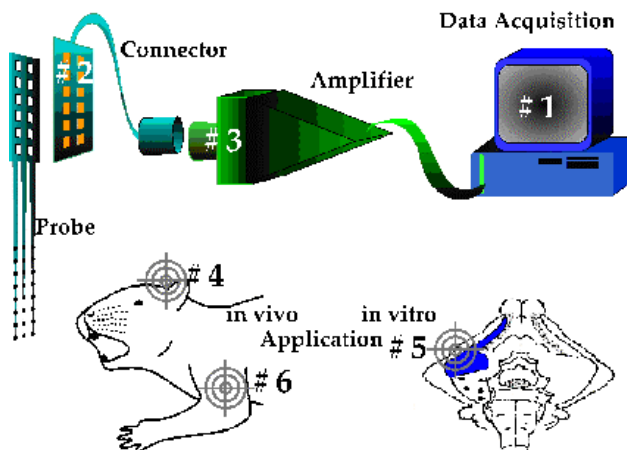


**Figure 1.1:** Overview of the project VSAMUEL. Counter clockwise from top right: #1 - Data acquisition system, hard- and software (Med. University of Lübeck, ISIP). #3 - Discrete and modular multi-channel amplifier (Thomas RECORDING). #2 - Custom designed connectors and passive batch fabricated multi-site microelectrode probes (ACREO AB). “Bull’s eyes” point to the area of application experiments: #4 - Cerebellum (Univ. of Antwerp), #5 - Cortex (INN Carlo Besta), #6 - Peripheral nerves (Aalborg University).

It is believed that a key to the understanding of the nervous system is to make *simultaneous* observations of the activity of a *large number* of cells.

One would thus like to insert a large number of recording sites – and the corresponding number of electrical “wires” – into the neural tissue, at the same time as the smallest possible tissue damage is desired. Silicon micromachining (Micro System Technology, MST), which is capable of producing structural

elements down to 1  $\mu\text{m}$  dimensions, and is inherently well suited for array based designs, has been employed in the VSAMUEL project to manufacture neural probes with several recording sites distributed on thin and narrow silicon shafts.

The purpose of this report is to document the Deliverable 2.1 “Custom designed 32 microelectrode probes” of VSAMUEL’s Work Package no. 2.

## 2. Design of silicon probes

### 2.1 General

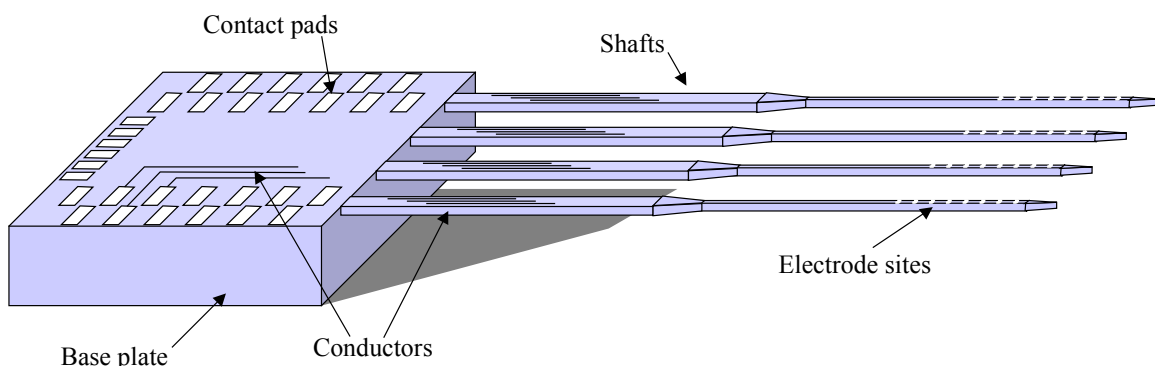


**Figure 2.1:** Schematic drawing of the probe structure (not to scale).

Figure 2.1 shows a schematic overview of the probe structure. The main design elements are:

- Thin, narrow and pointed Si shafts for penetration and insertion into the neural tissue.
- Microelectrode sites of Ir distributed over the frontal end of the shafts.
- A thicker Si base plate as a support for the contact pads, and to allow easy handling of the probes with tweezers.
- Metal (Au) contact pads for external electrical interconnection using ultrasonic wire bonding.
- Fine and narrowly spaced metal (Au) conductor traces to connect the electrode sites with the bond pads.

### 2.2 Layout

The layout of the probes (figure 2.2) was made in accordance with the needs of the project’s neuroscience groups [3]. Eight different probe designs were included (table 2.1). Nominally, at 100 % yield, each silicon wafer will produce 224 probes.

For all device designs (except M1) the shaft widths are 25  $\mu\text{m}$  at the active section of the shaft. The shaft width at the base plate is 75 - 200  $\mu\text{m}$  depending on the design. The shaft thickness is targeted to ~25  $\mu\text{m}$ , but can be varied with the wafer specification. The recording sites are 10  $\mu\text{m} \times 10 \mu\text{m}$  and the tip taper angles are 4°. A full documentation of the CAD-design is available in [4]. A summary of technical data and selected design drawings are appended at the end of this report.

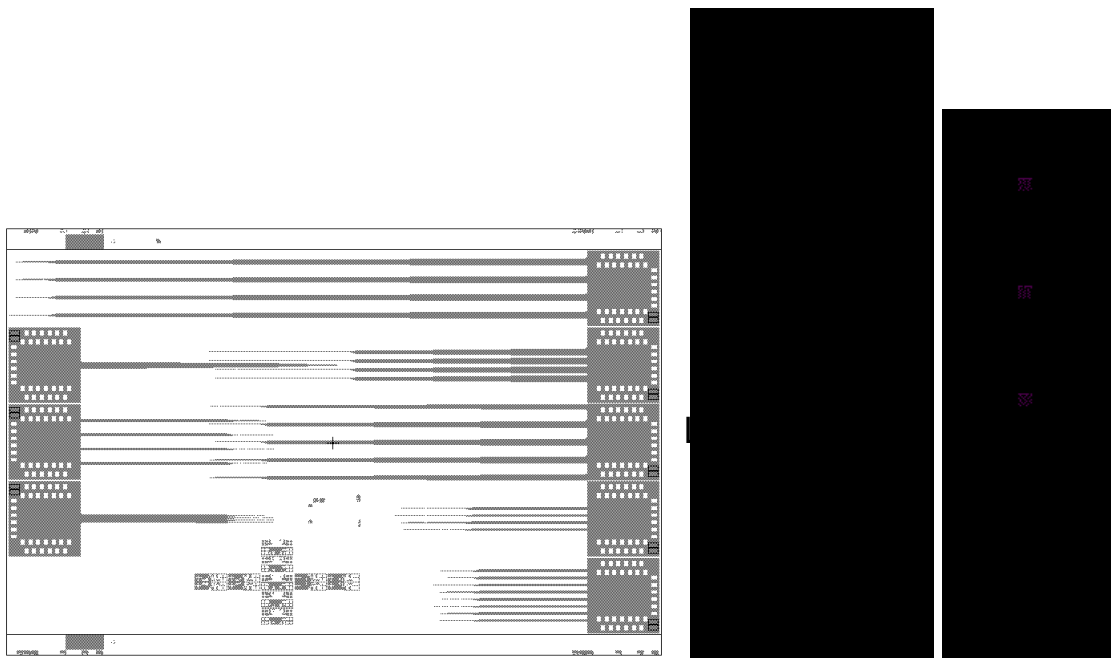


**Figure 2.2:** Layout of microelectrode probes.

**Table 2.1:** Selected design parameters of the eight probe designs

Design name	Number of shafts and recording sites	Shaft length (L), $\mu\text{m}$	Site c/c distance (a), $\mu\text{m}$	Shaft c/c distance (b), $\mu\text{m}$
M1 "Vertical"	1 shaft x 32 sites	7 000	50	--
M2 "Horizontal"	5 shafts x 6 sites	10 000	250	500
E1	4 shafts x 8 sites	5 000	100	400
E2	8 shafts x 4 sites	4 000	200, 200, 100	200
E3 "DCN"	4 shafts x 8 sites	5 000	200	200
K1	4 shafts x 8 sites	15 000	100	500
U1	4 shafts x 8 sites	10 000	100	250
U2	4 shafts x 8 sites	5 000	50	60

### 2.3 Manufacturing process

The silicon device manufacturing process is outlined in figure 2.3. Silicon-on-insulator (SOI) substrates (525  $\mu\text{m}$  Si/1.5  $\mu\text{m}$  SiO<sub>2</sub>/20  $\mu\text{m}$  Si or 374  $\mu\text{m}$  Si/1  $\mu\text{m}$  SiO<sub>2</sub>/25  $\mu\text{m}$  Si) were used, with the buried oxide layer acting as an etch-stop for the two deep silicon etches. The essential process steps are:

- PECVD silicon nitride thin-film deposition for isolation layers.
- Reactive Ion Etching (RIE) of isolation layers.
- Evaporation of Ti/Au and Ti/Ir for connectors and electrode sites, respectively.
- Step-and-repeat projection lithography, and lift-off patterning of metals (down to 1  $\mu\text{m}$  linewidth and spacing).
- Inductively coupled plasma deep reactive ion (ICP DRIE) Si etching on both sides of the wafer to form the probe shafts.
- Double-sided mask alignment for the lithography of the backside etch.
- Thick spin-on photo resist deposition (~15  $\mu\text{m}$ ) for etch masks during the DRIEs, and to protect the wafer front side during the final process steps.
- Release of probe shafts by etching of buried oxide in BHF.

The practical challenges of this process are e.g.

- The handling of wafers with - in the end of the process - long, thin and fragile probe shafts.
- The fine linewidths required, in order to get a large number of measurement sites distributed on as narrow probe shafts as possible.
- The risk of excessive bending of the probe shafts due to stress in the thin film layers.

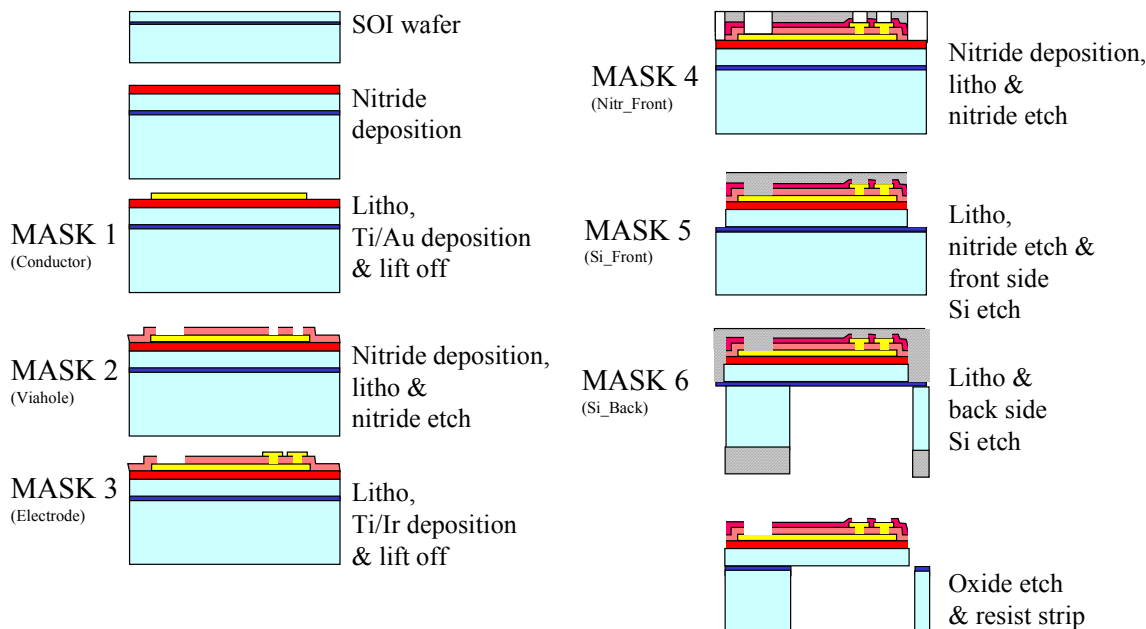


**Figure 2.3:** Schematic wafer cross sections illustrating the manufacturing process (not to scale).

### 3. Results

The work package has delivered prototypes at a number of instances, and with an increasing level of sophistication:

1. A first test-batch (# C225) with mechanical probes (no electrodes), designed before we had detailed knowledge of the requirements of the neuroscience groups (ready September 2000). Although the yield was very low, it showed the viability of the concept and gave us processing experience.
2. A second test-batch (# C247) with mechanical probes, this time designed according to the requirements of the neuroscience groups. Much better yield was achieved, and 97 probe chips were delivered to four partner groups in December 2000.
3. A test-batch (# C240) with recording electrodes on solid silicon (no shafts). Chips mounted and wire-bonded on PC-boards were delivered to three partners in January and early February 2001. These test chips have been used for electrode characterization studies [5].
4. The first "real" devices (# C250) with both micromachined probes and electrodes, mounted and wire-bonded on flexible printed circuits, were delivered to three groups in March 2001, and in an additional round in May 2001.

Figures 3.1 – 3.5 show some highlights of the accomplished micromachining results.

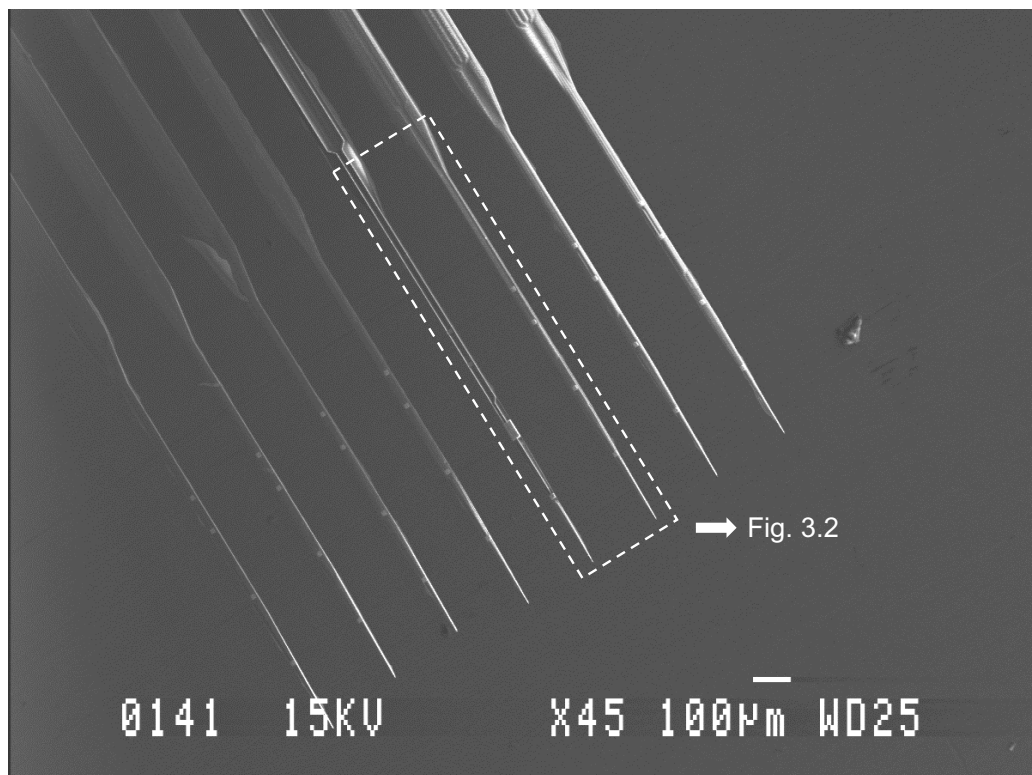


**Figure 3.1:** Scanning electron micrograph of silicon micromachined probes with 32 microelectrodes.

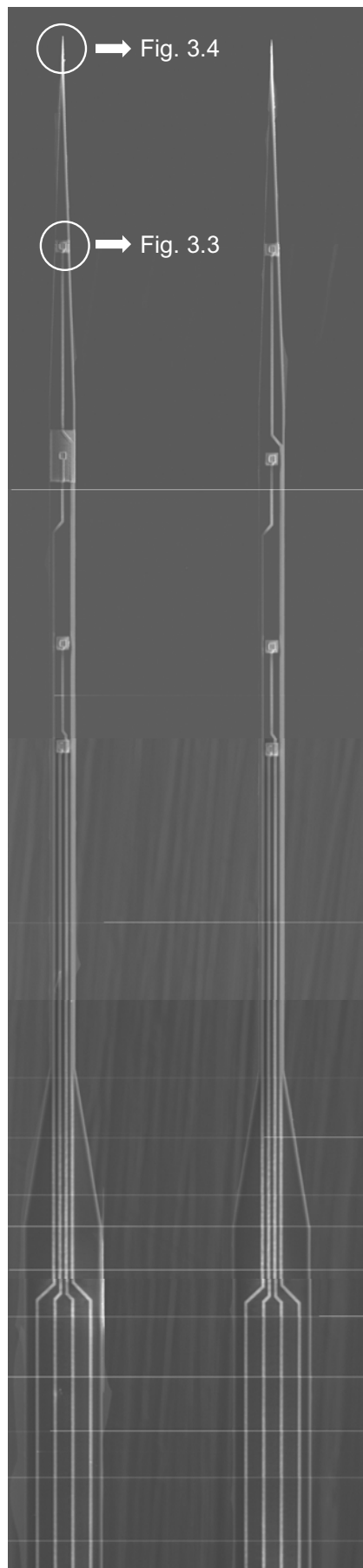


**Figure 3.2:** Scanning electron micrograph of two Si probe shafts with four Ir electrodes and Au conductor traces.

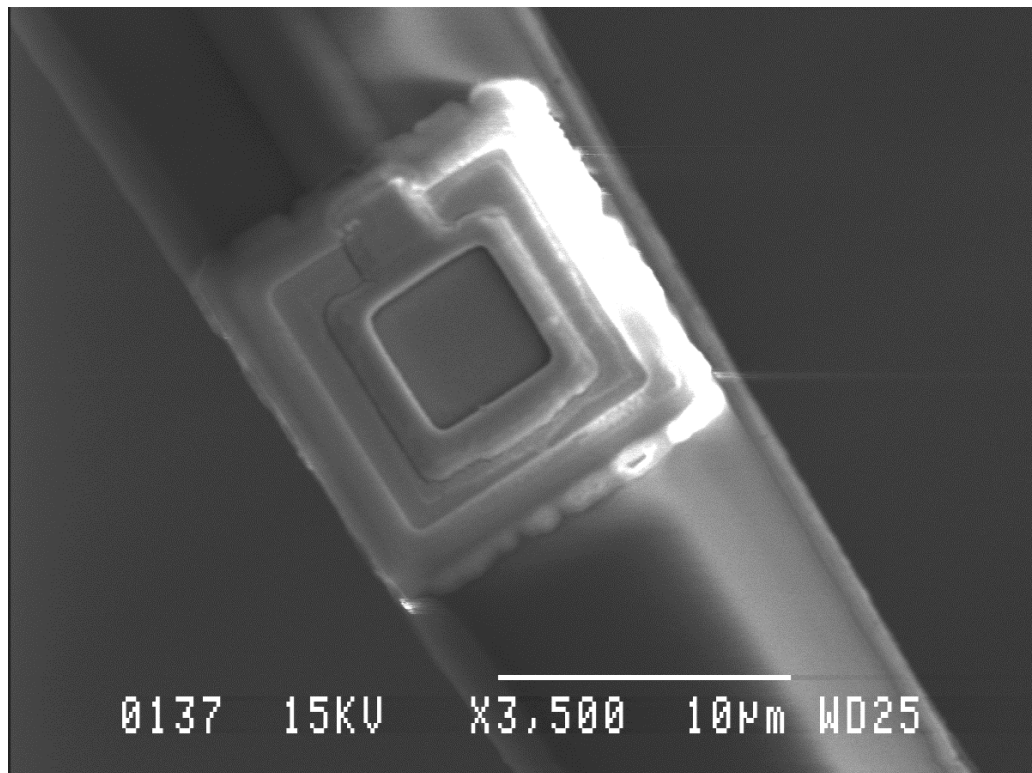


**Figure 3.3:** SEM close-up of one of the  $10 \mu\text{m} \times 10 \mu\text{m}$  Ir recording electrode sites.

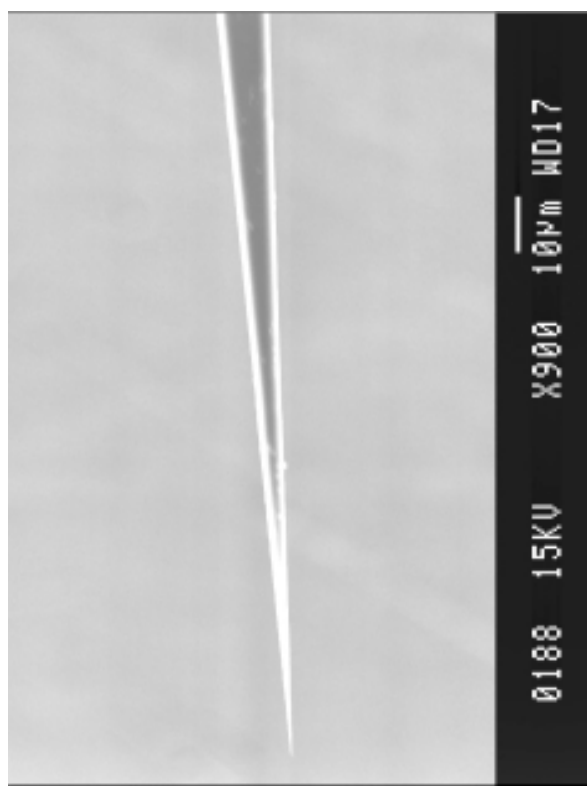


**Figure 3.4:** SEM close-up of probe tip designed with  $4^\circ$  taper angle.

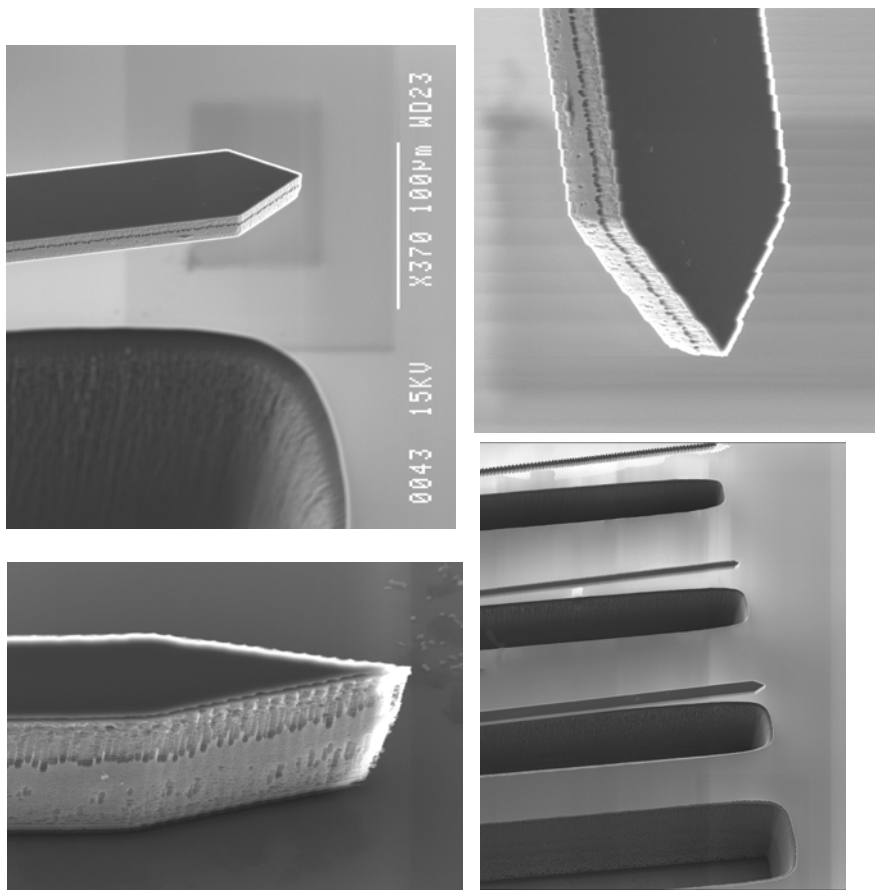


**Figure 3.5:** Scanning electron micrographs of test samples with DRIE etched silicon probe shafts (thickness 25 µm). Note: lateral dimensions are not identical to the final device design).

In order to interface the probe chips electrically, an interconnect and packaging scheme has been designed and implemented. A flexible printed circuit (FPC) solution is employed, allowing for flexible and precise positioning of the recording sites using micromanipulators. The probes which are supplied to the user groups are mounted on the FPC connectors, wire-bonded and glob-top protected as shown in figures 3.6 – 3.7. The design and manufacture of the connector has been reported in [6].



**Figure 3.6:** A silicon probe chip mounted on a flexible printed circuit. The left side of the printed circuit is designed to mate with the pre-amplifier of Work Package no. 3.



**Figure 3.7:** A set of probes ready to be delivered to a user group. The probe chips are mounted on flexible printed circuit substrates, wire-bonded, and glob-top protected.

A simple measurement set-up (figure 3.8) was used to verify the electrical functionality of the probes immediately after processing. A measurement cell consisting of a Pt wire electrode and a VSAMUEL probe immersed in a 0.9 % NaCl electrolyte was excited with sinusoidal input signal ( $u_1$ ). The resulting ac current ( $i$ ) through the cell was recorded as the ac voltage drop ( $u_2$ ) over a resistance ( $R$ ) in series with the cell (figure 3.8).

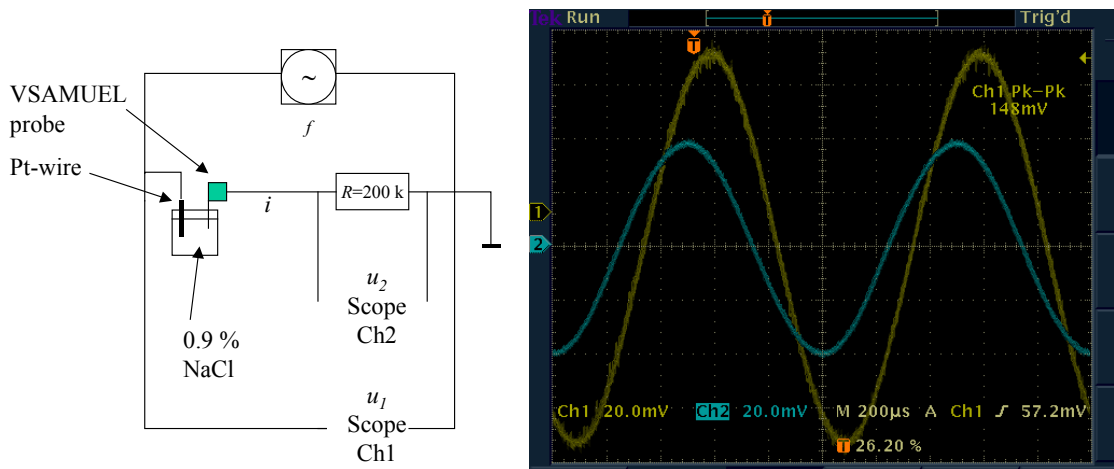


**Figure 3.8:** Measurement setup (left), and oscilloscope screen with recorded signals (right).

Qualitatively we have been able to verify a satisfactory process yield (including flexible printed circuit, wire-bonding and glob-topping), where a majority of the tested microelectrode recording sites transmits

electrical signals. It is generally also possible to identify the few larger electrodes (“lesioning electrodes”,  $\sim 1000 \mu\text{m}^2$  area) included in the design, by their larger signal response.

Quantitatively, the electrode impedance is a parameter of prime interest, since it determines the thermal (Johnson) noise and thus the ability to record small neural signals. Although more in-depth electrode characterization studies are in progress at Aalborg University [5], these crude initial measurements indicate that the magnitude of the as-processed electrode impedance typically lies in the  $1 \text{ M}\Omega$ -range @ 1 kHz (table 3.1). (Note that the excitation voltage is orders of magnitude larger than typical neural signals though.)

The impedance values are comparable to, or even lower than those of micromachined probes obtained from other sources are [7]. Preliminary experimental results further indicate that certain cleaning procedures potentially could lower the electrode impedances down to the  $300 \text{ k}\Omega$ -range.

**Table 3.1:** Typical measurement data ( $10 \mu\text{m} \times 10 \mu\text{m}$  Ir electrodes)

<b>Test conditions</b>		<b>Measured quantity</b>	<b>Typical value</b>
Excitation voltage, $u_1$	150 mV (pk-pk), sinus	Current, $i = u_2/R$	$\sim 100 \text{ nA}$ (pk-pk)
Excitation frequency, $f$	1 kHz	Magnitude of impedance, $z = (u_1/u_2 - 1)R$	$\sim 1 \text{ M}\Omega$
Sensing resistance, $R$	200 $\text{k}\Omega$		
Ambient	R.T. ( $\sim 21.5^\circ\text{C} - 23.5^\circ\text{C}$ )		

A three-point measurement would have been more stringent in order to eliminate the voltage drop over the Pt counter electrode. The results are, however, reasonably consistent with three-point measurements made in Aalborg. As the Pt electrode is large relative to the microelectrodes, we may argue that the contribution from the Pt electrode is negligible. The resistance of the on-chip conductor traces are in the interval  $200 \Omega - 1800 \Omega$ , and the spreading resistance of the saline solution is  $\sim 30 \text{ k}\Omega$  for a square electrode with side length  $10 \mu\text{m}$ . Both contributions can also be neglected.

## 5. References

- [1] European Commission, *Contract for shared cost RTD, No IST-1999-10073, Annex I – "Description of work"*, 1999.
- [2] Hofmann, U.G., et al., ”On the design of multi-site microelectrodes for neuronal recordings”, *Proc. MICRO.tec 2000*, VDE, Hannover, 2000.
- [3] Hofmann, U.G., *Project Deliverable Report, Deliverable 1.1 – Update on User Needs and Specifications*, February 2001.
- [4] Kindlundh, M., *Utväckningsrapport: Maskset VSAMUEL v 1.0*, 2000-08-29, ACREO internal report no. acr002962
- [5] Yoshida, K., Jensen, W., Norlin, P., Kindlundh, M. and Hofmann, U.G., “Characterization of silicon microelectrodes from the EU VSAMUEL project”, In J. Werner (Ed.), to be published with *Biomedizinische Technik*, Schiele & Schön GmbH, Bochum, 2001.
- [6] Norlin, P., *Project Deliverable Report, Deliverable 2.2 – Connectors for probes with 32 Channels*, ACREO report no. acr004423, 2001-02-13.
- [7] Hofmann, U.G., personal communication.

## Appendix: Summary of technical data and design drawings

**Table A.1:** Summary of general technical data

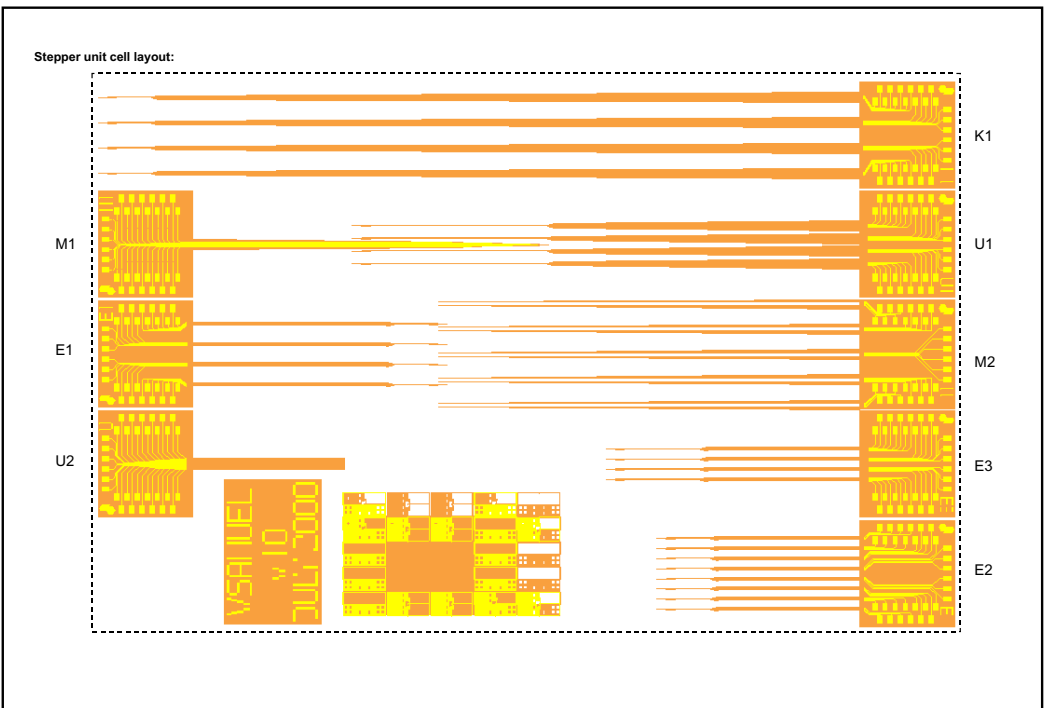
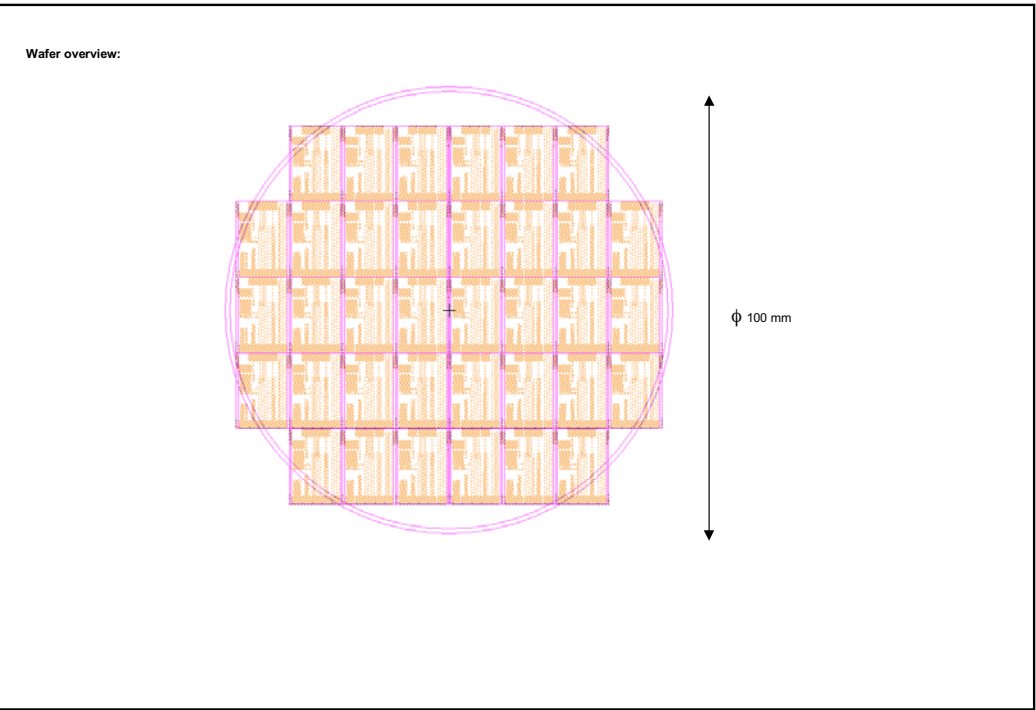
Design Element	Specification (typical values), comments
<b>Materials</b>	
Mechanical base structure	Silicon Silicon-on-insulator (SOI) wafers as starting material (Shin Etsu) 525 µm Si/1.5 µm SiO <sub>2</sub> /20 µm Si (C250, device batch), or 374 µm Si/1 µm SiO <sub>2</sub> /25 µm Si (C247, mechanical test)
Electrode sites	Iridium, e-beam evaporated Ti/Ir Thickness: ~300 Å/3500 Å
Connectors	Gold, e-beam evaporated Ti/Au Thickness: ~500 Å/2500 Å
Bond pads	Gold, as above.
Isolation layers	PECVD silicon nitride Thickness: 1 <sup>st</sup> layer ~1 µm, 2 <sup>nd</sup> and 3 <sup>rd</sup> layers ~0.5 µm
<b>Dimensions</b>	
Probe shaft	Width, w (at active region L1): 25 µm, except design M1 Width (at non active region, L-L1): 75 µm – 200 µm (*) Length, L: 4, 5, 7, 10 or 15 mm (*) Thickness: 20-25 µm
Electrode sites	Recording electrodes: 10 µm x 10 µm Lesioning electrodes: 21 µm x 47.5 µm or 20 µm x 50 µm (*)
Number of electrodes	32 (except M2: 30)
Position of electrodes	Pitch, a: 50-250 µm (*). First electrode distance from probe tip, c: 210 µm.
Conductor linewidths	(*) Min. 1 µm with 1 µm space. Wider where space available.
Bond pads	100 µm x 150 µm, spacing 100 µm. Two staggered rows along three sides of the base plate. 100 µm spacing between rows.
Number of shafts	1, 4, 5 or 8 (*)
Probe tip taper angle	4°
Base plate	2110 µm x 1875 µm (top surface) Thickness: 400 - 545 µm
<b>Marking/traceability</b>	All chips marked with design codes (M1, E1, ...). All chips marked with “VSAMUEL v1.0 JULY 2000” and Acreo-logotype. Bond pads marked with ID-codes: A1, A2, ...; B1, B2, ..., where A, B, ... = probe shaft starting from the left (tip pointing downwards) and 1, 2, ... = electrode site starting from the tip of each probe. All marks are in the Au-layer

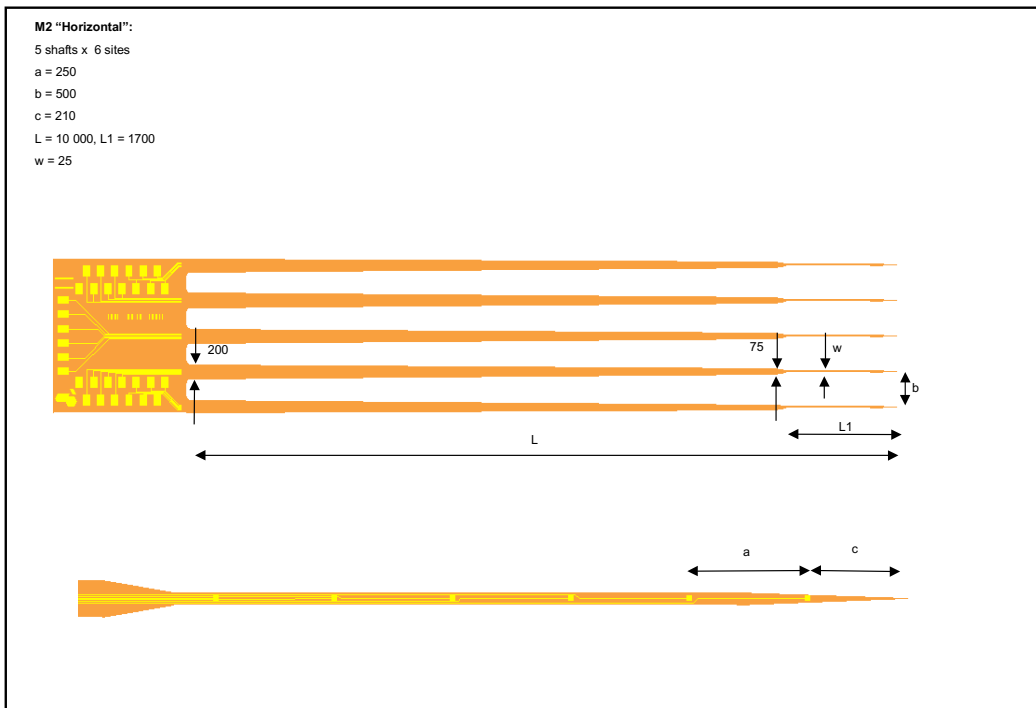
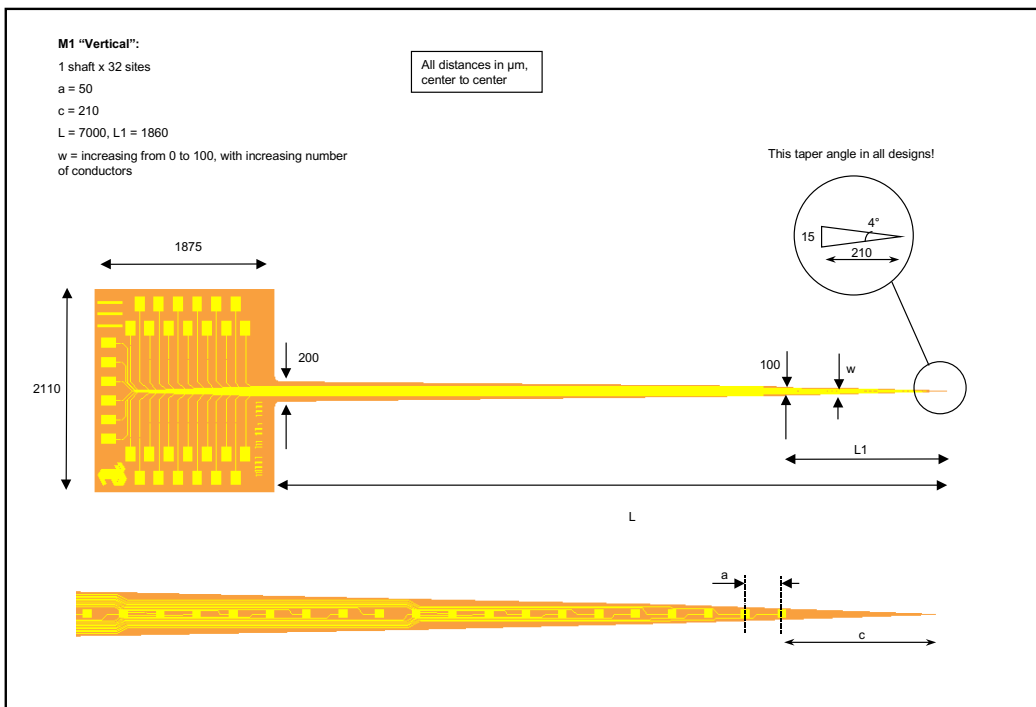
(\*) Varies between different probe designs. See table A.2 and design drawings.

Note: Some of the data are subject to process variations. Process records should be consulted for exact reference.

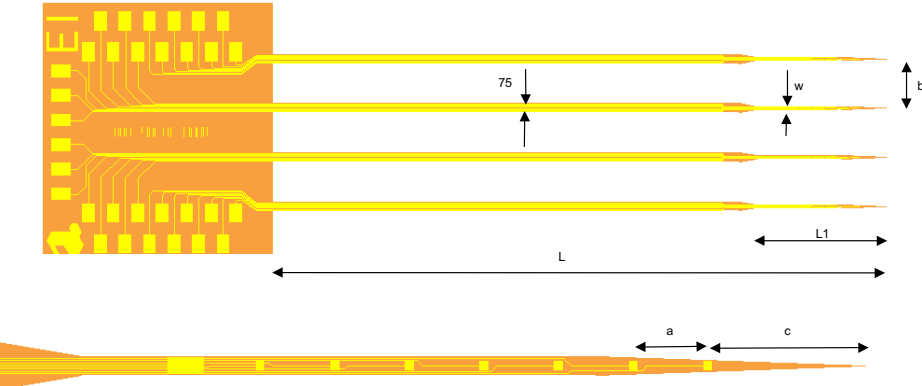
**Table A.2:** Summary of technical data varying between the eight probe designs

Design name	Number of shafts and recording sites	Shaft length (L), µm	Site c/c distance (a), µm	Shaft c/c distance (b), µm	Min linewidth, µm
M1 “Vertical”	1 shaft x 32 sites	7 000	50	--	Metal: 1 Space: 1
M2 “Horizontal”	5 shafts x 6 sites (=30)	10 000	250	500	Metal: 2 Space: 1
E1	4 shafts x 8 sites	5 000	100	400	Metal: 1.5 Space: 1
E2	8 shafts x 4 sites	4 000	200, 200, 100	200	Metal: 3 Space: 3
E3 “DCN”	4 shafts x 8 sites	5 000	200	200	Metal: 1.5 Space: 1
K1	4 shafts x 8 sites	15 000	100	500	Metal: 1.5 Space: 1
U1	4 shafts x 8 sites	10 000	100	250	Metal: 1.5 Space: 1
U2	4 shafts x 8 sites	5 000	50	60	Metal: 1.5 Space: 1

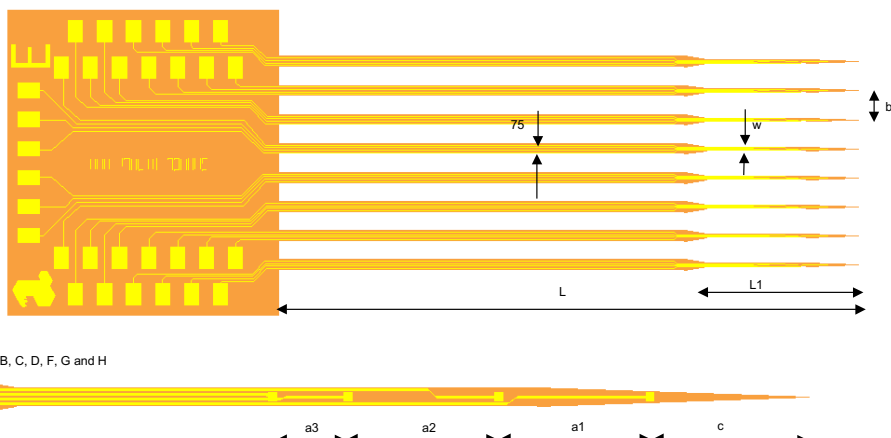




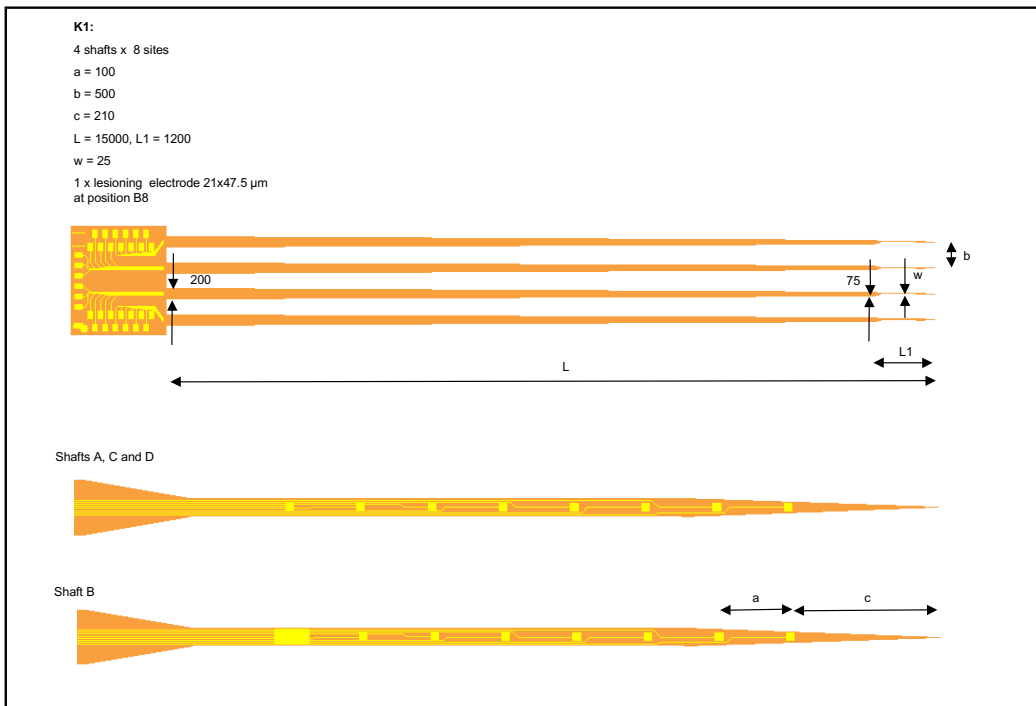
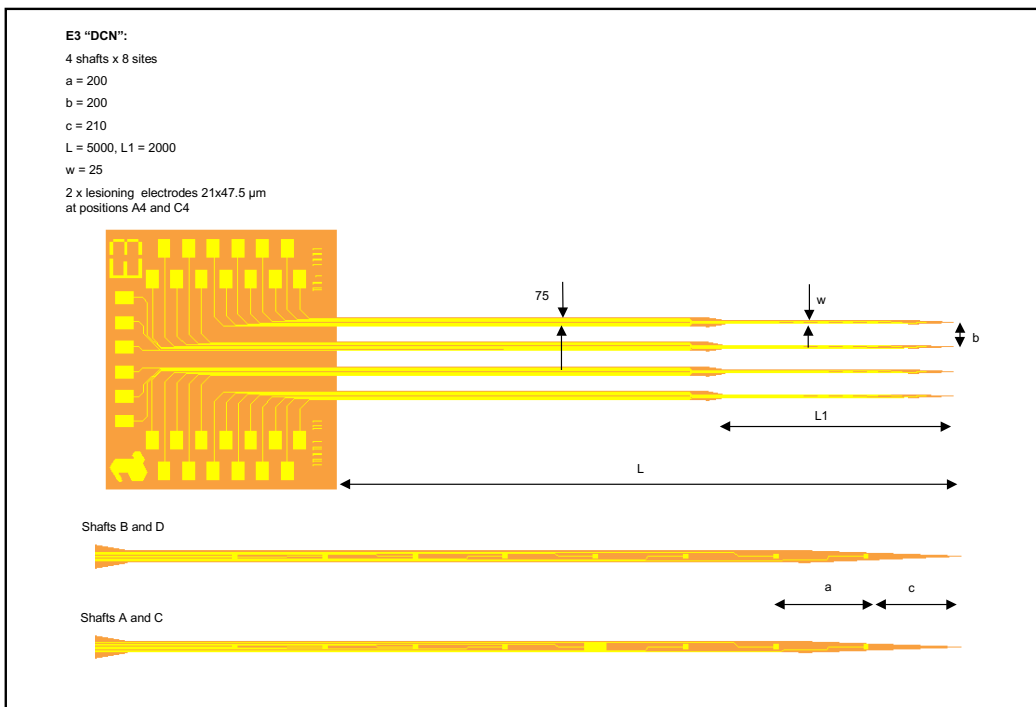
**E1:**  
 4 shafts x 8 sites  
 $a = 100$   
 $b = 400$   
 $c = 210$   
 $L = 5000, L1 = 1200$   
 $w = 25$   
 4 x lesioning electrodes  $21 \times 47.5 \mu\text{m}$  at positions A8, B8, C8 and D8

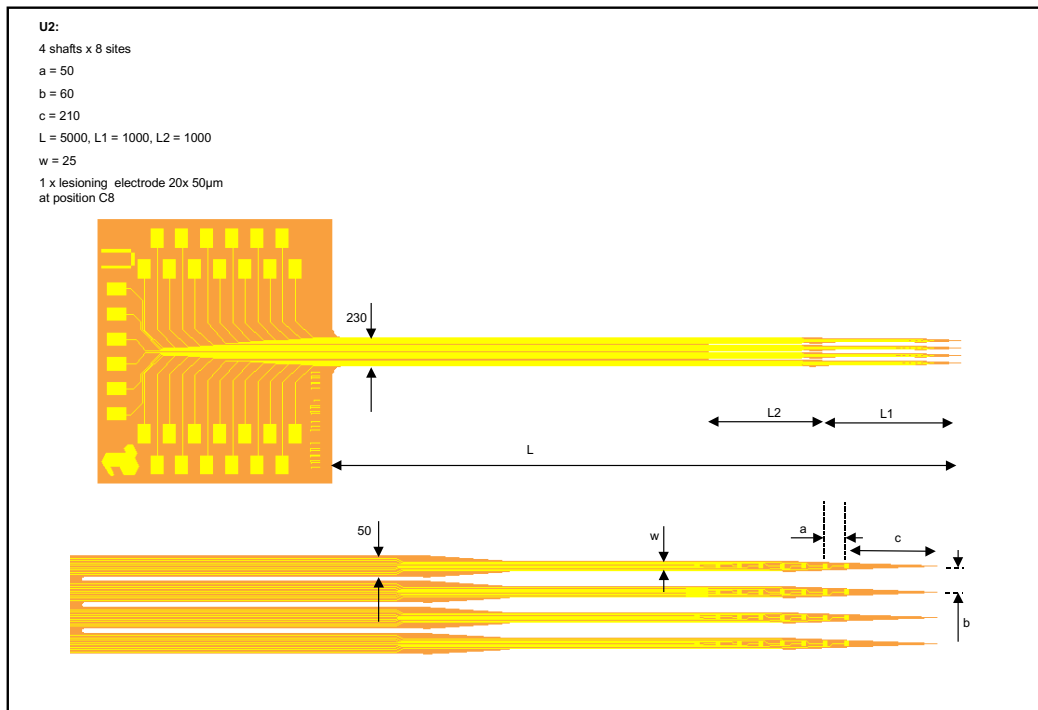
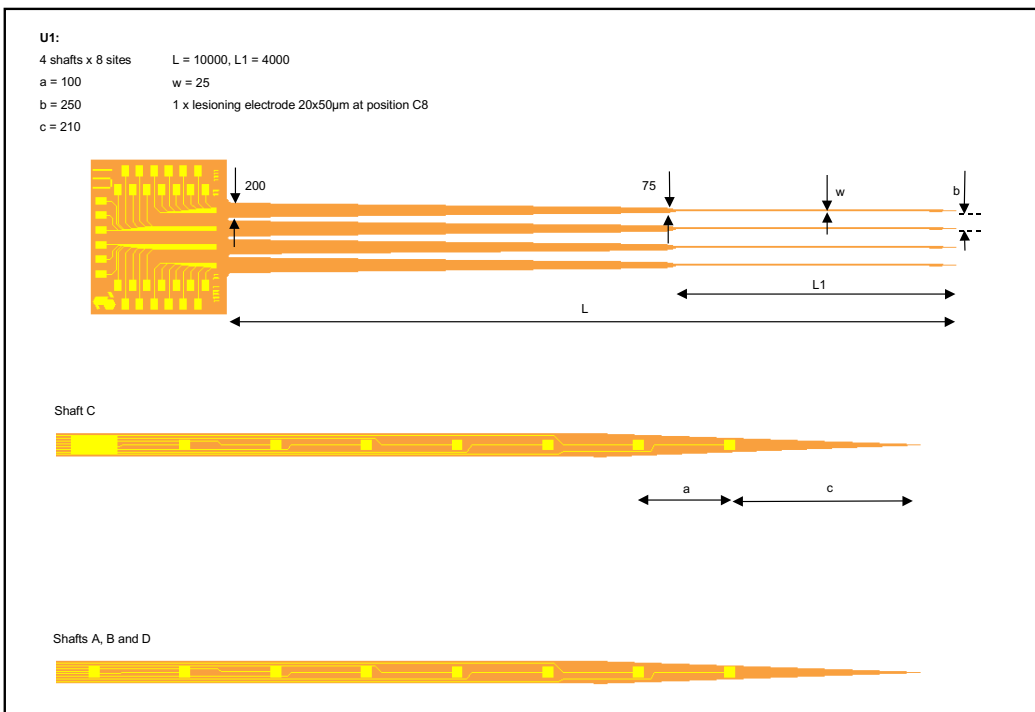


**E2:**  
 8 shafts x 4 sites       $L = 4000, L_1 = 1200$   
 $a_1 = 200, a_2 = 200, a_3 = 100$        $w = 25$   
 $b = 200$       1 x lesioning electrode  $21 \times 47.5 \mu\text{m}$  at position E2  
 $c = 210$



Shaft E





# **PROJECT DELIVERABLE REPORT**

## **INFORMATION SOCIETIES TECHNOLOGY (IST) PROGRAMME**



Project No. IST-1999-10073

Project acronym: VSAMUEL

Work Package No. 2  
Deliverable 2.3  
Custom designed 64 microelectrode probes

Date of Delivery: May 2002

Project Title:  
Development of a Versatile System for Advanced Neuronal Recordings with Multi-site  
Microelectrodes

Report prepared by:  
Peter Norlin and Maria Kindlundh  
Acreo AB

## 1. Background

The objective of the project VSAMUEL is to develop a system for the recording of multiple signals from neural tissue, and to demonstrate the system in different application experiments. The complete system consists of the following building blocks (figure 1.1):

- Micromachined fork-like silicon probes with multiple recording sites
- Pre-amplifier/amplifier hardware
- A connector solution, interfacing the miniaturized probes with the pre-amplifier
- Data acquisition/analysis hardware and software

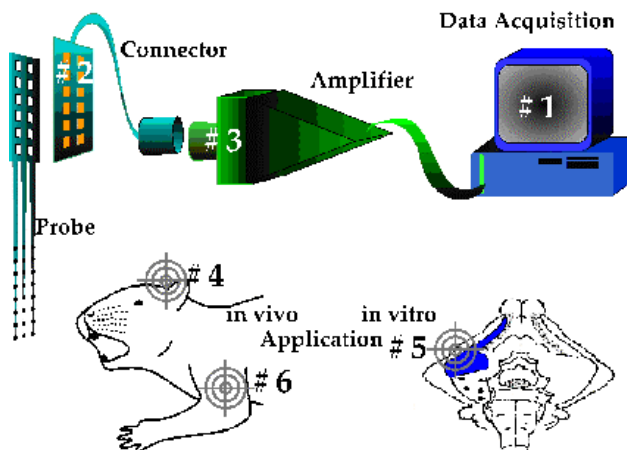


**Figure 1.1:** Overview of the project VSAMUEL. Counter clockwise from top right: #1 - Data acquisition system, hard- and software (Med. University of Lübeck, ISIP). #3 - Discrete and modular multi-channel amplifier (Thomas RECORDING). #2 - Custom designed connectors and passive batch fabricated multi-site microelectrode probes (Acreo AB). “Bull’s eyes” point to the area of application experiments: #4 - Cerebellum (Univ. of Antwerp), #5 - Cortex (INN Carlo Besta), #6 - Peripheral nerves (Aalborg University).

It is believed that a key to the understanding of the nervous system is to make *simultaneous* observations of the activity of a *large number* of cells.

One would thus like to insert a large number of recording sites – and the corresponding number of electrical “wires” – into the neural tissue, at the same time as the smallest possible tissue damage is desired. Silicon micromachining (Micro System Technology, MST), which is capable of producing structural

elements down to 1  $\mu\text{m}$  dimensions, and is inherently well suited for array based designs, has been employed in the VSAMUEL project to manufacture neural probes with several recording sites distributed on thin and narrow silicon shafts.

The purpose of this report is to document the Deliverable 2.3 “Custom designed 64 microelectrode probes” of VSAMUEL’s Work Package no. 2.

## 2. Design of silicon probes

### 2.1 General

Figure 2.1 shows a schematic overview of a VSAMUEL probe structure. The main design elements are:

- (a) Thin, narrow and pointed Si shafts for penetration and insertion into the neural tissue.
- (b) Microelectrode sites of Ir or Pt distributed over the frontal end of the shafts.
- (c) Fine and narrowly spaced metal (Au) conductor traces to connect the electrode sites with the bond pads.
- (d) Metal (Au) contact pads for external electrical interconnection using ultrasonic wire bonding.
- (e) A thicker Si base plate as a support for the contact pads, and to allow easy handling of the probes with tweezers.

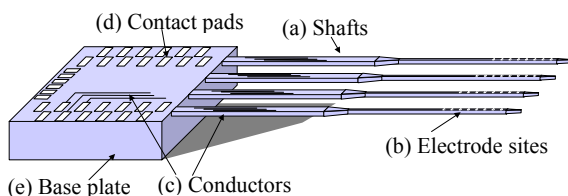


**Figure 2.1: Schematic drawing of the probe structure (not to scale).**

The current 64-site neural probes are the second generation of probes designed and fabricated within the VSAMUEL project. In the previous generation, probes with 32 electrode sites were manufactured, as reported in [1].

In summary, the following changes and improvements were made in the second design:

- The number of recording electrodes was doubled from 32 to 64.
- As a consequence the linewidths and spacing of the metal conductors were somewhat decreased.
- Based on the cooperating neuroscientists’ experience with the 32-site probes, a general review of the user-relevant design parameters (e.g. electrode distribution, shaft distribution, shaft length) was made, and requested changes implemented.
- A stereotrode concept (double-sites), enabling improved signal sorting algorithms, was included in some of the probe designs.
- A process for dual-frequency PECVD deposition of “stress-free” silicon nitride was tuned in, and employed in the manufacturing process. This is an alternative to stress compensating layers of SiN and SiO<sub>2</sub>.
- An improved process for evaporation of iridium electrode metal was tested.
- Increased experience with the manufacturing process, as well as analysis with scanning electron microscope (SEM) and focused ion beams (FIB) led to fine-tuning of several process and design parameters.

## 2.2 Layout

The design specification for the layout of the probes was determined in cooperation with the project's neuroscience groups. Eight different probe designs were included (fig. 2.2 and table 2.1). Nominally, at 100 % yield, each wafer will produce 204 probes.

The shaft thickness is 20  $\mu\text{m}$  - 30  $\mu\text{m}$ , but can be varied with the wafer specification. The recording sites are typically 10  $\mu\text{m} \times 10 \mu\text{m}$  and the tip taper angles are 4°.

A complete set of design drawings is available in appendix A.



**Figure 2.2:** Stepper unit cell with eight 64-site probe designs.

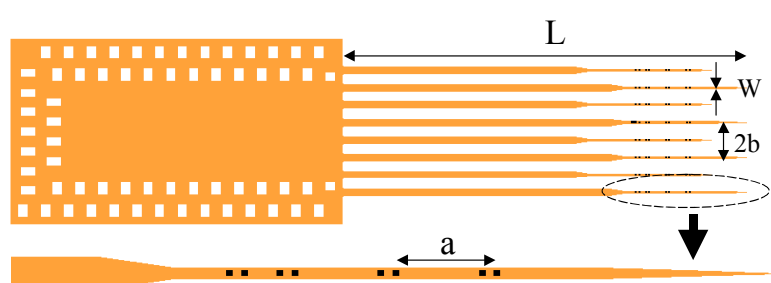


**Figure 2.3:** Close up of the CAD layout of a 64-site microelectrode probe. The example shows stereotrodes (double-site electrodes) and a special staggered shaft layout for improved penetration properties.

**Table 2.1:** Selected design parameters of the eight probe designs

Design name	Number of shafts and sites	Shaft length, $\mu\text{m}$ (L)	Shaft c/c distance, $\mu\text{m}$ (b)	Site c/c distance, $\mu\text{m}$ (a)	Min linewidth, $\mu\text{m}$	Shaft width at active region, $\mu\text{m}$ (w)
M3	2 shaft x 32 sites	7 000	1 000	50 (ss)	Metal: 1 Space: 1	Shaft width increasing from 0 to 100 to make room for 32 conductors.
M4	4 shafts x 16 sites	10 000	600	50 (ss)	Metal: 1 Space: 1.25	38
E4	4 shafts x 16 sites	5 000	400	100 (ds)	Metal: 1 Space: 1.25	38
E5	8 shafts x 8 sites	4 000 3 650	200	200, 200, 100 (ds)	Metal: 1.5 Space: 1.5	25.5
E6	4 shafts x 16 sites	5 000	400	100 (ss)	Metal: 1 Space: 1.25	38
K2	4 shafts x 16 sites	8 000	500	100 (ds)	Metal: 1 Space: 1.25	38
U3	3 shafts x 16 sites + 1 shaft x 14 sites (= 62 sites)	10 000	250	100 (ds)	Metal: 1 Space: 1.25	38
U4	8 shafts x 8 sites	5 000	60	50 (ss)	Metal: 1.5 Space: 1.5	25.5

ss = single site, ds = double site (stereotrode)

Several probes were designed with double site electrodes (stereotrodes), cf. figure 2.3. To record simultaneous activities from multiple neurons, the data must be processed by sorting algorithms in a data acquisition system. However, sorting algorithms based on recordings from single electrodes may have high error rates. In an effort to avoid these errors the *stereotrode* recording technique was developed [2]. Briefly, since the extracellular action potential varies inversely with the distance from the source, a signal recorded simultaneously with twin electrodes will have an amplitude ratio which will remain constant regardless of intrinsic variation in the absolute amplitude of the signal, and the amplitude ratio will in effect become a characteristic of that particular source.

### 2.3 Manufacturing process

The silicon probe fabrication process is outlined in figure 2.4 and in the following paragraphs (bold numbers refer to figure 2.4).

- (1) The probes were manufactured on silicon-on-insulator (SOI) substrates, with the purpose of the buried oxide to act as an etch stop for the subsequent two deep silicon etches.
- (2) An oxide film was thermally grown, alternatively a PECVD silicon nitride film was deposited, as the first isolation layer. Ti/Au was e-beam evaporated and patterned with a photo-resist lift-off process, to form conductor traces. 5X reduction step-and-repeat projection lithography was used with down to 1  $\mu\text{m}$  linewidths and spacing.
- (3) A new silicon nitride layer was deposited as an intermediate dielectric. Via holes were opened to the Au-layer using reactive ion etching (RIE) through a resist mask.
- (4) Ti/Pt was e-beam evaporated and patterned with lift-off, to form the electrode sites. (Ti/Ir was also used on one wafer. This wafer was, however, broken at a later stage in the process)
- (5) A final silicon nitride layer was deposited as a protective layer. Windows were opened to the bond pads and the electrode sites using RIE. The nitride covers the edges of the metal patterns for increased reliability in wet working environments.

- (6) With a resist mask the remaining nitride layer was first RIE etched, after which the top silicon layer was etched 20 - 30  $\mu\text{m}$  down to the buried oxide in an inductively coupled plasma deep reactive ion etching equipment (ICP DRIE).
- (7) A thick resist was spun on the wafer front side for protection. Double-sided mask alignment was used to pattern a thick resist on the wafer backside, which was etched the full 525  $\mu\text{m}$  down to the buried oxide in the ICP DRIE.
- (8) The shafts were released by first etching the buried oxide in RIE or HF, followed by a final resist strip.

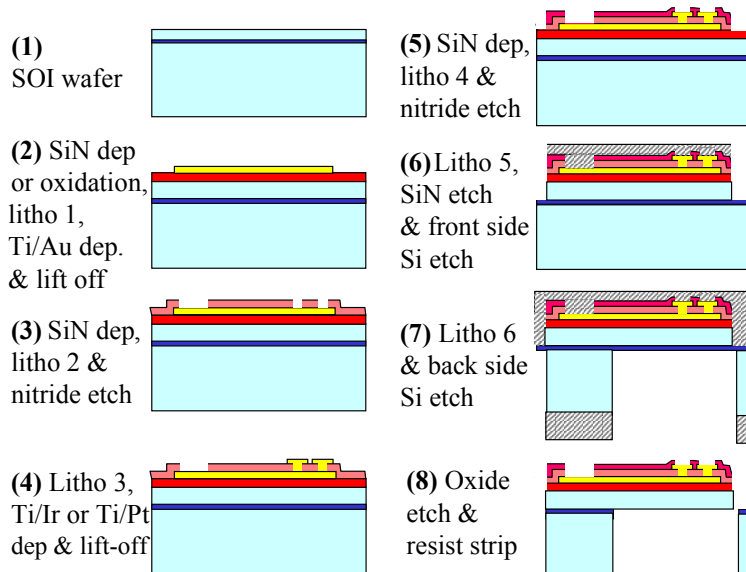


**Figure 2.4:** Schematic wafer cross sections illustrating the manufacturing process (not to scale).

In order to avoid stress induced bending of the silicon shafts two methods were employed. Thermally grown  $\text{SiO}_2$  and PECVD SiN have built-in stresses with opposite signs, and by using these two materials (in appropriate relative thickness proportions) for different dielectric layers, a stress compensated total structure can be achieved. In the second method, silicon nitride is deposited in a PECVD system working at dual frequencies. By shifting between the two frequencies in an optimized time cycle, virtually stress-free nitride layers can be deposited.

### 3. Results

#### 3.1 Micromachining results

Figures 3.1 - 3.3 show the result of the micromachining process.

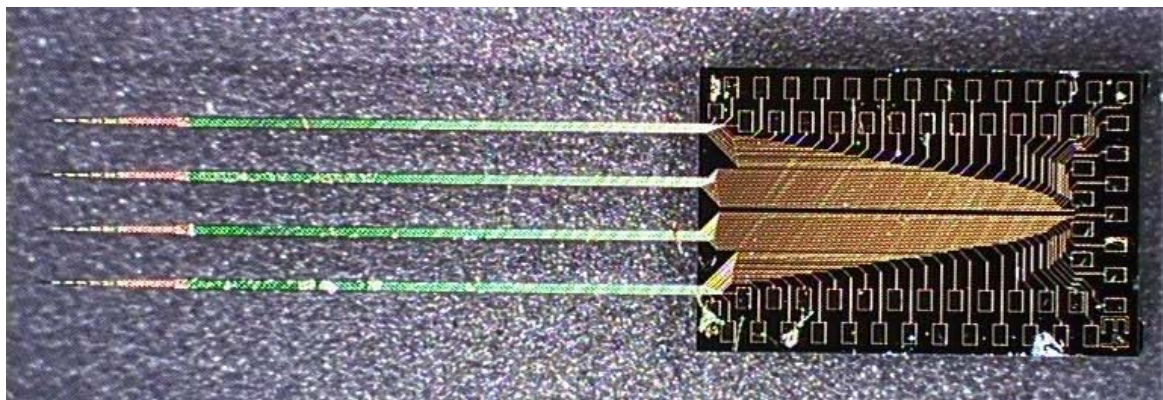


**Figure 3.1:** Photomicrograph of a 64-site neural probe, model E4.

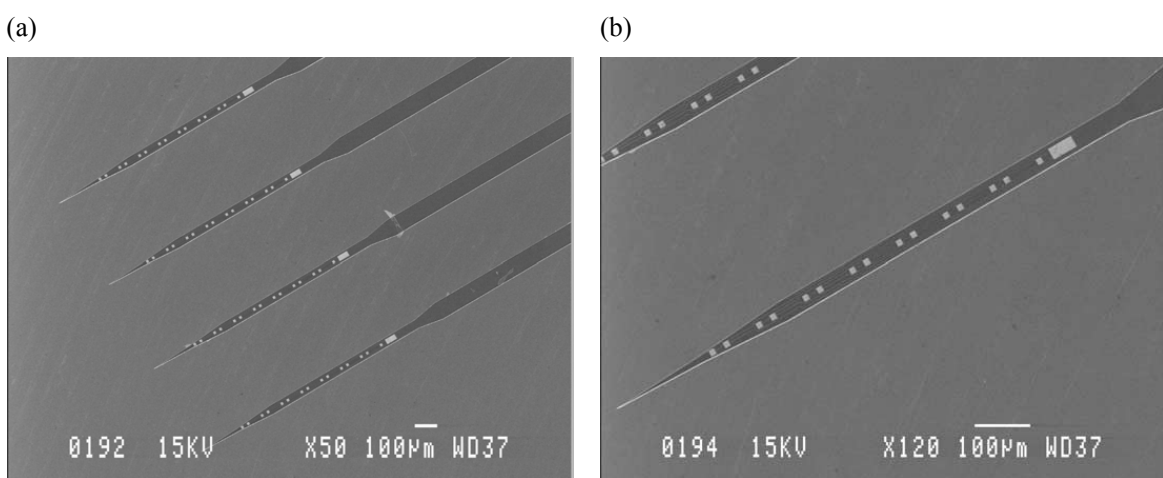


**Figure 3.2:** Scanning electron micrographs of a 64-site neural probe, model E4. (a) Four shafts with 16 electrodes each. (b) Close up of one of the shafts.

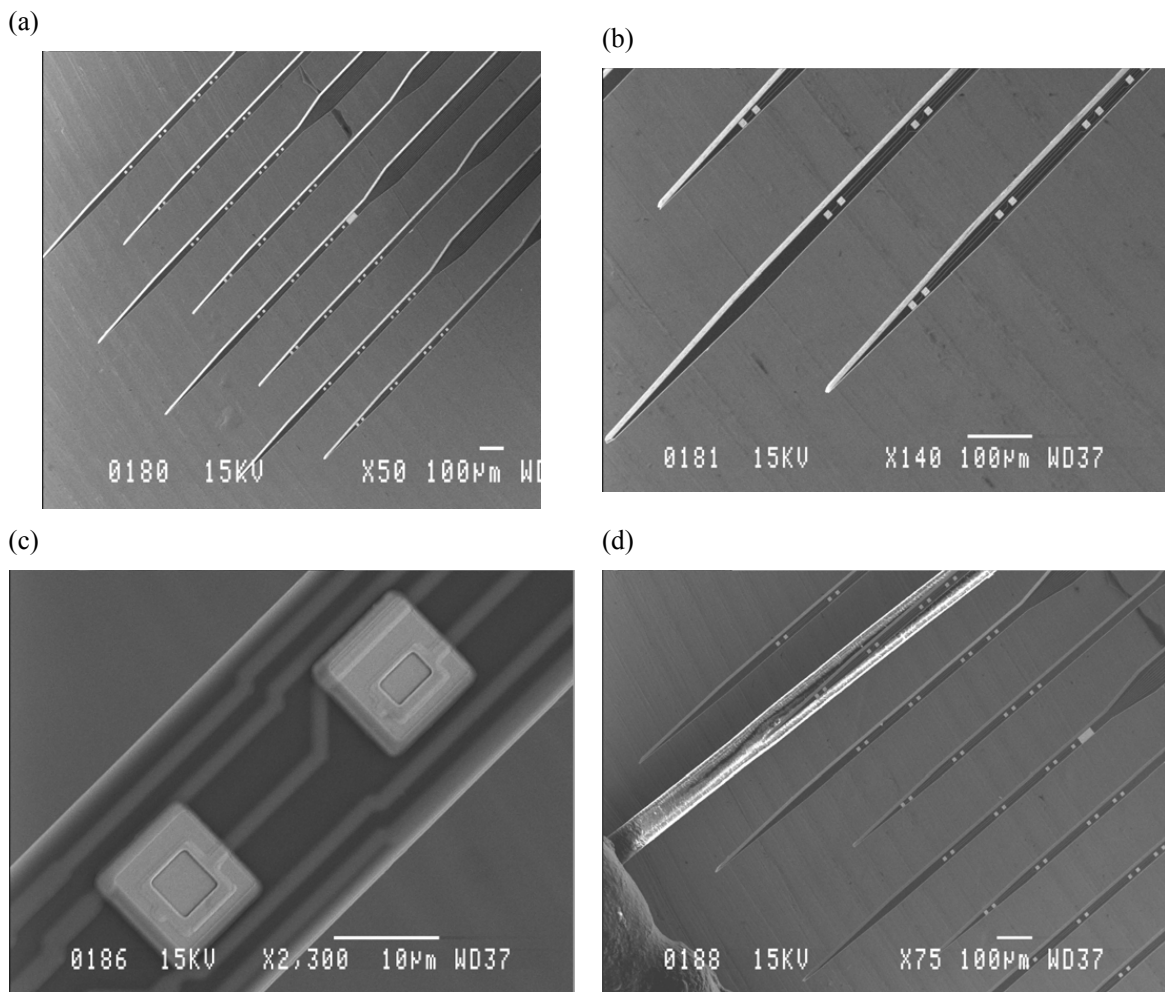


**Figure 3.3:** Scanning electron micrographs of a 64-site neural probe, model E5. (a) Eight staggered shafts with eight electrodes each. (b) Close-up of the shafts. (c) Close-up of electrode sites ( $10 \mu\text{m} \times 10 \mu\text{m}$ ) and conductors ( $1.5 \mu\text{m}$  wide). (d) Probe shafts ( $25 \mu\text{m}$  wide) shown compared to a human hair.

Both methods for thin film stress reduction appear to have been tuned in well. During processing, the stress was monitored on monitor wafers, using a profilometer and the wafer curvature method. The final bend of the probe shafts was measured by focusing an optical microscope at the probe tip and at the solid wafer surface, respectively. The scale on the focus wheel was calibrated with a known step height. Table 3.1 shows the resulting shaft bend angles measured at several positions on two wafers processed with dual frequency “stress-free” silicon nitride and stress compensating layers of silicon oxide and standard PECVD silicon nitride, respectively.

**Table 3.1:** Measured probe shaft bend angles after finalized processing

Method of stress reduction	Shaft length [mm]	Shaft bend angle [ °], average over a wafer	No of measurements
Stress free SiN	5	0.14	8
Stress free SiN	10	0.06	11
Std SiN + SiO <sub>2</sub>	5	0.08	7
Std SiN + SiO <sub>2</sub>	10	0.07	8

### 3.2 Electrical evaluation

Preliminary electrical measurements have been made to verify basic electrical functionality. A simple measurement set-up, previously described in [1], was used (improved upon as described in section 3.3). In short, a measurement cell consisting of a Pt wire electrode and a VSAMUEL probe immersed in a 0.9 % NaCl electrolyte was excited with sinusoidal input signal (150 mV p-p, 1 kHz). The resulting ac current through the cell was recorded as the ac voltage drop over a resistance in series with the cell. From this the electrode impedance magnitude could be calculated. Low electrode impedance is an essential property of the probes, as it is a basic condition for low noise levels.

As one of the probe designs (U3) had the electrodes varied in three different sizes, the electrode impedance could be measured and plotted vs. electrode area, see figure 3.4. The general signal response and the plotted area dependence indicate proper basic functionality of the probes. The absolute level of the impedance, measured at the standard electrode area ( $100 \mu\text{m}^2$ ), is  $\sim 5.5 \text{ M}\Omega$ . This value is rather high, though, compared to the  $\sim 2.3 \text{ M}\Omega$  measured in a previously fabricated (32-site) batch with Pt electrodes. Further analysis is needed to explain this result. As the underlying statistical sample of figure 3.2 is rather limited, a first measure would be to collect more data.

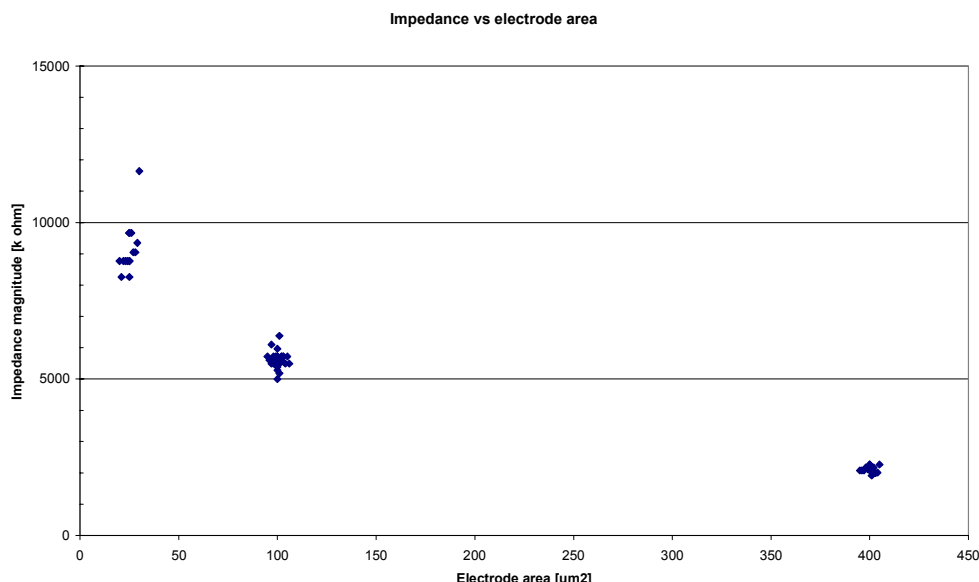


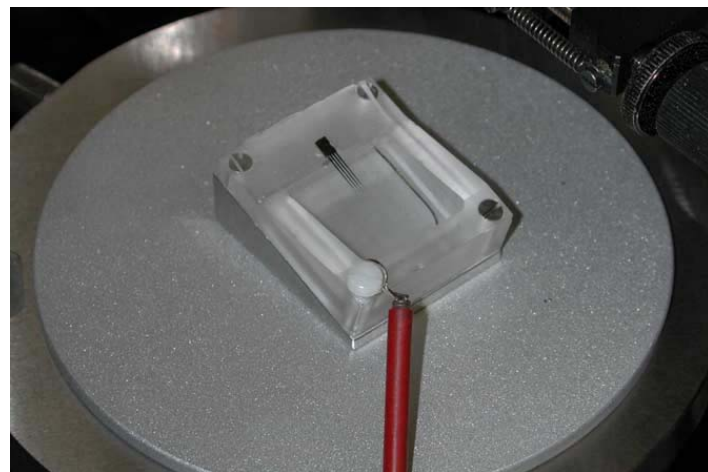
**Figure 3.4:** Impedance magnitude @ 1 kHz vs. Pt electrode area. ( $100 \mu\text{m}^2$  is the standard electrode size.)

### 3.3 Development of the measurement setup

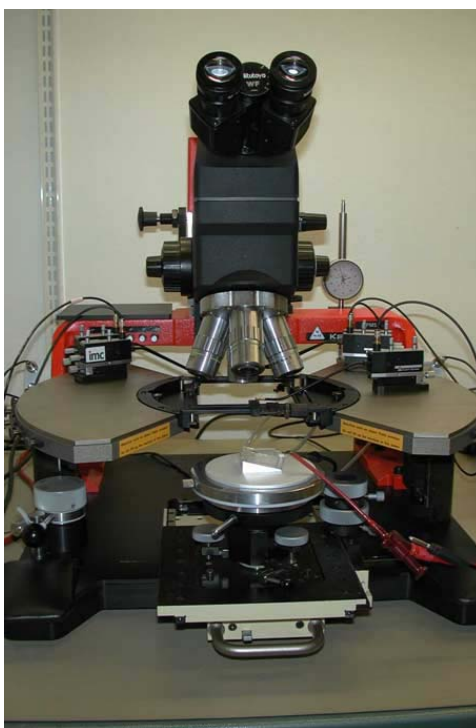
In earlier measurements we first mounted and wire-bonded the probes on flexible printed circuits. The flex circuit was fixated in a simple holder with the probe tips pointing downwards. The probe shafts were then lowered vertically into saline solution in the measurement cell (a small glass beaker). The back-end contact of the flex-circuit was contacted with standard oscilloscope probes. This working mode is quite unsatisfactory, however, if low quality probes are detected during the measurement. Both the flexible printed circuit and the labor intensive work of mounting and wire bonding the probe is than wasted on a defect sample.

As shown in figure 3.5, we have designed a measurement cell in which a naked probe chip can be fixated, pointing downward at an angle, so that the end of the shafts are immersed in saline. The entire cell can be placed on the chuck of a standard IC probe station, and the contact pads on the chip can be contacted with IC probe tips on micromanipulators.

(a)



(b)



(c)

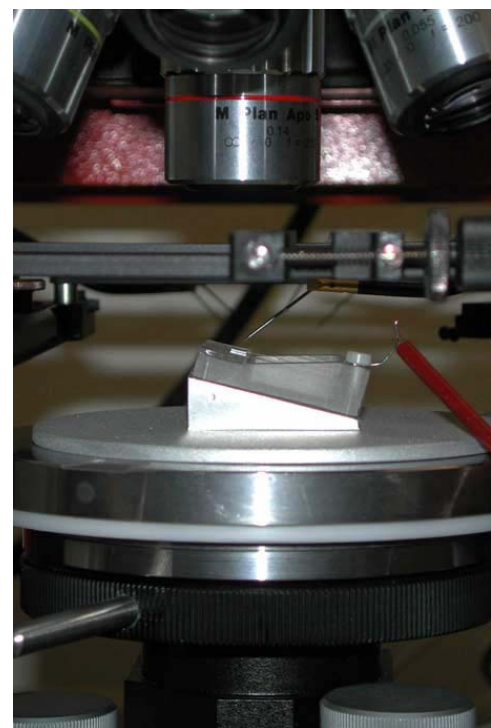


**Figure 3.5:** Photographs of the measurement cell for measurements on chip level in saline. (a) The cell shown with a neural probe chip and a Pt counter electrode. (b) The cell positioned on the vacuum chuck of an IC probe station. (c) Close-up showing an IC probe on a micromanipulator contacting a bond pad on the neural probe chip.

### 3.4 Dissemination of results

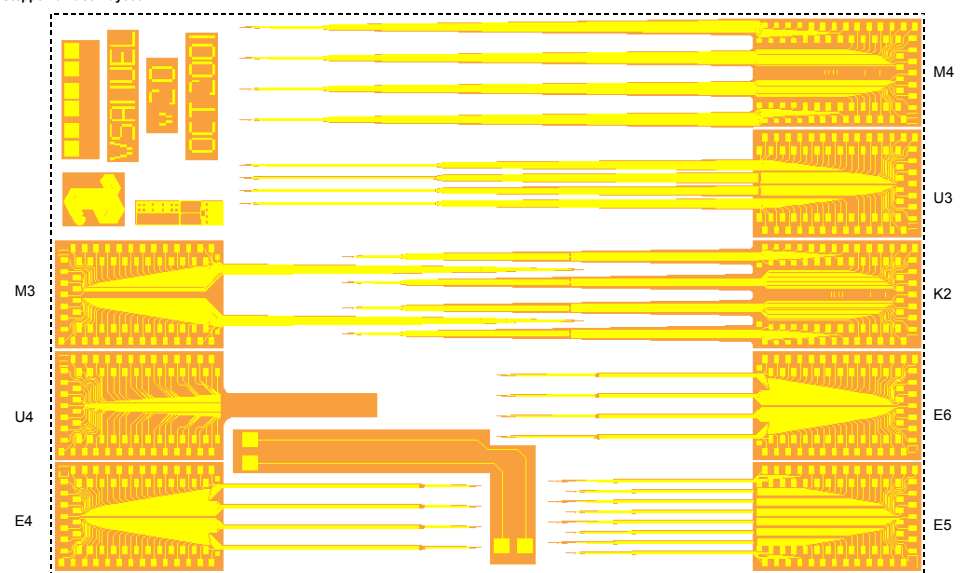
Part of this work was presented by Maria Kindlundh at the Micro Structure Workshop (MSW'02) in Bålsta, Sweden [3].

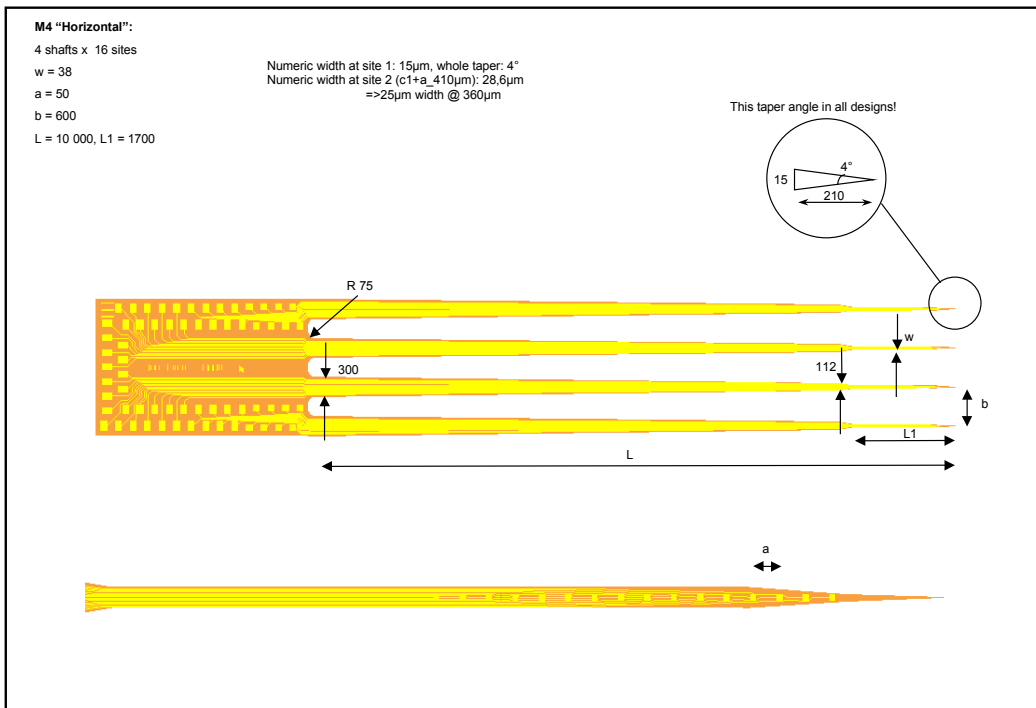
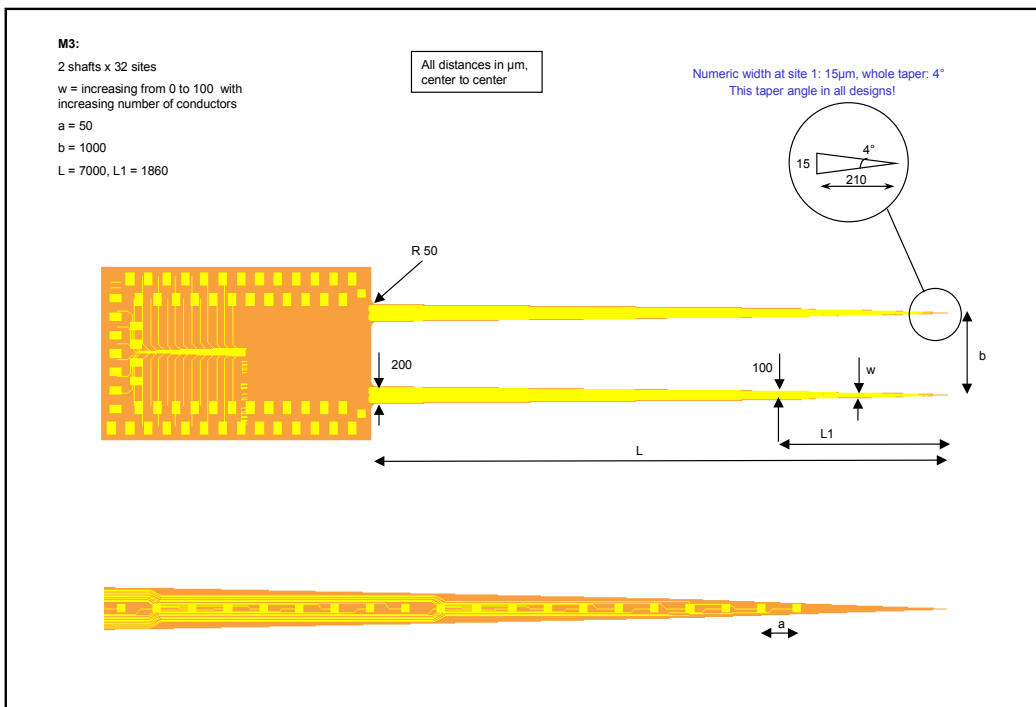
## References

- [1] Norlin, Kindlundh, *Project Deliverable Report: Deliverable 2.1 – Custom designed 32 microelectrode probes*, Acreo report no. acr005237, May 2001.
- [2] McNaughton, O’Keefe, Barnes, “The stereotrode: A new technique for simultaneous isolation of several single units in the central nervous system from multiple unit records”, *J. Neuroscience Methods*, **8**, 391-397 (1983).
- [3] Kindlundh, Norlin, Hofmann, ”Development of Multisite Microelectrodes for Neuroscience”, *Proc. 4th Micro Structure Workshop (MSW ’02)*, p. B8.1, Bålsta, 2002.

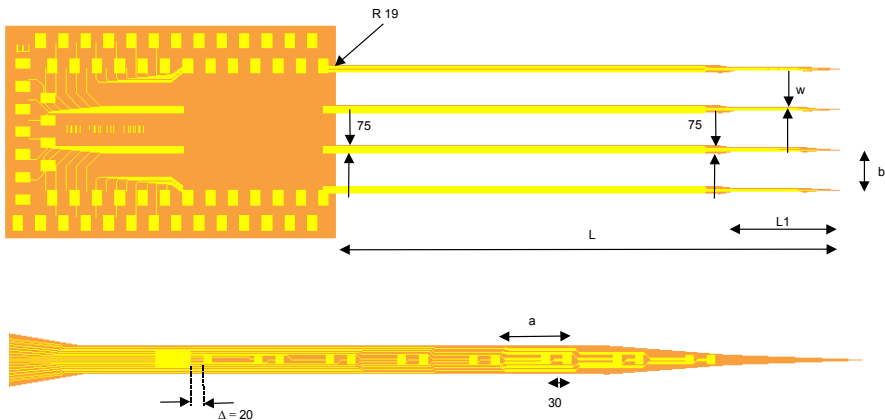
## Appendix A: Design Drawings

Stepper unit cell layout:

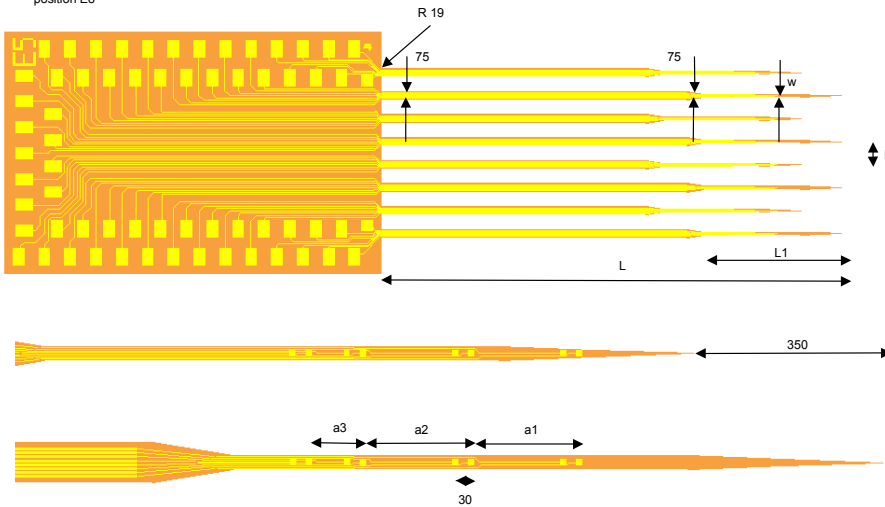


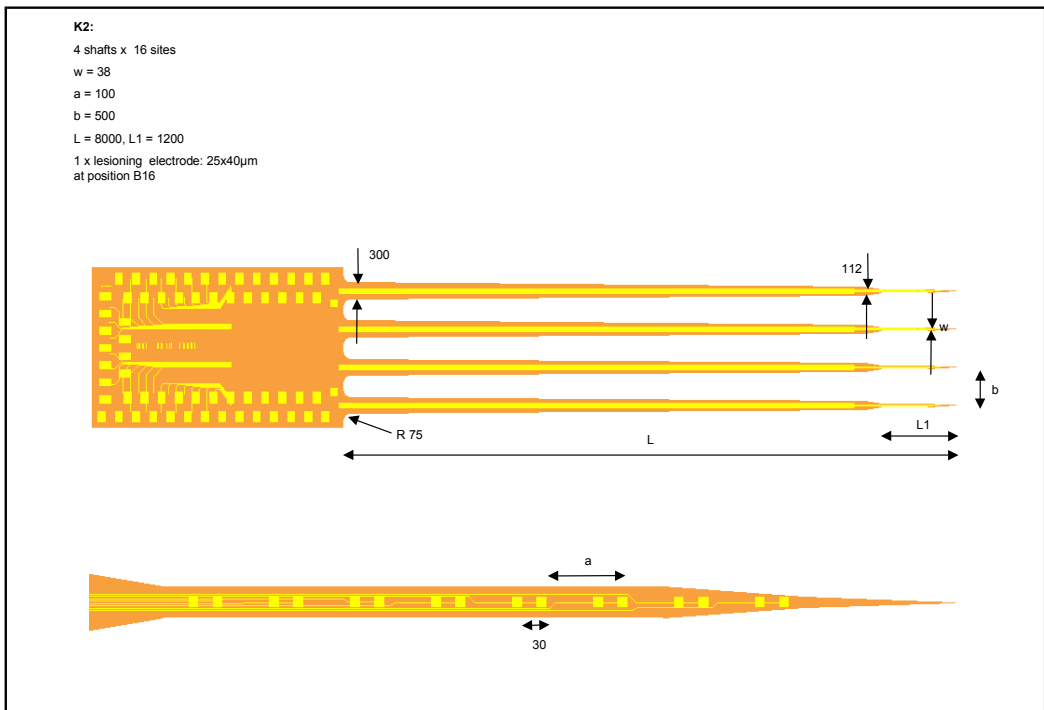
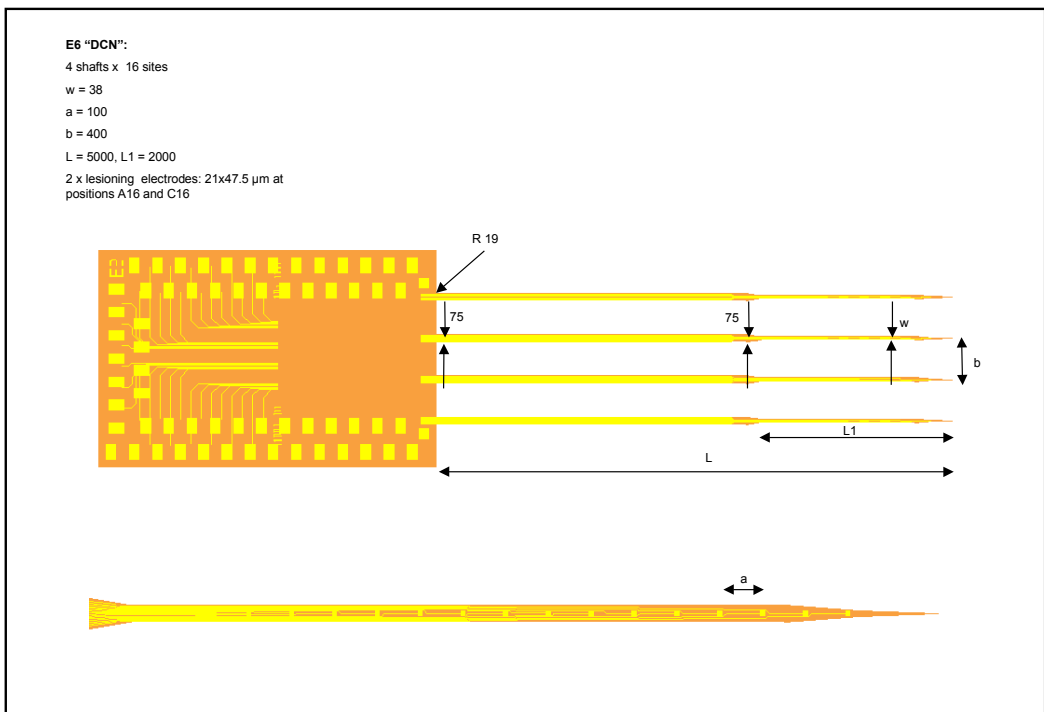


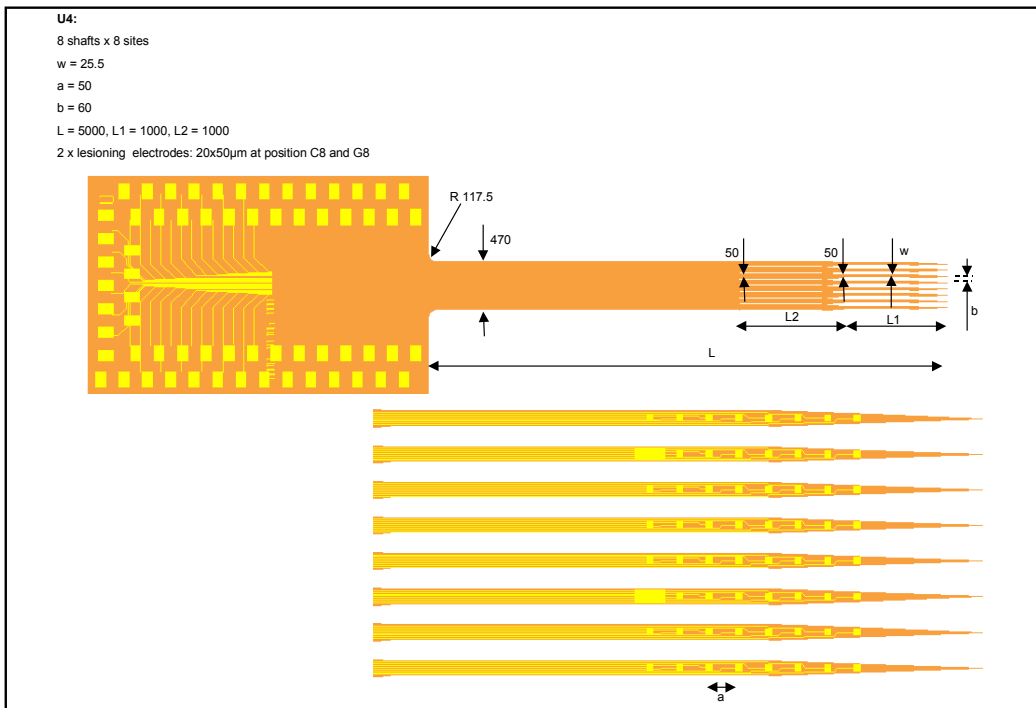
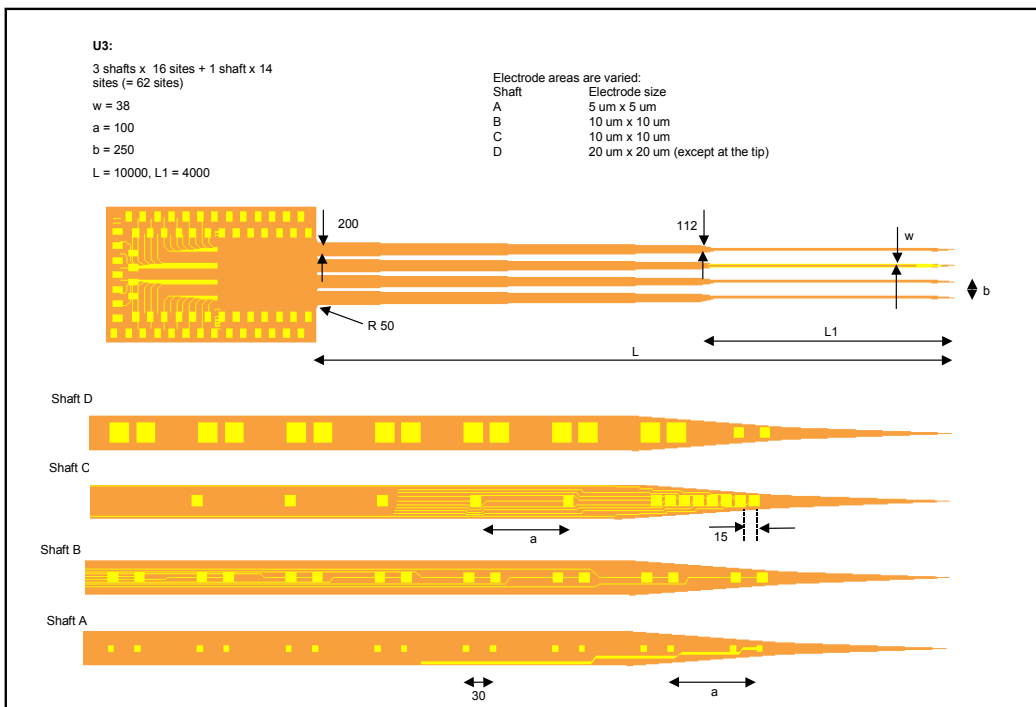
**E4:**  
 4 shafts x 16 sites  
 $w = 38$   
 $a = 100$   
 $b = 400$   
 $L = 5000, L1 = 1200$   
 4 x lesioning electrodes:  $21 \times 47.5 \mu\text{m}$  at positions A16, B16, C16 and D16



**E5:**  
 8 shafts x 8 sites  
 $w = 25.5$   
 $a1 = 200, a2 = 200, a3 = 100$   
 $b = 200$   
 $L = 4000/3650, L1 = 1200$   
 1 x lesioning electrode:  $21 \times 47.5 \mu\text{m}$  at position E8







# **PROJECT DELIVERABLE REPORT**

## **INFORMATION SOCIETIES TECHNOLOGY (IST) PROGRAMME**



Project No. IST-1999-10073

Project acronym: VSAMUEL

Work Package No. 2  
Deliverable 2.2  
Connector for Probes with 32 Channels

Date of Delivery February 13th 2001

Project Title:  
Development of a Versatile System for Advanced Neuronal Recordings with Multi-site  
Microelectrodes

Report prepared by: Peter Norlin, ACREO AB

## 1. Background

The objective of the project VSAMUEL is to develop a system for the recording of multiple signals from neural tissue [1-2]. The complete system consists of the following building blocks (figure 1.1):

- Micromachined fork-like silicon probes with multiple recording sites
- Pre-amplifier/amplifier hardware
- Data acquisition/analysis hardware and software

In order to interface the tiny silicon probe chips with the comparatively large pre-amplifier system, an interconnect and packaging scheme had to be developed. Flexible printed circuit (FPC) technology was identified as an attractive solution, allowing for flexible and precise positioning of the recording sites in the neural tissue using micromanipulators.

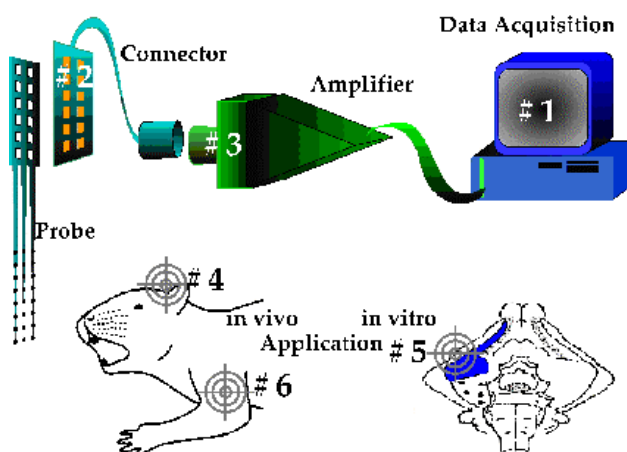


**Figure 1.1:** Overview of the project VSAMUEL. Counter clockwise from top right: #1 - Data acquisition system, hard- and software (Med. University of Lübeck, ISIP). #3 - Discrete and modular multi-channel amplifier (Thomas RECORDING). #2 - Custom designed connectors and passive batch fabricated multi-site microelectrode probes (ACREO AB). "Bull's eyes" point to the area of application experiments: #4 - Cerebellum (Univ. of Antwerp), #5 - Cortex (INN Carlo Besta), #6 - Peripheral nerves (Aalborg University).

The purpose of this report is to briefly document the Deliverable 2.2 ("Connector for probes with 32 channels") of the project's Work Package no. 2.

For an introduction to the FPC technology in general, the reader may consult e.g. reference [3].

## 2. Design

Figure 2.1 shows the lateral layout of the FPC. The front end is designed to fit the "base plate" and the bond pad positions of the silicon probe chip [4]. The back end is tailored to mate with the preamplifier's connector (Molex 52559, see data sheets in [5] or at [www.molex.com](http://www.molex.com)). The front end is stiffened in order to have a solid support for the probe chip and to be able to connect the FPC to a micromanipulator. The most important dimensions and design parameters are listed in section 5. The "pin sequence" of the outgoing terminals are defined in [6].

## 3. Manufacture

The FPCs were manufactured by HP Etch AB in Järfälla (Sweden) [7]. As we scanned the market this was the first company we found that actually manufactured flex circuits themselves locally. Others we talked to take orders for FPCs but use subcontractors abroad for the manufacture, which seemed less flexible for a prototyping situation and may require larger order quantities. The linewidth specifications offered from HP Etch (down to 20 – 30  $\mu\text{m}$ ) was also better than from the competitors.

Figure 3.1 shows four photographs of the manufactured circuits. The main building elements of the circuit are:

- Flex foil of polyimide.
- Conductor traces of copper.
- A cover layer of polyimide protecting the conductor traces (open at the contact areas at the front and back ends).
- Ni/Au metallization at the front and back end contacts.
- A thick stiffening of glass fiber epoxy (FR4) to stabilize the front end.
- A thin stiffening of polyester to give the back end the thickness required by the connector.

A punching tool was manufactured to cut the FPC foil into the desired shapes. According to the manufacturer the punching process is not very precise. For that reason a 1 mm margin was left on each side, and the board edges must be trimmed by hand if they are to be exactly fitted (i.e. at the connector end in order to fit the Molex connector). The samples we received seemed to be punched with quite good precision to begin with, though.

Further technical data are given in section 5.

The price charged was 12 kSEK for 50 units, plus a fixed cost of 3 kSEK for the punching tool.

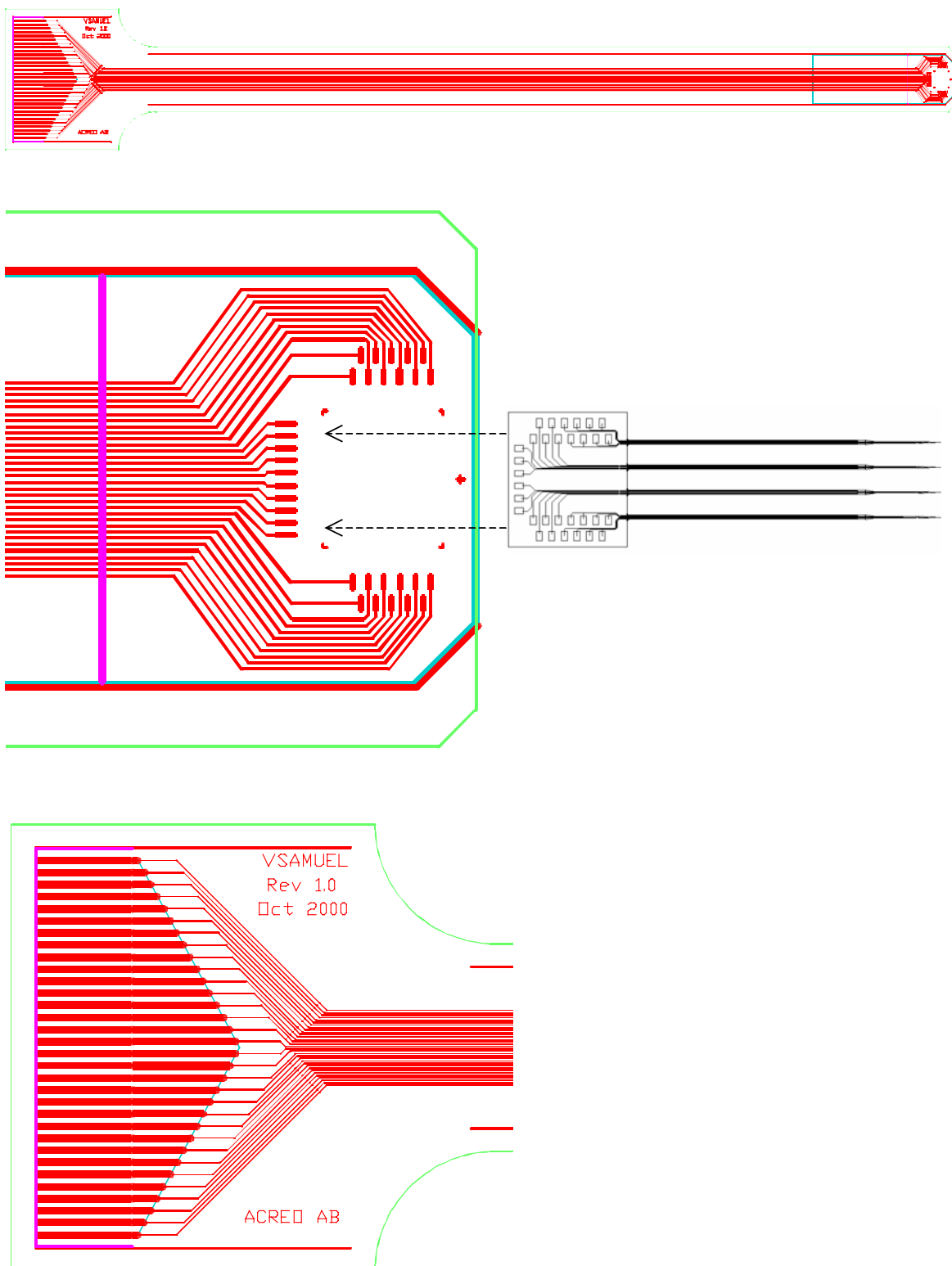


**Figure 2.1:** Top: Layout of the FPC. Middle: Close-up of the front end, designed for mounting and interconnect of a silicon probe chip (inset). Bottom: Close-up of back end designed to fit a Molex 52559 ZIF FPC connector.



**Figure 3.1:** Flexible printed circuit manufactured by HP Etch (125.5 mm x 8.6 mm).

## 4. Connecting the probe chips to the FPC

The probe chips are mounted on the FPCs with glue (cyanoacrylate or epoxy). Ultrasonic bond equipment (West Bond) is used to connect the Au bondpads on the chip to the corresponding bond pads on the FPC with gold wire. Finally an epoxy glob top (Emerson & Cuming, AMICON 50300/50400 series) will be applied to protect the chip and bond wires.

Ultrasonic bond tests were performed on test samples before the manufacture of the flex circuits. It was observed that the thickness of the Ni/Au contact metallization was critical for a satisfactory bond. A pad with a 6 um Ni layer was easy to make a good bond to, whereas it was difficult to bond to pads with a 3 um Ni layer.

Figure 4.1 shows a FPC with a demonstrator silicon probe glued in place.

Basic signal recordings have been verified using a VSAMUEL probe test chip mounted and wire-bonded to a FPC. A simple measurement set up was used in which the recording sites of the probe chip were immersed in a 0.9 % saline solution and a sinusoidal input signal from a function generator was provided through a Pt-wire electrode.



**Figure 4.1:** A silicon probe chip mounted on a FPC.

## 5. Summary of technical data

Design Element	Specification (typical values), comments
Total length of FPC	125.5 mm
Width of movable section	8.6 mm
Length of stiff area at front end	18 mm
Number of conductors and bond/contact pads	32
Conductor linewidth	Artwork dimensions: 50 um Final dimensions: 5 um overetch on each side of the conductor, i.e. final dimensions will be 40 um
Conductor min spacing	Artwork: 50 um
Bond pad dimensions	100 um x 300 um and 100 um x 400 um
Back end contact pad dimensions	Width 0.3, c/c 0.5 mm, spacing 0.2 mm
Distance chip front edge – FPC front edge	0.5 mm (Not edge-to-edge. Some area needed for the glob-top to make a good seal)
Cover layer	Opening at front end: 6 mm long, total FPC width. Opening at back end: ~3 – 6.5 mm. V-shaped edge to avoid breakage.
Marking/Traceability	Label "VSAMUEL Rev 1.0 Oct 2000 ACREO AB"
Alignment patterns	For chip positioning: Chevrons at chip corners

	(50 um wide Cu-lines, i.d. 2150 um x 1875 um) Center cross at front end (50 um wide Cu-lines) 100 um wide Cu lines for precise cutting of the side-edge, to align FPC pattern to ZIF connector.
Design layers	1 Punching tool, FPC perimeter 2 Conductors (Cu) 3 Coverlayer windows 4 Stiffened areas  Ni/Au contact metallization will be defined by the intersection of layers 2 and 3
CAD files and formats	Gerber photoplotter (.g01, ..., .g13) files are used for Cu conductor layer. AutoCAD (dwg) files are used for punching tool manufacture.
Specifications of ZIF connector to be connected at back end	Molex 52559  Catalog page: <a href="http://www.molex.com/product/ffc/52559.pdf?654">http://www.molex.com/product/ffc/52559.pdf?654</a> Sales drawing: <a href="http://www.molex.com/product/ffc/52559d.pdf?654">http://www.molex.com/product/ffc/52559d.pdf?654</a> (also in [5])  Recommended FPC dimensions: <input type="checkbox"/> Thickness (at contact region): 0.3 mm <input type="checkbox"/> Contact pattern: w 0.3 - 0.35 mm, c/c 0.5 mm, spacing 0.2 – 0.15 mm  Insertion depth: 2.45 mm
Output terminal definitions	See ref [6] (acr002863)
Flex foil	Material: Polyimide  Thickness: 50 um
Conductor traces	Material: Cu  Thickness: 5 um
Bond/contact pads	Material: Ni/Au  Thickness: 6 um/ 0.1 um
Cover layer	Material: Polyimide/epoxy glue  Thickness: 12. 5 um/12.5 um
Stiffened area (front end)	Material: Glass fiber epoxy, FR4  Thickness: ~ 1 mm
Stiffened area (back end)	Material: Polyester  Thickness: ~0.16 mm

## References

- [1] European Commission, *Contract for shared cost RTD, No IST-1999-10073, Annex I – "Description of work"*.
- [2] Hofmann et al., "On the design of multi-site microelectrodes for neuronal recordings ", *Proc. MICO.tec 2000*, VDE, Hannover.
- [3] Fjelstad, *Flexible Circuit Technology*, 2<sup>nd</sup> ed., Silicon Valley Publishers Group, Sunnyvale CA, 1998.

- 
- [4] Kindlundh, *Utvecklingsrapport: Maskset VSAMUEL v 1.0*, 2000-08-29, ACREO internal report no. acr002962
  - [5] Norlin, *Design inputs for VSAMUEL v 1.0 Flexible Printed Circuit (FPC)*, 2000-09-11, ACREO internal report no. acr003049.
  - [6] Norlin, *Contact/electrode cross reference. VSAMUEL design 1*, 2000-08-21, ACREO internal report no. acr002863.
  - [7] HP Etch AB, Elektronikgränd 6, Box 567, SE-175 26 Järfälla, Sweden, <http://www.hpetch.se>, contact: Ulf Carlström.

# **PROJECT DELIVERABLE REPORT**

## **INFORMATION SOCIETIES TECHNOLOGY (IST) PROGRAMME**



Project No. IST-1999-10073

Project acronym: VSAMUEL

Work Package No. 2  
Deliverable 2.4  
Connector for Probes with 64 Channels

Date of Delivery: May 2002

Project Title:  
Development of a Versatile System for Advanced Neuronal Recordings with Multi-site  
Microelectrodes

Report prepared by:  
Peter Norlin and Maria Kindlundh  
Acreo AB

## 1. Background

The objective of the project VSAMUEL is to develop a system for the recording of multiple signals from neural tissue, and to demonstrate the system in different application experiments. The complete system consists of the following building blocks (figure 1.1):

- Micromachined fork-like silicon probes with multiple recording sites
- Pre-amplifier/amplifier hardware
- A connector solution, interfacing the miniaturized probes with the pre-amplifier
- Data acquisition/analysis hardware and software

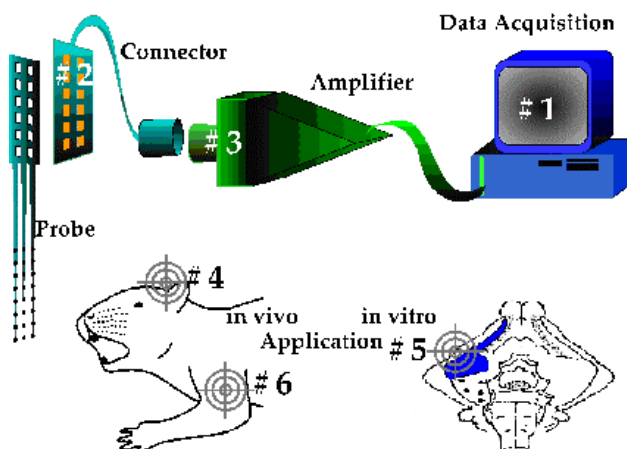


**Figure 1.1:** Overview of the project VSAMUEL. Counter clockwise from top right: #1 - Data acquisition system, hard- and software (Med. University of Lübeck, ISIP). #3 - Discrete and modular multi-channel amplifier (Thomas RECORDING). #2 - Custom designed connectors and passive batch fabricated multi-site microelectrode probes (Acreo AB). "Bull's eyes" point to the area of application experiments: #4 - Cerebellum (Univ. of Antwerp), #5 - Cortex (INN Carlo Besta), #6 - Peripheral nerves (Aalborg University).

In order to interface the tiny silicon probe chips with the comparatively large pre-amplifier system, an interconnect and packaging scheme had to be developed. Flexible printed circuit (FPC) technology was identified as an attractive solution, allowing for flexible and precise positioning of the recording sites in the neural tissue using micromanipulators.

The purpose of this report is to briefly document the Deliverable 2.4 ("Connector for probes with 64 channels") of the project's Work Package no. 2.

For an introduction to the FPC technology in general, the reader may consult e.g. reference [1].

## 2. Design

The 64-channel FPC is an extended version of the 32-channel FPC reported in [2]. The main new features are:

- Extension of conductors and contacts from 32 to 64 channels.
- The conductors and back-end contacts are distributed over two legs, which connect at the common probe chip end. The design is made with the intention that the FPC can be used with two different amplifier setups (see figure 2.1): A single 64-channel amplifier box (with two 32-pin connectors), alternatively two 32-channel boxes.
- Where space is available, conductor spacing has been increased in order to reduce cross-talk.
- A second metal layer has been added to the FPC, intended to improve shielding and noise properties (including two ground contacts on the backside, close to the back ends).

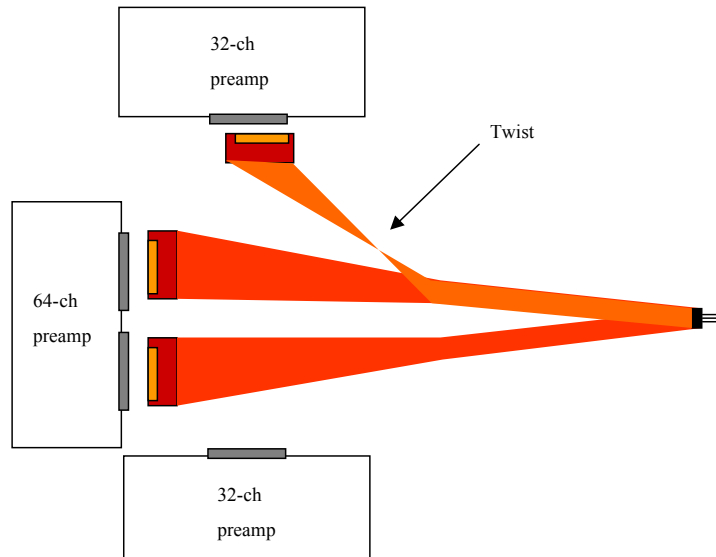


**Figure 2.1:** Schematic drawing of FPC in two possible setups - a single 64-channel amplifier box (with two 32-pin connectors), alternatively two 32-channel boxes.

Figures 2.2 - 2.3 show the lateral layout of the FPC. The front end is designed to fit the "base plate" and the bond pad positions of the silicon probe chip. The back end is tailored to mate with the preamplifier's connectors (Molex 52559, see data sheets [3]). The front end is stiffened in order to have a solid support for the probe chip and to be able to connect the FPC to a micromanipulator. The most important dimensions are listed in table 2.1. The "pin sequence" of the outgoing terminals is defined in [4].

**Table 2.1:** Selected design parameters

Design Element	Specification (typical values), comments
Total length of FPC (L)	138 mm
Diagonal length of movable parts (L1)	~93 mm
Length of stiff area at front end (L2)	18 mm

Width of movable sections (w)	8.4 mm
Separation of twin contacts (L3)	51 mm
Number of conductors and bond/contact pads	64
Conductor linewidth (std dimension, where space is available)	Artwork dimensions: 100 um, 120 um space Final dimensions: ~5 um overetch on each side of the conductor, i.e. final dimensions will be ~90 um, 130 um space
Conductor linewidth (min)	Artwork dimensions: 50 um, 50 um space Final dimensions: ~ 40 um, 60 um space
Bond pad dimensions	100 um x 200 um
Back end contact pad dimensions	Width 0.3, c/c 0.5 mm, spacing 0.2 mm
Distance chip front edge – FPC front edge	0.5 mm (Not edge-to-edge. Some area needed for the glob-top to make a good seal)

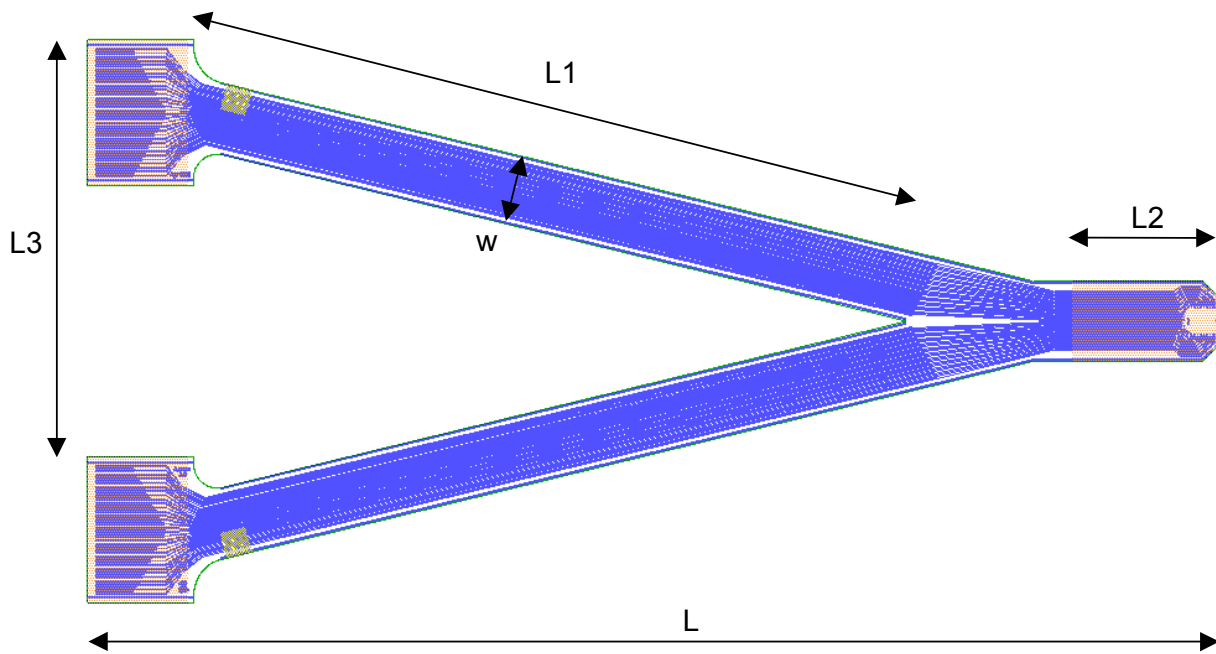


**Figure 2.2:** CAD layout of the FPC.

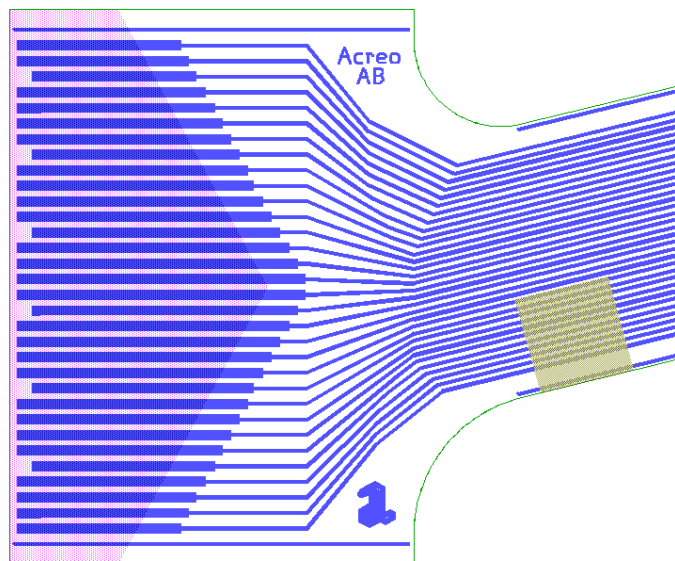
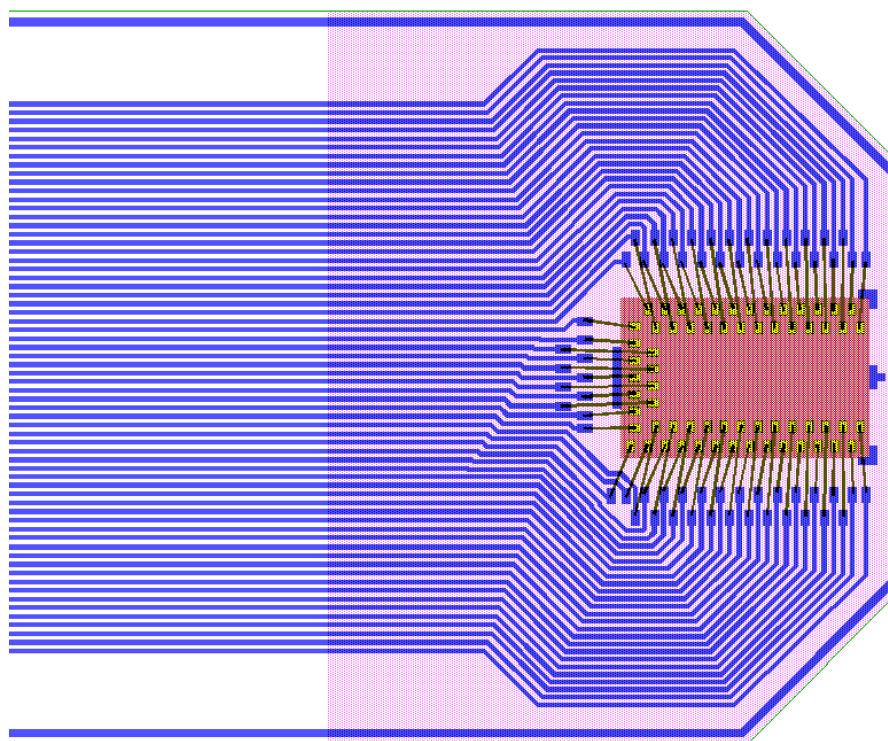


**Figure 2.3:** Top: Close-up of the front end, designed for mounting and interconnect of a silicon probe chip (base plate shown inset with bond wires). Bottom: Close-up of back end designed to fit a Molex 52559 ZIF FPC connector.

### 3. Manufacture

The FPCs were manufactured according to our design by HP Etch AB in Järfälla (Sweden) [5]. Figure 3.1 shows a photograph of one of the manufactured circuits. The main building elements of the circuit are:

- Flex foil of polyimide.
- Conductor traces of copper.
- Shielding layer of copper.
- Two cover layers of polyimide, protecting the conductor traces (open at the contact areas at the front and back ends) and the shielding layer (open at two contacts at the back end).
- Ni/Au metallization at the front and back end contacts.
- A thick stiffening of glass fiber epoxy (FR4) to stabilize the front end.
- A thin stiffening of polyester to give the back end the thickness required by the connector.

A punching tool was manufactured to cut the FPC foil into the desired shapes.

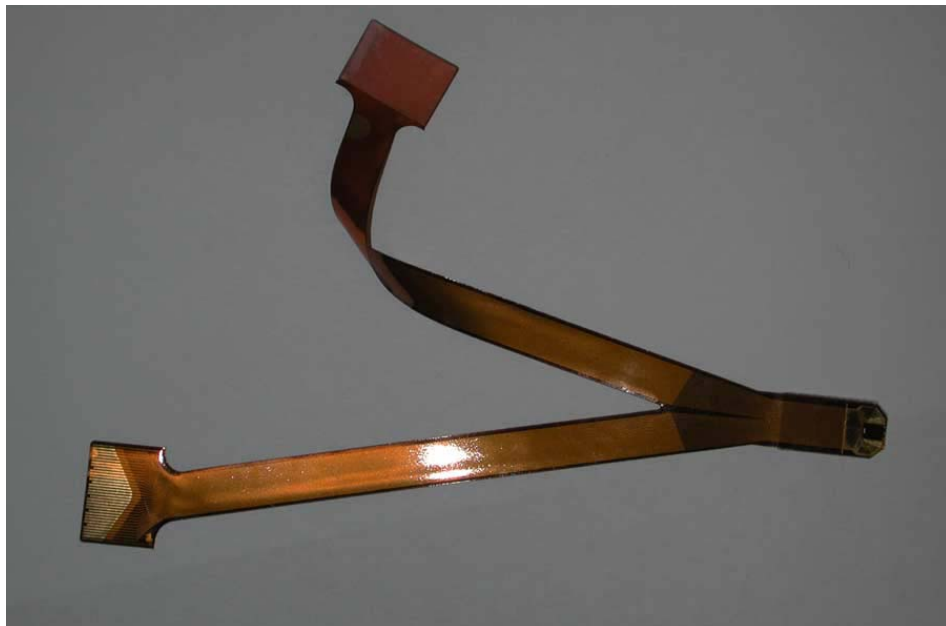


**Figure 3.1:** 64-channel flexible printed circuit manufactured by HP Etch (138 mm x 69 mm).

Probe chips were glued to the FPC, electrically connected with ultrasonic wire bonding and glob-top protected, using the same methods as described in [2].

### References

- [1] Fjelstad, *Flexible Circuit Technology*, 2<sup>nd</sup> ed., Silicon Valley Publishers Group, Sunnyvale CA, 1998.
- [2] Norlin, *Project Deliverable Report: Deliverable 2.2 – Connector for Probes with 32 Channels*, Acreo report no. acr005237, May 2001.
- [3] Molex 52559, Catalog page: <http://www.molex.com/product/ffc/52559.pdf?654>, Sales drawing: <http://www.molex.com/product/ffc/52559d.pdf?654>

- 
- [4] Kindlundh, *Contact/electrode cross reference. VSAMUEL design 2*, Acreo report no. acr007335, May 2002.
  - [5] HP Etch AB, Elektronikgränd 6, Box 567, SE-175 26 Järfälla, Sweden, <http://www.hetch.se>, contact: Ulf Carlström.

# **PROJECT DELIVERABLE REPORT**

## **INFORMATION SOCIETIES TECHNOLOGY (IST) PROGRAMME**



Project No. IST-1999-10073

Project acronym: VSAMUEL

Work Package No. 4  
Deliverable 4.1  
Data Acquisition System for 32 Channels

December 2000  
Software on CD-ROM

Project Title:  
Development of a Versatile System for Advanced Neuronal Recordings with Multi-site Microelectrodes

Report prepared by: A. Folkers, ISIP, Med. University of Lübeck

# System Overview

## ***Hardware setup for 32 channel data acquisition system***

One M67 PCI board from Innovative Integration with OMNIBUS A4D4 modules and two TERM boards serve as basic hardware for data acquisition. The A4D4 modules are attached to the M67 board which resides in a PCI slot of the host PC, while the TERM boards are external. The core of the M67 board is a Texas Instrument TMS320C6701 digital signal processor (DSP). The DSP controls the A4D4 modules and the TERM boards. Each TERM board provides 16 differential input channels. These channels are multiplexed by means of four multiplexers onto four channels which serve as input for one A4D4 module. The A4D4 modules are able to convert four analog channels (+/- 10V) to digital values at a time. The host PC and the M67 board are connected via the PCI bus. The current host system consists of a 500 MHz Pentium III with 256 MB SDRAM (Synchronous DRAM) on a Nexcom/Interlogic Industries Mainboard. It has two SCSI harddrives IBM DNES-309170W with 8 GB storage each.

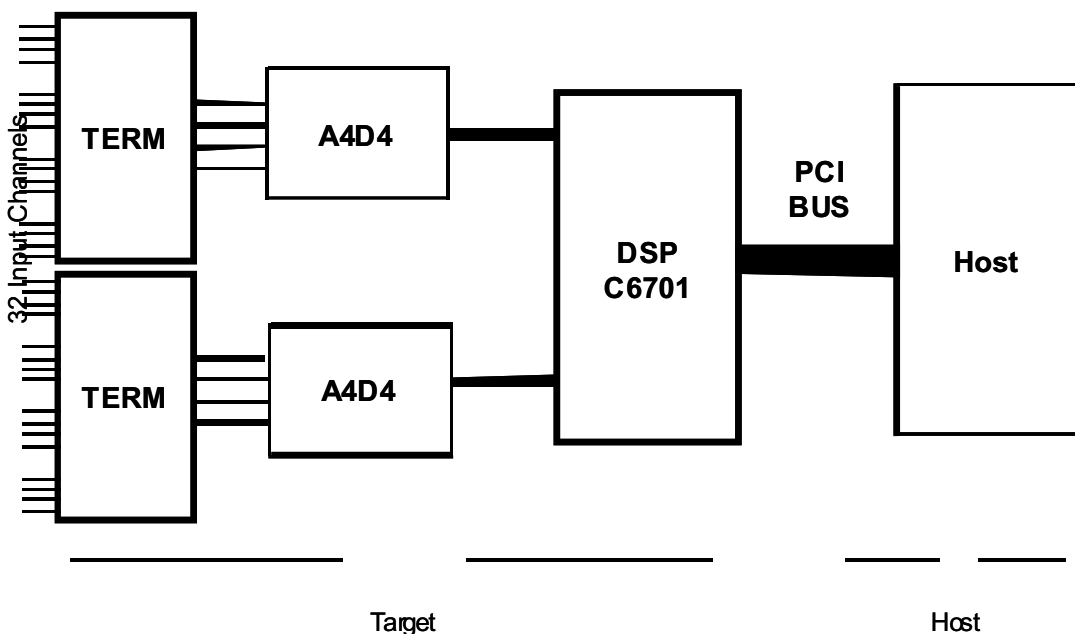


Figure 1: DSP hardware overview

## ***Software Setup***

The host is running under Microsoft Windows NT 4.0 Service Pack 6. We are using Borland C++ Builder 5.0 for host side software development, which includes development of a graphical user interface (GUI) and the software interface to the M67 board.

The software for the DSP board (target) is developed using TI Code Composer Studio 1.20.

## **Target Site Software**

The target site software has to accomplish the following tasks

1. acquire data from input channels
2. transfer the data to host
3. react on commands

The software structure reflects these tasks by having three main modules, one for each task. Furthermore there is a module which handles a global queue and one which provides a high resolution clock. In the following each module is discussed:

### ***Data Acquisition Module:***

The data acquisition is done within an interrupt service routine (ISR) which is triggered by the conversion ready signal from one A/D converter. A timer triggers the A/D conversion at a rate which corresponds to the selected sampling rate. The input channels cannot be read using a single A/D conversion as we can only sample eight channels at a time with two A4D4 modules. Therefore, in order to sample all 32 muxed input channels we need to iterate four times, where in each iteration a new set of eight input channels is multiplexed onto the input channels of the A4D4 modules. This imposes a lag between “neighbouring” channels of up to 10 microseconds. The actual trigger rate is sampling rate times four. The data which is read from the A/D converters (ADC) and stored into a global queue. In Figure 2 the data acquisition is illustrated.

### ***Data Transfer Module:***

The data transfer is executed from the main loop. The function polls the size of the global queue and if it contains enough data it sends a packet via the PCI bus to the host. Hereby two alternating buffers located in the shared memory of host and target are used. After a packet is written to a buffer the number of this buffer is transferred to the host as notification that a new buffer has arrived. On host site an event is generated which triggers the execution of a virtual interrupt service routine. This routine copies the respective buffer from shared memory into a receiving queue on the host.

### ***Command Module:***

The command module is supposed to handle commands send by the host to the target, so e.g. the data acquisition and data transfer can be started and stopped by sending such commands. These commands are send using a mailbox system provided by the M67 board. A mailbox can receive and store a 32 bit value. A message arriving at a mailbox generates an interrupt on the target which in turn triggers the execution of an ISR that sets a flag. From the main loop a command handler routine polls for that flag and executes the respective command.

### ***Queue Module:***

The queue module provides a global queue that buffers the acquired data until it is send to the host.

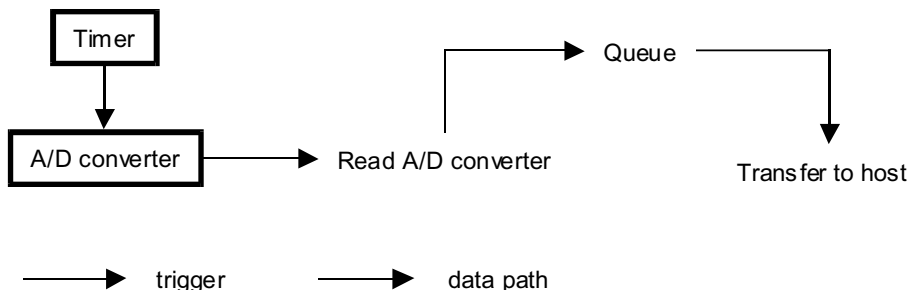


Figure 2: Data acquisition on DSP board

## Host Site Software

The host site software has essentially three parts:

1. Data reception and storage.
2. Data organization
3. Data visualisation

### ***Data reception and storage***

The data, acquired or computed by the target board, is send to the host via the PCI bus. The reception of data is driven by events. Events are generated within the software library from Innovative Integration every time a new packet arrives in an input buffer. Therefore, the host is notified for every buffer arriving and copies the data from each buffer into the main queue. From this queue the data needs to be distributed to different software modules, which e.g. store or visualize the data. Figure 3 illustrates the flow of data.

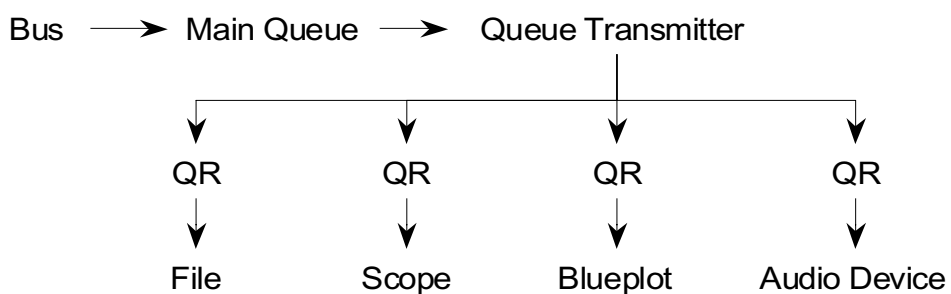


Figure 3: Data flow in host application

The distribution is centralized in a so called queue transmitter which is associated with several queue receivers. The queue transmitter can access the main queue and transmits buffers from this queue to its associated queue receivers. A queue receiver can be dynamically associated and deassociated with the queue transmitter. Each queue receiver has an own queue into which the data is copied. Furthermore, the queue receiver can decimate the data in order to deal with the specific requirements of its associated software module. This applies e.g. to realtime visualisation where not every sample point can be plotted and therefore only every third point is transferred into the queue receiver queue.

The class diagramm in Figure 4 shows the respective classes in UML notation. Classes are represented by rectangles with three parts. The top shows the name of the class, the middle part contains the fields, and the bottom part is a list of methods. The rhombus symbolizes aggregation, while a plain line represents an association.

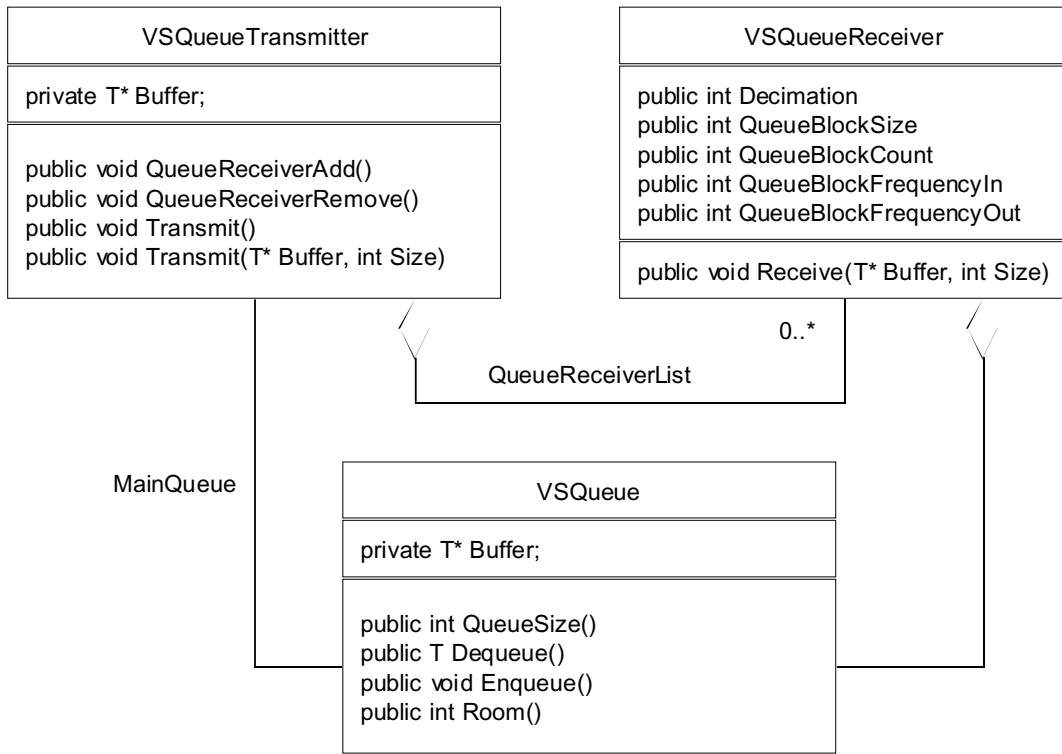


Figure 4: Class diagramm of queue, queue transmitter and queue receiver

A queue transmitter contains a list of queue receivers and it has a pointer to the main queue. The content of the main queue is distributed to the queue receivers within the method `Transmit()` which copies a chunk from the queue into the buffer and calls the `Receive` method of every queue receiver. The `Transmit()` method is called periodically.

The `QueueBlockFrequencyIn` is the number of arriving queue blocks per second. `QueueBlockFrequencyOut` is the number of queue blocks that can be processed in one second. The `Decimation` is computed from `QueueBlockFrequencyIn` and `QueueBlockFrequencyOut`.

The actual transfer from a queue receiver to its associated software module is organized by an active transfer object. This object periodically issues transfer events which are handled by an appropriate method in the respective software module. This method retrieves data from the queue of the queue receiver and processes it, e.g. stores it into a file.

In Figure 5 the active transfer object is described in detail. The `OnTransfer` event triggers a call of method `Transfer()` in a data processor, e.g. the scope. From method `Transfer()` the method `Process()` is called, reading data from the queue associated with the active transfer object via its queue receiver. The method `Start()` of `VSActiveTransfer` add the queue receiver to the global queue transmitter and calls the method `Start()` of the data processor. The counterpart is the method `Stop()` of class `VSActiveTransfer` which removes the queue receiver from the global queue transmitter and calls the method `Stop()` of the data processor.

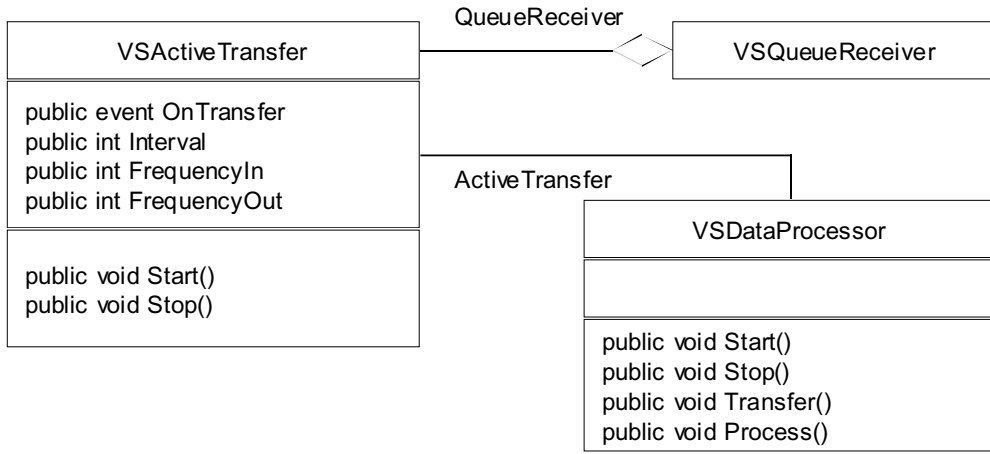


Figure 5: Class diagramm for active transfer and data processor

### ***Data organization***

Through the GUI the user works with experiments. An experiment consists of the following parameters:

- Experiment Identifier
- Comment
- Start Timestamp
- End Timestamp
- Sampling Rate
- Probe Identifier
- Raw Data Format Description

These parameters of an experiment are preliminary. In future versions an experiment scheduler will be implemented, providing different actions to be executed at certain time. Alternatively, manual triggering of stimuli will be possible.

In the following sections the graphical userinterface is introduced.

### **Main window**

The main window of the GUI is shown in Figure 6. It consists of a menu, a player/recorder panel, a visualisation tool panel, and an information tabular.



Figure 6: Main window of graphical user interface

The file menu contains the following entries:

- New Experiment
- Open Experiment
- Close Experiment
- Exit

With New Experiment a dialog is opened which is used to configure an experiment. This dialog is described in the next section. With Open Experiment an old experiment can be retrieved from disk and the data can be visualised using the tools and player panel.

From the target menu one can open or close the target. The dialog menu provides access to the amplifier setup form and to the probe setup form.

The player/recorder panel consists of buttons which are used to control the experiment. After creation of a new experiment the recording can be started. After the acquisition is stopped or after opening an old experiment one can browse through the data using the play, pause, fast forward, and fast backward button.

The main window shows the parameters of an experiment in a table.

### New Experiment

The New Experiment form is used to configure a new experiment. Each experiment should have a short descriptive name. A longer description can be added in the comment textfield. With the filename one can control where the experiment will be stored. The probe which will be used can be selected and, finally one can set the sampling rate and the input range for the incoming data. Figure 7 shows the form.

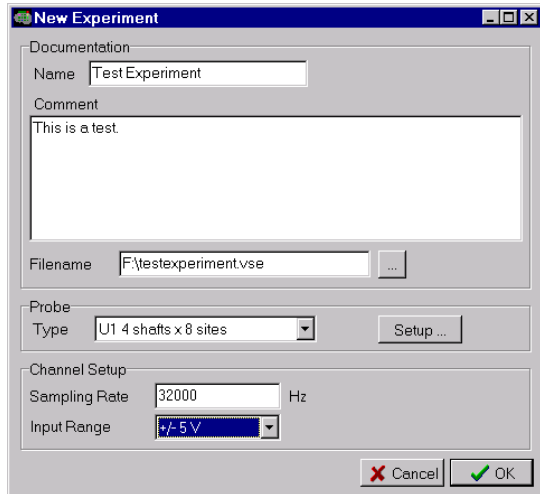


Figure 7: Configuring a new experiment

### Probe Setup:

Within the probe setup dialog new designs of probes can be entered or existing designs can be edited. The interface assumes that a probe has one or more shafts, where each shaft is occupied by a certain number of recording sites, which in turn are vertically oriented on the shaft. The position of the shaft is defined by the position of its tip. The position of each recording site is specified by the distance to the tip of the shaft. Given these informations the spatial relation of two recording sites can be derived easily.

Additionally, the mapping of recording site onto channel number is defined in this dialog. In Figure 8 the probe setup dialog is shown.

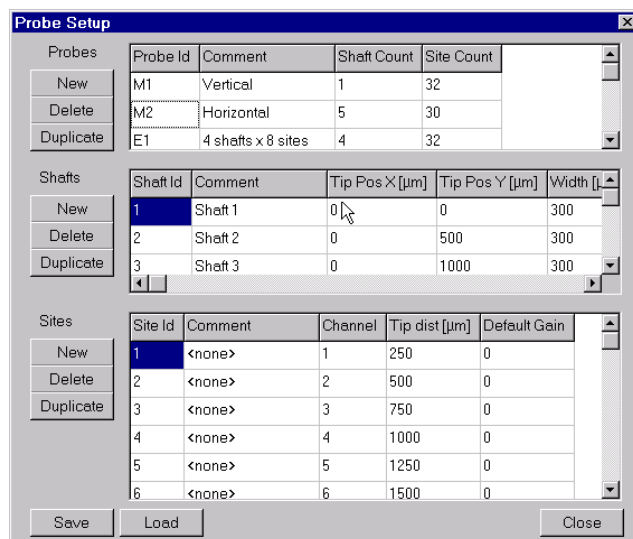


Figure 8: Probe setup dialog

### Amplifier Setup:

The gain of each site of the current probe can be set in the amplifier setup. A schema of the probe is drawn in the upper half of the window as shown in Figure 9

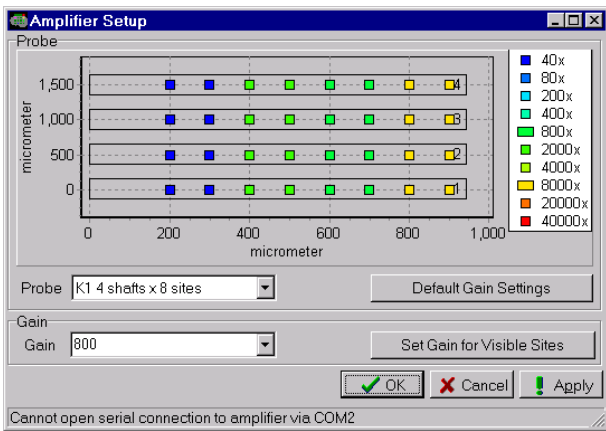


Figure 9: Amplifier setup dialog

The gain value can either be selected by using the gain combobox or by clicking onto the legend. The current setting of a gain value is indicated by different colors for each site. Each probe has a default gain value setting which can be set by pushing the “Default Gain Settings” button. A set of sites can be selected by zooming into the schema of the probe such that only the desired sites are visible. Then the desired gain can be set for these sites using button “Set Gain for Visible Sites”.

The dialog is synchronized with the setting at the amplifier, i.e. manual changes at the amplifier will be visible in this dialog.

#### **Data Visualisation:**

Currently the data is visualized either by an oscilloscope-like window or by a blueplot. Furthermore, one channel can be played using the audio device. Scope, blueplot, and audio output can be turned off independently using the ON/OFF switch at the lower left corner of each window. The gauge at the bottom of each window shows the fill state of the associated queue of this data processing module. If it starts growing, the module is not able to process the data at the speed at which it is delivered. One should consider to turn off the module in this case.

Scope:

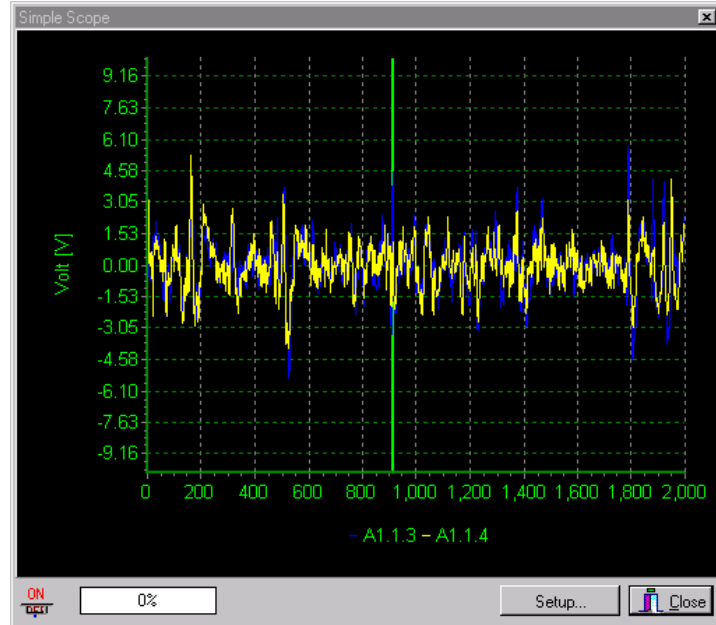


Figure 10: Simple Scope

The scope shows incoming data at a rate of 16 kHz without decimation. The scope is configured in the Scope Setup dialog - shown in Figure 11 - which provides access to the single traces of the scope. Each trace can be configured to show the signal of an arbitrary recording site. The color and linewidth is freely configurable. The scale on the y-axis is in Volt and corresponds to the input levels at the A4D4 boards. On the x-axis the offset in sample points relative to the leftmost sample point is shown.

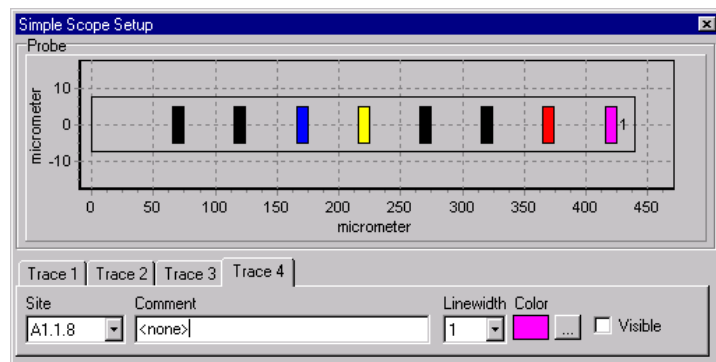


Figure 11: Setup dialog for scope

Blueplot:

The blueplot (Figure 12) shows the amplitude of each channel coded in color. The x-axis of the blueplot is labeled in the same matter as at the scope. Currently all 32 channels are shown without respect to their spatial position. This will be changed in future version where the spatial position of the recording site will be regarded.

Furthermore, a colormap is displayed. The color mapping can be controlled by mouse using the sliders in the colorbar. They define the range of data values which is mapped onto the colors. The current color resolution is set to 256, i.e. the defined range is divided into 256 bins, and each is mapped onto a different color. If the range has length zero, the sliders define a threshold.

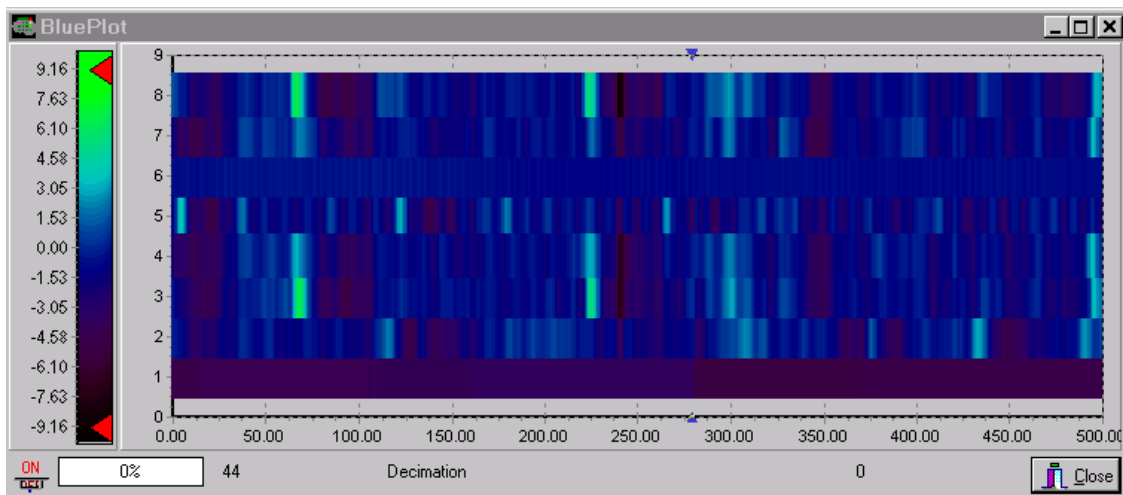


Figure 12: Blueplot

#### Audio:

One channel can be send to the audio device. In the audio dialog a site can be selected. It is shown in Figure 13.

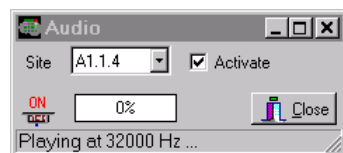


Figure 13: Audio output selection

# PROJECT DELIVERABLE REPORT

INFORMATION SOCIETY TECHNOLOGIES  
(IST)  
PROGRAMME



Project No. IST-1999-100073

Project Acronym: VSAMUEL

Work Package No. 4

Deliverable 4.2

Data Acquisition 64 channels including compression schemes

July 2002  
Software on CD-ROM

Project Title:

Development of a Versatile System for Advanced Neuronal Recordings with Multi-site  
Microelectrodes

Report prepared by:  
A. Folkers, ISIP, University of Lübeck

## 1 Introduction

The project VSAMUEL aims to develop easy-to-use instrumentation for multi-channel recordings from functioning and living nervous tissue spanning a broad range of neurobiological questions. Figure 1 presents an overview of all project partners and their tasks. The group at Acreo is developing silicon-based microelectrodes with up to 64 recording sites, Thomas RECORDING GmbH designed a 64 channel preamplifier and main amplifier, and at ISIP the data acquisition system for 64 channels is build. The whole system is evaluated by the experimental partners for different application area, i.e. peripheral nerves, cerebellum, and cortex. In this deliverable we focus on the development of the data acquisition system.

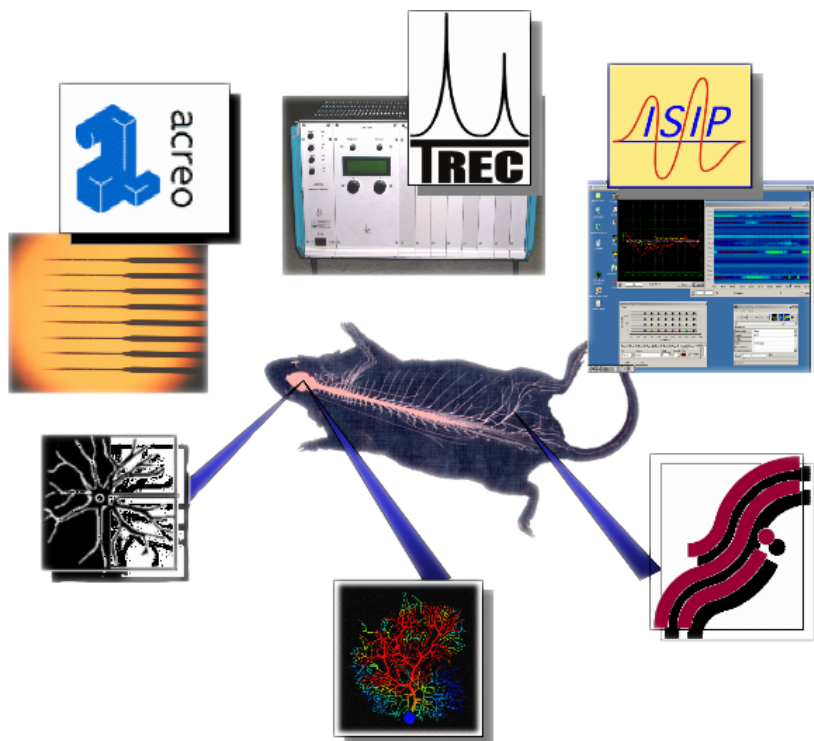


Figure 1: Overview of the project VSAMUEL. Clockwise from top left: Custom designed connectors and passive batch fabricated multi site microelectrode probes (Acreo AB, Kista), Discrete and modular multi-channel amplifier (Thomas RECORDING GmbH, Giessen), Data acquisition system, hard- and software (ISIP, University of Lübeck), and the experimental partners with their area of application, i.e. Peripheral nerves (SMI, Aalborg University), Cerebellum (BBF, University of Antwerp), and Cortex (INN Carlo Besta, Milano).



Figure 2: M67 DSP board equipped with two analog digital conversion modules

## 2 Hardware Overview

The data acquisition system is based on off-the-shelf DSP boards (M67) residing in a modern personal computer running Windows NT/2000. Each DSP board can be extended with analog digital conversion (ADC) modules. We are using two AD16 modules per board, which together provide the ability to record from 32 channels simultaneously without multiplexing. DSP Boards and the AD conversion modules are manufactured by Innovative Integration, California, USA. Figure 2 shows the board equipped with ADC modules.

The M67 board has a single digital signal processor, i.e. a TMS3206701 processor (Texas Instruments, Dallas, TX, USA) clocked at 160 MHz with 128KB onchip memory. The CPU is provided with three different types of external memory: asynchronous SRAM (ASRAM, 512KB), synchronous DRAM (SDRAM, 16 MB), and synchronous burst SRAM (SBSRAM, 1MB). Furthermore, it has different external timers, interfaces for digital input or output, and a FIFO port for communication with other boards.

The AD16 module provides the M67 board with 16 channels of high speed 195 kHz, 16-bit resolution analog input to digital output conversion (A/D) per module site. There are 16 A/D converters for simultaneous conversion on all channels. Each of the 16 input channel consists of a high precision, DC accurate sigma-delta A/D converter (AD7722, Analog Devices, Norwood, MA, USA) with front end conditioning circuitry, which removes the need for multiplexers. The A/D converters are clocked either using a DDS timer of the M67 board or an external clock. Conversion results are transferred into a FIFO (this FIFO has no connection with the FIFO port of the M67) which can store up to 512 16-bit samples. The AD16 triggers an interrupt of the DSP when the FIFO contains a certain amount of samples. Usually this threshold is set to half of the samples which can be stored in total. This interrupt is serviced by a routine running on the DSP which fetches the data from the FIFO and stores it into the onchip memory using a DMA transfer. The block scheme in Figure 3 shows the arrangement of the hardware components and the data flow for one DSP board.

The boards are connected with the host system via the PCI bus. The current host

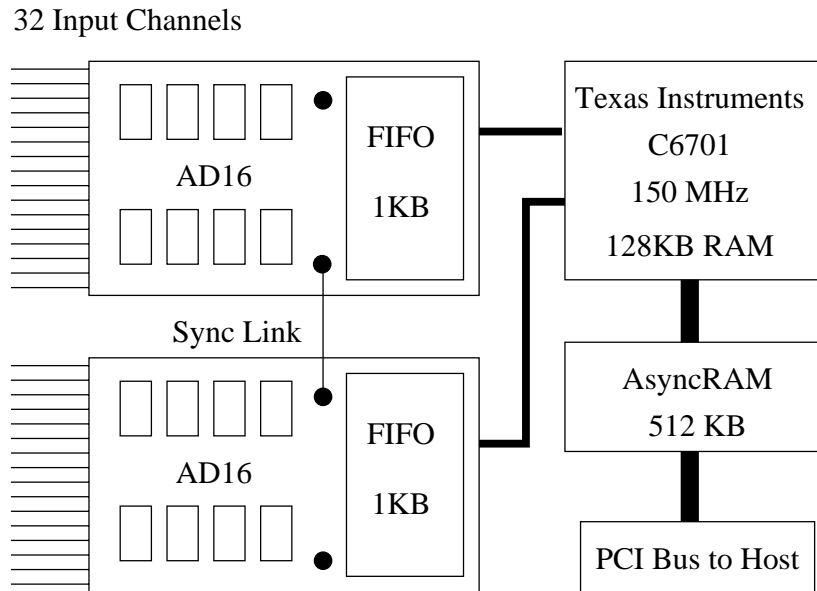


Figure 3: Hardware Overview

system consists of a 1GHz Pentium III with 256 MB SDRAM (Synchronous DRAM) on DSM Slot CPU. It has two SCSI harddrives IBM DPSS-336950N with 36 GB storage each.

## 2.1 Add-ons for 64 channel data acquisition

The data acquisition system for 64 channels needs two M67 boards both equipped with two AD16 modules. Simultaneous data acquisition with two boards requires synchronization of the AD conversion hardware. This is done by two different means.

First, the clocks of the DSP boards that drive the AD16 modules must be synchronized. The M67 board has a connector for a so called Sync-Link cable which provides the clock signals of one board to another board. We call the board which provides the clock signals *master* and the other is called *slave*. When synchronized the master board DDS timer clock signal is also used by the slave board, which then ignores its own DDS timer. Thus, all four AD16 boards are using the same clock. Note that the clock rate ranges from

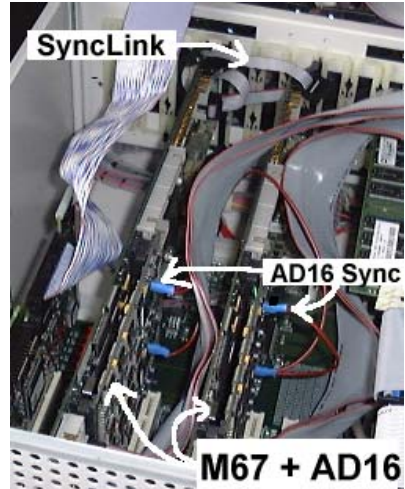


Figure 4: Synchronization Cabling for two DSP Boards

640 kHz to 6.4 MHz. Therefore, the SyncCable should be as short as possible in order to prevent the clock signal from being distorted.

Second, the single AD converters on the AD16 modules need to be synchronized with each other as well. For this purpose each AD16 module has a SyncOut and a SyncIn pin. The AD16 modules are connected in a row using these pins, whereby the first AD16 in the row functions as master which triggers the synchronization. All other modules use the sync signal generated by the master AD16.

Figure 4 illustrates how the synchronization connections are made. Both mechanism together make a simultaneous AD conversion on all 64 channels possible.

## 2.2 Connection between main amplifier and AD conversion modules

The interface of the AD16 module for analog input signals is a 50 pin latch connector. Each AD converter on the AD16 module has two input lines, therefore 32 pins of the latch connector are used for the 16 differential AD converters. On the other hand, the main amplifier provides 64 single-ended analog signal lines in form of a 68 pin SCSI plug. The remaining four pins are connected to analog ground. In order to connect the main amplifier to the 64 channel data acquisition system we need an adapter from 68 pin SCSI onto the four 50 pin latch connectors of the four AD16 modules. Thus we have designed a so called *SCSI to Latch board* which performs just this adaptation. Hereby, all minus input line of the AD converters are connected to the same ground and the plus input lines are connected to a channel from the main amplifier.

### 3 DSP Application

The DSP application is the program which runs on the DSP board. It has four major tasks:

1. acquire data from analog input channels,
2. process the data,
3. transfer the data to host, and
4. react on commands.

The software structure reflects these tasks by having four main modules, one for each task. In the following we discuss each module.

#### 3.1 Data Acquisition Module

The data acquisition is driven by interrupts. It reacts on the FIFO "threshold reached" interrupts of the AD16 modules. After both modules have triggered the interrupts, two DMA<sup>1</sup> transfers are started which transfer the data from both FIFOs into the DSPs internal memory. Here the data is stored into so called frames. A frame consists of several sample point blocks, whereby a sample point block contains the samples from all channels taken at the same point in time. After a frame has been filled it is passed to the processing module. The data is processed and then the frame is passed to the transfer module, and finally back to the data acquisition module. The exchange of frames is implemented by means of frame queues. There are three such queues which contain either empty frames, filled frames, or processed frames. Figure 5 shows the data flow within the DSP application.

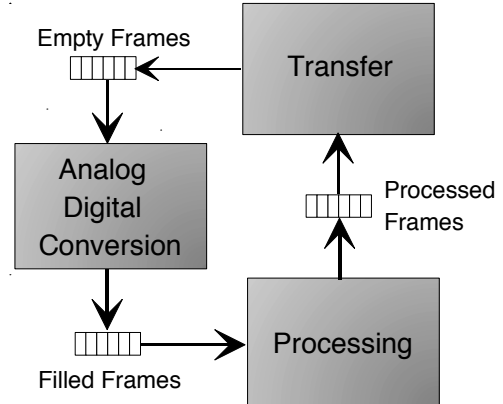


Figure 5: Frame Management within DSP application

#### 3.2 Processing Module

The acquired data can be processed differently. We have implemented a short time Fourier transform for a single channel. Furthermore the data can be filtered by an IIR filter on all 32 channels. We are currently developing a signal processing framework based on the wavelet transform. Within this framework the DSP will perform the decomposition of the signal into its wavelet coefficients (see also Section 5.2).

<sup>1</sup>DMA denotes Direct Memory Access, which is a mechanism to transfer data without using the main CPU

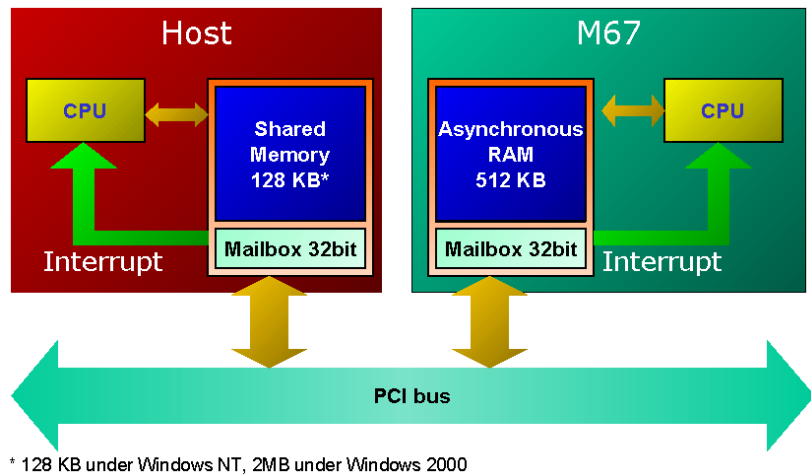


Figure 6: Communication channels between host and target

### 3.3 Communication between host and target

Host and targets, i.e. PC and M67 boards, respectively, are connected via the PCI bus. Data can be transferred from host to target and vice versa. There are two mechanisms one for small messages and one for large amounts of data which are illustrated in Figure 6.

First we focus on the transfers of large amounts of data. The target can read from or write into a shared memory section within the host. Data transfers are always performed via the Asynchronous RAM (ASRAM) on the target, i.e. for transfers from target to host the data must be read from ASRAM, and for transfers from host to target the data is received in the ASRAM. The M67 can perform busmaster transfers, i.e. data can be read or written without burdening the target or the host CPU. Instead, transfers are executed by a special controller chip, the V360 PCI to local bus bridge (V3 Semiconductors). After the transfer has been completed the controller notifies the target by triggering an interrupt.

For small messages we use a mailbox system. A *mail* is a 32 bit value. The board supports two mailboxes. They can be accessed in a synchronous way: For example, if we want to send a message to the target, then we can write the value into the mailbox on the host and it is sent to the target. Now the target must read the mailbox before a new value can be written by the host. If the target tries to read the mailbox when no message has been sent by the host, the target is blocked until a value is available. Using these mailbox functions, target and host can be synchronized. But synchronous communication is error prone, because messages need to be sent in the correct order which introduces a great dependency between target source code and host source code. This is why we do not use the synchronized mailboxes. Instead, we use an asynchronous approach which is also supported. A write to a mailbox can trigger an

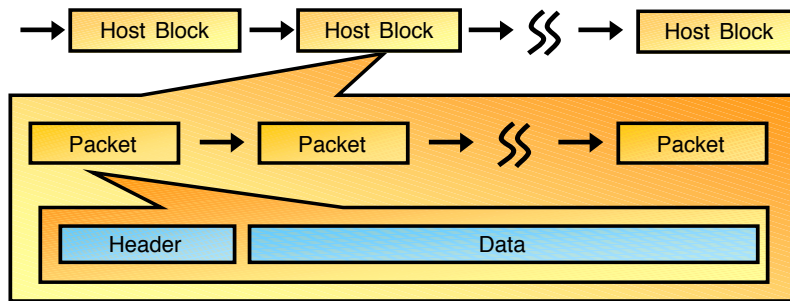


Figure 7: Data Transfer Protocol

interrupt. Thus the host can interrupt the target and also the other way around, the target can interrupt the host. By using the interrupt signal we do not need to check for new messages actively, which saves valuable cpu cycles.

### 3.4 Data Transfer Module

After processing, or after acquisition, if only raw data is requested, the data must be transferred to the host. This task is implemented in the data transfer module. Since busmaster transfers, as described in the previous section, have to use the ASRAM as source for transfers into the shared memory on the host site, the first step is the transfer of the acquired data from internal DSP memory into the external ASRAM (see also Figure 3). Hereby the data is put into packets. Each packet has a header and a data section. The header contains information about the data, like e.g. the size, whether a trigger signal has been received, the type of the data, and a consecutive number of the packet. Several packets together form a host block. After a host block has been transferred from target to host, the target notifies the host using the mailbox communication so that it can fetch the new host block. Note, that we start a new busmaster transfer for each packet, but notify the host not until a complete host block has been transferred. This is done in order to keep the number of events which are generated by the notification as low as possible. Figure 7 illustrates the data organization of the busmaster transfers.

### 3.5 Commands Module

In the DSP application a single task, the control task, receives messages sent by the host and also sends messages to the host. The 32 bit messages have three parts: a receiver tag (8 bit), a command tag (8 bit), and a data part (16 bit). The control task routes the messages according to the receiver tag. In order to set the sampling rate within the ADC module the host sends a message with receiver equal to `ADC_MODULE`, command is `SET_SAMPLING_RATE`, and the data contains the sampling rate. In case that the value exceeds the 16 bit of the data part, we use two or more messages.

### 3.6 Extensions for 64 channel data acquisition

The acquisition from 64 channels is implemented by using two DSP boards. Therefore, we have two instances of the DSP application. As described in Section 2.1 we have a master board and a slave board. Similarly we also have a master DSP application and a slave DSP application, which run on master and slave board, respectively, and differ in some details. On data acquisition start command the master DSP application initializes the DDS timer and synchronizes the ADCs on the AD16 modules, while the slave DSP application does not perform these steps. Despite these details both DSP application are identical. Note, that the start command must be sent to the slave DSP application first, to ensure that it is ready for acquisition when the master DSP application enables the timer.

## 4 Host Application

The host application provides a user interface through which new experiments can be created and old experiments can be reviewed. It has several means of visualization, e.g. a virtual scope, a blue plot, and a spectrogram. The host application receives the data from the target and stores it into a file on hard disk together with an experiment documentation file. The experiment documentation includes an experiment identifier, a global comment, an experiment log book, the sampling rate, the used probe and amplification settings. In review mode the user can browse through the data of an old experiment using controls similar to controls of a CD player. Recapitulating the host application performs three main tasks:

- Data reception and storage,
- Data organization, and
- Data visualization.

### 4.1 Data flow

The data, acquired or computed by the DSP applications, is send to the host via the PCI bus. The reception of data is driven by events. The events are generated within the software library from Innovative Integration every time the DSP application sends a notification mail which indicates that a new host block has been stored in the shared memory. The host application copies the data from the host block in shared memory into the entry queue of the respective board which sent the data. The data of the entry queues is merged into the main queue (see also Figure 6 and Section 3.4). From this queue the data is distributed to different software modules, which e.g. store or visualize the data. Figure 8 illustrates the flow of data within the host application. The data flow in replay mode is quite similar. Instead of receiving data from the DSP application, the data is retrieved from a file on hard disk and then put into the main queue.

The distribution is centralized with a so called queue transmitter which is associated with several queue receivers. The queue transmitter can access the main queue and transmits data from this queue to its associated queue receivers. A queue receiver can be dynamically associated and deassociated with the queue transmitter. Each queue receiver has an own queue into which the data is copied. The queues used by queue receivers and the queue transmitter are instances of VSDataQueue. This class has several features. First it organizes its data in data blocks. This is e.g. used to have a transparent access to complete sample points which contain multiple samples, i.e. 32 when acquiring data from 32 channels. The data queue would be configured to access its data in blocks of length 32. The VSDataQueue maintains 64 bit counters for the head and tail of the queue. These counters are e.g. used as unique time stamps for sample points throughout a whole experiment, because even at a sampling rate of 50 kHz they do not wrap until 11 million years. VSDataQueue keeps track of its new

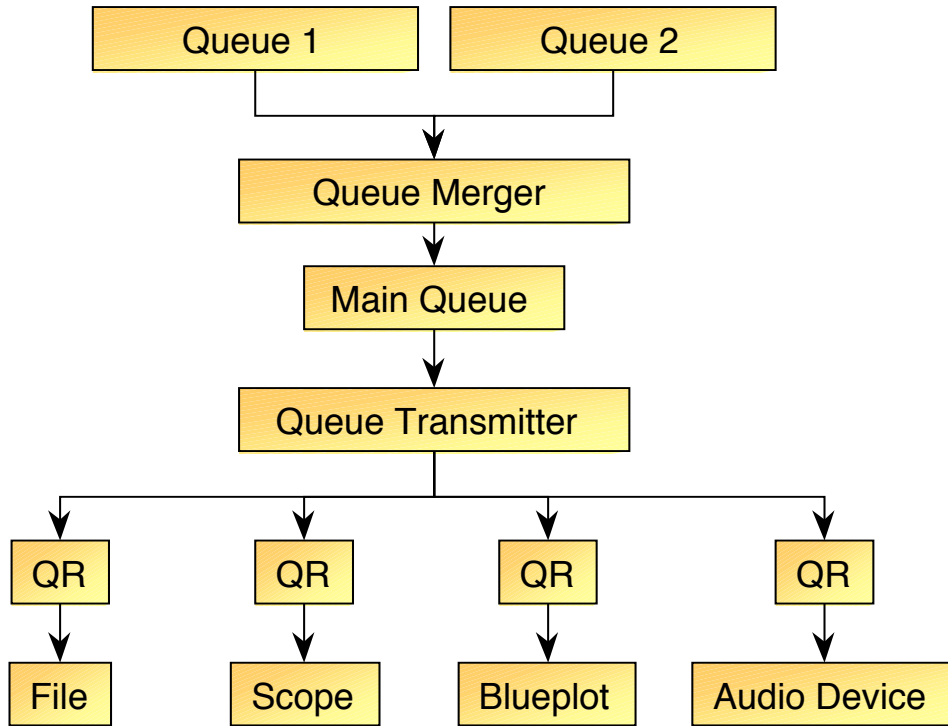


Figure 8: Data flow within host application. The data arrives via the PCI bus and is stored into queue 1, when it comes from the first DSP board, or into queue 2 if it was sent by the second DSP board. The data of both queues is merged by the queue merger and then put into the main entry queue. From here, the queue transmitter copies the data to its associated queue receivers (QR) which in turn provide it to their respective visualization module.

data blocks, i.e. it distinguishes between data that was already read and data which was enqueued but not read. It provides a pointer to the next new data block. The VSDDataQueue has a stop index, which indicates up to which data block data should be enqueued. Usage of the stop index can be turned on and off. Finally, a VSDDataQueue can transfer its data to another queue with support of decimation. The decimation feature is e.g. used to support different time scales in the scope or in the blue plot.

## 4.2 Dialogs and visualization modules

In the following sections we describe the graphical user interface of the data acquisition software.

#### 4.2.1 Main Window

After the program has been started the main window appears. The main window has a menu bar with three items: File, Target, and Dialog. In the File menu one can create, open, save, and close experiments. Furthermore, the program can be closed. The Target menu can be used to open and close a DSP board, to select a special DSP application and to initialize the DSP board and run the DSP application. One can test whether the DSP application is working properly or not with menu item "Is Alive?". The result is shown in the status bar. If no target is opened, it is possible to select one board at menu item Select Target, after selection the respective board is opened and the DSP application is started. Success is indicated by a message in the status bar. Before starting a new experiment the DSP application must run. From the Dialog menu one can open the Probe Setup Dialog and the Amplifier Setup Dialog (see Section 4.2.4 and Section 4.2.3).

The New Experiment menu item brings up a dialog which is described in Section 4.2.2. When a new experiment has been created and the DSP application has been properly initialized, data acquisition may be started by pressing either the Play or the Rec button. If the data acquisition is started with the Play button, data is acquired but not stored to disk. This mode may be used to view the current signal. Start the acquisition with Rec button in order to acquire data into a file on hard disk. By pressing Play button in record mode and Rec button in play mode one can switch between both modes, respectively. During acquisition different visualization modules can be used to display the data. Table 1 shows which button activates which module. The acquisition is stopped when the user presses the Stop button. Then by default, the experiment is opened and can be reviewed. Note, that it is only opened successfully, when data was actually recorded to disk. If not, the message "Experiment has no rawdata" appears in the status bar and the application is ready to open another experiment or create a new one.

To review old experiments the user needs to open it: use the File|Experiment Open menu item and select a \*.vse file in the file selection dialog. If the experiment was opened successfully, replay can be started by pressing the Play button. The scrollbar can be used to jump to specific positions within the file. Press the left or right arrows to move in small steps (50 ms) backward or forward, respectively. For large steps (250 ms) click into the area beside the thumb of the scroll bar. The replay speed can be changed using the speed track bar. Note, that the speed trackbar changes the number of sample points which are displayed per second and not the time scale. It can be reduced down to zero, i.e. replay pauses. The maximum speed is equal to the actual sampling rate.

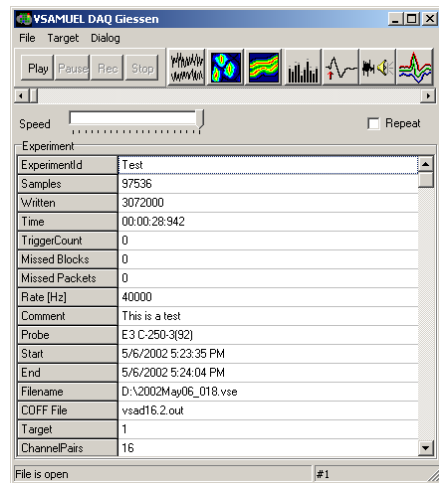


Figure 9: Main Window

	Virtual scope		Scope for triggered acquisition
	Blue plot		Audio output dialog
	Spectrogram in time frequency mode		Spike plot
	Spectrogram in waterfall mode		

Table 1: Activation of visualisation voudles

Check the repeat check box, when replay should start from the beginning if the end of file is reached.

When the speed is set to zero, the visualization modules are not updated, even if the position within the file is changed with the scroll bar. However, the visualization modules are updated, when replay is paused by pressing the Pause button. One can switch from pause mode into play mode with the Play button.

Different kind of information about the experiment is shown in the table of the main window. During acquisition one can see the number of samples which have been acquired, and how much data has been written to disk. There is a timer, indicating how much time has elapsed since the beginning of the acquisition.

The visualization modules are opened with the buttons at the upper right corner of the main window. Table 1 lists for each icon the respective visualization module. A visualization module is closed by pressing the respective button if it is already open.

#### 4.2.2 New Experiment

In the new experiment dialog (Figure 10) the user can change the parameters which are described below. Press button OK to accept the experiment settings. A new experiment is created and the DSP application is initialized appropriately. If this was sucessfull, a message in the status bar of the main window indicates how to proceed, i.e. press the Play or Rec button to start acquisition, or press the Stop button to cancel. Close the dialog New Experiment with button Cancel, when no new experiment should be created.

**Name** Experiment identifier

**Comment** A comment which should summarize the overall setting of the experiment

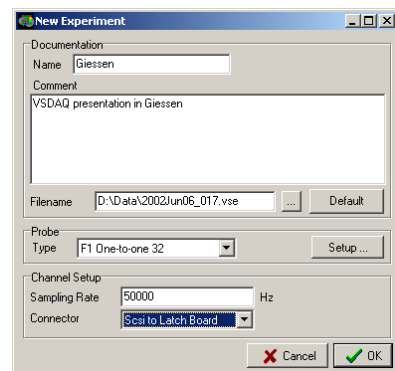


Figure 10: Configure a new experiment

**Filename** File where the experiment will be stored. There are two files per experiment. The .vse file which contains the experiment description, and the .rawdata file which contains the raw data. The name is generated by default using the structure <year><month><day>\_<number>. One can also select a filename in a file select dialog (push button with the three dots), or enter a name manually. Pressing the button Default generates a default name.

**Probe Type** Select the probe which is used in the experiment. New probes can be added in the probe setup dialog which is opened by button Setup.

**Sampling Rate** Enter the sampling rate at which the data should be acquired. The rate can range between 5 kHz and 50 kHz.

**Connector** Select the kind of connection used between DSP board and main amplifier. This parameter is used for internal remapping of the channels, which is necessary because channel 1 of the amplifier must not necessarily connected with channel 1 of the DSP board. In the current setting we use a custom designed connector, the so called SCSI to Latch Board which adapts the SCSI connector coming from the main amplifier to the latch connectors used for input into the DSP board (see Section 2.2).

#### 4.2.3 Probe Setup

Within the probe setup dialog new designs of probes can be entered or existing designs can be edited. The interface assumes that a probe has one or more shafts, where each shaft is occupied by a certain number of recording sites, which in turn are vertically oriented on the shaft.

Therefore, the dialog shows three lists: At top the list of probes, in the middle the list of shafts of the currently selected probe and at the bottom the list of recording sites of the currently selected shaft. In the table which has the input focus the currently selected item is marked by a dashed line around a cell in the row, in both other tables the selected items are

marked by a blue background of one cell in the row. On the left of each table there are three buttons, which create a new item, delete an item, or duplicate an item in the respective table. For example to enter a new probe of type E1 one would select a present instance of E1 and duplicate it. It is appended at the end of the list of probes and can be selected. Now one can enter a new comment or number and modify the

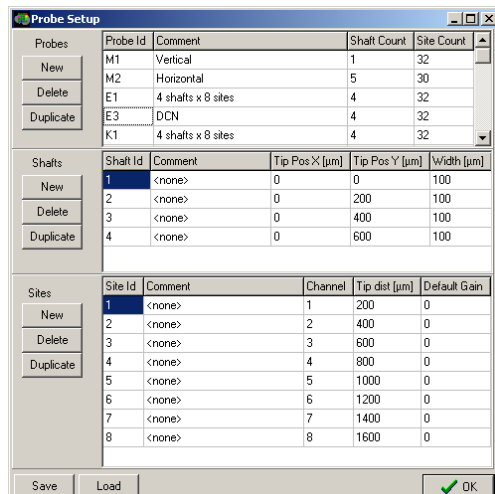


Figure 11: Probe setup dialog

shaft and site configuration with respect to the acutal probe. The position of the shaft is defined by the position of its tip. The position of each recording site is specified by the distance to the tip of the shaft. Given these informations the spatial relation of two recording sites can be derived easily. Additionally, the mapping of recording site onto channel number is defined in this dialog. Note, that channel numbers start at 1.

#### 4.2.4 Amplifier Setup

The gain of each site of the current probe can be set in the amplifier setup. A schema of the probe is drawn in the upper half of the window as shown in Figure 12. The gain value can either be selected by using the gain combobox or by clicking onto the legend. The current setting of a gain value is indicated by different colors for each site. Each probe has a default gain value setting which can be set pushing the Default Gain Settings button. A set of sites can be selected by zooming into the schema of the probe such that only the desired sites are visible. Then the desired gain can be set for these sites using button Set Gain for Visible Sites.

The dialog is synchronized with the setting at the main amplifier, i.e. manual changes at the amplifier are visualized by the dialog and vice versa. Manual changing of the gain at the main amplifier can be locked using the button Lock. The button indicates the current state by showing the text "Locked" or "Unlocked". The gain settings are transferred to the amplifier when the Apply button is pressed.

#### 4.2.5 Blueplot

The blueplot shows the signal on all channels simultaneously. Hereby the amplitude of each channel is coded by color. On the x-axis the time scale is shown, and the y-axis indicates the sites of the probe. The blueplot arranges signals from the sites with respect to their spatial arrangement, i.e. the channels from one shaft are displayed in a group.

On the left a colormap is displayed. The color mapping can be controlled by mouse using the sliders in the colorbar. They define the range of data values which is mapped onto the colors. If the range has length zero, the sliders define a threshold. It is also possible to change the color map using the combo box at the bottom of the color bar.

#### 4.2.6 Spectrogram

The spectrum of a single channel is visualized with the spectrogram. The selected channel is transformed by a short time windowed Fourier transform and the log magnitude of the coefficients is displayed, with respect to the selected mode. The spectrogram

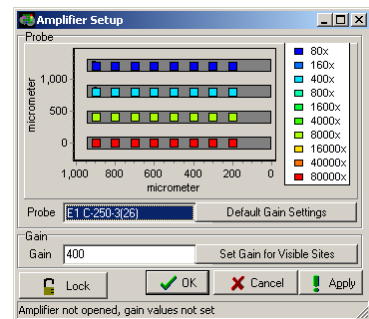


Figure 12: Amplifier setup dialog

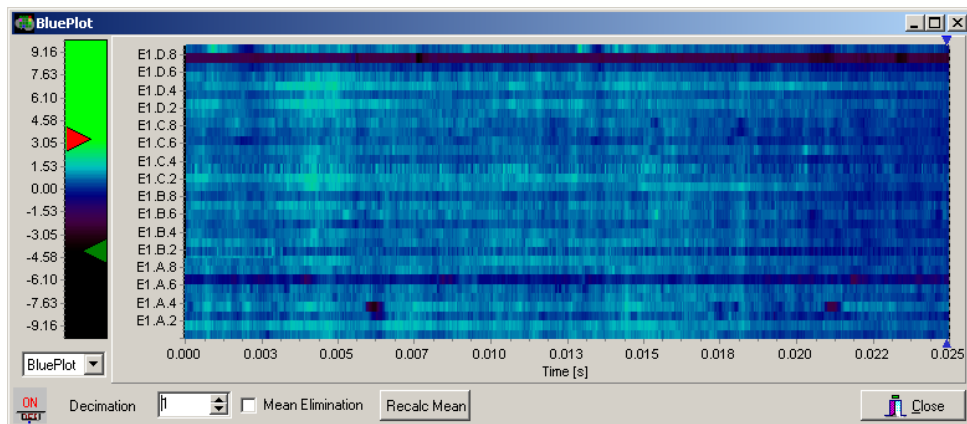


Figure 13: Blueplot

has two modes: the time frequency mode and the waterfall mode which are shown in Figure 14 and 15, respectively. In time frequency mode the time scale is on the x-axis and the frequency on the y-axis. The log magnitude of the coefficients is coded into a color. This color mapping can be adjusted with the color bar on the left side. The time frequency mode visualizes the spectrum over a long period of time. In waterfall mode the frequency is indicated by the x-axis and the log magnitude on the y-axis. The magnitude of each coefficient is represented by a bar of respective height. Each bar has a little dot on top which indicates the maximum of this bar during the last few windows (currently three windows, at a window size of 512 samples for the Fourier transform). We provide five different windows, i.e. Rectangle, Hanning, Hamming, Blackman, and Bartlett window (see also Section 5.1). The waterfall mode shows the spectrum only over a short period, but visualization of peaks is better then in the time frequency mode.

The spectrogram is useful to locate noise sources which cause peaks at certain frequencies. The example in Figure 14 shows peaks at 19.5 kHz and at 15.8 kHz, while in Figure 15 a peak at 24 kHz is present. This can be at least give a hint which device might cause the noise.

#### 4.2.7 Scope and Scope Setup

With the scope (Figure 16) one can visualize the signals of several selected recording sites. The scope has a multiple traces (currently 32), and each trace has independent settings for recording site, color, scale, and line width. These parameters are set in the scope setup dialog (Figure 17). The traces can be spread or overlaid by the track bar on the right of the scope setup dialog. A recording site is assigned to a trace by selecting it in the probe schema or in the site combo box. A scope setup can be stored into a file and retrieved by using the save and load buttons, respectively. The scope is reset back into its initial state by the reset button. The trace which displays a recording site

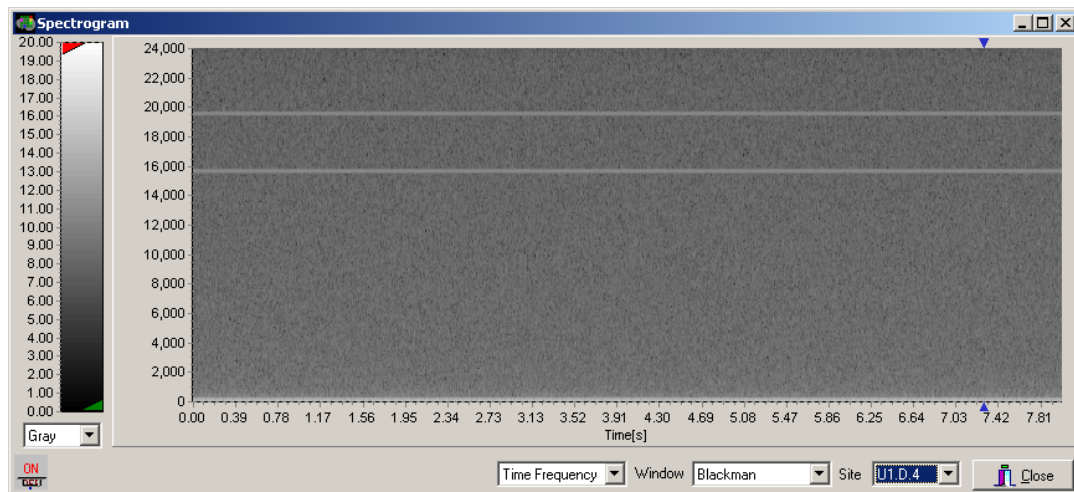


Figure 14: Spectrogram in time frequency mode

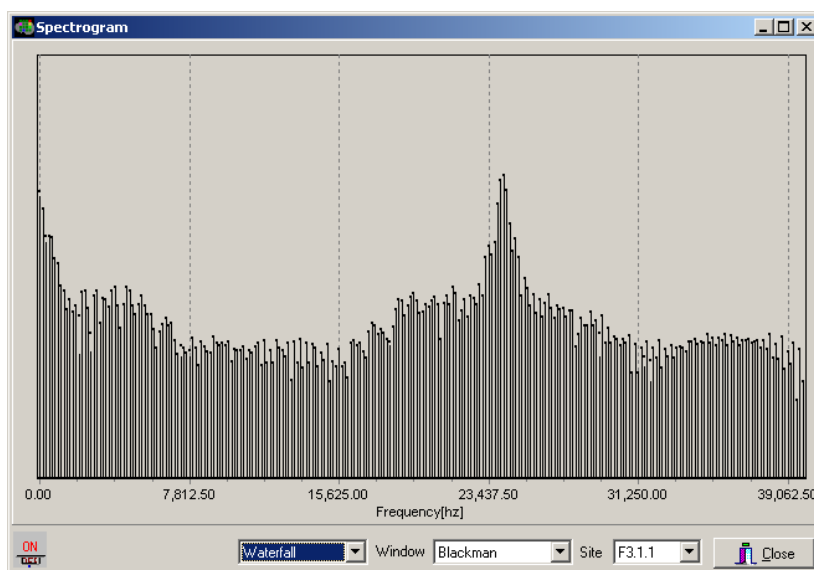


Figure 15: Spectrogram in waterfall mode

can be selected by clicking with the right mouse button on this site within the probe schema.

The scope has a zoom feature, i.e. the user can select a rectangular region within the scope axis, which is in turn enlarged. The region is specified by pressing the left mouse button at the upper left corner of the rectangle and holding it while the mouse is moved to the lower right corner, which is pinned down by releasing the left mouse button. Note that it is important to specify the upper left corner first, because specifying any other corner first invokes the unzoom function.

The time scale of the scope can be changed with the decimation control. A decimation value of  $k$  means that only every  $k$ -th sample is visualized. In terms of time scale we enlarge the time scale on the x-axis by a factor of  $k + 1$ .

As an experimental feature it is possible to denoise a single channel from within the scope. Please note, that this feature is not meant to be permanently included into the scope in this form. In fact it is just included for debugging and testing the wavelet denoising methods. This is why a few restrictions apply in order to let the denoising work properly. First just one trace is allowed to be active. Two active traces will spoil the result. The decimation should be set to zero, because otherwise the denoising module will not receive the full signal but an downsampled version and will therefore not return the expected results. When denoising is enabled a red trace will appear which shows the result. Note, that the denoising module introduces a delay of the signal, that depends on the depth of the filter bank. The input signal is also shown with this delay, such that direct comparison of both signal and denoised signal is possible. If the signal was sampled at a high rate then it might be necessary to reduce the replay speed, because at full speed not all data is visualized and therefore

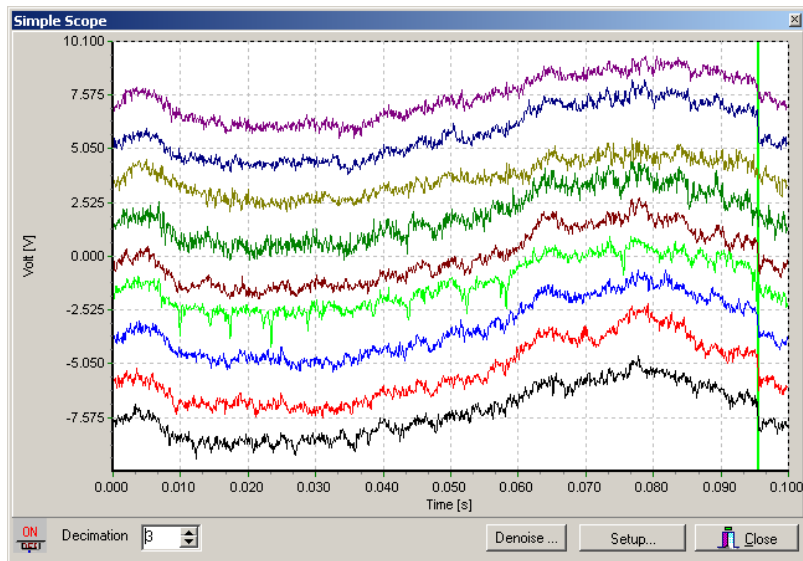


Figure 16: Scope with showing selected channels of the 32 channel probe

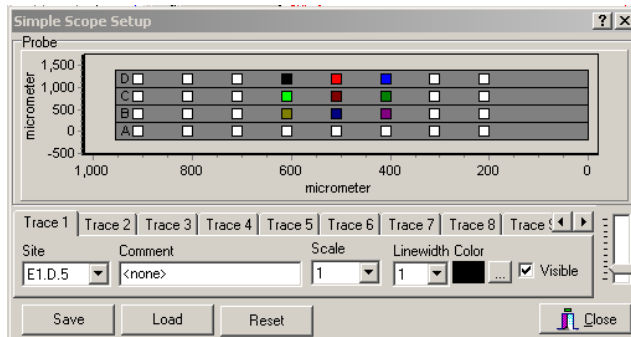


Figure 17: Scope setup dialog

the denoiser does also not get the full signal. This causes visible jumps in the result. The denoising setup dialog is described in a separate section, i.e. Section 4.3.

#### 4.2.8 Audio

The signal from a single recording site can be selected for audio output in this dialog (Figure 18). Note, that in replay mode the speed must be set to maximum, in order to have a gap free audio output. As maximum sampling rate 48 kHz are allowed, which is supported by modern sound boards. If the actual sampling rate is higher, then audio output is not possible.

The signal can be filtered using a wavelet decomposition to eliminate selected frequency bands (see Section 5.4). The filter is configured with the filter setup dialog shown in Figure 19. First, a wavelet can be chosen, whereby currently only the Daubechies 2 wavelet is supported. Next, the decomposition level must be specified. This number determines into which frequency bands the signal is decomposed by the wavelet filter bank. A frequency band is kept when the check box is checked or eliminated if the check box is unchecked.

#### 4.2.9 Spike Plot

In the spike plot (Figure 20) the spikes of a single recording site are visualized. Hereby the maximum and minimum hull, and the average over all spikes is shown. The detection of spikes is implemented with a threshold. This threshold can be determined

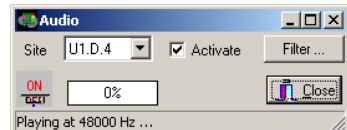


Figure 18: Audio output dialog

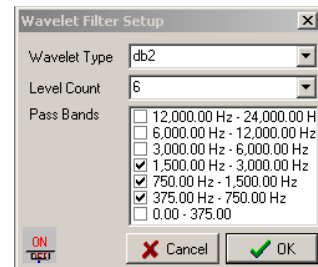


Figure 19: Wavelet filter setup dialog

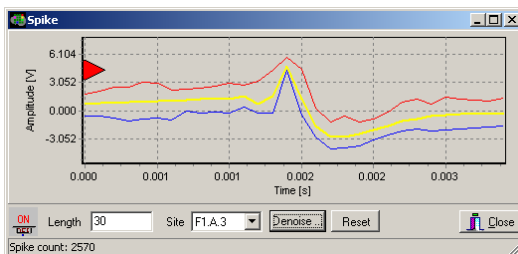


Figure 20: Spike plot



Figure 21: Trigger scope

with the red and green triangles on the left axis which correspond to a maximum or minimum threshold, respectively. Note, that usually only one of them should be used. If a threshold is changed the spike plot is cleared automatically. To clear it manually push the Reset button. The length of the snippets around a spike in sample points can be set in the Length edit field. Select the recording site with the combo box. The Denoise button opens the wavelet denoise setup dialog.

#### 4.2.10 Trigger Scope

The trigger scope is used for triggered data acquisition. The DSP application detects the trigger signal and marks the corresponding sample point. The host application uses these marks and visualizes the signal around the trigger in the trigger scope. The presented signal can be manually accepted or discarded by the user. The pre and post trigger period is configured in the trigger setup dialog. Furthermore, the number of sweeps over which the average is computed can be specified. The setup of the trigger scope is the same as the setup for the scope described in Section 4.2.7. In Figure 21 the trigger scope is shown: the green line indicates the trigger point of time and the black line is the trigger signal which was also recorded.

### 4.3 Wavelet denoising setup

The wavelet denoiser as described in Section 5.4.2 has several parameters which are set in the wavelet denoising setup dialog. The setup dialog is depicted in Figure 22 and shows the specific setup which was used to obtain the result in Figure 23. In particular the following parameters can be set:

**Wavelet Type** Select the actual wavelet, such as e.g. "Daubechies 2". Currently only "db2" is supported.

**Level Count** Select the number of levels of the wavelet decomposition. This number determines the number of frequency bands available. You can select levels from 1 to 6.

**Window Length** The window length is the number of samples which should be used to estimate the thresholds. Note, that some threshold estimators only use the window length and the noise estimation.

**Threshold Estimator** There are four different strategies available to estimate the thresholds, i.e. MiniMaxi, VisuShrink, Sure, SureShrink. For a detailed description refer to Section 5.4.2

**Threshold Method** Either "hard" or "soft" can be selected. Hard threshold means that all coefficients less than the threshold are set to zero and all others are kept as is. In case of soft thresholding the magnitude of coefficients which are greater than the threshold is reduced by the threshold.

**Thresholding Mode** Choose between continuous or single. In continuous mode the thresholds are computed for each window, in single mode the thresholds are computed for the first window and then used for the subsequent windows without change. One can force a recomputation by pressing button "Recalc".

**Threshold** The current thresholds with their respective frequency band are shown and can be changed by the user. The thresholds can range between 0 and 32768. However in continuous mode they keep on changing, and therefore manual change of the thresholds make only sense in single mode. In particular the threshold for the lowest frequency band can be set to 32768 in order to obtain a high pass filtered denoised signal.

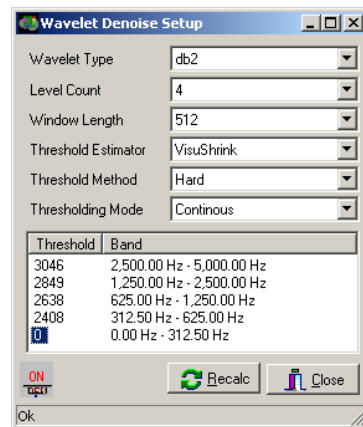


Figure 22: Wavelet denoising setup

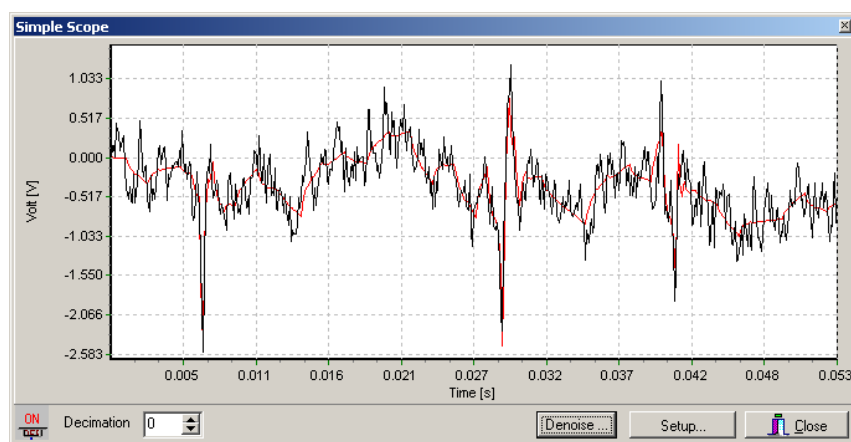


Figure 23: Wavelet denoising

## 5 Online Processing

### 5.1 Fourier transform

The computation of the short time Fourier transform has been implemented within the DSP application and also within the host application. The short time Fourier transform is implemented by a fast discrete Fourier transform applied on certain time window of the signal. Thus we compute the coefficients  $S_{w,d}(k)$  which depend on the window function  $w$  and the time window of signal  $s(n)$  selected by offset  $d$ :

$$S_{w,d}(k) = \sum_{n=0}^{N-1} s(n+d)w(n)e^{-j(2\pi/N)nk}$$

The length  $N$  of the window is chosen as a power of 2, and it determines the resolution in frequency domain, i.e. the width of the frequency band represented by a single Fourier coefficient. We provide different windows taken from [2], which are described in the following, whereby  $M = N - 1$ :

#### Rectangular

$$w(n) = \begin{cases} 1, & 0 \leq n \leq M, \\ 0, & \text{otherwise} \end{cases}$$

#### Bartlett (triangular)

$$w(n) = \begin{cases} 2n/M, & 0 \leq n \leq M/2 \\ 2 - 2n/M, & M/2 < n \leq M \\ 0, & \text{otherwise} \end{cases}$$

#### Hamming

$$w(n) = \begin{cases} 0.54 - 0.46 \cos(2\pi n/M), & 0 \leq n \leq M, \\ 0, & \text{otherwise} \end{cases}$$

#### Hanning

$$w(n) = \begin{cases} 0.5 - 0.5 \cos(2\pi n/M), & 0 \leq n \leq M, \\ 0, & \text{otherwise} \end{cases}$$

#### Blackman

$$w(n) = \begin{cases} 0.42 - 0.5 \cos(2\pi n/M) + 0.08 \cos(4\pi n/M), & 0 \leq n \leq M, \\ 0, & \text{otherwise} \end{cases}$$

The Fourier coefficients are used by the spectrogram visualization module.

## 5.2 Wavelets

In this section a short introduction into wavelets and the wavelet transform is given. As W. Sweldens indicates in [3] it is hard to give the definition of a "wavelet", but they could be vaguely described with the following sentence:

"Wavelets are **building blocks** that can **quickly decorrelate** data"

This sentence reflects three of the main features of wavelets. First, we can see them as *building blocks* for general data sets. More precisely, an arbitrary set of data can be represented by a linear combination of wavelets. And even more precisely, if we denote wavelets by  $\psi_j$  and the coefficients by  $\gamma_j$ , a general function  $f$  can be written as:

$$f = \sum_j \gamma_j \psi_j$$

The second property is the capability of wavelets to *decorrelate* data. In other words the coefficients  $\gamma_j$  can provide a more compact representation of the data. This feature is e.g. very useful for compression of the data. We only need to store the few coefficients that contain the main information, while we are still able to get a good approximation of the original data. In order to obtain a good decorrelation of the data, the respective wavelet should be constructed such that it resembles the data in some way.

Finally, as third property, we want to have quick algorithms for the computation of the coefficients from the data, and also vice versa, for the reconstruction of the original data from the coefficients. In other words, the time complexity of such algorithms should be in the order of the size of the data.

## 5.3 Wavelet transform implementation

The discrete wavelet transform is often implemented with two FIR filters: a low pass filter  $\tilde{h}$  and a high pass filter  $\tilde{g}$ . The coefficients of both filters are derived from the particular wavelet that was chosen. The signal is filtered with both filters and subsequently both results are downsampled by a factor of two. By this *decomposition* step we obtain a high pass part of the signal, the detail coefficients  $\gamma$  and a low pass part, also called the approximation coefficients  $\lambda$ . The decomposition is inverted by the reconstruction step. First detail and approximation coefficients are upsampled by inserting zeros, and subsequently the upsampled coefficients are filtered by the reconstruction filters  $h$  and  $g$ . Adding the results yields the signal  $\hat{s}$ . In Figure 24 both steps, decompostion and reconstruction, are shown. If we suppose that the chosen wavelet allows perfect reconstruction of the signal, then the only effect of the filter bank in Figure 24 is a delay, i.e  $\hat{s}(n) = s(n - k)$  where  $k > 0$  is the delay, which depends on the order of the wavelet filters.

However, a straight forward implementation of this filter bank scheme leads to an algorithm which is not optimal. In the decomposition step the signal  $s$  is filtered with an FIR filter  $h$  (note, that this is not the particular  $h$  from the filter bank) and afterwards

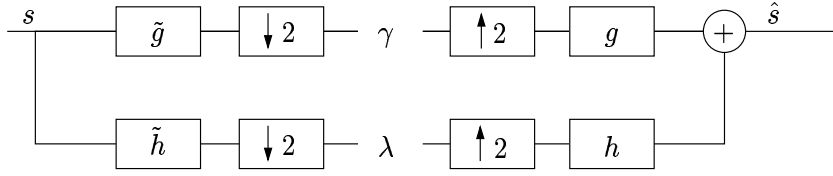


Figure 24: Single level decomposition and reconstruction filter bank

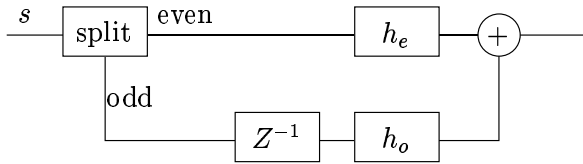


Figure 25: Efficient implementation of a FIR filter followed by a subsampler

the downsampler discards half of the result. We do not need to compute the elements, which are discarded anyway, when we replace the FIR filter  $h$  and the downsampler by a split operator with subsequent filtering as shown in Figure 25. The split operator extracts the even and odd samples from signal  $s$  and they are separately filtered by  $h_e$  and  $h_o$ , respectively. In  $h_e$  we have the coefficients of  $h$  with even indices and in  $h_o$  the coefficients of  $h$  with odd indices. In other words, we filter the even samples of  $s$  with the even coefficients of  $h$  and the odd samples of  $s$  with the odd coefficients of  $h$ . Note, that the odd samples are delayed to account for the delay between even and odd samples. Finally, we add odd and even parts and get the result. Hereby, the number of operations is reduced by a factor of two.

In the reconstruction step we apply an FIR filter  $h$  on an upsampled signal. The upsampling is done by insertion of zeros after each sample. It follows that during convolution with  $h$  half of the multiplications yield zero. These multiplications are omitted when we use the implementation drawn in Figure 26. The signal is filtered by  $h_e$  and  $h_o$  separately and then both results are merged so that we obtain the result.

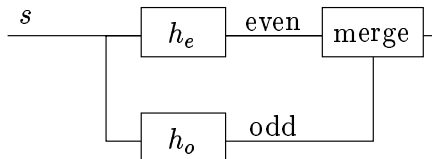


Figure 26: Efficient implementation of upsampling with subsequent FIR filter

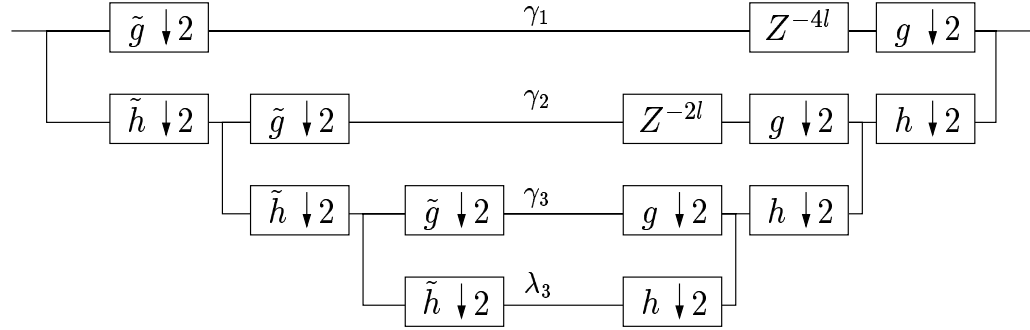


Figure 27: Wavelet filter bank of depth three

## 5.4 Wavelet filter bank

A wavelet filter bank decomposes the signal into a number of frequency bands. The bandwidth of the frequency bands is cut into halves in each step. In Figure 27 an example of a filter bank with depth three is given. On the left side are the decomposition steps and on the right side the reconstruction steps. Each filter-downsampling and filter-upsampling block can be implemented as described in the previous section. At each step in the decomposition we get coefficients representing the details or high frequencies and those representing the approximation or low frequencies of the input signal of the respective step. The approximation is used by the next step for further decomposition. Let  $n$  denote the number of steps, then we end up with the detail coefficients  $(\lambda_j, j = 1, \dots, n)$  at each step and the approximation coefficients of the last step ( $\gamma_n$ ).

For reconstruction the detail coefficients of the first steps must be delayed to account for the delay of the reconstructed approximation coefficients. The overall delay of the filter bank is  $(2^{n+1} - 2)l$ , where  $l$  is the delay of the used wavelet filter. Note, that the delay grows exponentially in the depth of the filter bank.

### 5.4.1 Low pass, band pass, and high pass wavelet filter

We can use the wavelet coefficients to implement low pass, band pass, and high pass filter. This is simply done by setting the coefficients to zero, which represent the frequency band, that we want to suppress. We yield for instance a high pass filter if we set the coefficients  $\lambda_{n-1}$  to zero, and a low pass filter if the coefficients  $\gamma_0$  are eliminated. One drawback of this method is that we cannot choose the cut off frequencies for the high pass, band pass, or low pass filters arbitrarily. Instead we are restricted to positions that are presentable as sampling rate divided by  $2^j, j > 0$ . However, this restriction does not seem to be a problem for applications in neural recordings. In Figure 28 an example of a high pass filtered signal is shown.

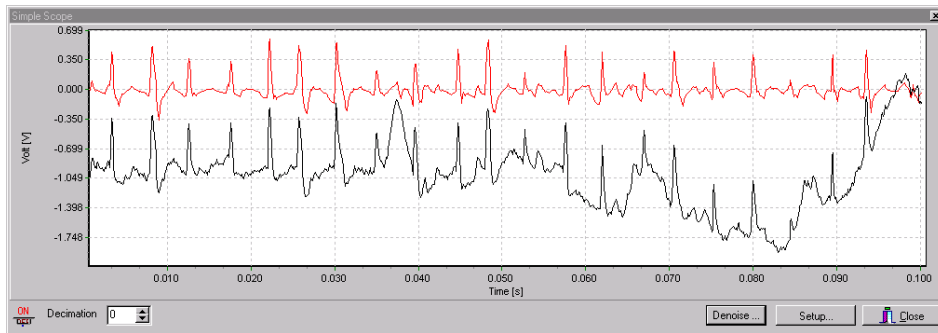


Figure 28: High pass filter implemented with a wavelet filter bank. The lower trace shows the orginal signal, and the upper trace the high pass filtered version. The frequency band 0-312.5Hz has been discarded. Note, that the shape of the action potentials is nicely preserved.

#### 5.4.2 Wavelet denoising

The wavelet denoising works on the coefficients computed within the filter bank. The first step is the estimation of the standard deviation of the noise, which is supposed to have a Gaussian Distribution. We use the detail coefficients of the first step for this estimation, since these coefficient mainly represent the noise if noise is present. The standard deviation is estimated within a time window of given length  $N$ :  $\hat{\sigma} = \text{Median}(|\gamma_{0,k} : k \leq k < N|)/0.6745$ . This median estimator is robust against outliers in the coefficients, that represent the signal instead of noise. All detail coefficients are divided by  $\hat{\sigma}$  and we obtain coefficients with normally distributed Gaussian noise. Using these coefficients we estimate the thresholds.

Currently there are four different strategies available to estimate the thresholds. They are described in the following tabular. Threshold are estimated within a time window and we denote the length of the window with  $N$ . The level is denoted by  $j \in 1, \dots, n$  and the threshold for a certain level with  $T_j$ .

MiniMaxi	$T_j = \begin{cases} 0 & N/2^j \leq 32 \\ 0.3936 + 0.1829 \log_2(N/2^j) & \text{otherwise} \end{cases}$
VisuShrink	$T_j = \sqrt{(2 \log(N/2^j))}$
Sure	Estimation of $T_j$ is based on Steins Unbiased Risk Estimate as described in [1]
SureShrink	Combination of Sure and VisuShrink where based on a certain criteria one of both strategies is selected. It is supposed to handle the case that the coefficients are sparse.

The threshold can be applied "hard" or "soft". Hard thresholding means that all coefficients less than the threshold are set to zero and all others are kept. In case of

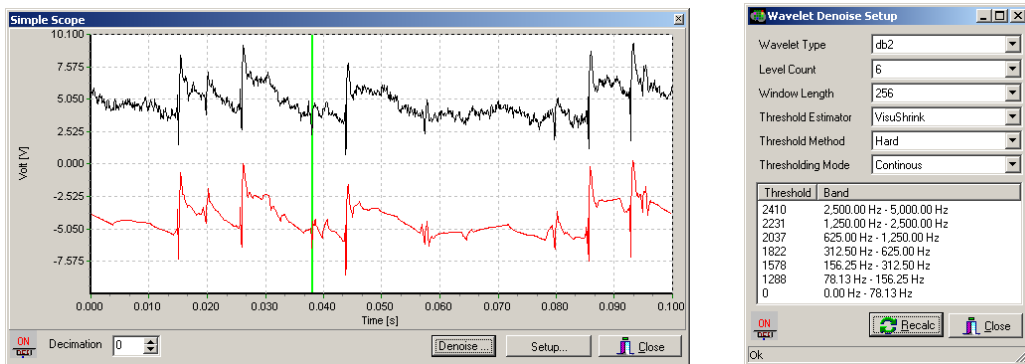


Figure 29: Denoising of a neural recording

soft thresholding the magnitude of coefficients which are greater than the threshold is reduced by the threshold.

$$\eta_s(x, T) = \begin{cases} \text{sign}(|x| - T) & |x| > T \\ 0 & \text{otherwise} \end{cases}$$

Note, that soft thresholding reduces the magnitude of all coefficients, thus in general we will find a reduced maximum peak to peak amplitude in the denoised signal.

The wavelet denoiser has two threshold estimation modes, i.e. either continuous or single. In continuous mode the thresholds are computed for each time window of length  $N$  samples, in single mode the thresholds are computed for the first  $N$  samples, i.e. the first time window, and then used for the subsequent windows without change. This is somewhat faster, but the result is not as good as in the continuous mode.

In Figure 29 the result of the denoising is shown for one example neural recording. The denoise setup is displayed on the right side and indicates that we used the Daubechies 2 wavelet. The filter bank depth was 6 and the time window had length 256. The thresholds were estimated by the VisuShrink method and were applied "hard". For each time window new thresholds were estimated, as we used the continuous mode. In the table we see the thresholds of each frequency band that were used for the last window. Inspecting the result we observe that the noise which is clearly visible in the upper trace is nicely removed in the lower trace, while the shape of the spikes was preserved.

## 6 Summary

This workpackage has delivered a data acquisition system which allows simultaneous recording from 64 channels. The software provides different means of visualization and online processing, like e.g. virtual scope, blue plot, and spectrogram. A scheme for compression has been prepared by a wavelet based transformation which provides different possibilities for compression. Moreover, the wavelet decomposition is suitable for online spike detection and spike classification, whereby the actual implementation of respective methods will be the subject of the further development. The software is adapted to the amplifier developed within workpackage 3, which gain settings can be controlled.

## References

- [1] David L. Donoho and Iain M. Johnstone. Adapting to unknown smoothness via wavelet shrinkage. *Journal of the American Statistical Association*, 90(432):1200–1224, 1995.
- [2] A V Oppenheim and R W Schafer. *Discrete-time signal processing*. signal processing series. Prentice Hall, 1989.
- [3] W. Sweldens. The lifting scheme: A new philosophy in biorthogonal wavelet constructions. In A. F. Laine and M. Unser, editors, *Wavelet Applications in Signal and Image Processing III*, pages 68–79. Proc. SPIE 2569, 1995.

# PROJECT DELIVERABLE REPORT

INFORMATION SOCIETY TECHNOLOGIES  
(IST)  
PROGRAMME



Project No. IST-1999-100073

Project Acronym: VSAMUEL

Work Package No. 4  
Deliverable 4.3  
Data Acquisition System for 128 channels

September 2003  
Software on CD-ROM

Project Title:  
Development of a Versatile System for Advanced Neuronal Recordings with Multi-site  
Mircoelectrodes

Report prepared by:  
A. Folkers and U.G. Hofmann, ISIP, University of Lübeck

## 1 Introduction

The project VSAMUEL aims to develop easy-to-use instrumentation for multi-channel recordings from functioning and living nervous tissue spanning a broad range of neurobiological questions. Figure 1 presents an overview of all project partners and their tasks. The group at Acreo is developing silicon-based microelectrodes with up to 64 recording sites, Thomas RECORDING GmbH designed a 64 channel preamplifier and main amplifier, and at ISIP the data acquisition system for 128 channels is build. The whole system is evaluated by the experimental partners for different application area, i.e. peripheral nerves, cerebellum, and cortex. In this deliverable we focus on the development of the data acquisition system.

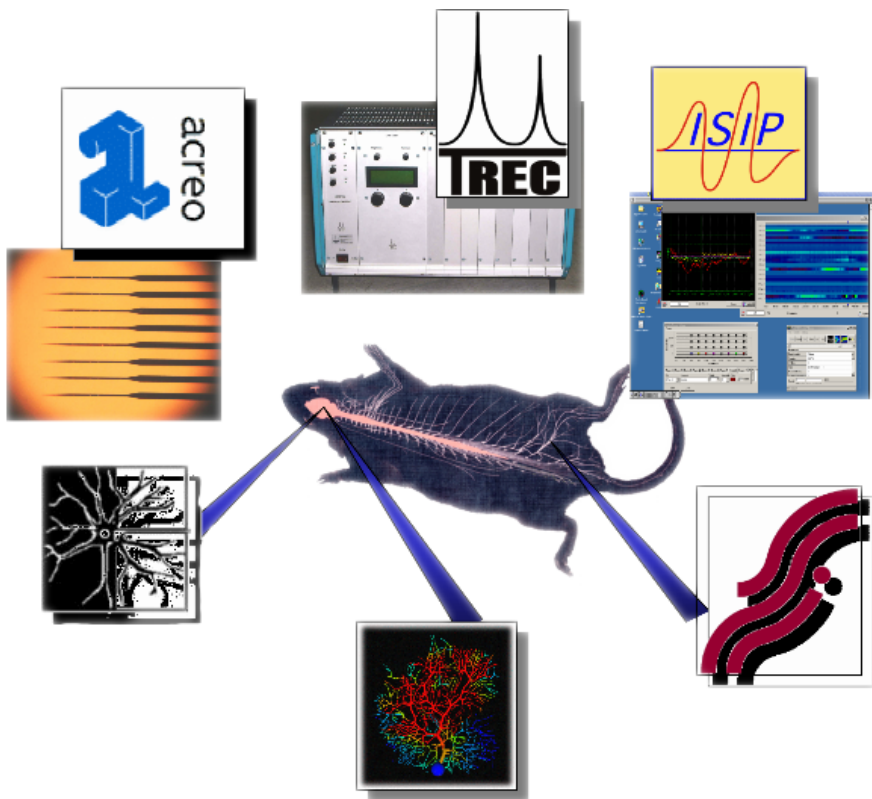


Figure 1: Overview of the project VSAMUEL. Clockwise from top left: Custom designed connectors and passive batch fabricated multi site microelectrode probes (Acreo AB, Kista), Discrete and modular multi-channel amplifier (Thomas RECORDING GmbH, Giessen), Data acquisition system, hard- and software (ISIP, University of Lübeck), and the experimental partners with their area of application, i.e. Peripheral nerves (SMI, Aalborg University), Cerebellum (BBF, University of Antwerp), and Cortex (INN Carlo Besta, Milano).



Figure 2: M67 DSP board equipped with two analog digital conversion modules

## 2 Hardware Overview

The data acquisition system is based on off-the-shelf DSP boards (M67) residing in a modern personal computer running Windows 2000. Each DSP board can be extended with analog digital conversion (ADC) modules. We are using two AD16 modules per board, which together provide the ability to record from 32 channels simultaneously without multiplexing. DSP Boards and the AD conversion modules are manufactured by Innovative Integration, California, USA. Figure 2 shows the board equipped with ADC modules.

The M67 board has a single digital signal processor, i.e. a TMS3206701 processor (Texas Instruments, Dallas, TX, USA) clocked at 160 MHz with 128KB onchip memory. The CPU is provided with three different types of external memory: asynchronous SRAM (ASRAM, 512KB), synchronous DRAM (SDRAM, 16 MB), and synchronous burst SRAM (SBSRAM, 1MB). Furthermore, it has different external timers, interfaces for digital input or output, and a FIFO port for communication with other boards.

The AD16 module provides the M67 board with 16 channels of high speed 195 kHz, 16-bit resolution analog input to digital output conversion (A/D) per module site. There are 16 A/D converters for simultaneous conversion on all channels. Each of the 16 input channel consists of a high precision, DC accurate sigma-delta A/D converter (AD7722, Analog Devices, Norwood, MA, USA) with front end conditioning circuitry, which removes the need for multiplexers. The A/D converters are clocked either using a DDS timer of the M67 board or an external clock. Conversion results are transferred into a FIFO (this FIFO has no connection with the FIFO port of the M67) which can store up to 512 16-bit samples. The AD16 triggers an interrupt of the DSP when the FIFO contains a certain amount of samples. Usually this threshold is set to half of the samples which can be stored in total. This interrupt is serviced by a routine running on the DSP which fetches the data from the FIFO and stores it into the onchip memory using a DMA transfer. The block scheme in Figure 3 shows the arrangement of the hardware components and the data flow for one DSP board.

The boards are connected with the host system via the PCI bus. The current host

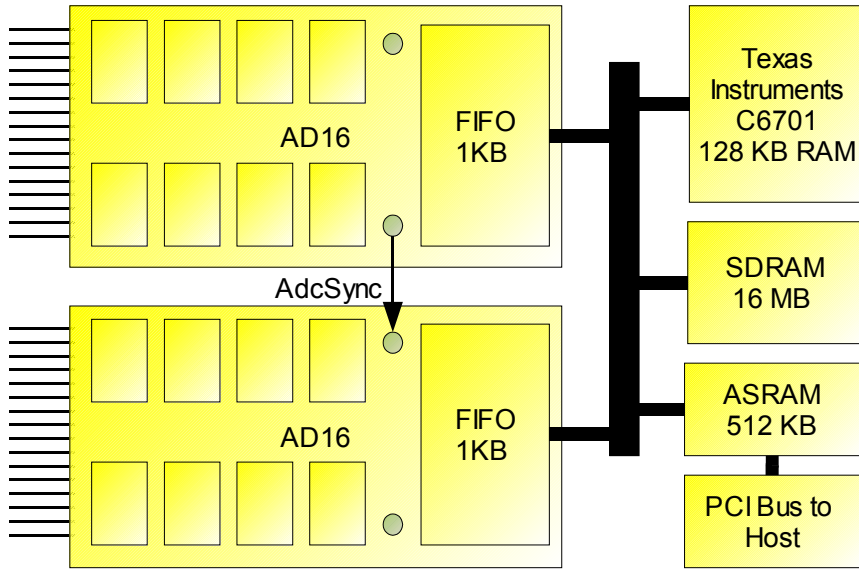


Figure 3: Hardware Overview

system consists of a 1GHz Pentium III with 256 MB SDRAM (Synchronous DRAM) on DSM Slot CPU. It has two SCSI harddrives IBM DPSS-336950N with 36 GB storage each.

## 2.1 128 channel data acquisition system prototype

We use four M67 boards to acquire data from 128 channels each channel at a sampling rate of 50 kHz with 16 bit resolution. In Figure 4 a block scheme illustrates the main components of the 128 channel data acquisition system prototype. The boards reside in a 19 inch industrial PC chassis which has a backplane providing space for up to 16 PCI boards with full extend. The M67 equipped with AD16 modules blocks two PCI slots as the AD16 modules sit upon the M67 base board in a second level which extends the height of the board such that one neighbouring PCI slot should not be used due to the danger of short circuits. However, to resolve the heat problem of the AD16 modules a heatspreader was constructed which extends the height, so that an M67 with AD16 modules plus heatspreader uses two the space of two slots anyway. In order to acquire data synchronously on all boards different mechanisms were

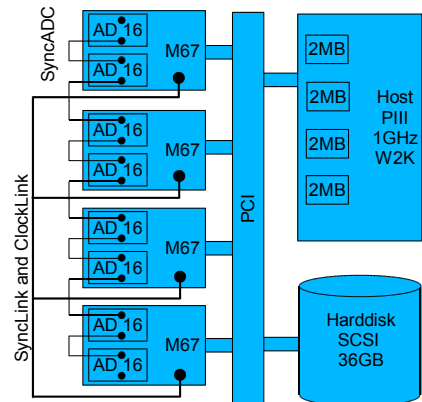


Figure 4: Synchronization Cabling and integration into Host PC with four DSP Boards

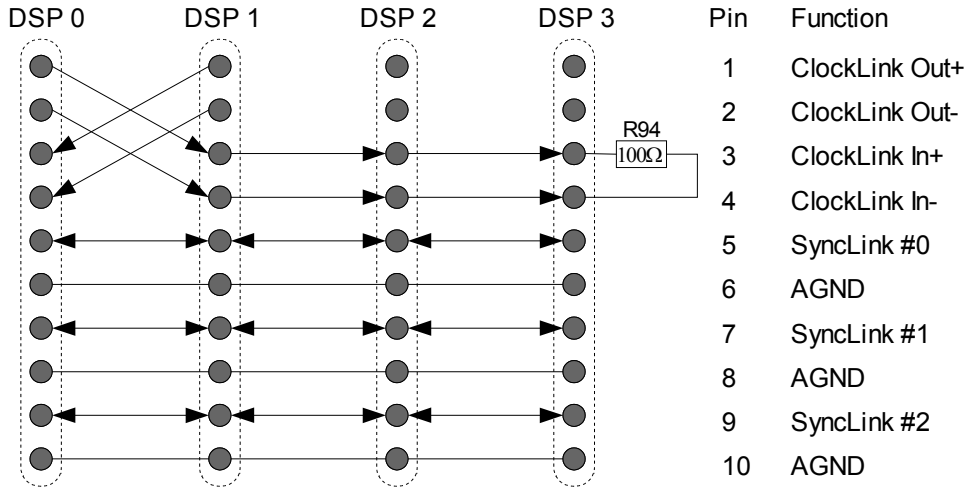


Figure 5: Layout of the SyncLink/ClockLink cable

applied as described in the following paragraph.

First, the clocks of the DSP boards that drive the AD16 modules must be synchronized. The M67 board features a so called SyncLink and ClockLink interface which can be used to synchronize multiple M67 boards. For our application we utilized the ClockLink part of this interface which provides the clock of the DDS timer of the M67 board 0 to the other boards. The boards are connected as indicated in Figure 5. DSP board 0 generates the clock while the other boards are configured within the DSP application to use this clock instead of their own DDS clock. Note the 100 Ohm resistor which terminates the ClockLink bus. By default each board has such an resistor, i.e. R94. This resistor must be removed from DSP 1 and DSP 2 in order to obtain a clean clock signal on all boards. If not removed the bus will be terminated multiple times which results in a lower termination resistance. The AD16 modules have sigma-delta analog digital converters (ADC) which use 64 times oversampling and divide the input clock by 2 so that the bus must carry a 6.4 MHz clock for acquisition at 50 kHz.

Second, due to the oversampling the ADCs need to be further synchronized. In particular they should transfer their ADC result on the same clock edge into the result registers. This is supported by the AdcSync Pins of an AD16 through which a synchronization clock can be connected to the AD16. We use module 0 on DSP board 0 to generate this AdcSync clock and the other boards are connected in a row to this clock. This configuration is performed within the DSP application. We connect the AdcSync In pin of AD16 module 1 with AdcSync Out pin of AD16 module 0, then AdcSync Out of AD16 module 1 with AdcSync In of AD16 module 0 on DSP board 1, and so on.

Figure 4 illustrates how the synchronization connections are made. Both mechanism together make a simultaneous AD conversion on all 128 channels possible. Figure 6



Figure 6: 128 channel data acquisition system (from top)

shows the actual 128 channel data acquisition system from top. The upmost board is the slot CPU featuring a Pentium III 1GHz processor with 256 MB main memory and onboard graphic chip and network adapter. Below the slot CPU the four M67 boards are located which are equipped with AD16 modules on the right side below the fans (see Section 2.3 for more details about the heat problem). The yellow cable on the left end of the M67 boards is the SyncLink/ClockLink cable. It was customized from an unshielded twisted pair cable and FC-10 pin connectors according to the layout shown in Figure 5.

The prototype uses one AD16 module per M67 board. However, the missing AD16 module is simulated realistically by the DSP application and thus the host receives data of 64 acutally sampled channels and 64 simulated channels, which are in our case set to zero. In the back side view of Figure 7 one can see the four input cables which establish the connection between the ScsiToLatch board and one Ad16 on each M67. The ScsiToLatch board adapts a 68 pin Scsi connector to four 50 Pin latch connector which corresponds to the interface provided on the M67 board. The ScsiToLatch boards fits mechanically into a PCI slot, but without having any electrical connection. We used 50 pin airflow ribbon cables in order to preserve the air circulation inside the

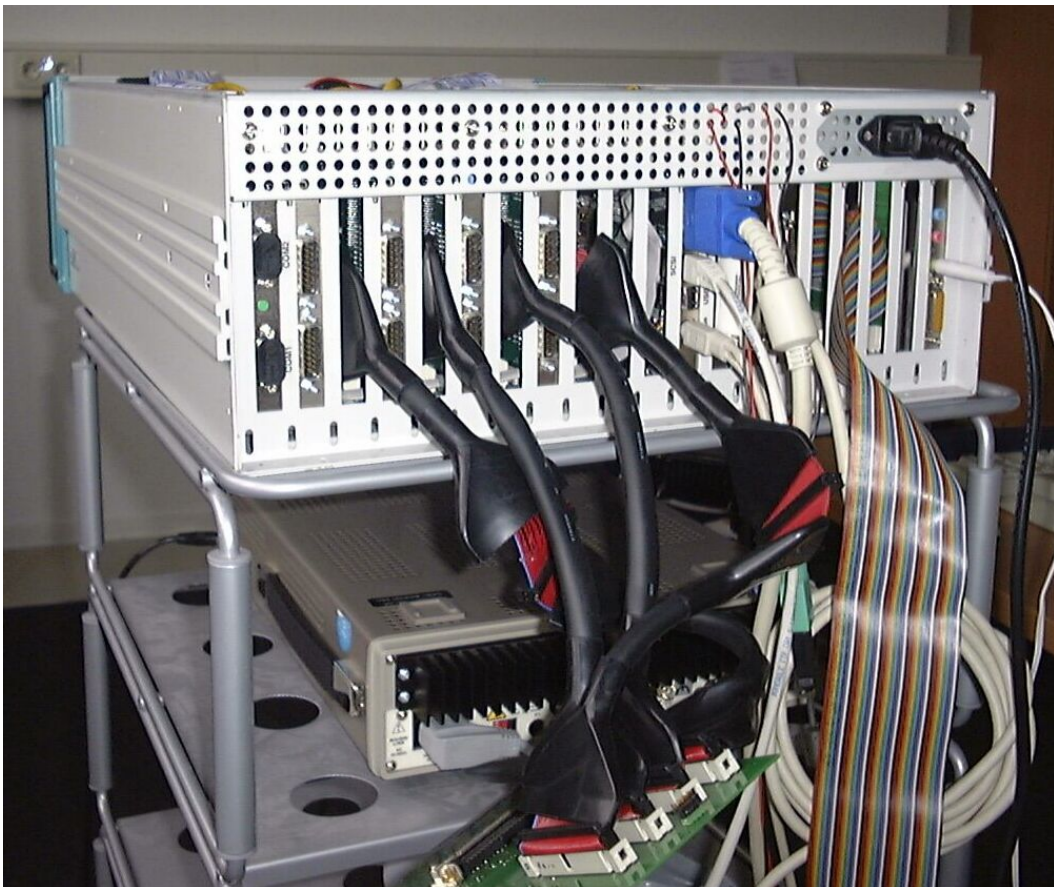


Figure 7: 128 channel data acquisition system (backside)

cabinet as good as possible. However, due to the thermal problems the 128 channel system prototype was operated without internal cabling of the M67 boards and the ScsiToLatch board. Instead the cables were directly lead out of the cabinet, as shown in Figure 7.

## 2.2 Test runs with four M67 Board

We performed different test runs with the 128 channel data acquisition prototype. The analog input feed in from a signal gernerator. We used a 900 Hz sine wave with 10 V peak to peak amplitude. The data was acquired at 50 kHz per channel and it is shown as a blueplot in Figure 6 and in scope view in Figure 7. Note, that half of the channels have been filled with zeros as they are simulated by the DSP application, while the other half contains acutally sampled data.

The second run was performed with a 2.3 kHz input square signal with 5 V peak-to-peak voltage. Figure 9 shows four channels of the acquired data, each channel recorded on a different M67 board. The overlay of these four channels in Figure 10 shows that these channels are perfectly synchronized. However, we did not acutally remove the

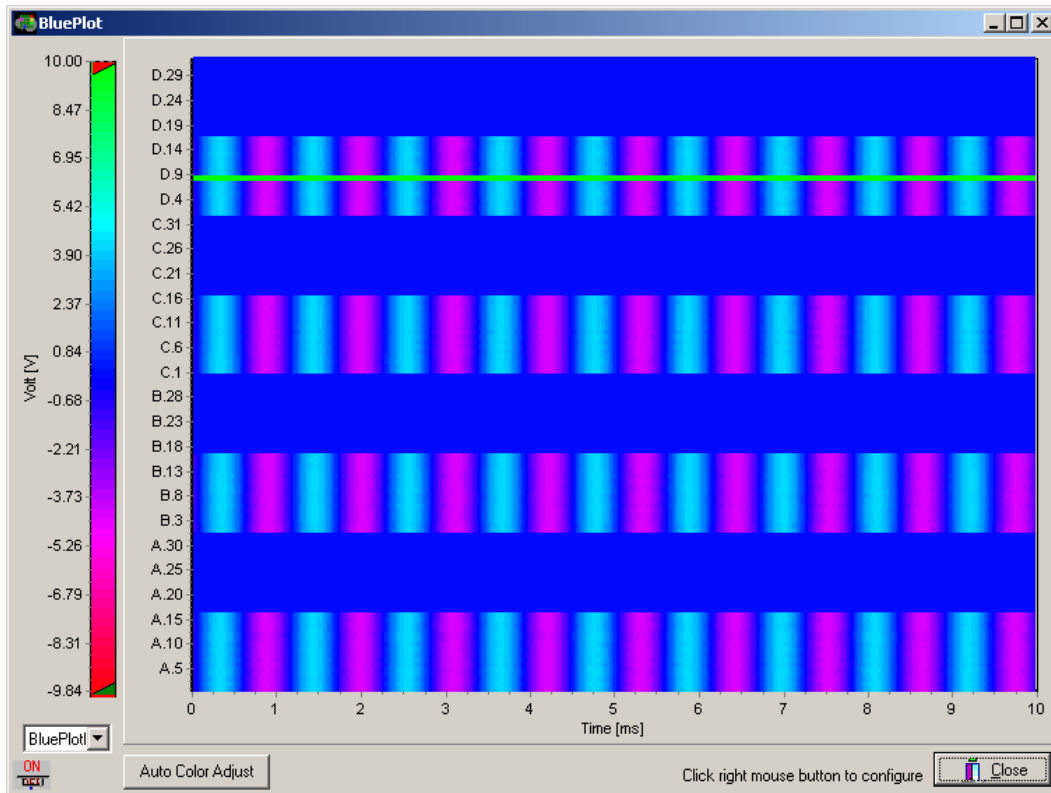


Figure 8: Blueplot of 128 channel recording. Actually sampled data on 64 channels plus 64 simulated. One channel defect due to a problem with the ribbon cable.

resistor R94, and as a consequence in some tests the data acquisition was not completely synchronized.

### 2.3 Thermal issues

In a series of test runs it appeared that the AD16 modules have a thermal problem. We tested different combinations of M67 boards equipped with two Ad16 modules:

- Combination A with M67 board G274, Ad16 modules B145-1 and B138
- Combination B with M67 board G244, Ad16 modules B145-2 and B144
- Combination C with M67 board G275, Ad16 modules B149 and B140

Combination A and B both showed similar thermal problems. These thermal problems caused the data acquisition hardware to break down at a room temperature over 25° Celcius. In order to resolve the thermal problems we made several different approaches. Finally, a heat spreader designed by Innovative Integration for a pair of Ad16 modules combined with additional fans and air holes in the cabinet resolved this

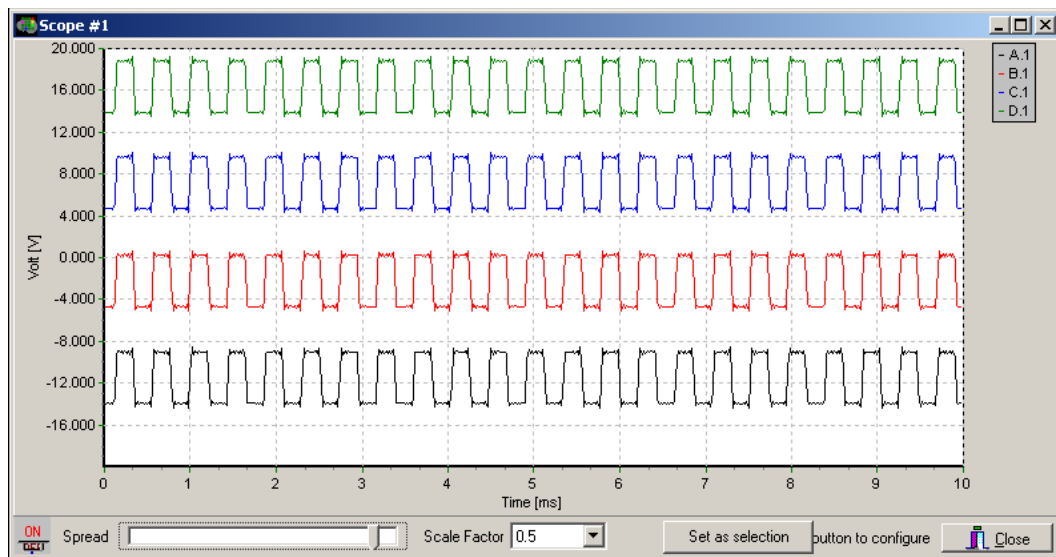


Figure 9: 2.3kHz Square signal acquired at 50 kHz on four different M67 boards



Figure 10: Overlay of the four channels in Figure 9 with spread set to zero



Figure 11: M67/Ad16 board equipped with heat spreader

problem for room temperatures up to 30 °Celcius. This was tested for combination A and B. However, the third combination C worked stable without additional cooling in our prototype system at a room temperature of 23° Celcius for 16 hours recording data to disk from 32 channels at 50 kHz per channel.

The heat spreader assembled together with a pair of Ad16 modules is shown in Figure 11. The additional fans and the air holes are shown in Figures 12 and 13.

We also tested an completely different cabinet design which is shown in Figure 14. This design features additional cooling through several fans. However, the combination A worked not stable in this cabinet, i.e. the data acquisition stopped after 30 minutes at a room temperature about 24° Celcius. However, the combination B which does not have heatspreader worked stable over 18 hours in at a room temperature at about 32° Celcius.

Our tests lead to the conclusion that the thermal stability of Ad16 modules differs individually, which in turn means that the thermal behaviour of each Ad16 module should be checked, before being used in a productive system.



Figure 12: 128 channel data acquisition system prototype with additional fans

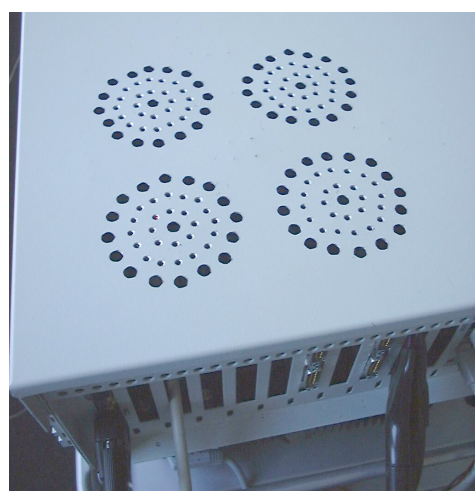


Figure 13: Additional air holes



Figure 14: Small cabinet with improved air flow due to mulitple fans with M67/Ad16 board equipped with heat spreader

### 3 DSP Application

The DSP application is the program which runs on the DSP board. It has four major tasks:

1. acquire data from analog input channels,
2. acquire digital input,
3. process the data,
4. transfer the data to host, and
5. react on commands.

The software structure reflects these tasks by having four main modules, one for each task. In the following we discuss each module.

#### 3.1 Data Acquisition Module

The data acquisition is driven by interrupts. It reacts on the FIFO "threshold reached" interrupts of the AD16 modules. After both modules have triggered the interrupts, two DMA<sup>1</sup> transfers are started which transfer the data from both FIFOs into the DSPs internal memory. Here the data is stored into so called frames. A frame consists of several sample point blocks, whereby a sample point block contains the samples from all channels taken at the same point in time. After a frame has been filled it is passed to the processing module. The data is processed and then the frame is passed to the transfer module, and finally back to the data acquisition module. The exchange of frames is implemented by means of frame queues. There are three such queues which contain either empty frames, filled frames, or processed frames. Figure 15 shows the data flow within the DSP application.

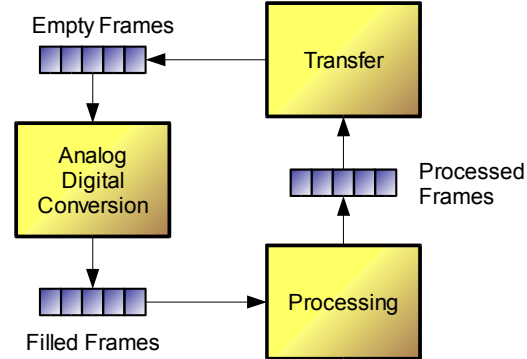


Figure 15: Frame Management within DSP application  
The diagram illustrates the data flow within the DSP application. It shows four main components: Transfer, Analog Digital Conversion, Processing, and a queue of Empty Frames. The Transfer module receives Processed Frames from the Processing module and sends Empty Frames to the Analog Digital Conversion module. The Analog Digital Conversion module receives Empty Frames from the Transfer module and sends Filled Frames to the Processing module. The Processing module also sends Processed Frames back to the Transfer module. The queue of Empty Frames is used to store frames waiting to be processed or transferred.

#### 3.2 Processing Module

The acquired data can be processed differently. Beside IIR filtering and short time Fourier transform, which were implemented, but which are currently not used, we developed a semiautomatic tool which can generate a linear assembler routines that

<sup>1</sup>DMA denotes Direct Memory Access, which is a mechanism to transfer data without using the main CPU

implement wavelet decomposition and reconstruction algorithm based on the lifting scheme. The procedure is described in more detail in Section 5.3.

The generated code uses the capabilities of the C6701 at a great extend. The basic optimization strategy was to process multiple channels in parallel. Note, that 'in parallel' is meant literally. The C6701 has two register sets, each having 16 general purpose registers of 32 bit width. Each register set is associated with several operation units, which can perform operations in parallel. We managed to process four channels in parallel. This implementation uses the minimum number of registers per channel. However, all the 32 registers are directly or indirectly (counters, parameters) neccessary for the optimized implementation.

```

; Step 1, predict
|| LDW .D2T2 *+c[i],cst2 ; load constant
|| LDDW .D1T1 **states1[0],temp1_i:temp1_ii ;
|| LDDW .D2T2 **states2[1],temp1_iii:temp1_iv ;
|| STW .D1T1 a_i,**states1[0] ;
|| STW .D2T2 a_iii,**states2[2] ;
|| STW .D1T1 a_ii,**states1[1] ;
|| STW .D2T2 a_iv,**states2[3] ;
|| ADDAW .D1 states1,4,states1 ;
|| ADDAW .D2 states2,4,states2 ;
MPYSP .M1 temp1_i,cst2,temp1_i ;
|| MPYSP .M2 temp1_iii,cst2,temp1_iii ;
MPYSP .M1 temp1_ii,cst2,temp1_ii ;
|| MPYSP .M2 temp1_iv,cst2,temp1_iv ;
|| LDW .D2T2 *+c[2],cst2 ; load constant
MV .L1 a_i,temp2_i ;
|| MV .D1 a_ii,temp2_ii ;
|| MV .L2 a_iii,temp2_iii ;
|| MV .D2 a_iv,temp2_iv ;
MPYSP .M1 temp2_i,cst2,temp2_i ;
|| MPYSP .M2 temp2_iii,cst2,temp2_iii ;
MPYSP .M1 temp2_ii,cst2,temp2_ii ;
|| MPYSP .M2 temp2_iv,cst2,temp2_iv ;
ADDSP .L1 temp1_i,temp2_i,temp1_i ;
|| ADDSP .L2 temp1_iii,temp2_iii,temp1_iii ;
ADDSP .L1 temp1_ii,temp2_ii,temp1_ii ;
|| ADDSP .L2 temp1_iv,temp2_iv,temp1_iv ;
LDDW .D1T1 **states1[2],temp2_i:temp2_ii ;
|| LDDW .D2T2 **states2[3],temp2_iii:temp2_iv ;
LDDW .D1T1 **states1[0],temp3_i:temp3_ii ;
|| LDDW .D2T2 **states2[1],temp3_iii:temp3_iv ;
|| STW .D1T1 temp2_i,*+states1[0];
|| STW .D2T2 temp2_iii,*+states2[2];
|| STW .D1T1 temp2_ii,*+states1[1];
|| STW .D2T2 temp2_iv,*+states2[3];
|| STW .D1T1 d_i,*+states1[4];
|| STW .D2T2 d_iii,*+states2[6];
|| STW .D1T1 d_ii,*+states1[5];
|| STW .D2T2 d_iv,*+states2[7];
|| ADDAW .D1 states1,8,states1 ;
|| ADDAW .D2 states2,8,states2 ;
SPINT .L1 temp3_i,temp3_i ;
|| SPINT .L2 temp3_iii,temp3_iii ;
SPINT .L1 temp3_ii,temp3_ii ;
|| SPINT .L2 temp3_iv,temp3_iv ;
SPINT .L1 temp1_i,temp1_i ;
|| SPINT .L2 temp1_iii,temp1_iii ;
SPINT .L1 temp1_ii,temp1_ii ;
|| SPINT .L2 temp1_iv,temp1_iv ;
ADD .S1 temp3_i,temp1_i,d_i ;
|| ADD .D1 temp3_ii,temp1_ii,d_ii ;
|| ADD .S2 temp3_iii,temp1_iii,d_iii ;
|| ADD .D2 temp3_iv,temp1_iv,d_iv ;
INTSP .L1 d_i,d_i ;
|| INTSP .L2 d_iii,d_iii ;
INTSP .L1 d_ii,d_ii ;
|| INTSP .L2 d_iv,d_iv ;

```

Figure 16: Linear assembler code fragment which implements a prediction lifting step.

In Figure 16 a fragment of the generated assembler code is shown. The equivalent C code is

```

/* Step 1, predict */
cst = c[1];
temp1 = states[1];
states[1] = a;
temp1 = temp1 * cst;
cst = c[2];
temp2 = a;
temp2 = temp2 * cst;
temp1 = temp1 + temp2;
temp3 = states[2];
states[2] = states[3];

```

```

states[3] = d;
temp1 = (int)temp1;
d = temp3 + temp1;

```

These instructions implement a prediction lifting step like

$$d_l^{(k+1)} = d_l^{(k)} + [c_0 a_{l-1}^{(k)} + c_1 a_{l-2}^{(k)}] \quad (1)$$

where the brackets denote the rounding operation. A assembly code line has four columns: optional parallel bars, instruction, operation unit, operands. The parallel bars || indicate parallel execution of the instructions in this line and the previous line. Execution of one instruction happens in several phases, which number differs from instruction to instruction. The MV instruction only needs one phase, while the LDW needs five phases. Therefore the constants loaded from `c[1]` is available in cst2 at the fifth parallel bar. Note, that the linear assembler is translated into the actual assembler, and during translation NOPs are inserted where needed. One way to optimize the code is to rearrange the instructions such that as few NOPs as possible are inserted. Because we process four channels in parallel we can make an efficient use of as many operation units as possible.

A comparison of the C implementation and the linear assembler implementation reveals that the linear assembler is about four times faster than then C implementation. Both are translated using the maximum optimization level (-o3) of the compiler and assembler. However, some optimizations were disabled, like e.g. non-interruptable code, because the code needs to be interruptible in the DSP application.

The real time implementation must process the data as fast as it is acquired. For example a wavelet decomposition of depth six requires 64 sample points and if we record at 50 kHz we have 1.28 ms between every new block. Since the DSP application needs some time to transfer data from the ADC modules to into the CPU and then further into the ASRAM for subsequent transmission to the host, which sums up to about 0.33 ms, there is even less time. The generated implementation for db2 works at 50 kHz, while the implementation for db6 works up to 44 kHz sampling rate.

### 3.3 Communication between host and target

Host and targets, i.e. PC and M67 boards, respectively, are connected via the PCI bus. Data can be transferred from host to target and vice versa. There are two mechanisms one for small messages and one for large amounts of data which are illustrated in Figure 17.

First we focus on the transfers of large amounts of data. The target can read from or write into a shared memory section within the host. Data transfers are always performed via the Asynchronous RAM (ASRAM) on the target, i.e. for transfers from target to host the data must be read from ASRAM, and for transfers from host to target the data is received in the ASRAM. The M67 can perform busmaster transfers, i.e. data can be read or written without burdening the target or the host CPU. Instead, transfers are executed by a special controller chip, the V360 PCI to local bus bridge

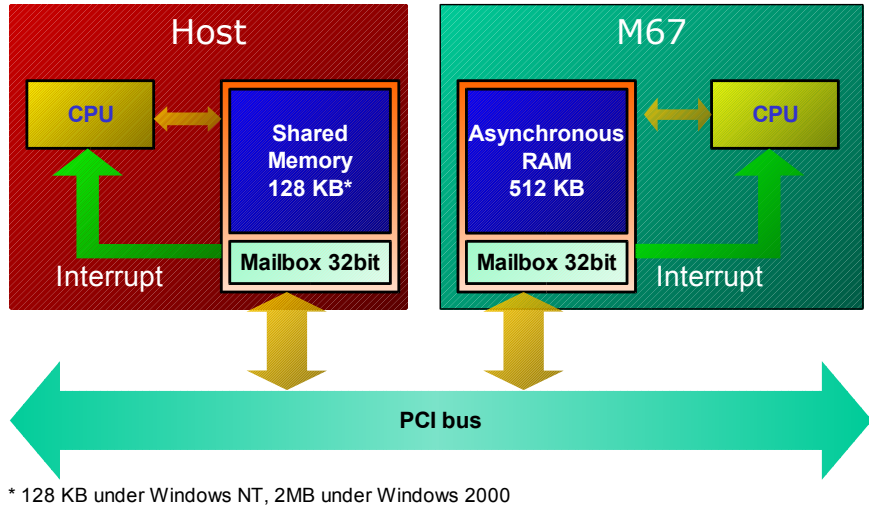


Figure 17: Communication channels between host and target

(V3 Semiconductors). After the transfer has been completed the controller notifies the target by triggering an interrupt.

For small messages we use a mailbox system. A *mail* is a 32 bit value. The board supports two mailboxes. They can be accessed in a synchronous way: For example, if we want to send a message to the target, then we can write the value into the mailbox on the host and it is send to the target. Now the target must read the mailbox before a new value can be written by the host. If the target tries to read the mailbox when no message has been sent by the host, the target is blocked until a value is available. Using these mailbox functions, target and host can be synchronized. But synchronous communication is error prone, because messages need to be sent in the correct order which introduces a great dependency between target source code and host source code. This is why we do not use the synchronized mailboxes. Instead, we use an asynchronous approach which is also supported. A write to a mailbox can trigger an interrupt. Thus the host can interrupt the target and also the other way around, the target can interrupt the host. By using the interrupt signal we do not need to check for new messages actively, which saves valuable cpu cycles.

### 3.4 Data Transfer Module

After processing, or after acquisition, if only raw data is requested, the data must be transferred to the host. This task is implemented in the data transfer module. Since busmaster transfers, as described in the previous section, have to use the ASRAM as source for transfers into the shared memory on the host site, the first step is the transfer of the acquired data from internal DSP memory into the external ASRAM (see also Figure 3). Hereby the data is put into packets. Each packet has a header and a data section. The header contains information about the data, like e.g. the size,

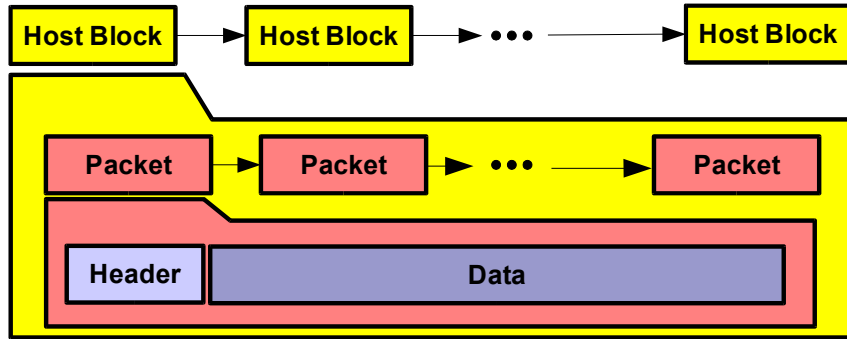


Figure 18: Data Transfer Protocol

whether a trigger signal has been received, the type of the data, and a consecutive number of the packet. Several packets together form a host block. After a host block has been transferred from target to host, the target notifies the host using the mailbox communication so that it can fetch the new host block. Note, that we start a new busmaster transfer for each packet, but notify the host not until a complete host block has been transferred. This is done in order to keep the number of events which are generated by the notification as low as possible. Figure 18 illustrates the data organization of the busmaster transfers.

### 3.5 Commands Module

In the DSP application a single task, the control task, receives messages sent by the host and also sends messages to the host. The 32 bit messages have three parts: a receiver tag (8 bit), a command tag (8 bit), and a data part (16 bit). The control task routes the messages according to the receiver tag. In order to set the sampling rate within the ADC module the host sends a message with receiver equal to `ADC_MODULE`, command is `SET_SAMPLING_RATE`, and the data contains the sampling rate. In case that the value exceeds the 16 bit of the data part, we use two or more messages.

### 3.6 Extensions for multi board data acquisition

The acquisition from 128 channels is implemented by using four DSP boards. Therefore, we have four instances of the DSP application. As described in Section 2.1 we have a master board and three slave boards. Similarly we also have a master DSP application and a slave DSP application, which run on master and slave board, respectively, and differ in some details. Actually, it is the same DSP application running in master or slave mode, which can be configurated by the host application with the `SET_MASTER` command. On data acquisition start command the master DSP application initializes the DDS timer and synchronizes the ADCs on the AD16 modules, while the slave DSP application does not perform these steps. Despite these details both DSP application are identical. Note, that the start command must be sent to the slave DSP applications

first, to ensure that they are ready for acquisition when the master DSP application enables the timer.

## 4 Host Application

The host application provides a user interface through which new experiments can be created and old experiments can be reviewed. It has several means of visualization, i.e. a virtual scope, a blue plot, and a spectrogram. The host application receives the data from the data acquisition hardware and stores it into a file on hard disk together with the experiment documentation. The experiment documentation includes an experiment identifier, a global comment, the sampling rate, and the used probe with filter, subsampling, and amplification settings. In playback mode the user can browse through the data of a recorded experiment using controls similar to controls of a CD player and a browse bar. Furthermore, different offline analysis methods can be applied to selected data. Recapitulating the host application performs three main tasks:

- Data reception and storage,
- Data organization,
- Data visualization, and
- Data analysis.

### 4.1 Retrieving data from multiple boards

The acquisition of data from multiple boards introduces two main problems. First, the data arrives independently from each DSP board and, second, the data must be merged into a single stream. Thus the data arrival must first be synchronized and then data can be merged which includes a lot of small copy operations and must be optimized to work fast enough. The acquisition task is implemented within a couple of classes which are shown in Figure 19. Each board is represented by an instance of VSDSPBoard which is derived from TIIDSPCComp a class supplied in a library from II. Multiple instances of VSDSPBoard are combined in class VSDAQHardware. There is one instance of VSDAQHardware which is located in the VSDAQServer instance. Data is written to disk using an instance of VSFileWriter. For data acquisition the VSDAQServer instance starts an instance of VSACquireThread which uses the DAQHardware and the FileWriter in VSDAQServer to retrieve and store the data. Additionally the acquire thread performs the configured online processing and it puts the data into the main data buffer for visualization.

Figure 20 shows how these classes interact during acquisition. Data arrival is indicated by a certain message from the DSP application. On message reception the MessageReceive method of the respective VSDSPBoard instance is called in the scope of a thread running within the DSP board driver with high priority. This method sets the HostBlockRecvEvent which indicates that a new host block has arrived from the respective DSP application. On the other hand the acquire thread waits in method WaitForNextHostBlock until the host block receive event of each DSP board is set. If any board did not send new data then a time out occurs and the acquire thread

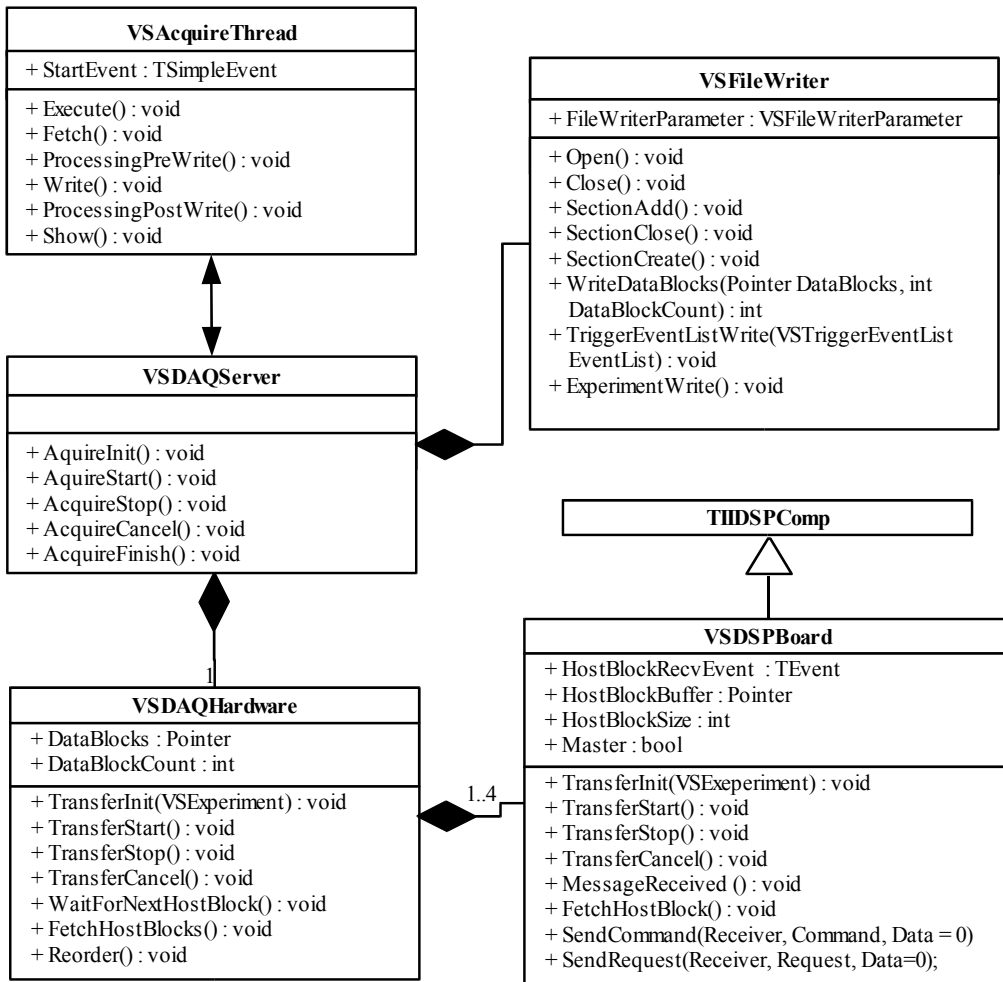


Figure 19: Classes which coordinate and perform the data acquisition from mulitple DSP boards.

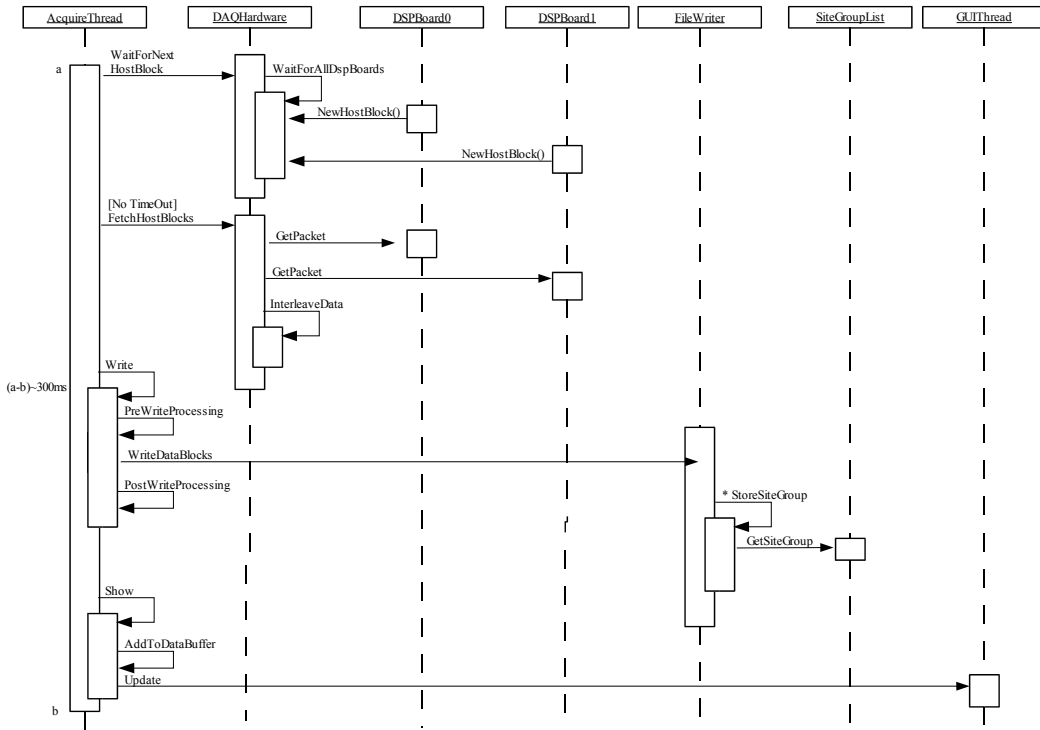


Figure 20: Interaction of classes during data acquisition.

terminates. However, if all boards delivered their host block the acquire thread fetches the data from all DSP boards and merges it into a single stream within method FetchHostBlocks. The merge operation is shown in Figures 21 and 22. The data blocks are then processed in the ProcessingPreWrite method, then written to disk, and again processed in the ProcessingPostWrite method. The actual processing performed in both methods depends on the storing mode and Table 1 shows the different cases. Data is written to disk with the FileWriter in method WriteDataBlocks. The SiteGroupList in FileWriterParameter contains the parameters which determine subsampling and filter settings for the acquired data.

StoringMode	ProcessingPreWrite	ProcessingPostWrite
Raw	nothing	Wavelet filter bank
RawFiltered	Wavelet filter bank	nothing
Wavelet Coefficients	Wavelet decomposition and coefficient delay	Coefficient processing and wavelet reconstruction

Table 1: Post- and pre-write processing

We now focus on the merging of raw data from multiple DSP boards, shown in

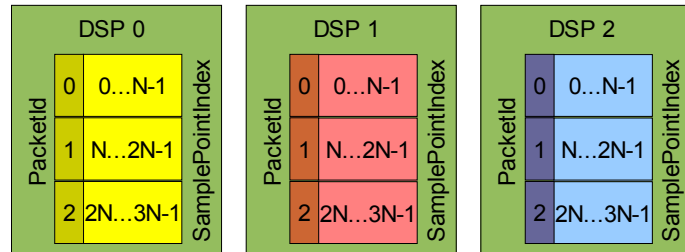
Figure 21. Each DSP board acquires from 32 channels at 16 bit. Therefore one sample point has 64 bytes. A host block is divided into packets, where each packet has a header and a data part. The packet header contains a packet id and also some other information, e.g. trigger detection timestamps, which is not used during merge. The packet id is used to detect packet losses. If the host was for some reason not able to fetch the data in time packets might have been overwritten by the DSP application. In this case the sequence of packet ids will not be steadily increasing, but there will be a gap, which can be detected. The data part contains N sample points. First we merge the packets into a data buffer so that the N sample points from three DSPs form a block in memory. Then this block is reordered such that each sample point forms single block in memory. In the actual implementation these operations, i.e. the merging and the reorder, have been combined into one assembler routine which performs both operation at the same time. The fast implementation was essential for the acquisition of data from multiple DSP boards and has been successfully used to acquire data from 128 channels with a Pentium III, 1GHz at 50 kHz per channel to disk.

## 4.2 Distribution of data to visualization modules

The central data structures are VSRingBuffer and derived from that class the class VSDataBuffer. The class VSRingBuffer implements a ring buffer, which holds a certain amount of data and overwrites old data when the new data does not fit into the free space. Data can be added or removed at head and at the tail of this particular ring buffer, which is used during forward and backward playback from disk. Counters and indices of VSRingBuffer are bytes oriented. In order to support blocks of multiple bytes the class VSDataBuffer is derived from VSRingBuffer. VSDataBuffer divides the actual buffer into data blocks. All data blocks have the same size given on construction of an instance. Through the class each data block can be addressed by a global 64 bit index. The class provides a mechanism to keep track of already read data and newly added data. In Figure 23 a class diagram illustrates the features of VSDataBuffer and VSRingbuffer.

The data is distributed to different visualisation modules by class VSDataBufferView which is associated with VSModule. Details of both classes are shown in Figure 24. With the class VSDataBufferView one can extract a segment of data blocks from the associated VSDataBuffer instance. Hereby it supports decimation of data in two modes, i.e. nearest neighbour and maximum over the decimation interval. VSModule provides an interface for the main dialog to all visualization modules and visualization modules can execute methods of the main dialog through the VSModule class. Thus each visualisation dialog has an own instance of VSModule. On the other hand the main dialog maintains a list of VSModule instances which is used to triggered different actions on all modules. If for instance the visualization modules need to be updated the method the main dialog calls the Update method of each VSModule instance in the list. The same mechanism is used for Allocate, Deallocate, and Reset.

### Shared Memory



### DataBuffer

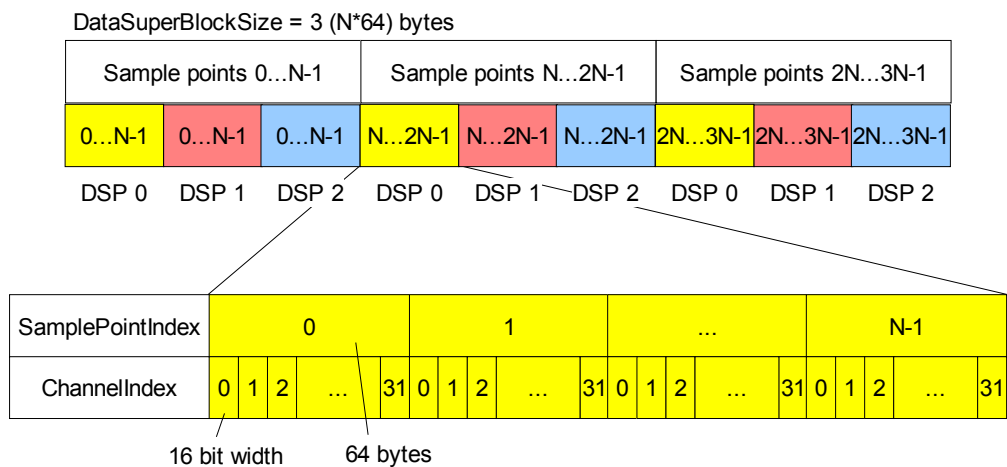


Figure 21: Merging of raw data from three DSP boards into a single stream.

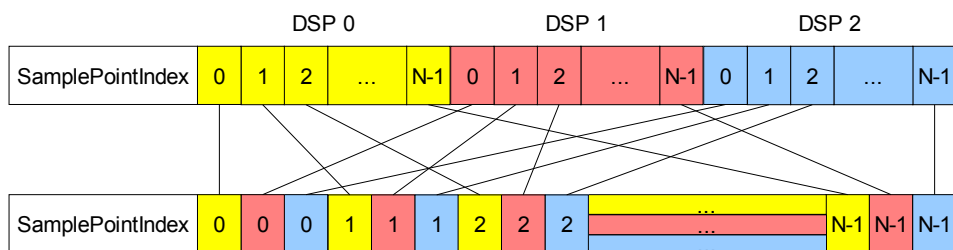


Figure 22: Reorder merged data blocks.

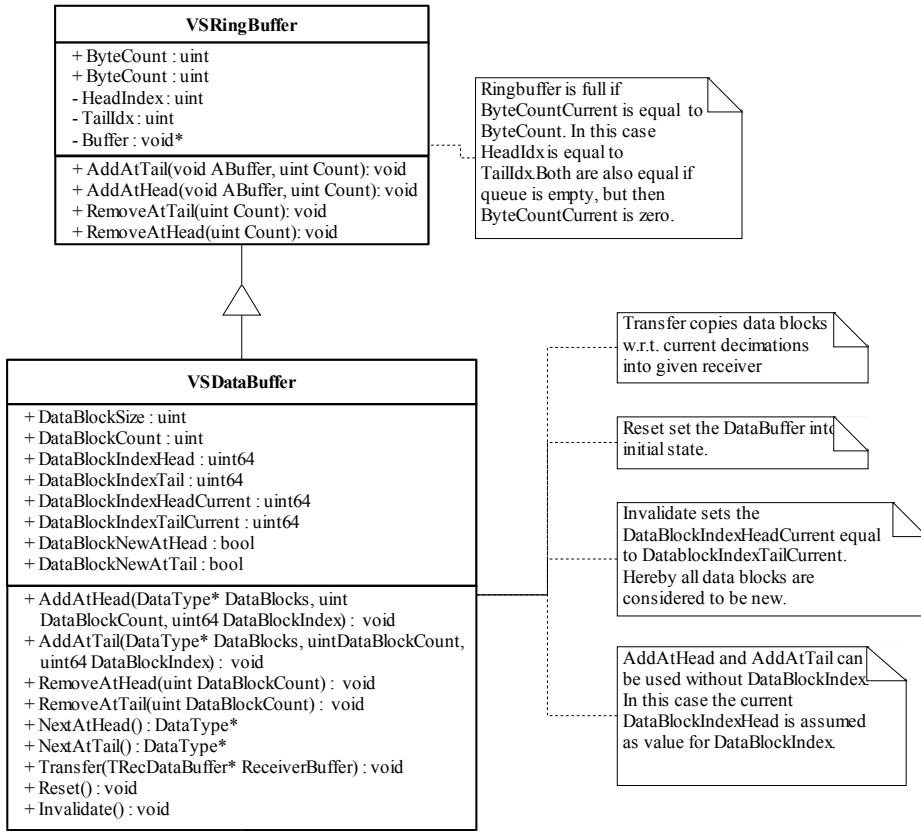


Figure 23: VSDataBuffer und VSRingBuffer

### 4.3 Dialogs and visualization modules

In the following sections we describe the graphical user interface of the data acquisition software.

#### 4.3.1 Main Window

After the program has been started the main panel which is shown in Figure 25 appears. The main panel contains a row of buttons and the browse bar. The buttons are divided into three groups. The first group of buttons (green symbols) is used in playback mode. The user can open an experiment with the leftmost button (green arrow up over rectangle) and is closed with the green cross button. The buttons for Stop, Play forward, Pause, and Play backward use the well-known symbols which we find on CD players. The next group of buttons with red symbols is used during data acquisition. The red star button opens the dialog for configuring a new experiment. After experiment configuration, which is described in the next paragraph, the user can start the data acquisition either in play or in record mode with the red play or record

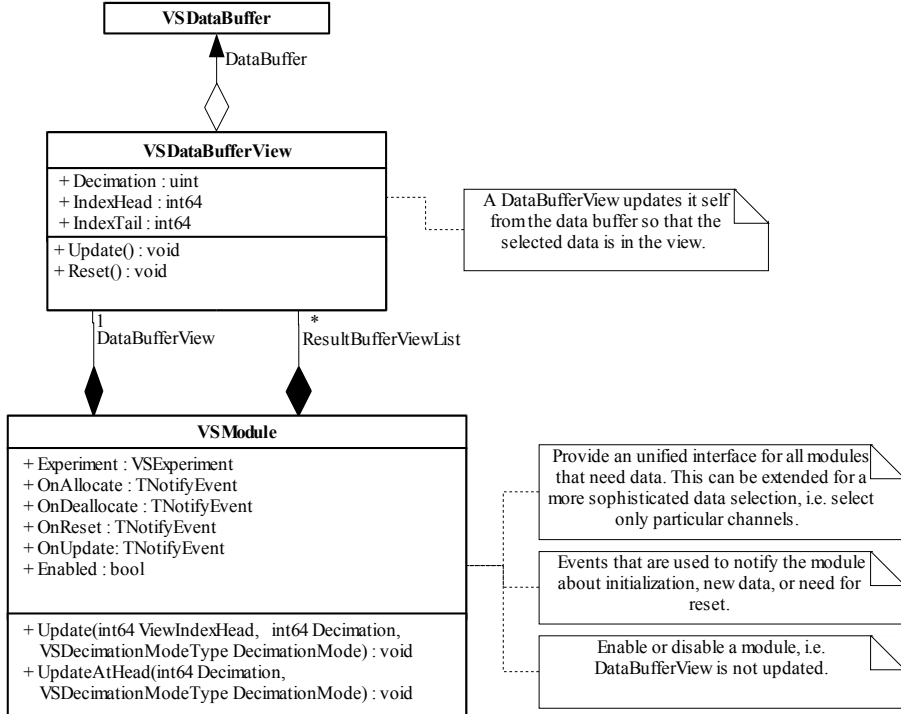


Figure 24: VSDataBuffer, VSDataBufferView, VSModule

button, respectively. In play mode data is acquired but not saved to disk, in record mode the data additionally stored to disk. The user can switch between record and play mode. Hereby a new section is generated, each time the user switches from play mode into record mode. With the red cross button the experiment can be stopped. With read arrow down the DSP application is started on the data acquistion hardware. with the red questionmark button one can test if the DSP application is working properly. The third group of buttons provides access to various tools and features. By click on the wrench button one can create analyzer instances which apply different filter or analysis methods to the current signal. Details about analyzer configuration are given in Section 4.3.10. The next button in the row open blueplot, scope, spectrogram, spike plot visualization dialogs, which are described in the next sections. Additionally the amplifier setup dialog can be opened with the button showing an amplifier symbol. The last button in the row quits the application.

#### 4.3.2 Reviewing Experiments

An experiment is opened using a default file selection dialog which is activated on pushing the green arrow up button. Parameters of the experiment are retrieved from file and the visualization modules are shown. The playback is controlled by the buttons with green symbols, which are adopted from symbols used for tape decks or cd players. The left and right arrow buttons start playback in backward or forward direction. The

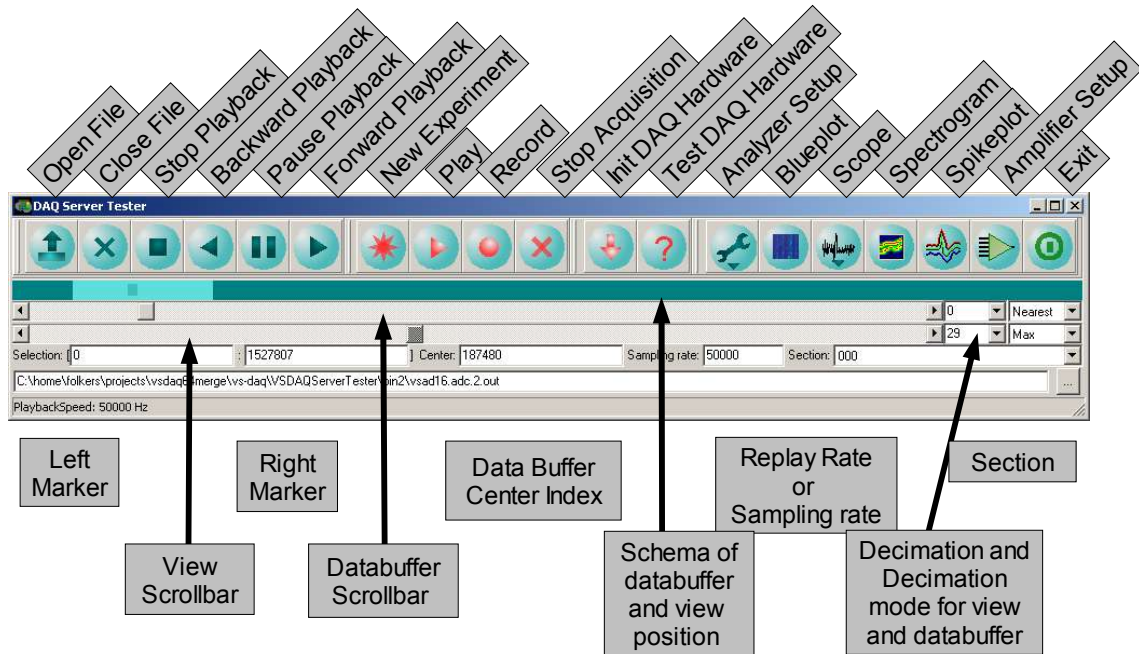


Figure 25: Main panel

button with two vertical bars pauses the playback and the rectangle button stops the playback.

More sophisticated browsing is provided by the browse bar, which is below the large buttons and which consists from top to bottom of an overview schema, a scroll bar for rough navigation and a scrollbar for fine navigation. On the right side of fine navigation scroll bar a combo box which controls the decimation of the shown data, i.e. one can change the time scale with this parameter. A decimation value of e.g. 1 implies that only every second value is shown which corresponds to a time scale of 2. In the rightmost combobox one can choose the method used for decimation. If the mode is set to nearest, the signal at multiples of decimation+1 is shown, if it set to max, then the maximum between muliples of decimation+1 is shown. The bottom row contains edit fields to set the selection manually and to jump to a certain position. Additionally, the playback frequency can be modified.

The overview schmema illustrates three things:

- Selection within the current experiment section
- Part of the experiment section which is currently in memory, i.e. the data buffer
- Position of the current view within experiment section

A click with the left mouse button onto the schema sets the left selection marker and a click with the right mouse button onto the schema sets the right selection marker.

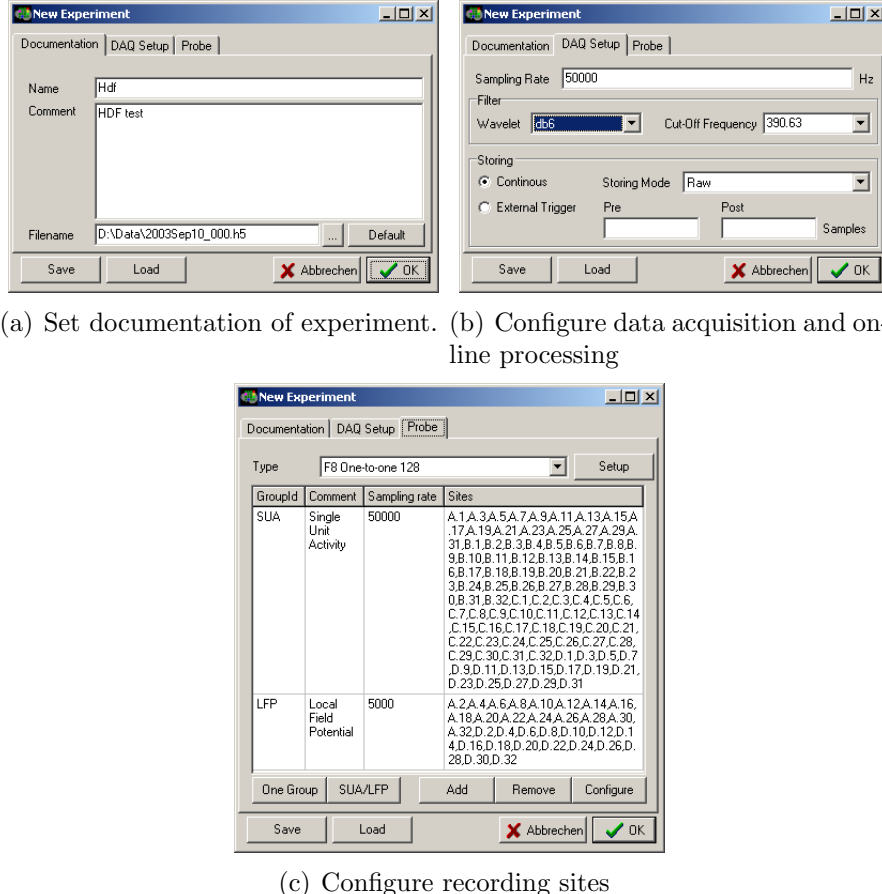


Figure 26: Configure a new experiment

Holding the mouse buttons and moving the mouse moves the selection marker accordingly. Selection and data buffer position are independent from each other.

The data buffer position is moved with the scroll bar below the schema. While the scroll bar thumb is moved the new position of the data buffer is indicated in the schema. As soon as the scroll bar thumb is released the data buffer is actually updated.

The view position is modified by the second scroll bar of the browse bar. On moving the scroll bar thumb visualization modules are steadily updated.

The visualization modules are opened with the buttons at the upper right corner of the main window. A visualization module is closed by pressing the respective button if it is already open.

### 4.3.3 New Experiments

In the new experiment dialog is organized in three pages, i.e. Documentation, DAQ Setup, and Probe shown in Figures 26(a), 26(b), and 26(c).

- Documentation (Figure 26(a))

**Name** Experiment identifier

**Comment** A comment which should summarize the overall setting of the experiment

**Filename** File where the experiment will be stored. There are two files per experiment. The .vse file which contains the experiment description, and the .rawdata file which contains the raw data. The name is generated by default using the structure <year><month><day>\_<number>. One can also select a filename in a file select dialog (push button with the three dots), or enter a name manually. Pressing the button Default generates a default name.

- DAQ Setup (Figure 26(b))

**Sampling Rate** The sampling rate can be chosen arbitrarily between 5 kHz and 50 kHz.

**Filter** A wavelet can be selected with a certain cut-off frequency. The possible cut-off frequencies depend on the sampling rate and can be computed as sampling rate divided by 2 to the power of decomposition depth. Currently decomposition depth is restricted to a maximum of 6, corresponding to six available cut-off frequencies.

**Storing** There are two options for data acquisition, i.e. continuous and triggered acquisition. In case of continuous data acquisition the application stores all sample points to hard disk. In this case the user can also choose if raw data, filtered data, and wavelet coefficients shall be stored. The filter settings are defined in the site group setup available on the probe page. If the data should be acquired based on a trigger, one must set the External Trigger radio item. Triggered data acquisition supports only raw data. In the Pre and Post edit fields the number of sample points for pre- and post-trigger interval are set.

- Probe (Figure 26(c))

**Type** The probe which will be used in the experiment can be selected. Beside the predefined probes one can setup own designs in the probe setup dialog which can be reached with the Setup button. It is described in Section 4.3.4.

**Site Groups** Each recording site provided by the selected probe can be assigned to a single site group. A site group in turn is associated with acquisition parameters which apply for all sites in the site group. The Probe page shows all site groups in a spreadsheet containing from left to right the site group identifier, a comment, the sampling rate used for storing and the sites assigned to the group. The buttons at the left lower corner of the spreadsheet create two default setup. One Group creates a single site group which contains all available sites and SUA/LFP creates two groups with

appropriate comments, however, the sites need to be assigned in the site group configure dialog. A new site group is added with the Add button and an existing site group is removed with the Remove button. Configure opens the site group setup dialog which is described in Section 28. Remove and Configure are applied to the currently selected site group in the spreadsheet.

With the Save and Load buttons the complete experiment parameters can be stored in a or retrieved from a file which should have the extension \*.esp. If a file default.esp exists in the working directory of the application this default experiment settings are loaded from this file on startup. Therefore, the user can store any setting with this name in order to obtain the favourite settings. Experiment settings can also be stored with other names.

With button OK the experiment settings are accepted. A new experiment is created and the DSP application is initialized appropriately. If this was sucessfull, a message in the status bar of the main window indicates how to proceed, i.e. press the Play or Rec button to start acquisition, or press the Stop button to cancel. Close the dialog New Experiment with button Cancel, when no new experiment should be created.

#### 4.3.4 Probe Setup

Within the probe setup dialog new designs of probes can be entered or existing designs can be edited. The interface assumes that a probe has one or more shafts, where each shaft is occupied by a certain number of recording sites, which in turn are vertically oriented on the shaft.

Therefore, the dialog shows three lists: At top the list of probes, in the middle the list of shafts of the currently selected probe and at the bottom the list of recording sites of the currently selected shaft. In the table which has the input focus the currently selected item is marked by a dashed line around a cell in the row, in both other tables the selected items are marked by a blue background of one cell in the row. On the left of each table there are three buttons, which create a new item, delete an item, or duplicate an item in the respective table. For example to enter a new probe of type F1 one would select a present instance of F1 and duplicate it. It is appended at the end of the list of probes and can be selected. Now one can enter a new comment or number and modify the shaft and site configuration with respect to the acutal probe. The position of the shaft is defined by the position of its tip. The position of each recording site is specified by

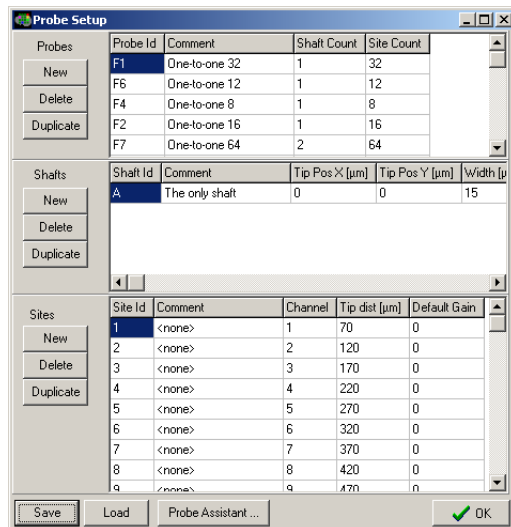


Figure 27: Probe setup dialog

the distance to the tip of the shaft. Given these informations the spatial relation of two recording sites can be derived easily. Additionally, the mapping of recording sites onto channel number is defined in this dialog. Note, that channel numbers start at 1.

The Probe Assistant button opens a dialog where one can enter the design parameters of a probe in order to generate such a Probe for the probe setup dialog. With the Load and Save buttons collections of probes can be retrieved from or stored into a file on disk, respectively. OK closes the probe setup dialog.

#### 4.3.5 Site group setup

Recording sites are assigned to a site group in the site group setup dialog (Figure 28). It contains a list of available sites and a list of site already assigned to this site group. With the arrow buttons one can add or remove one or multiple sites to and from the site group. The group identifier and a comment can be set in the respective edit field. A decimation value can be defined, which basically determines at which sampling rate the data will be stored. If decimation is zero every sample is stored, for decimation equal 1, every second sample is stored, and so on. Finally, one can set a filter for the site group which can either be a high pass, a low pass, or a all pass, i.e. no filter. The cut off frequency is specified in the DAQ Setup page of the New Experiment dialog. If the filter has been disabled at this place, then the filter configuration of the site group will be ignored.

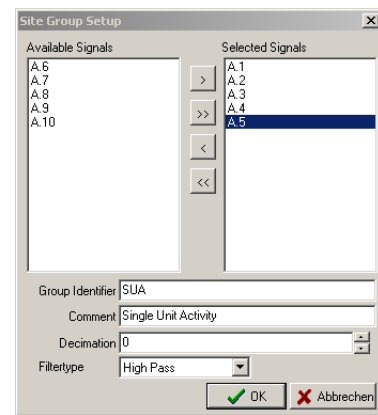


Figure 28: Site group setup dialog  
The gain of each site of the current probe can be set in the amplifier setup. A schema of the probe is drawn in the upper half of the window as shown in Figure 29. The

#### 4.3.6 Amplifier Setup

The gain of each site of the current probe can be set in the amplifier setup. A schema of the probe is drawn in the upper half of the window as shown in Figure 29. The

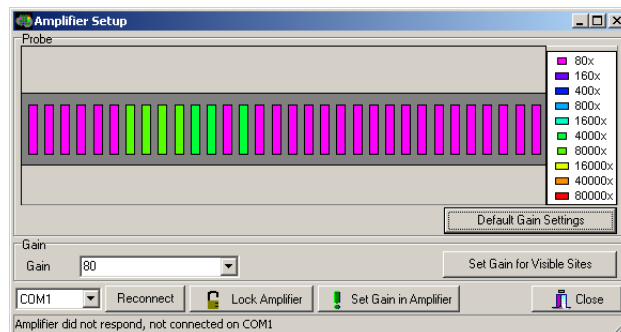


Figure 29: Amplifier setup dialog

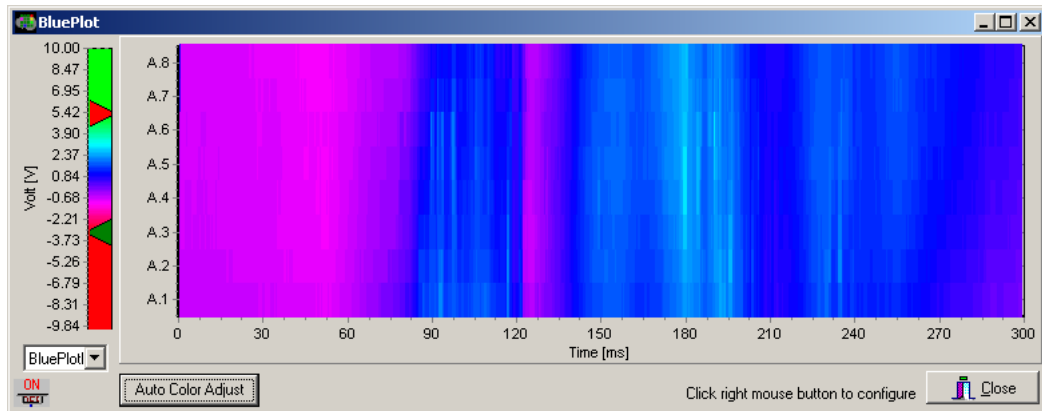


Figure 30: Blueplot

gain value can either be selected by using the gain combobox or by clicking onto the legend. The current setting of a gain value is indicated by different colors for each site. Each probe has a default gain value setting which can be set pushing the Default Gain Settings button. A set of sites can be selected by zooming into the schema of the probe such that only the desired sites are visible. Then the desired gain can be set for these sites using button Set Gain for Visible Sites.

The dialog is synchronized with the setting at the main amplifier, i.e. manual changes at the amplifier are visualized by the dialog and vice versa. The data is send via a serial port which can be selected in the combobox in the lower left corner. The connection to the amplifier is established by a click on the Reconnect button. Manual changing of the gain at the main amplifier can be locked using the button Lock Amplifier. The button indicates the current state by showing the text "Locked" or "Unlocked". The gain settings are transferred to the amplifier when the Set Gain in Amplifier button is pressed.

#### 4.3.7 Blueplot

The blueplot shows the signals of the selected sites simultaneously. Hereby the amplitude of each channel is coded by color. On the x-axis the time scale is shown, and the y-axis indicates the site names. Note, that some site names may not appear, if there is not enough room. The time label can be either the sample point index or time in seconds, milliseconds, or microseconds.

On the left a colormap is displayed. The color mapping can be controlled by mouse using the sliders in the colorbar. They define the range of data values which is mapped onto the colors. If the range has length zero, the sliders define a threshold. It is also possible to change the color map using the combo box at the bottom of the color bar. With the Auto Color Adjust the color mapping is adapted to the values, which are currently displayed. The mapping is adjusted such that the median of the values is mapped on the center color and the minium and maximum values are set to a multiple

of mean squared median deviation (Scale factor is currently equal four).

With a click of the right mouse button into the blueplot the trace setup popup menu appears. New traces can be added and existing ones can be removed. To each trace a recording site or results produced by current analyzers can be assigned. The setup can be cleared, loaded, or stored. Furthermore a default trace setup can be generated, in which there is a trace for each recording site, such that the blueplot shows all recordings as default. The default setup is also used in the beginning.

#### 4.3.8 Spectrogram

The spectrum of a single channel is visualized with the spectrogram. The selected channel is transformed by a short time windowed Fourier transform and the log magnitude of the coefficients is displayed, with respect to the selected mode. The spectrogram has two modes: the time frequency mode and the waterfall mode which are shown in Figure 31 and 32, respectively. In time frequency mode the time scale is on the x-axis and the frequency on the y-axis. The log magnitude of the coefficients is coded into a color. This color mapping can be adjusted with the color bar on the left side. The time frequency mode visualizes the spectrum over a long period of time. In waterfall mode the frequency is indicated by the x-axis and the log magnitude on the y-axis. The magnitude of each coefficient is represented by a bar of respective height. Each bar has a little dot on top which indicates the maximum of this bar during the last few windows (currently three windows, at a window size of 512 samples for the Fourier transform). We provide five different windows, i.e. Rectangle, Hanning, Hamming, Blackman, and Bartlett window (see also Section 5.1). The waterfall mode shows the spectrum only over a short period, but visualization of peaks is better then in the time frequency mode.

Futhermore the spectrogram includes a zoom function, which enables the user to focus on a certain frequency range. This improves the detection of peaks. The frequency range is specified in the respective edit fields and it used when the user pushes the Apply button.

The spectrogram is useful to locate noise sources which cause peaks at certain frequencies. The example in Figure 31 shows a wide peak between 2.5 and 3.5 kHz and a narrow one at about 300 Hz, both are also visible in Figure 32. So this information can be at least a hint which device might cause the noise. Also spike activity is visible as the Fourier coefficients bin the range of 300 up to 1.5 kHz have a higher magnitude during spike activity.

#### 4.3.9 Scope and Scope Setup

The host application supports muliple scope with independend configurations. A click on the scope button on the main panel opens a popup menu which is shown if Figure 33. The user can add a new scope with the Add Scope menu item or remove all scopes with the Clear entry. Currently available scopes are shown at the bottom of the popup menu. Each Scope menu entry has the same submenu where the user can remove,

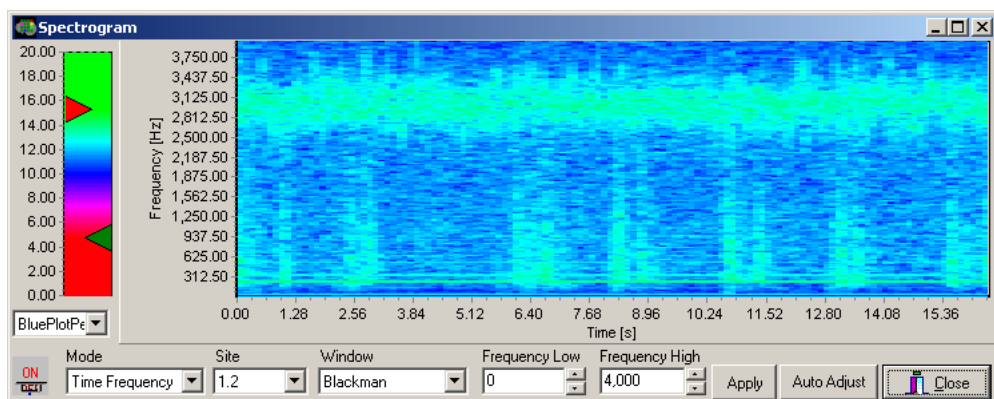


Figure 31: Spectrogram in time frequency mode

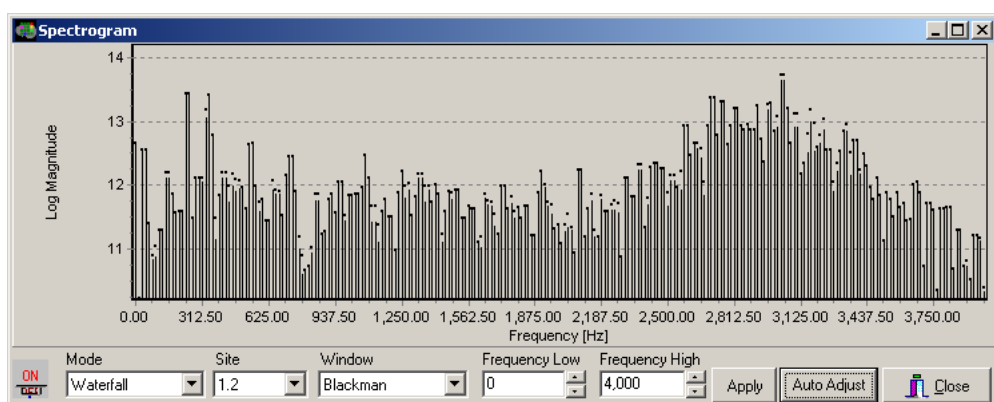


Figure 32: Spectrogram in waterfall mode

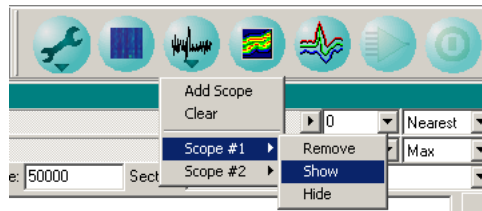


Figure 33: Scope popup menu with two available scopes

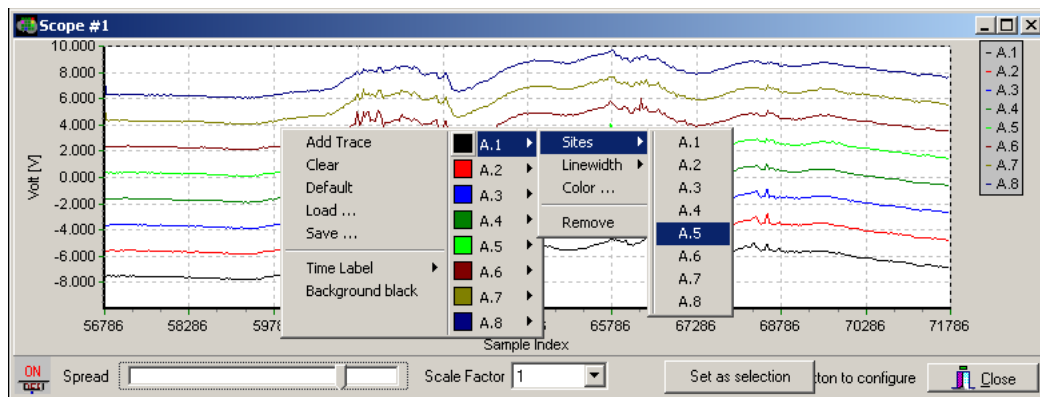


Figure 34: Scope showing 8 channel of neural recording, where the user is about to assign recording site A.5 to trace 1 using the trace setup popup menu.

show, or hide the respective scope.

With the scope (Figure 34) one can visualize the signals of several selected recording sites. The scope supports an arbitrary number of traces only limited by the host resources, and each trace has independent settings for recording site, color, and line width. These parameters are set in the scope trace setup popup menu, which can be reached by a click with the right mouse button into the scope dialog. Figure 34 shows how recording site is assigned to the a trace. In the present case recording site A.5 is about to be assigned to the first trace. Similarly the line width and the color can be changed in the Color and Line Width submenu. Time axis label can be set to be either the sample index or the time in seconds, milliseconds, or microseconds. The background color of the scope can be toggled between white and black with the respective menu item in the scope trace setup menu. A scope setup can be stored into a file and retrieved by using the Save and Load menu items, respectively. Additionally, one can clear the whole setup and one can also generate a default setup, which has a trace for each recording site used in the experiment. Finally, the results of present analyzer items can be assigned to traces. With this feature the user can directly compare input and result signals.

The traces can be spread or overlaid with the Spread track bar in the lower left corner of the scope dialog. A global scale factor can be selected from the Scale

combobox, which is applied to all traces before visualization. Note, that the units on the y-axis are also scaled w.r.t. the global scale factor.

The scope has a zoom feature, i.e. the user can select a rectangular region within the scope axis, which is in turn enlarged. The region is specified by pressing the left mouse button at the upper left corner of the rectangle and holding it while the mouse is moved to the lower right corner, which is pinned down by releasing the left mouse button. Note that it is important to specify the upper left corner first, because specifying any other corner first invokes the unzoom function.

#### 4.3.10 Analyzer Setup

Offline analysis is supported through so called analyzer objects. An arbitrary subset of signals from recording site form the input of an analyzer object and depending on the method assigned to the analyzer it produces a set of results. Currently, the result can either be new continuous signal or a list of time stamps. However, the implementation can be extended to support also other result types. Figure 35(b) shows the popup menu which opens on click onto the wrench button in the main panel. With the Add Analyzer entry the user opens the dialog with which an analyzer object can be configured. The dialog is shown in Figure 35(a). On the left side the available signals, i.e. the raw data of the experiment, are shown, while on the right side a list shows which signals have been selected as input into the analyzer object. The Method combobox shows the selected analyzer method, e.g. filter, denoising, or spike detection. In the name edit field the user can enter a descriptive for this particular analyzer. However, this field has also a default value. The Cancel button closes the dialog without any further action. With Ok a new analyzer object is created, if at least one input signal has been specified.

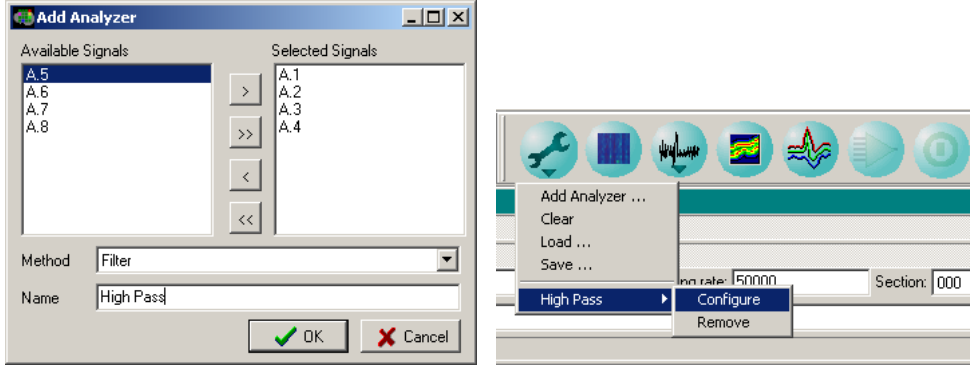
Referring again to Figure 35(b) the new analyzer object is represented by a new entry at the bottom of the popup menu. With the submenu of this entry one can reach the configuration dialog of the analyzer object. The configuration dialog depends on the selected method.

#### 4.3.11 Spike Plot

In the spike plot (Figure 37) the spikes of a single recording site are visualized. Hereby the maximum and minimum hull, and the average over all spikes is shown. Spike events are detected by threshold passing. The threshold can be applied directly to the magnitude of the raw data values or to the result of the non-linear energy operator (NEO) with subsequent averaging [3]. The NEO is defined as

$$x_{neo}(n) = x(n)^2 - x(n-1)x(n+1). \quad (2)$$

The values in  $x_{neo}$  become large if the input signal  $x$  changes rapidly. The operator acts as a high pass filter. The results must be averaged to eliminate peaks which are due to noise. We obtain the result in Figure 36 by averaging with a 20 tap Bartlett window. The upper trace shows the neural recording (50 kHz at 16 bit) while the lower



(a) Configure a new analyzer object.

(b) Analyzer setup popup menu

Figure 35: Analyzer Setup

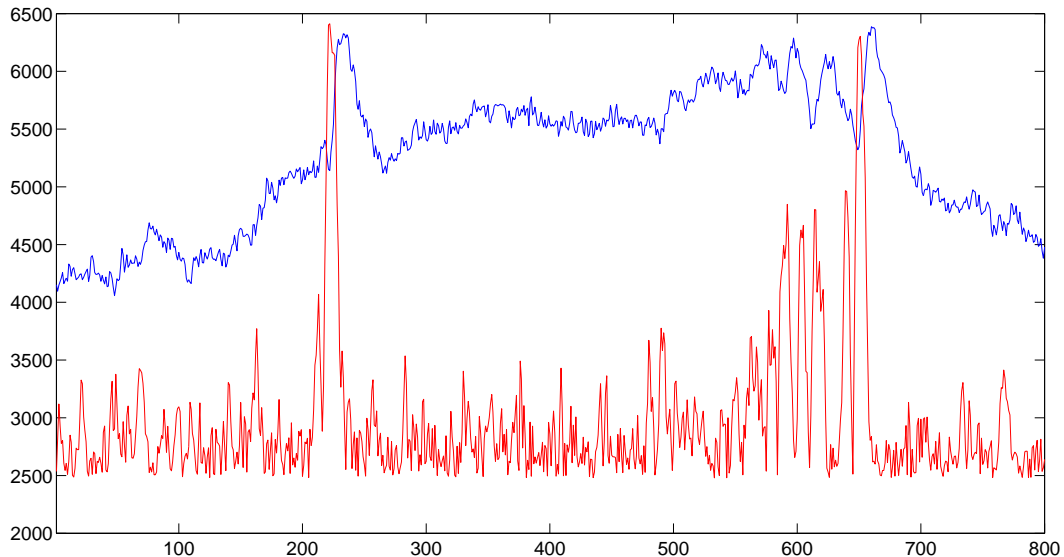


Figure 36: Non linear energy operator

trace shows the NEO result which is devided by  $2^8$  in order to move it into the same value range as the neural recording.

The threshold can be determined with the red and green triangles on the left axis which correspond to a maximum or minimum threshold, respectively. Note, that they are symmetrically as the detection is applied to the magnitude of the raw data. If a threshold is changed the spike plot is cleared automatically. To clear it manually push the Reset button. The length of the snippets around a spike in sample points can be set in the Length edit field. Select the recording site with the combo box.

#### 4.4 Wavelet denoising setup

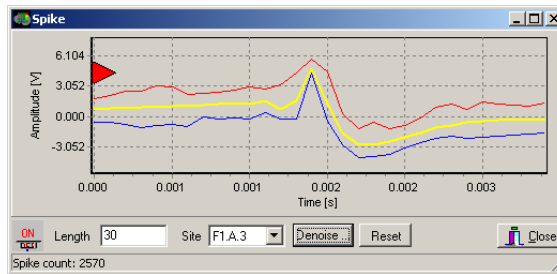


Figure 37: Spike plot

The wavelet denoiser as described in Section 5.7 has several parameters which are set in the wavelet denoising setup dialog. The setup dialog is depicted in Figure 38 and shows the specific setup which was used to obtain the result in Figure 39. In particular the following parameters can be set:

**Wavelet Type** Select the actual wavelet, such as e.g. "Daubechies 4". Currently db2, db4, and db6 are supported.

**Precision** Wavelet coefficients can either be in 32 bit floating point (single) precision or in 16 bit integer precision.

**Level Count** Select the number of levels of the wavelet decomposition. This number determines the number of frequency bands available. You can select levels from 1 to 6.

**Window Length** The window length is the number of samples which should be used to estimate the thresholds. Note, that some threshold estimators only use the window length and the noise estimation.

**Threshold Estimator** There are four different strategies available to estimate the thresholds, i.e. MiniMaxi, VisuShrink, Sure, SureShrink. For a detailed description refer to Section 5.7

**Threshold Method** Either "hard" or "soft" can be selected. Hard threshold means that all coefficients less than the threshold are set to zero and all others are kept as is. In case of soft thresholding the magnitude of coefficients which are greater than the threshold is reduced by the threshold.

**Thresholding Mode** Choose between continuous or single. In continuous mode the thresholds are computed for each window, in single mode the thresholds are com-

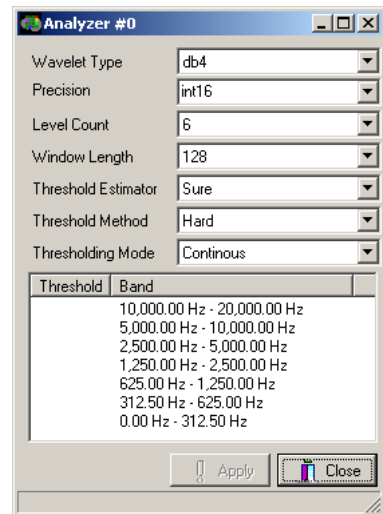


Figure 38: Wavelet denoising setup. You can select levels from 1 to 6.

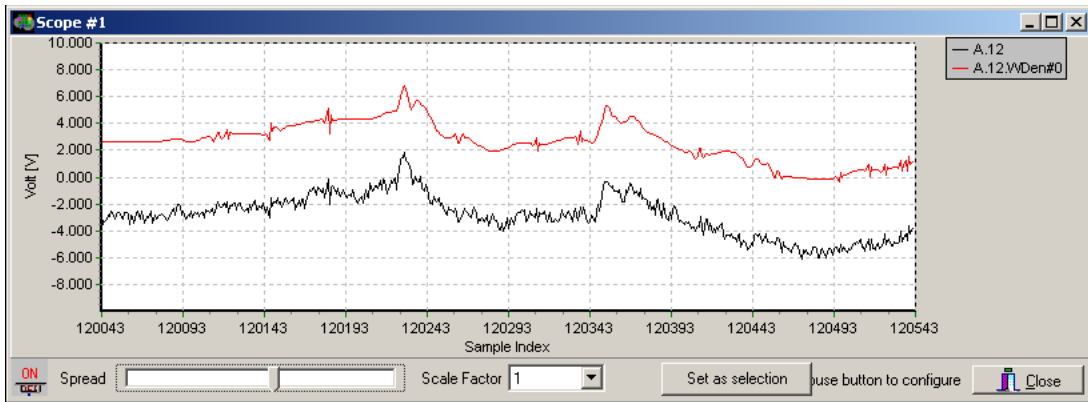


Figure 39: Wavelet denoising

puted for the first window and then used for the subsequent windows without change. One can force a recomputation by pressing button "Recalc".

**Threshold** The current thresholds with their respective frequency band are shown and can be changed by the user. The thresholds can range between 0 and 32768. However in continuous mode they keep on changing, and therefore manual change of the thresholds make only sense in single mode. In particular the threshold for the lowest frequency band can be set to 32768 in order to obtain a high pass filtered denoised signal.

## 4.5 Linux Port

We tried to port the host application to work under Linux. The basic idea was to use the CLX class library from Borland which is very similar to the currently used class library VCL. However, several issues occurred which finally prevent the success of this port:

- Drivers for DSP hardware did not work as supposed
- Kylix does not work properly under current Linux distribution. It needs Redhat 7.2, a fact that is not well documented and which turned up after trying Suse 8.1 and Redhat 8.0.
- Compiler features were not available under Kylix, but needed for code reuse
- The important class TChart was not available as CLX Version under Windows.

As a conclusion we could state, that a port is theoretically possible, however it would take a huge effort to circumvent all the tool and driver related issues.

## 5 Online Processing

### 5.1 Fourier transform

The spectrogram is based on the short time Fourier transform which is computed within the host application. The short time Fourier transform is implemented by a fast discrete Fourier transform applied on certain time window of the signal. Thus we compute the coefficients  $S_{w,d}(k)$  which depend on the window function  $w$  and the time window of signal  $s(n)$  selected by offset  $d$ :

$$S_{w,d}(k) = \sum_{n=0}^{N-1} s(n+d)w(n)e^{-j(2\pi/N)nk}$$

The length  $N$  of the window is chosen as a power of 2, and it determines the resolution in frequency domain, i.e. the width of the frequency band represented by a single Fourier coefficient. We provide different windows taken from [4], which are described in the following, whereby  $M = N - 1$ :

#### Rectangular

$$w(n) = \begin{cases} 1, & 0 \leq n \leq M, \\ 0, & \text{otherwise} \end{cases}$$

#### Bartlett (triangular)

$$w(n) = \begin{cases} 2n/M, & 0 \leq n \leq M/2 \\ 2 - 2n/M, & M/2 < n \leq M \\ 0, & \text{otherwise} \end{cases}$$

#### Hamming

$$w(n) = \begin{cases} 0.54 - 0.46 \cos(2\pi n/M), & 0 \leq n \leq M, \\ 0, & \text{otherwise} \end{cases}$$

#### Hanning

$$w(n) = \begin{cases} 0.5 - 0.5 \cos(2\pi n/M), & 0 \leq n \leq M, \\ 0, & \text{otherwise} \end{cases}$$

#### Blackman

$$w(n) = \begin{cases} 0.42 - 0.5 \cos(2\pi n/M) + 0.08 \cos(4\pi n/M), & 0 \leq n \leq M, \\ 0, & \text{otherwise} \end{cases}$$

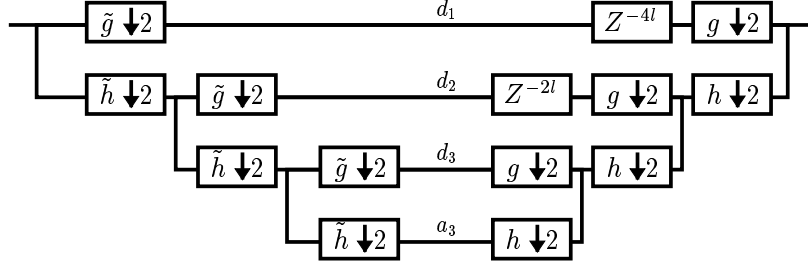


Figure 40: Filter bank with three levels.

## 5.2 Wavelet transform and lifting scheme

The signal is decomposed into  $N+1$  subbands by a  $N$ -level wavelet transform (WT). The subbands  $d_j, j = 1, \dots, N$  represent the frequency band  $[F/2^{j+1}, F/2^{j+2}]$  and the subband  $a_N$  represents  $[0, F/2^{N+1}]$ . Fig. 40 shows the filter bank for  $N = 3$ . In each step the signal is decomposed by applying complementary filters to  $a_j$ , i.e. a high pass  $\tilde{g}$  and a low pass  $\tilde{h}$ , which are determined by the selected wavelet. The results of both filter operations are subsampled by a factor of two, leading to subbands  $d_{j+1}$  and  $a_{j+1}$ . Note, that the number of coefficients in  $d_{j+1}$  and  $a_{j+1}$  is equal to the number of coefficients in  $a_j$ . The wavelet transform is implemented using the lifting scheme which is faster than the standard implementation (Fig. 40). It is done in-place, and with a small modification it implements a WT that maps integers onto integers [1] while preserving the possibility of perfect reconstruction. Therefore, this implementation of the WT is well suited for realtime processing using digital signal processors (DSP).

The lifting scheme provides another point of view to the wavelet transform. Basically it consists of three stages, which are a *split*, a *predict*, and an *update* stage as illustrated in Fig. 41 [5]. First the signal is split such that we obtain two sequences  $d_j$  and  $a_j$  which in our case consist of sample points with odd and with even indices, respectively. Now, we predict the values in  $d_j$  based on  $a_j$  as  $P(a_j)$ . Under the assumption that the signal is continuous we have a good chance that our prediction is rather close to the actual values. We compute the difference between prediction and actual

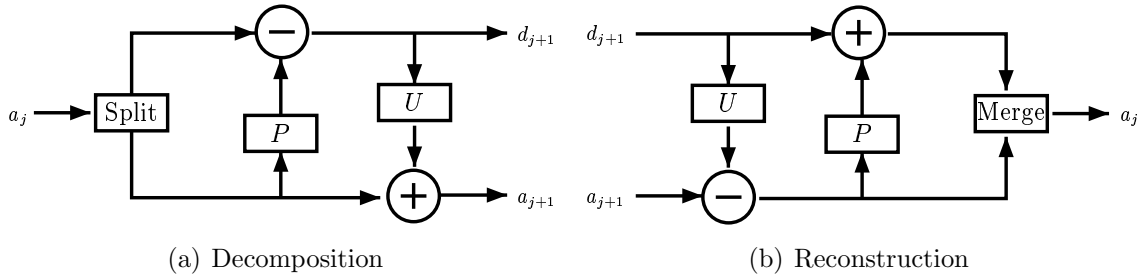


Figure 41: Basic structure of the lifting scheme

values, and keep these values which are likely to be small:  $d_{j+1} = d_{j+1} - P(a_{j+1})$ . In order to preserve certain properties of the original signal in the coefficients  $a_j$  e.g. the mean value, we need the third stage, which is the update stage. Hereby, the values in  $a_j$  are modified by using an appropriate update operator on values in  $d_j$  and  $U(d_j)$ :  $a_{j+1} = a_{j+1} + U(d_{j+1})$ .

The perfect reconstruction property of the lifting scheme is obvious, because we can obtain  $a_j$  from  $a_{j+1}$  and  $d_{j+1}$  by inverting the data flow and the signs as shown in Fig. 41(b). Note, that this holds for arbitrary predict and update operators. Therefore, if these operators include a rounding to the next integer we obtain a wavelet transform that maps integer onto integers. It is possible to implement arbitrary wavelet transformations as shown in [1] by using multiple prediction and update operators successively. The respective operators are computed according to the given mother wavelet.

Using the lifting scheme and a routine optimized for our DSP, we can apply a six level Daubechies 2 decomposition filter bank on 32 channels sampled at 50 kHz in real time.

### 5.3 Wavelet FIR filter to lifting scheme

The Daubechies wavelets and also other wavelets are usually available as two FIR filters a high and a low pass filter which can be directly used for implementation using convolution with subsequent downsampling. These coefficients of these filters can be used to derive the equivalent lifting scheme. It would be out of scope of this paper to explain all the details, however, we will outline the semiautomatic generation of lifting steps given the wavelet as FIR filters. A tool programmed by C. Valens, who also wrote a tutorial about the lifting wavelet transform ([6]), is used to generate all possible decomposition into lifting steps, given the FIR filters. The result is stored as a text file. The number of possible decompositions grows exponentially in the order of the FIR filters. We need to pick one of the computed decompositions. Hereby, the computed decompositions need to be processed further. In this processing, which is implemented in Matlab, we try to extract a constant K from the first step, which is, however, not possible in every case. Only decompositions from which we can extract a constant can be used. At this point one needs to choose a decomposition manually, which at the moment is a try and error procedure, but could be put onto an objective basis by computing features for each decomposition like e.g. number of factors, maximum shift, or range of the constants. With a particular decomposition one can generate source code, which can either be C-Code, C6701 Linear Assembler, or Pentium III Assembler. There are prepared templates to compile the C version such that one can use the generated implementation from Matlab and compare the results with the corresponding implementation in the Matlab wavelet toolbox. The code generation provides the choice between a version that computes floating point wavelet coefficients and another version that computes 16 integer coefficients, except for the linear assembler generation, which only supports the integer version.

The generated C code can be used in the host and the DSP application, linear assembler is only usable for the DSP application while the Pentium III assembler needs

at Pentium III or compatible processor to be executed. The host application source code has an interface which provides easy integration of generated Pentium III code (VSWaveletImplementationInt16, VSWaveletImplementationSingle).

## 5.4 Host versus DSP based wavelet transformation

Regarding the architecture of the data acquisition system we have the choice of performing the wavelet transformation with the DSP and host or only with the host. It turned out that the DSP is able to compute a db6 decomposition of depth 6 on 32 channels at 44 kHz and it is probably possible to compute the db4 decomposition at 50 kHz, though not yet tested. The reconstruction however remains the job of the host application in any case. It is an option to perform the whole processing on the host which has some advantages:

- Software maintainance is easier
- Memory usage is not a hard constraint, e.g. allowing floating point wavelet coefficients
- Speed increase of commonly available desktop CPUs can be easily utilized

On the other hand there are also advantages of the DSP:

- Reliability due to Real Time OS
- Scalability, if the number of channels is doubled from 32 of 64 this does not imply that the host CPU must also be twice as fast

A test with our host (Pentium III, 1GHz) showed that it was possible to record to disk from 32 channels at 50kHz and to perform a db4 wavelet decomposition and reconstruction on all channels. However, visualization was restricted. Therefore a system for 32 channels which performs the processing completely on the host needs at least a CPU in the category of (Pentium 4, 2GHz).

## 5.5 Integer versus floating point wavelet coefficients

The wavelet transform which maps onto 16 bit integer coefficients has the advantage that the result does not need more space. However, this advantage is accompanied by some disadvantages. With using the lifting scheme we preserve the perfect reconstruction property of the whole filterbank. However, the coefficient values need to be kept in the 16 bit range. By default the values of the wavelet coefficients after one step can be by factor  $\sqrt{2}$  larger than the input values. In order to prevent this overflow the implementation scales the approximation coefficients by  $1/\sqrt{2}$  and the detail coefficients by  $\sqrt{2}$  assuming that the details are likely to be small. However, it turned out that there are some cases, i.e. input signals with high amplitude and high frequency, an overflow in the detail coefficients occurs. This can be avoided



Figure 42: Low pass filter implemented with a wavelet filter bank. The lower black trace shows the original signal, the middle trace the db4 low pass filtered , and the upper trace the db2 low pass filtered version. The frequency bands 6.25-25kHz have been discarded.

by decreasing the scale factor even further. On the other hand this scale factor introduces large quantization errors, which become unacceptable e.g. in case of our db6 implementation.

This issue can be avoided if we do not compute integer coefficients, but 32 bit floating point coefficients. These will use twice as much memory, but the scaling described in the previous paragraph is not necessary, and therefore the quantization error is reduced. An additional advantage is that the floating point version is faster to compute since it does not need the rounding operation in each lifting step.

## 5.6 Low pass, band pass, and high pass wavelet filter

We can use the wavelet coefficients to implement low pass, band pass, and high pass filter. This is simply done by setting the coefficients to zero, which represent the frequency band, that we want to suppress. We yield for instance a high pass filter if we set the coefficients  $\lambda_{n-1}$  to zero, and a low pass filter if the coefficients  $\gamma_0$  are eliminated. One drawback of this method is that we cannot choose the cut off frequencies for the high pass, band pass, or low pass filters arbitrarily. Instead we are restricted to positions that are presentable as sampling rate divided by  $2^j, j > 0$ . However, this restriction does not seem to be a problem for applications in neural recordings. In Figure 42 an example of a low pass filtered signal is shown.

## 5.7 Wavelet denoising

The wavelet denoising works on the coefficients computed within the filter bank. The first step is the estimation of the standard deviation of the noise, which is supposed to have a Gaussian Distribution. We use the detail coefficients of the first step for

this estimation, since these coefficient mainly represent the noise if noise is present. The standard deviation is estimated within a time window of given length  $N$ :  $\hat{\sigma} = \text{Median}(|\gamma_{0,k} : k \leq k < N|)/0.6745$ . This median estimator is robust against outliers in the coefficients, that represent the signal instead of noise. All detail coefficients are divided by  $\hat{\sigma}$  and we obtain coefficients with normally distributed Gaussian noise. Using these coefficients we estimate the thresholds.

Currently there are four different strategies available to estimate the thresholds. They are described in the following tabular. Threshold are estimated within a time window and we denote the length of the window with  $N$ . The level is denoted by  $j \in 1, \dots, n$  and the threshold for a certain level with  $T_j$ .

MiniMaxi	$T_j = \begin{cases} 0 & N/2^j \leq 32 \\ 0.3936 + 0.1829 \log_2(N/2^j) & \text{otherwise} \end{cases}$
VisuShrink	$T_j = \sqrt{(2 \log(N/2^j))}$
Sure	Estimation of $T_j$ is based on Steins Unbiased Risk Estimate as described in [2]
SureShrink	Combination of Sure and VisuShrink where based on a certain criteria one of both strategies is selected. It is supposed to handle the case that the coefficients are sparse.

The threshold can be applied "hard" or "soft". Hard thresholding means that all coefficients less than the threshold are set to zero and all others are kept. In case of soft thresholding the magnitude of coefficients which are greater than the threshold is reduced by the threshold.

$$\eta_s(x, T) = \begin{cases} \text{sign}(|x| - T) & |x| > T \\ 0 & \text{otherwise} \end{cases}$$

Note, that soft thresholding reduces the magnitude of all coefficients, thus in general we will find a reduced maximum peak to peak amplitude in the denoised signal.

The wavelet denoiser has two threshold estimation modes, i.e. either continuous or single. In continuous mode the thresholds are computed for each time window of length  $N$  samples, in single mode the thresholds are computed for the first  $N$  samples, i.e. the first time window, and then used for the subsequent windows without change. This is somewhat faster, but the result is not as good as in the continuous mode.

We compare the denoising of a neural recording using different wavelets, i.e. Daubechies wavelets with 2 and 4 vanishing moments (db2 and db4). Both denoise setups are displayed in Figure 43. The filter bank depth was 5 and the time window had length 32. The thresholds were estimated by the Sure method and were applied "hard". For each time window new thresholds were estimated, as we used the continuous mode. Inspecting the result in Figure 44 we observe that the noise which is clearly visible in the upper trace is nicely removed in the lower trace, while the shape of the spikes was preserved. Note that the result of the db4 denoising is smoother than the result of the db2 denoising.

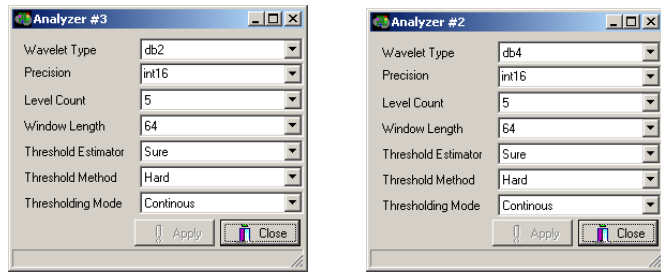


Figure 43: Denoising of a neural recording



Figure 44: Denoising with db2 and db4 of a neural recording

## 6 Summary

This workpackage has delivered a data acquisition system prototype which allows simultaneous recording from 128 channels. The software provides different means of visualization and online processing, like e.g. virtual scope, blue plot, and spectrogram. The graphical user interface has been greatly enhanced regarding design, usability, and speed. A semiautomatic tool to generate source code which implements wavelet decomposition and reconstruction filter banks based on the lifting scheme has been developed. It can generate C code and also optimized assembler code for Pentium III and compatible processors, as well as for the C6701 signal processor.

## References

- [1] I. Daubechies and W. Sweldens. Factoring wavelet transforms into lifting steps. *J. Fourier Anal. Appl.*, 4(3):245–267, 1998.
- [2] David L. Donoho and Iain M. Johnstone. Adapting to unknown smoothness via wavelet shrinkage. *Journal of the American Statistical Association*, 90(432):1200–1224, 1995.
- [3] K H Kim and S J Kim. Neural spike sorting under nearly 0 db signal-to-noise ratio using nonlinear energy operator and artifial neural network classifier. *IEEE Transaction on Biomedical Engineering*, 47:1406–1411, 2000.
- [4] A V Oppenheim and R W Schafer. *Discrete-time signal processing*. signal processing series. Prentice Hall, 1989.
- [5] W. Sweldens. The lifting scheme: A new philosophy in biorthogonal wavelet constructions. In A. F. Laine and M. Unser, editors, *Wavelet Applications in Signal and Image Processing III*, pages 68–79. Proc. SPIE 2569, 1995.
- [6] C Valens. The fast lifting wavelet transform. Tutorial, 1999.